VARIABILITY OF THE SUBTROPICAL FRONT IN THE TASMAN SEA

Robert Owain Smith

A thesis submitted for the degree of

Doctor of Philosophy

at the University of Otago, Dunedin,

New Zealand.

December 2017

Abstract

The subtropical front (STF) is a fundamental feature of the Southern Ocean. It separates waters in the subtropical gyres from Subantarctic waters. At present however only a rudimentary understanding exists about its temporal variability. Variations in the physical state of the STF (i.e. its location, intensity and hydrography) have implications for atmospheric circulation, marine productivity and climate. This thesis focuses on improving temporal understanding of this major Southern Ocean front. Observations of the temporal variability of the STF in the Tasman Sea are presented. These are obtained through a synthesis of repeat hydrographic sections and remotely sensed sea surface temperature (SST) and sea surface salinity (SSS) data. This work aims to contribute to an improved understanding of how the physical state of the STF varies in time, and of role that topography and surface winds play in this variability.

Using three hydrographic surveys and remotely sensed SST data collected during the austral autumns of 2007, 2008 and 2011, the interaction of the south subtropical front (S-STF) with topography around southern New Zealand is investigated. The poleward limit of the S-STF is found to be remarkably consistent, crossing the Macquarie Ridge north of a seamount at 49.6°S, before turning equatorward east of 166°E to follow the upper continental shelf. This is contrary to some previous descriptions that placed the S-STF lying across the Snares Shelf close to 47.5°S. Cross-frontal temperature and salinity gradients at the S-STF are also found to be intensified in regions of shallow bathymetry. Both results are attributed to topographic steering of the S-STF by bathymetry at approximately 500 m depth.

Thermal fronts detected using thirty years (1982-2011) of remotely sensed SST data are combined with 27 months (2013-2015) of remotely sensed SSS data, to provide new insights on the typical position and seasonal migration of the S-STF in the Tasman Sea. By examining thirty year annual-mean and seasonal-mean distributions of hundreds of thermal fronts that are identified as likely to be surface expressions of the S-STF, a long-term, statistical view of the S-STF's position in the western and eastern Tasman Sea is developed. It is apparent that seasonal migrations of the S-STF in these locations do not exceed 1°, contrary to a recent suggestion that the subtropical frontal zone undergoes a global, seasonal shift of 5-7°. The

distributions of thermal fronts also contain an intriguing suggestion that the S-STF might behave bimodally at the Macquarie Ridge.

SSTs across the S-STF south of New Zealand exhibit marked interannual variability. SST variability in this region may have significant impacts on regional climate. Recent studies have shown that variability in the basin-wide wind stress curl significantly influence SSTs in other parts of the South Pacific subtropical gyre. Using thirty years of remotely sensed SST and atmospheric reanalysis data, variability of subtropical and Subantarctic SSTs at the S-STF south of New Zealand are found to be significantly lag-correlated to both basin-wide and local-scale winds. Potential mechanisms linking SST with variations in the South Pacific wind field are also discussed.

Acknowledgments

I first wish to express my sincere thanks to my supervisor, Dr Ross Vennell, for his guidance, encouragement and support throughout this thesis. I am also deeply thankful to Dr Helen Bostock and Dr Mike Williams from the National Institute of Water and Atmospheric Research, New Zealand for their exceptional professional support and guidance as I have pursued this research. I am deeply grateful for the opportunities they have provided me to participate in the TAN1106 cruise and to collaborate with them both. It has been a huge privilege to work with them. I would like to express my gratitude to the Captain, Crew and Scientific staff for their valuable assistance in collecting the data on RV Tangaroa voyages TAN0704, TAN0803 and TAN1106. I would also like to thank the three reviewers for their helpful comments and suggestions on our paper.

I would also like to express my sincere thanks to Nick Rayner from the Met Office Hadley Centre, UK for encouraging me to pursue a PhD and for numerous rewarding discussions since my research journey began. I also gratefully acknowledge all the support and advice that has been given to me from many academic staff and students within the Department of Marine Science and the Department of Geology at the University of Otago. In addition, I wish to acknowledge Dr Patrick Hyder (Met Office Hadley Centre, UK), Dr David Smeed (National Oceanography Centre, UK), Dr Steve Chiswell (NIWA, NZ), Dr Phil Sutton (NIWA, NZ), Dr Melissa Bowen (University of Auckland, NZ), Dr Steve Rintoul (CSIRO, Australia) and Prof. Richard Karsten (Acadia University, USA) for the fruitful discussions over the past several years that have been much appreciated. Thanks also go to Prof. Peter Cornillon for providing me with a copy of the SIED code. I also acknowledge the support I received for this work from a University of Otago Doctoral Scholarship.

I would like to express my sincere thanks to my grandparents, Ron and Mary, my parents, Ruth and Bryan, and my brother Mike for their endless love and encouragement throughout this work, which has truly helped see me through. I would also like to express my gratitude for all the love and support given to me by the Kearney family in Auckland. Last but by no means least, thank you to Emma Kearney, to whom I owe the submission of this thesis. Thank you for your amazing love, support and patience as I tackled this goal.

Contents

List of Tables

List of Figures

Chapter 1

Thesis motivation and overview

1.1 Motivation

Oceanic fronts are relatively narrow zones of enhanced horizontal gradients in hydrographic properties (i.e. temperature, salinity, nutrients), which separate broader zones with distinct water masses and/or stratification (Fedorov, 1986; Belkin, 2002; Belkin et al., 2009). They are apparent throughout the world's oceans, occurring over a wide range of space and time scales, from tens of metres to thousands of kilometers (Belkin et al., 2009). The interaction of water masses at oceanic fronts can drive vigorous air-sea interactions (Chelton et al., 2004; Small et al., 2008), along-front currents (Fedorov, 1986), the formation of eddies (Manucharyan and Timmermans, 2013) and both upwelling (Sokolov and Rintoul, 2007b; Matano and Palma, 2008; Carranza et al., 2017) and subduction (Spall, 1995). In turn, these processes redistribute heat, salt, gases (like CO2), nutrients and organic matter both within and between ocean basins (Robinson, 2010; Talley et al., 2011; Dufour et al., 2015). As a result, oceanic fronts are recognised as playing important functions within both the ocean-atmosphere system (e.g. Small et al., 2014; Kida et al., 2015; Stukel et al., 2017) and in marine ecosystems (e.g. Bost et al., 2009; Woodson and Litvin, 2015).

This work focuses on the physics and variability of the Subtropical Front (STF), a large-scale oceanic front that defines the northern boundary of the Southern Ocean (Talley et al., 2011). The STF extends almost continuously around the Southern Hemisphere (except for the South American sector) at approximately 40°S (Fig. 1.1) and marks the water mass boundary between warmer, saline Subtropical Water (STW) contained in the subtropical gyres and cooler, fresher Subantarctic Water (SAW) of the Subantarctic Zone (SAZ) (Deacon, 1982; Belkin and Gordon, 1996). Around much of the globe, the STF is distinguished by a 400-500 km wide Subtropical Front Zone (STFZ) that is enclosed by two strong temperature-salinity fronts: the North Subtropical Front (N-STF) and South Subtrop-

ical Front (S-STF) (Belkin and Gordon, 1996), which extend down to around 250-500 m depth (Belkin and Gordon, 1996; Sutton, 2001; Tomczak et al., 2004; Hamilton, 2006).

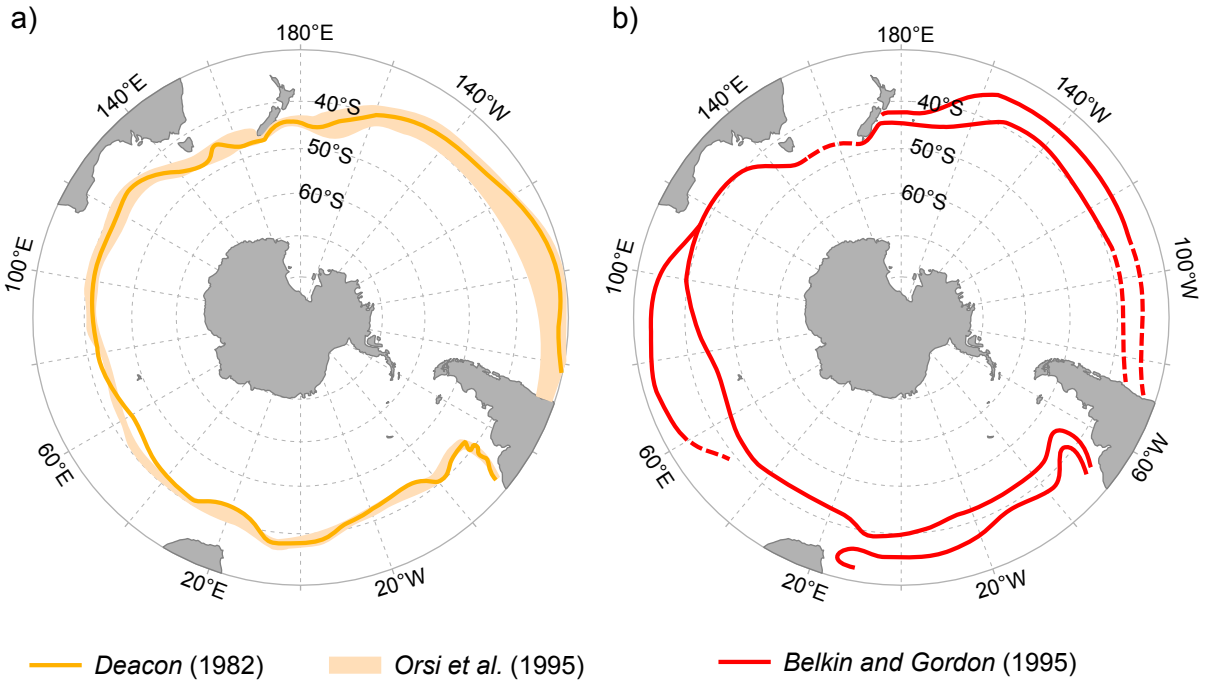

Figure 1.1: Climatological position of the STF from (a) Deacon (1982) and Orsi et al. (1995), (b) Belkin and Gordon (1996).

Improving our understanding of the spatial and temporal variability of the STF is important because of its potential influence on the global ocean and climate system. The position and temperature differential across the STF may significantly influence the mean state and variability of mid-latitude atmospheric circulation (e.g.Minobe et al. 2008; Nakamura et al. 2008), and possibly global climate (Bard and Rickaby, 2009; Beal et al., 2011). Observations and numerical model experiments show that SST anomalies in the water masses that converge at the STF can significantly influence both air temperature and rainfall over nearby landmasses, including South Africa (Reason and Jagadheesha, 2005) and New Zealand (Sutton et al., 2005). Water mass interactions occurring at the STF may also lead to the formation of subduction of central waters (Szymanska and Tomczak, 1994; Hamilton, 2006), as well as eddy formation and shedding (James et al., 2002), which strongly influence the exchange of heat, salt, nutrients and gases between the Subantarctic and subtropics (Stammer, 1998; Jayne and Marotzke, 2002; Karstensen and Quadfasel, 2002; Dufour et al., 2015).

Variability in the position and hydrography of the STF are also important for marine ecosystem functioning. In some sectors of the Southern Ocean, such as the South America and New Zealand sector, the STF is a major region of biological productivity (Moore et al., 1999; Murphy et al., 2001; Sutton, 2001; Sokolov and Rintoul, 2007b), caused by

the cross-frontal mixing of warm, macronutrient-poor and micronutrient-rich STW and cool, macronutrient-rich yet micronutrient-poor SAW(Butler et al., 1992; Boyd et al., 1999). In turn, the STF is an important sink for atmospheric carbon dioxide (Currie and Hunter, 1998; Currie et al., 2011) and a foraging hotspot for mobile marine vertebrates (Bost et al., 2009). Accurate knowledge of the present-day physics and variability of the STF is also crucial for interpreting changes in the position of the STF recorded over geological time-scales (Kohfeld et al., 2013; Bostock et al., 2015), as well as for understanding how the STF and its oceanography might change in response to future climate change.

To date, the general position, structure and hydrography of the STF have mostly been studied using historical hydrographic sections (see e.g. Deacon 1982; Orsi et al. 1995; Belkin and Gordon 1996) and more recently, from climatologies of satellite and Argo float data (Graham and de Boer, 2013). These analyses show that the STF is typically a distinct feature in synoptic-scale data (see e.g. Belkin and Gordon, 1996; Rintoul et al., 1997; Sutton, 2001; James et al., 2002; Sokolov and Rintoul, 2002; Tomczak et al., 2004; Hamilton, 2006), yet it is rarely seen in climatological fields of temperature or salinity based on long-term averages (Tomczak and Godfrey, 2003; Tomczak et al., 2004). As a result, the STF has traditionally been considered as a frontal system that undergoes large short-term and seasonal variability in position (Tomczak et al., 2004). In a few locations, where long-term, repeat observations of the STF have been possible, topographic steering (Rintoul et al., 1997; Shaw and Vennell, 2001; Sutton, 2001; Hopkins et al., 2010) and variable atmospheric forcing (Jeffrey, 1986; Burls and Reason, 2006) appear to be important factors controlling the position and intensity of the STF. However, throughout much of the Southern Ocean, the STF has historically been poorly sampled in time, leaving it's temporal variability and the underlying drivers still poorly understood (Sokolov and Rintoul, 2002).

The Tasman Sea is a marginal sea in the South Pacific that contains a section of the global STF (Section 2.8). Here, the observational record of the STF is rather sparse and sporadic, particularly away from the land boundaries of Australia and New Zealand (see e.g. Hamilton, 2006). It is also a region where the STF not only intercepts the shallow and complex ridges and New Zealand submarine plateaux (Heath, 1985), but where it is also exposed to higher seasonal and interannual atmospheric variability than elsewhere in the Southern Hemisphere (Streten, 1980; Jeffrey, 1986). These conditions make the Tasman Sea a prime location to better understand how the physical state of the STF varies in time, and to study the role that variable seafloor topography and atmospheric forcing play in this variability.

1.2 Research Questions

This work contributes to an improved observational understanding of the temporal variability of the STF, by combining information obtained from repeat hydrographic sections, remotely sensed 'snapshots' of SST and long-term data records of remotely sensed SST and SSS images obtained in the Tasman Sea.

There are two overarching questions that motivate this work:

- **How does the physical state of the STF vary in time south and west of New Zealand?**
- **What roles do topographic steering and wind forcing play in this variability?**

To address these questions, this research examines temporal variability of the STF in the Tasman Sea through the analysis and synthesis of three major observational data sets. These data sets consist of: five hydrographic sections and remotely sensed SST images collected during the austral autumns of 2007, 2008 and 2011; a 30 year (1982-2011) data set of monthly composite remotely sensed SST images; and a 27 month (2013-2015) data set of monthly composite remotely sensed sea surface salinity (SSS) images.

Analyses in **Chapter 3** are based on an extensive data set collected as part of several hydrographic surveys supported by NIWA as part of its Government-funded core research, undertaken on the RV *Tangaroa* between 2007 and 2011. This data set is the outcome of multidisciplinary collaborations and fieldwork undertaken over several years, which I participated in during the 2011 hydrographic survey of the Solander Trough. The contents of **Chapter 3** are published in Deep Sea Research Part I (Smith et al., 2013) and are the result of collaborations that developed through this fieldwork. As this Chapter served as initial study, parts of the introduction in the published work that are relevant throughout this thesis were synthesied into **Chapter 2**.

1.3 Overview of the Thesis

The remainder of this thesis is divided into six chapters:

Chapter 2 gives background and context for the thesis research. It provides an overview of current knowledge of the global STF, with a focus on its localised section in the Tasman Sea.

In **Chapter 3**, the pathway and temporal variability of the S-STF and its interaction with marked topography around southern New Zealand are investigated. This Chapter is an observational study based on hydrographic sections and remotely sensed SST data collected

during the austral autumns of 2007, 2008 and 2011 in the region of the Macquarie Ridge, Solander Trough and the Campbell Plateau. Aims: (1) to resolve varying historical locations given for the STF and S-STF south of New Zealand and (2) to examine how the front responds to shallow topography.

Chapter 4 develops and implements a suite of techniques to detect and to characterise thermal fronts within remotely sensed SST images. Surface thermal fronts are identified using an existing histogram-based edge detector, which is applied to a 30 year time series (1982-2011) of remotely sensed SST images. Then, a new algorithm is developed to characterise the thermal properties of each front, which in turn is applied to the detected thermal fronts. The resulting 30 year data set (1982-2011) of thermal front locations and properties is used throughout **Chapter 5** and **6**, to assess the occurrence and the variability of surface temperature expressions of the STF in the Tasman Sea.

In **Chapter 5**, patterns of thermal front occurrence in the Tasman Sea are analysed and their relation to spatial and seasonal variability of the surface expressions of the N-STF and S-STF is examined, using comparisons with satellite-derived estimates of SSS. Aims: (1) to understand whether surface expressions of the N-STF and S-STF south and west of New Zealand can be identified in remotely sensed SST data, and (2) to investigate whether the extensive 30 year time series of thermal front locations can provide new detail to the hydrographic-based understanding of the variability of the N-STF and S-STF, and their relationship with topography and wind forcing.

In **Chapter 6**, SST variability across the S-STF around southern New Zealand is analysed and compared with variability in local-scale and basin-wide surface winds over the South Pacific in order to assess their possible relationships. 30 year time series (1982-2011) of subtropical and Subantarctic SSTs, and the temperature differential across the S-STF around southern New Zealand, are derived from the data set developed in **Chapter 4**. Cross-correlations are used to assess the relationship between SST variability across the S-STF around southern New Zealand and winds over the South Pacific. Aim: to understand whether basin-wide changes in winds over the South Pacific, which appear to strongly influence surface water mass properties and circulation in the Tasman Sea, also influence SST variability across the S-STF around southern New Zealand.

Chapter 7 summarises the major results and findings and recommends directions for future research.

Chapter 2

Literature Review

This chapter provides background and context for the thesis research. It is divided into three main parts. Firstly, it describes the structure and the oceanographic significance of Southern Ocean fronts (Sections 2.1-2.2). Secondly, it reviews previous research on the Subtropical Front and its variability at a global scale (Sections 2.3-2.5). Thirdly, it summarises current knowledge of the oceanography of the Tasman Sea and its local section of the Subtropical Front (Sections 2.6-2.9). This local section of the global Subtropical Front is the subject of this thesis.

2.1 The frontal structure of the Southern Ocean

The Southern Ocean encompasses the vast oceanic regime surrounding Antarctica. Broadly speaking, it is bounded to the north by the STF and to the south by the Antarctic continent (Talley et al., 2011). Observations show that temperature and salinity do not vary gradually from north to south over the breadth of the Southern Ocean, but rather there are several fronts that separate wider zones of relatively homogenous surface waters (see e.g. Deacon 1937; Orsi et al. 1995; Belkin and Gordon 1996) (Fig. 1.1, 2.1).

These fronts arise as interfaces between different upper ocean water masses that are forced to converge, or diverge, by the surface westerly winds between 40°S and 60°S (Talley et al., 2011). Analyses of hydrographic data have revealed that these fronts extend zonally around the Southern Ocean and, with the exception of the STF, are continuous around Antarctica (see e.g. Orsi et al., 1995; Belkin and Gordon, 1996; Sokolov and Rintoul, 2009a). Within the fronts, the currents are typically strong and flow eastward, whilst within the oceanic zones between the fronts, the flow is dominated by eddies and is typically weaker and more sporadic (Talley et al., 2011). The five principal fronts and oceanographic zones of the Southern Ocean, together with their associated water masses, are illustrated in Figure 2.1

and 2.2. The principal fronts are: Subtropical Front (STF), Subantarctic Front (SAF), Polar Front (PF), Southern ACC Front (SACCF) and the Southern Boundary (SB).

Classically, studies have used hydrographic survey data to establish the location and structure of Southern Ocean fronts (see e.g. Deacon,1937; 1982; Orsi et al., 1995; Belkin and Gordon, 1996; Sokolov and Rintoul, 2002). The fronts are associated with transitions between distinct water properties (i.e. temperature, salinity, dissolved oxygen), which provides a means of identifying their positions (Belkin and Gordon, 1996). A range of "indicators" of these transitions have subsequently been identified - for example, the location of a particular isohaline at a specified depth (see e.g. Orsi et al., 1995; Belkin and Gordon, 1996; Sokolov and Rintoul, 2002 for overviews of these indicators). These indicators are not absolute, since the water properties at fronts vary both zonally and temporally, though processes including air-sea interaction and cross-frontal mixing (Belkin and Gordon, 1996). Several studies have used these indicators to map the pathway of the Southern Ocean fronts, based on composites of historical hydrographic survey data (Deacon, 1982; Orsi et al., 1995; Belkin and Gordon, 1996). One realization of the configuration of the fronts and zones found within the Southern Ocean, derived from historical hydrographic data by Orsi et al. (1995), is summarised in Figure 2.2.

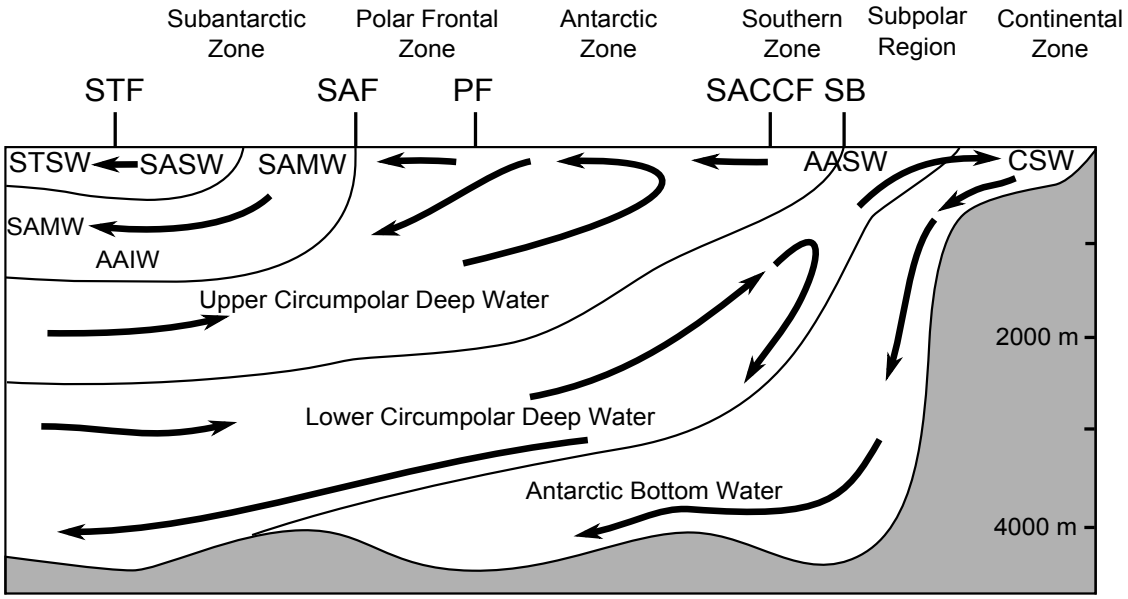

Figure 2.1: Schematic meridional section of the Southern Ocean showing the main fronts, zones, water masses and meridional circulation (arrows). Front acronyms: Subtropical Front (STF), Subantarctic Front (SAF), Polar Front (PF), Southern ACC Front (SACCF) and Southern Boundary (SB). Water mass acronyms: Subtropical Water (STW), Subantarctic Water (SAW), Subantarctic Mode Water (SAMW), Antarctic Intermediate Water (AAIW), Antarctic Surface Water (AASW) and Continental Shelf Water (CSW). Adapted from Talley et al. (2011, Figure 13.4)

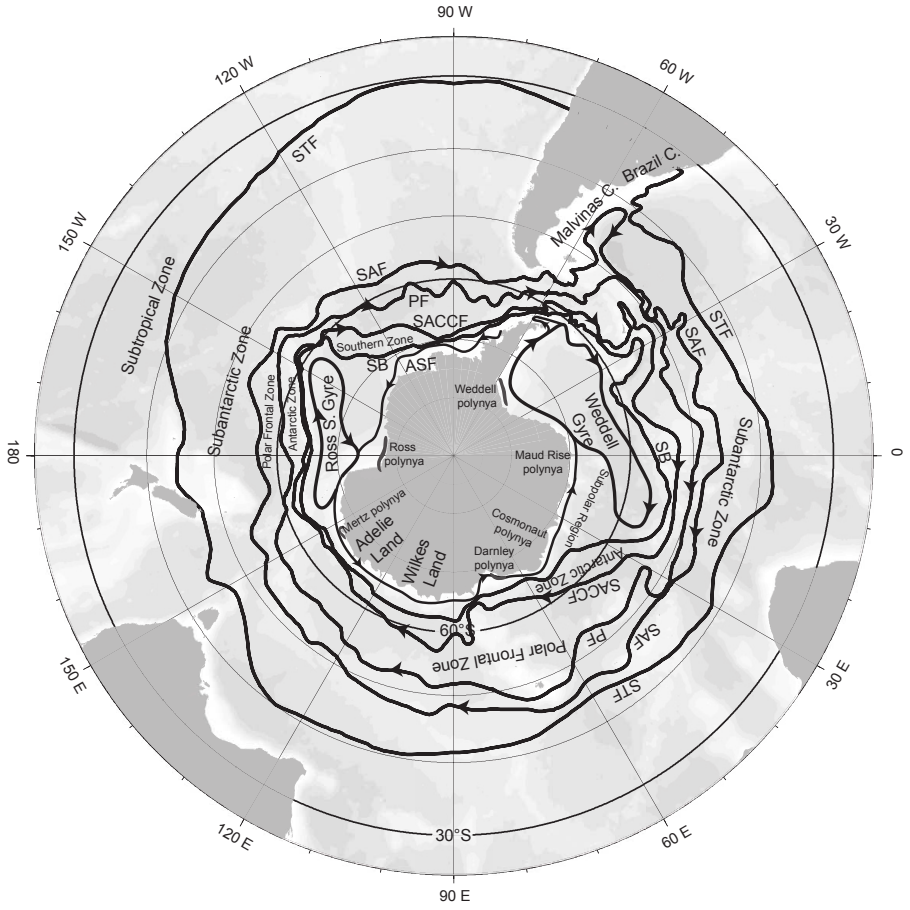

Figure 2.2: Schematic of the main fronts and oceanographic zones of the Southern Ocean. Front acronyms: Subtropical Front (STF), Subantarctic Front (SAF), Polar Front (PF), Southern ACC front (SACCF), Southern Boundary (SB) and Antarctic Slope Front (ASF). Reproduced from Talley et al. (2011, Figure 13.1). Also shown is the bathymetry (gray shading).

2.2 Significance of the Southern Ocean fronts

The main fronts of the Southern Ocean are important components of the coupled ocean-atmosphere system. They are associated with basin- or hemispheric-scale currents that redistribute physical and biogeochemical water properties throughout the Southern Ocean and in turn, can impact on the overlying atmosphere and Southern Ocean ecosystems.

Observations, together with atmospheric model experiments, show the position and strength of oceanic fronts that extend into the mid-latitudes, such as the STF and SAF, may considerably influence circulation in the overlying atmosphere (Chelton et al., 2004; Minobe et al., 2008; Nakamura et al., 2008; Small et al., 2008). For example, persistent, large-scale SST fronts in the mid-latitudes have been found to strongly affect tropospheric circulation above the marine atmospheric boundary layer (up to 15-20 km above the sea surface) through maintaining sharp gradients in the overlying surface air temperature and pressure fields (Mi-

nobe et al., 2008) and also to anchor the track of atmospheric depressions (Nakamura et al., 2008), thus influencing weather patterns on a regional scale. It has further been suggested that meridional shifts of the STF might act as a moderator of global climate by affecting the strength of the global ocean thermohaline circulation e.g. through regulating the leakage of warm, saline water from the Indian Ocean to the Atlantic via the Agulhas system and in turn, the transport of heat and salt to the Atlantic meridional overturning circulation (Bard and Rickaby, 2009; Beal et al., 2011).

The Southern Ocean fronts represent important regions for water mass convergence and their subsequent ventilation of the ocean's interior (Tomczak and Godfrey, 2003). The STF and SAF, for example, are associated with the formation and subduction of central waters that make up the waters of the permanent thermocline of the Southern Hemisphere (McCartney, 1977; Szymanska and Tomczak, 1994; Morris et al., 2001; Rintoul and England, 2002; Karstensen and Quadfasel, 2002; Tomczak and Godfrey, 2003). This ventilation transports heat and salt, along with greenhouse and other gases, into the subtropical thermocline and in doing so, is thought to act as a partial buffer for changes in the earth's climate system (Karstensen and Quadfasel, 2002).

In many sectors of the Southern Ocean, the convergence of water masses at the Southern Ocean fronts establish horizontal gradients of density and pressure that in turn, induce large-scale zonal flow around the Southern Ocean. For example, much of the strong (~130 Sv), eastward flow of the Antarctic Circumpolar Current (ACC) is concentrated in jets that are associated with the SAF, PF and SACCF (Talley et al., 2011), with generally weaker (3-60 Sv) and primarily upper-ocean flows associated with the STF (Stramma et al., 1995). These flows form a unique quasi-circumpolar link that connects the southern limits of the Atlantic, Indian and Pacific Ocean and enables water properties and climate anomalies to be transmitted between the basins and influence both global and regional climate (Rintoul, 2007).

In some sectors of the Southern Ocean, the Southern Ocean fronts are regions of enhanced marine productivity and biomass compared to the inter-frontal zones. For example, several studies using remotely sensed ocean color images have shown persistent regions of elevated surface chlorophyll *a* (chl-*a*) concentration in the vicinity of the Southern Ocean fronts, particularly in regions where these fronts encounter large bathymetric features (Comiso et al., 1993; Moore et al., 1999; Moore and Abbott, 2000, 2002; Sokolov and Rintoul, 2007b). These persistent phytoplankton blooms are stimulated through localised increases in upwelling resulting from flow-topography interactions, which increases the input of limiting nutrients from subsurface waters into the mixed layer (Sokolov and Rintoul, 2007b).

The Southern Ocean fronts, and their associated physical processes, also play an important role in the global carbon cycle. The Southern Ocean is a net sink for atmospheric CO2 and

is one of the main conduits for anthropogenic CO2 to enter the oceans (Fletcher et al., 2006; Khatiwala et al., 2009; Lenton et al., 2013). The enhanced primary productivity associated with sections of the Southern Ocean fronts, such as the STF and PF, makes these fronts important sinks for CO2 (Currie and Hunter, 1998; Moore et al., 1999; Currie et al., 2011)

The Southern Ocean fronts are further known to play an important role in influencing the distribution and abundance of marine animals. The fronts act as barriers that divide distinct zooplankton and mesopelagic fish species (Robertson et al., 1978; Deacon, 1982). In some sectors of the Southern Ocean, the fronts are also economically important fisheries. For example, the section of the global STF that lies over the Chatham Rise, east of New Zealand, is an area of enhanced primary productivity (Bradford-Grieve et al., 1997; Murphy et al., 2001; Sokolov and Rintoul, 2007b) that supports a commercially significant deep-water fishery for species including orange roughy and hoki (Nodder et al., 2003; Ministry of Fisheries, 2008). Top predators such as sea birds and marine mammals have also been found to strongly associate with sections of the STF and PF, undertaking foraging trips from hundreds of kilometers away due to availability of more predictable and abundant prey (Bost et al., 2009).

This thesis studies the nature of the variability of one of these major Southern Ocean frontal systems: the Subtropical Front (STF). The following sections review current knowledge on the hydrography of the global STF (Section 2.3), how it varies in time (Section 2.4) and the physical mechanisms that drive this variability (Section 2.5).

2.3 The Southern Ocean Subtropical Front

The oceanic thermocline is linked with the atmosphere through the Subtropical Convergence Zone (SCZ) (Tomczak and Godfrey, 2003; Steele et al., 2009). This broad oceanic region stretches around the Southern Hemisphere between approximately 20°S and 45°S, located between the core of the Trade Winds and the maximum westerlies (Stramma et al., 1995; James et al., 2002; Tomczak and Godfrey, 2003; Tomczak et al., 2004; Steele et al., 2009). This region is characterised by positive wind-stress curl in the atmosphere, which drives convergence of Ekman transport and the ventilation of upper ocean waters into the subtropical thermocline (Stramma et al., 1995; James et al., 2002; Tomczak and Godfrey, 2003; Tomczak et al., 2004; Steele et al., 2009). Situated towards the poleward side of the SCZ is a quasi-circumpolar band of enhanced meridional temperature and salinity gradients, originally described as the “subtropical convergence” (Deacon1933; 1937), but commonly referred to as the STF (see e.g. Stramma and Peterson, 1990; Stramma et al., 1995; Orsi et al., 1995 for useful summaries of STF nomenclature).

The STF defines the boundary between the warmer, saltier waters of the subtropical gyres and the SAZ (Deacon, 1982; Edwards and Emery, 1982) (Fig. 2.1, 2.2) and thus, is regarded

as marking the equatorward limit of the Southern Ocean (Talley et al., 2011). The STF extends almost continuously around the Southern Hemisphere (except for the South American sector) at approximately 40°S (Deacon, 1982; Orsi et al., 1995; Belkin and Gordon, 1996) (Fig. 2.3). From the confluence of the Brazil Current and Falkland / Malvinas Current in the South Atlantic (Stramma and Peterson, 1990; Stramma et al., 1995), the STF extends eastward into the South Atlantic and southern Indian Ocean at latitudes of between 35-45°S, passing south of Australia and New Zealand before trending towards the northeast across the South Pacific, reaching the western coastline of Chile close to 30°S (Fig. 2.3).

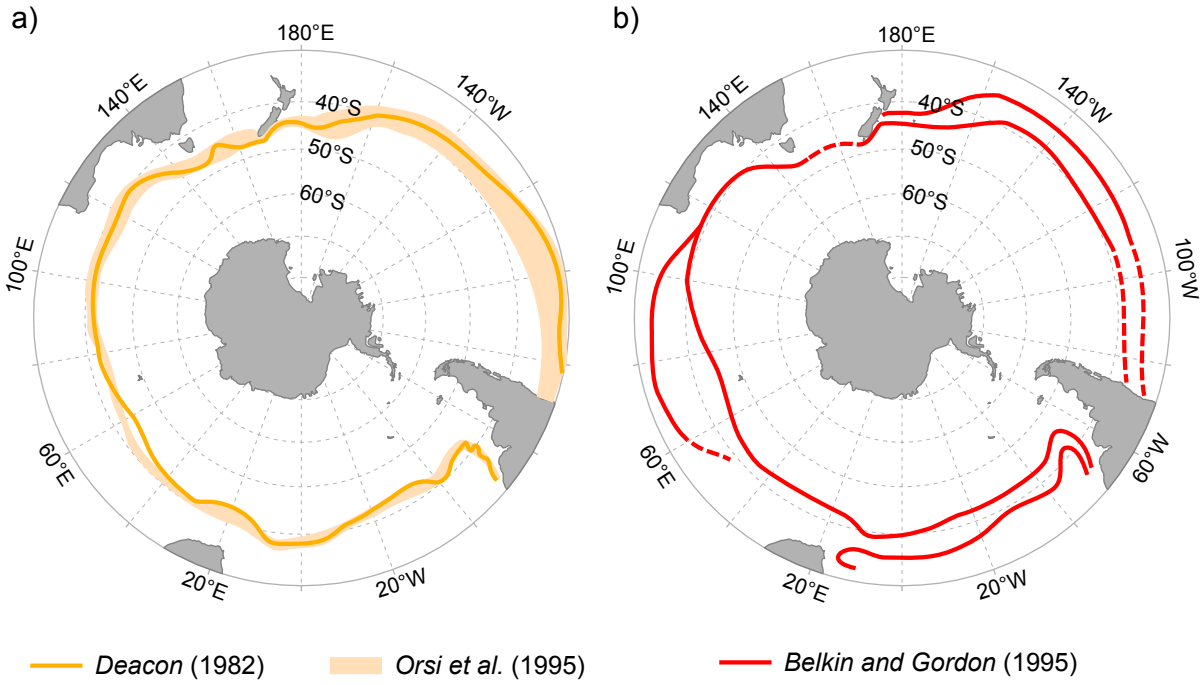

Figure 2.3: Climatological position of the STF from (a) Deacon (1982) and Orsi et al. (1995), (b) Belkin and Gordon (1996).

The STF is a distinct feature in hydrographic sections, where it is generally characterised by elevated horizontal temperature and salinity gradients that extend from the surface to depths of at least 250 m (Belkin and Gordon, 1996; James et al., 2002). During the austral summer, the sub-surface expression of the STF can be capped by a shallow (~50 m depth), warm mixed layer (James et al., 2002; Tomczak et al., 2004). In these conditions, the STF appears to produce a surface temperature front at about the same location as its sub-surface expression, possibly due to entrainment of water from the warm and cold sides of the STF into the overlying mixed layer (James et al., 2002). In contrast, the STF is relatively indistinct in long-term mean property distributions, possibly due to large time-variability in its position (Tomczak and Godfrey, 2003).

Based on data available at the time, Deacon (1933) described the STF as a zonal band where salinity decreases sharply by around 0.5 psu and temperature drops by at least 4°C

moving south, and Deacon (1945) further reports the temperature in the STF as approximately 10°C (14°C) in winter (summer) and the salinity as approximately 34.9. Today however, the axial-properties of the STF are now known to vary considerably between different sectors of the Southern Hemisphere, as a result of inflows of water from the western boundary currents, together with the gradual modification of water mass properties through air-sea exchange and across-front mixing (Belkin and Gordon, 1996). Consequently, a mixture of global and regional definitions have been used to help identify the STF in local hydrographic survey data. Excellent summaries of these definitions are given in Belkin and Gordon (1996), Sokolov and Rintoul (2002) and Hamilton (2006).

In the Southern Hemisphere, the term "Subtropical Front" has traditionally been used to define a single, well-defined front separating STW and SAW (e.g. Deacon,1933; 1937; 1945; 1982; Edwards and Emery, 1982; Orsi et al., 1995; Sokolov and Rintoul, 2002 among others). However, in a study of the western South Pacific Ocean, Belkin (1988) discovered a double-front zone and distinguished the region of convergence between STW and SAW as a 400-500 km wide Subtropical Front Zone (STFZ) that is enclosed by two sharp fronts: the North STF (N-STF) and the S-STF. The STFZ is typically covered by a layer in the upper 50–100 m composed of a modified SAW, this being a mixture of SAW and STW (Belkin, 1988; Hamilton, 2006), which is driven north and east over the STFZ by prevailing westerly winds (Hamilton, 2006). The N-STF is a shallower feature that delimits the northern extent of the modified surface SAW, whilst the deeper S-STF is the main front of the STFZ, and defines the poleward extent of sub-surface STW (Hamilton, 2006). The general pathway of the STF based on the work of Belkin and Gordon (1996), which incorporates the more detailed definition of a double structure for the STF, is shown in Figure 2.3b.

This thesis uses the term 'STF' in reference to the traditional definition of the Subtropical Front, this being the strongest front separating STW and SAW, which Hamilton (2006) found would typically be the S-STF - and uses the detailed definitions of STFZ, N-STF and S-STF when discussing the new results in this thesis and those studies that specifically used these definitions.

Classically, the STF has been described as having a continuous, eastward flowing geostrophic current associated with it (see e.g. Stramma and Peterson, 1990; Stramma, 1992; Stramma et al., 1995). The current associated with the front is described as weakening as it flows eastward (Stramma and Peterson, 1990; Smythe-Wright et al., 1998). At the western borders of the ocean basins, subtropical inflows from the western boundary currents establish a large density gradient across the STF and as a consequence, these sections of the STF are associated with a strong eastward-flowing geostrophic current (Stramma et al., 1995; Graham and de Boer, 2013). The STF generally becomes more strongly density compensated moving eastward across each ocean basin i.e. the effect of temperature and salinity gradients

across the front on density largely oppose one-another, resulting in a weak density structure (Tippins and Tomczak, 2003). As a result, large gradients of temperature and salinity can exist across the STF on the eastern sides of the basins, but weaker geostrophic flow (James et al., 2002; Sokolov and Rintoul, 2002; Tippins and Tomczak, 2003; Graham and de Boer, 2013). The transport associated with this current has been estimated at approximately 60 Sv (1 Sv $= 10^6 m^3 s^{-1}$) to the southeast of South Africa, reducing to 20 Sv around 75°E and to 10 Sv southwest of Australia (Stramma and Peterson, 1990; Stramma, 1992; Stramma et al., 1995). South of Australia, the STF becomes more strongly density compensated and the current said to be associated with the STF weakens further, to a transport of less than 3.5 Sv east of 130°E (Stramma et al., 1995; Schodlok et al., 1997; Rintoul and Bullister, 1999; James et al., 2002). As the STF passes around southern New Zealand, there is only a weak (1-2 Sv), eastward flow of STW (Morris et al., 2001; Sutton, 2003; Chiswell et al., 2015).

More recent work has challenged the traditional concept of a continuous, circumpolar current band associated with the STF (Sokolov and Rintoul, 2002; 2007a; 2009a; Graham and de Boer, 2013). In particular, Graham and de Boer (2013) used 10 years (1999-2009) of remotely sensed SST and SSH data to study the physical characteristics of the STF. Their analyses suggest that strong currents, defined in terms of gradient maxima of SSH, do not align with the STF in a continuous way around the Southern Ocean; rather, the STF is only 'associated' with strong currents on the western sides of basins. In these locations, the STF coincides with strong currents from the eastward extension of the western boundary current of the Southern Hemisphere subtropical gyres. These strong currents are seasonally stable and are marked by narrow bands of high SST and SSH gradients, features which Graham and de Boer (2013) refer to as the Dynamic Subtropical Front (D-STF). The pathways of the D-STF and the STF diverge towards the centre of each basin, with the D-STF turning southeast to merge with the SAF (see Fig. 3 in Graham and de Boer (2013)). Towards the centre and east of each basin, the STF loosely coincides with a broad region of enhanced SST gradients and weak currents (SSH gradients) that Graham and de Boer (2013) refer to the as "subtropical frontal zone", inferring an association between these enhanced SST gradients and the STFZ defined by previous hydrographic studies (e.g. Belkin, 1988; Belkin and Gordon, 1996; Sutton, 2001). In these regions, the STF is more strongly density compensated, associated with weaker flows and is a relatively diffuse feature (e.g. James et al., 2002; Sokolov and Rintoul, 2002; 2007a; 2009a; Tippins and Tomczak, 2003; Burls and Reason, 2006; Hamilton, 2006; Graham and de Boer, 2013). These contrasting spatial characteristics make it hard to generalize globally about the STF, so research into the STF inherently has to be at the basin-scale.

2.4 Temporal variability of the Subtropical Front

While there have been many detailed studies into spatial variability of the STF (Section 2.3), few studies have had sufficient repeat measurements to enable the temporal variability of the STF to be assessed.

Much of the present knowledge about the STF position and variability is limited to analyses of historical hydrographic sections. Historical locations given for the STF and S-STF from hydrographic surveys suggest that STF migrates over a large (5-6°) latitudinal range on some time-scales, in some sectors of the Southern Hemisphere - for instance, in the central and eastern South Atlantic (Deacon, 1937; Belkin and Gordon, 1996; Smythe-Wright et al., 1998). The STF appears to migrate over a much smaller latitudinal range within other sectors of the Southern Hemisphere, such as the southeast Indian Ocean (Sokolov and Rintoul, 2002) and Tasman Sea, where the position of the STF has been inferred to be relatively constant (Hamilton, 2006). However, many of the hydrographic sections used in these comparisons are separated by periods of several years to decades, making it difficult to determine time scales of this frontal variability.

There are only a few locations where systematic measurements along cruise tracks have enabled time scales of STF variability to be assessed with much confidence. For instance, four XBT lines along cruise tracks of Antarctic supply vessels have been repeatedly sampled during the austral summer in the Indian Ocean sector of the Southern Ocean (Nagata et al., 1988; Sokolov and Rintoul, 2002). These data show the latitudinal position of the STF varying on an interannual time scale by 3.5°, 3° and 5.5° in the southwestern and central Indian Ocean (Nagata et al., 1988) and by about 2° in the southeastern Indian Ocean (Sokolov and Rintoul, 2002).

Seasonal observations of the STF and S-STF also exist along repeat sections in the South Atlantic and southern Indian Ocean (Rintoul et al., 1997; Smythe-Wright et al., 1998; James et al., 2002; Sokolov and Rintoul, 2002). These observations suggest that the S-STF undergoes a seasonal migration of approximately 2.5° of latitude in the central and eastern South Atlantic Ocean (Smythe-Wright et al., 1998), with seasonal movements south during summer and north during winter. The STF appears to undergo a smaller seasonal migration of 1-2° of latitude in the southeast Indian Ocean (James et al., 2002; Rintoul et al., 1997; Sokolov and Rintoul, 2002). However, most the seasonal observations of the STF and S-STF in these locations come from cruises undertaken during the summer months (Oct-Mar). With only one or two observations in the winter months, it remains uncertain how well these estimates of the front's seasonal migration separate seasonal from interannual signals.

Over the central and eastern parts of each basin, away from areas of shallow topography and strong currents, there are conflicting accounts in the literature as to whether the STF (or

S-STF) undergoes a small (i.e. 1-2°) or large (i.e. 5-7°) seasonal migration. Observations from hydrographic sections, described above, suggest that the S-STF may migrate over a seasonal range of up to a couple of degrees of latitude (Rintoul et al., 1997; James et al., 2002; Sokolov and Rintoul, 2002). Based on three years (2002-2004) of satellite SST data, Burls and Reason (2006) found seasonal shifts of SST gradients in the STFZ in the southeast of the South Atlantic (0°E) were rather indistinct. Their results indicate gradients of SST at the approximate position of the S-STF in the North Atlantic migrate by <1° latitude between austral summer and winter (Fig. 3 in Burls and Reason, 2006). More recently, however, it has been proposed by Graham and de Boer (2013) that the STFZ - which is traditionally described as being enclosed by the N-STF and S-STF (e.g. Belkin, 1988; Belkin and Gordon, 1996; Hamilton, 2006) - undergoes a much larger seasonal migration northward of 5-7° between the austral summer and winter in the central and eastern parts of each basin. This ambiguity regarding seasonal migration of the STF introduces considerable uncertainty in interpreting what physical mechanisms control the fronts position and its variability. The question of S-STF seasonal migration, whether it is small (i.e. 1-2°) or relatively large (i.e. 5-7°), is one of the topics that is addressed in this thesis (see **Chapter 5**).

Since the mid-1990s, a number of studies have taken advantage of long-term data sets of remotely sensed SST and SSH images to identify the STF and monitor seasonal and interannual changes in its location and intensity (e.g. Chiswell, 1994; Uddstrom and Oien, 1999; Shaw and Vennell, 2001; Burls and Reason, 2006; Hopkins et al., 2010; Billany et al., 2010; Graham and de Boer, 2013; Fernandez et al., 2014). Ocean remote sensing offers systematic, repeat measurements of oceanographic surface variables such as SST, SSH and in recent years, SSS (Font et al., 2004; Lagerloef et al., 2008). These data can potentially provide thousands of high-resolution (1-30 km), repeat observations of the surface expressions of the STF over several years to decades, in areas where the historical hydrographic data are poorly sampled.

To date, however, studies of the STF based on remotely sensed data have mostly been limited to locations where the STF is either (i) quasi-persistent and spatially stable - such as in the sector east of New Zealand (e.g. Chiswell, 1994; Uddstrom and Oien, 1999; Shaw and Vennell, 2001; Hopkins et al., 2010) or (ii) weakly density compensated and associated with strong flows - such as on the western side of the basins (e.g. Billany et al., 2010; Graham and de Boer, 2013; Fernandez et al., 2014). In these locations, the STF is clearly identifiable in long-term averages of SST and SSH by a gradient maxima (see e.g. Graham and de Boer, 2013). Outside these narrow regions, the association between particular frontal features seen in SST images and the surface expressions of the N-STF and S-STF are much less certain (e.g. Uddstrom and Oien, 1999; Kostianoy et al., 2004; Burls and Reason, 2006; Graham et

al., 2013). This hampers the use of remotely sensed SST data to study temporal variability of the STF, a point that further motivates the work presented in **Chapter 3** and **Chapter 5**.

2.5 Physical mechanisms controlling the Subtropical Front: topographic and atmospheric influences

From studies of the STF and subtropical gyres conducted over the past several decades, topography and both local-scale and basin-wide atmospheric forcing have emerged as factors that may play important roles in determining the position and intensity of the STF, as well as the hydrographic conditions at the front.

2.5.1 Topographic steering

Sea floor topography has been found to affect the position and intensity of Southern Ocean fronts, including sections of the STF (e.g. Gille, 1994; Moore et al., 1999; Shaw and Vennell, 2001; Dong et al., 2006; Sokolov and Rintoul, 2009a; Hopkins et al., 2010). The mechanisms of this topographic influence involve the conservation of potential vorticity (Stewart, 2008). The potential vorticity (PV) of a fluid parcel is defined as:

$$PV = \frac{\zeta + f}{H}, \tag{2.1}$$

where ζ is relative vorticity, f is the planetary vorticity (Coriolis parameter), imparted on fluid by the Earth's rotation and H is the depth of the water. The relative vorticity (ζ) is the vorticity due to flow in the ocean, and is estimated from rate of change of horizontal velocities (u, v) as:

$$\zeta = \frac{\partial v}{\partial x} - \frac{\partial u}{\partial y}. \tag{2.2}$$

In most of the interior ocean (i.e. away from western boundaries), the planetary vorticity is much larger than the relative vorticity (e.g. $f \gg \zeta$). Therefore, ζ can be ignored and the potential vorticity can be approximated as:

$$PV \approx \frac{f}{H}. \tag{2.3}$$

Barotropic flow within the ocean tends to conserve potential vorticity, following contours of constant PV. The conservation of potential vorticity can be approximated as:

$$PV \approx \frac{f}{H} = const. \tag{2.4}$$

A consequence of the conservation of potential vorticity is that barotropic flow within the ocean is steered by major topographic structures. As an example of topographic steering, consider a zonal current in the Southern Ocean that extends from the surface to the sea floor and encounters a mid-ocean ridge. Upon encountering the ridge, depth (H in eq. 2.4), will decrease. In order to conserve potential vorticity (PV), planetary vorticity (f) must reduce and so the current is deflected towards the equator. Moving off the ridge, depth will increase and to conserve potential vorticity, planetary vorticity must increase and so the current is displaced poleward.

In a recent study, Sallée et al. (2008) outline three typical regimes of topographic interaction for Southern Ocean fronts:

1. Firstly, where the fronts are constrained to pass over shallow plateau or ridges, the intensity of their flow decreases and they tend to move equatorward to conserve their potential vorticity, turning poleward after crossing each topographic feature. This behaviour has been observed at a number of topographic features in the Southern Ocean, for instance, at the Kerguelen Plateau (70-80°E) and southeastern Indian Ridge (140-160°E) for the PF and SAF (Moore et al., 1999; Sallée et al., 2008) and at the Macquarie Ridge (~160°E) for the SAF, where narrow gaps in the ridge create fixed pathways for flow to pass through (Sallée et al., 2008; Sokolov and Rintoul, 2009a).

2. Secondly, where the fronts encounter large changes in depth associated with major topographic structures, they have been observed to be steered around them and across contours of potential vorticity, for instance, at the Campbell Plateau (170°E) for the SAF (Sallée et al., 2008; Sokolov and Rintoul, 2009a). In these areas, flow associated with the fronts intensifies and large-scale meandering tends to be inhibited (Moore et al., 1999; Sallée et al., 2008).

3. Thirdly, downstream of topographic constraints, the position of the fronts tends to be highly variable in space. Such behaviour has been attributed to the intensification of fronts in areas of shallow bathymetry leading to increased baroclinic instabilities and eddy activity downstream of the topographic constraints (see e.g. Huppert and Bryan, 1976; Moore et al., 1999).

Topographic steering is thought to influence the position of some sections of the STF and its variability. For instance, in the western Tasman Sea, Jeffrey (1986) found the positions of the N-STF and S-STF were relatively fixed, and speculated this was as a result of topographic control from the Tasman Shelf. Rintoul et al. (1997) suggested steering of the STF in the southeast Indian Ocean by the bottom topography might explain the relative stability of the

front location observed over several years in a trough between the Tasmanian continental shelf and the South Tasman Rise, where bathymetry shelves steeply from more than 3000 m depth to < 1000 m. Topographic influence on the STF has also been reported along the southeast coastline of the South Island of New Zealand and east of New Zealand, across the Chatham Rise (Heath, 1985; Uddstrom and Oien, 1999; Shaw and Vennell, 2001; Hopkins et al., 2010). In these locations, the mean and seasonal pathways of the STF closely follow the steeply shelving bathymetry of the upper continental slope of South Island, New Zealand and, in turn, the southern slope of the Chatham Rise, at between approximately 250 m and 600 m depth (Heath, 1985; Chiswell, 1994; Uddstrom and Oien, 1999; Shaw and Vennell, 2001; Hopkins et al., 2010) (Fig. 2.5). Along the southeast coastline of South Island, New Zealand, interannual variability of the STF location is also relatively small, which has been related to strong topographic control of the continental shelf (Hopkins et al., 2010).

2.5.2 Local-scale atmospheric forcing

The STF is located on the poleward side of the SCZ, on the southern edge of the atmospheric subtropical high pressure belt (Jeffrey, 1986; James et al., 2002; Tomczak and Godfrey, 2003; Tomczak et al., 2004). This region is characterised by positive wind-stress curl in the atmosphere and Ekman convergence in the ocean (Stramma et al., 1995; James et al., 2002).

The convergence of Ekman transport associated with wind stress curl can lead to frontogenesis (Roden, 1975) and it has been suggested that the existence and variability of the STF is related to wind stress curl forcing within the SCZ (Deacon, 1982; James et al., 2002). For instance, the average position of the STF has been related to local wind forcing within the SCZ by Deacon (1982). He found that the climatological position of the STF lay reasonably close to the maximum wind stress curl within the SCZ and inferred that there might be some association between the position of the two features. Although the two features are closely aligned in some sectors of the Southern Hemisphere, such as the southwest South Atlantic Ocean and in the southwest and southeast of the Indian Ocean (see Fig. 1 in Deacon, 1982), in others, such as the southern Indian Ocean and southeast of New Zealand, they are separated by several degrees of latitude. In a recent study, De Boer et al. (2013) similarly note that the climatological position of the STF is not consistently aligned with the annual-mean position of the maximum in the wind stress curl field in the Southern Hemisphere. This decoupling suggests that any association between the position of the STF and wind forcing within the SCZ is likely to be more complex than the generalised description given by Deacon (1982).

In a more recent study, James et al. (2002) present evidence that the subsurface expression of the STF in the southeast Indian Ocean can become decoupled from the sea surface during

the austral summer by a surface mixed layer. In turn, they speculate that the position of the STF might be determined by wind stress curl forcing within the SCZ during the austral winter, with the STF retaining this winter-time position during the austral summer due to the formation of a shallow mixed layer isolating the sub-surface expression of the STF from atmospheric forcing. Further research is needed however to confirm this hypothesis.

There is also evidence that the positions of the N-STF and S-STF are related to the latitudinal position of the subtropical high pressure belt (Jeffrey, 1986). Based on historical hydrographic data, Jeffrey (1986) estimated and compared positions for the N-STF and S-STF in the Tasman Sea during three different atmospheric forcing conditions. These forcing conditions corresponded to periods when the poleward edge of the subtropical high pressure belt lay at between: (1) 31-35°S, (2) 35-39°S and (3) 39-43°S latitude. The positions of the N-STF and S-STF were found to be displaced poleward with a poleward shift of the subtropical high pressure belt, with the N-STF affected noticeably more than the S-STF.

Further research is needed to whether the relationship described by Jeffrey (1986) can be generalized - for example, whether or not seasonal variability in the atmospheric conditions translates to seasonal variability of the N-STF and S-STF. Streten (1980) analyzed variability in the latitudinal position of the Southern Hemisphere subtropical high pressure belt and found the smallest seasonal variability in the southern Indian and South Atlantic Ocean (0-4°) and the largest in the western South Pacific (>8°). If the latitudinal position of the N-STF and S-STF is seasonally coupled to that of the subtropical high pressure belt, then it would be anticipated that seasonal migrations of the two front's might be larger in regions of larger seasonal shifts of the subtropical high pressure belt (i.e. in the western South Pacific). However, at present there remain insufficient seasonal observations of the S-STF to test this idea. Data from hydrographic surveys suggest that the STF shifts seasonally by approximately 1-2° of latitude in the South Atlantic and southeast Indian Ocean (Section 2.4), but it is not yet clear how much the S-STF migrates seasonally in the Tasman Sea. Whether seasonal variability in the subtropical high pressure belt translates to seasonal variability of the N-STF and S-STF is a topic that this thesis hopes to shed further light on (see **Chapter 5**).

2.5.3 Basin-scale atmospheric forcing

The STF defines the poleward boundary of the subtropical gyre circulations in the Southern Hemisphere, marking the southern limit of warm, saline STW contained inside the gyres (Stramma, 1992; Stramma et al., 1995). The pattern of circulation within the subtropical gyres is determined by the rotational component, or curl, of the basin-wide wind stress field, which is anti-cyclonic (counter-clockwise) in the Southern Hemisphere (Talley et al., 2011). Within the subtropical gyres, the pattern of wind stress curl drives Ekman convergence in the

surface layer, downward Ekman pumping and an equatorward, depth-integrated flow in the ocean interior. This is balanced by narrow, intense poleward flows of STW in the western boundary currents (Tomczak and Godfrey, 2003; Talley et al., 2011).

For the South Pacific subtropical gyre, several previous studies have demonstrated links between variations in basin-wide wind stress curl and various components of the subtropical gyre (e.g. Roemmich et al., 2007; Hill et al., 2008, 2010, 2011; Fernandez et al., 2014). A summary of key work is given here and expanded on in **Chapter 6**. Roemmich et al. (2007) related a strengthening of the South Pacific gyre observed between the 1990s and 2000s to increased wind stress curl over a broad region of the South Pacific gyre, east of New Zealand. Hill et al. (2008) revealed temperature and salinity of STW in the poleward extension of the East Australian Current (EAC) were related to inter-annual variability in basin-wide South Pacific wind stress curl. Using an idealized numerical model experiment, Hill et al. (2010) demonstrated perturbations in wind stress curl east of New Zealand can introduce sea level variability throughout the New Zealand region and in turn, modify the strength of the EAC system, through the propagation of oceanic Rossby waves. Hill et al. (2011) revealed stronger wind stress curl over the South Pacific gyre leads to a poleward expansion of the South Pacific gyre, with stronger circulation in the latitude range of New Zealand and a weakening of circulation north of New Zealand. In a recent study Fernandez et al. (2014) revealed a warming trend of 0.42°C decade^{-1} in the temperature of STW in the South Pacific gyre east of New Zealand between 1992 and 2012 and related this to increasing poleward flows of STW into the region via the western boundary current system under increased South Pacific wind stress curl.

These demonstrable links between variations in basin-wide wind stress curl and various components of the South Pacific subtropical gyre raise the question of whether the influence of wind stress curl variability extends to other parts of the subtropical gyre system? Much like in the EAC extension (e.g. Hill et al., 2008) and in the western boundary currents east of New Zealand (e.g. Fernandez et al., 2014), SSTs at the STF around southern New Zealand show considerable variability on inter-annual and longer time scales (Shaw et al., 1999; Shaw and Vennell, 2001; Hopkins et al., 2010). The relation of temperature and frontal variability in the area south of New Zealand to changes in wind stress curl over the South Pacific gyre however has not yet been explored, and provides motivation for work presented in this thesis (see **Chapter 6**).

2.6 Focus region: the Tasman Sea and waters around southern New Zealand

This research focuses on the STF in the Tasman Sea and in the waters around southern New Zealand (146-175°E, 43-50°S). The physical properties of the STF in these areas, their variability and also their relationship with bathymetry and wind forcing, will be investigated in **Chapters 3**, **5** and **6**.

Studying the STF in the Tasman Sea and around southern New Zealand has several advantages:

- Firstly, the Tasman Sea contains both extreme characters of the STF: the STF has a diffuse character to the west of New Zealand, over the Tasman Sea (see e.g. Stramma et al., 1995; Hamilton, 2006), and a dynamic character along the southeast coastline of the South Island of New Zealand (see e.g. Sutton, 2003; Graham and de Boer, 2013). This makes the Tasman Sea an ideal region to explore and better understand the temporal variability of the STF.

- Secondly, in this sector of the Southern Ocean the STF is exposed to strong seasonal and interannual variability in atmospheric forcing (Jeffrey, 1986; Tomczak and Godfrey, 2003) and it also intercepts the shallow and complex New Zealand submarine plateaux (Fig. 2.5-2.6). These characteristics of the study region provide unique opportunities for better understanding the influence that both the large-scale wind field and seafloor topography can exert on the STF.

- Thirdly, extensive work has previously gone into reconciling the structure and sometimes conflicting definitions of the STF in the southwest Pacific (Hamilton, 2006), providing an accurate baseline for identifying the N-STF and S-STF that is lacking in other areas of the Southern Hemisphere.

- Fourthly, the area south of New Zealand is one of few locations in the Southern Hemisphere where hydrographic surveys have sampled along similar sections several times over consecutive years (**Chapter 3**). This provides repeat hydrographic data that are exploited in this thesis to better understand temporal variability of the sub-surface expression of the STF.

- Finally, in the context of the physical oceanography of the southwest Pacific, the Tasman Sea and area around southern New Zealand are poorly covered when compared to the western boundaries of Australia and New Zealand. By examining these areas using repeat hydrographic and remote sensing observations, this thesis can potentially help contribute to our regional understanding of Tasman Sea oceanography.

The following sections provide an overview of the major bathymetric features (Section 2.7) and physical oceanography (Section 2.8) of the Tasman Sea and the waters around southern New Zealand (146-180°E, 30-51°S).

2.7 Regional Bathymetry

The regional circulation of the western South Pacific is severely constrained by the New Zealand continental shelf, together with several other significant topographic features (Fig. 2.4).

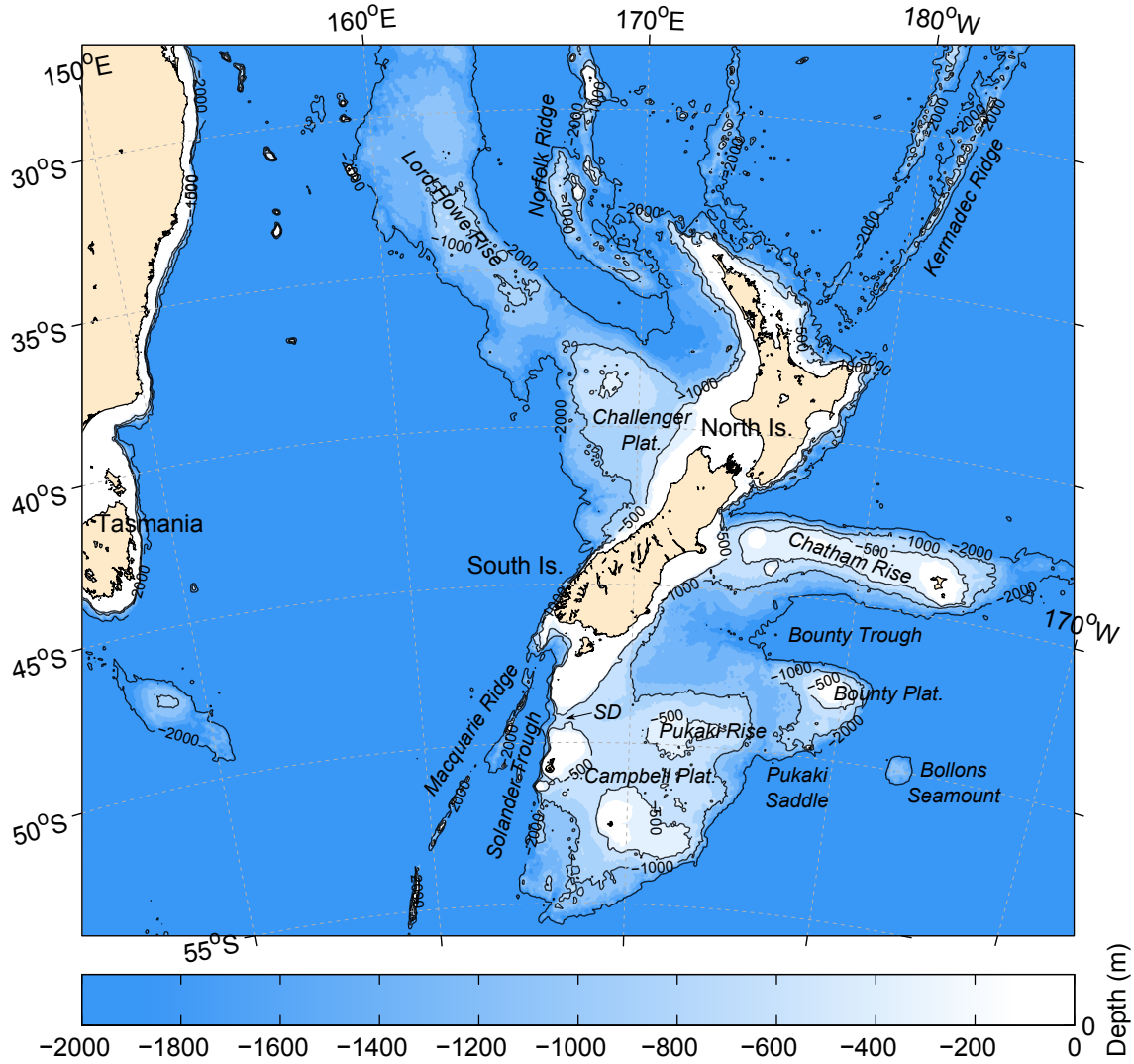

Figure 2.4: Bathymetry of the western South Pacific. The 500 m, 1000 m and 2000 m isobaths are shown as solid black lines and major geographic and topographic features refereed to in the text are labeled (SD-Snares Depression).

The circulation of the Tasman Sea, situated between Australia and New Zealand, is influenced by three major topographic features: Lord Howe Rise, Norfolk Ridge and Challenger Plateau (Fig. 2.4). The Lord Howe Rise is a submerged plateau 185-370 km wide that extends southward ~2000 km from the central Coral Sea (20°S, 160°E) to the Challenger Plateau (40°S, 167°E), at water depths of 1000-3000 m (Standard, 1961; Przeslawski et al., 2011; Williams et al., 2011). Further east lies the Norfolk Ridge (168°E), comprising an elongated chain of seamounts and plateaus that extend northward from New Zealand and shoal to depths of 1200-200 m (Williams et al., 2011). South of the Lord Howe Rise and west of New Zealand lies the Challenger Plateau, a broad (~500 km) submarine platform that rises from water depths of ~3000 m to 450 m at its crest (Ridgway and Dunn, 2003).

The eastern border of the Tasman Sea encompasses the two main islands of New Zealand - North Island and South Island - and an extensive continental shelf, which begins at about 34°S and extends in a southward orientation to near 49°S (Fig. 2.4). The continental shelf rises abruptly from the ocean floor (4000-1000 m) to depths of less than 200 m and constitutes a major topographic barrier to circulation around the north, east and south of New Zealand.

The circulation south of New Zealand is further complicated by several significant topographic features, including Macquarie Ridge, Campbell Plateau and Bounty Plateau (Fig. 2.4). Macquarie Ridge stretches southwest from the South Island of New Zealand and comprises an undulating structure that varies from depths >3000 m at gaps in the ridge, shoaling to depths <100 m at a series of sea mounts (Fig. 2.4) (Conway et al., 2012). East of Macquarie Ridge lies the Campbell Plateau, a submerged continental platform that extends poleward for ~1100 km from the southern edge of the South Island of New Zealand (Neil et al., 2004). The western and southern margins of Campbell Plateau rise steeply from more than 4000 m to depths of between 1000-600 m, shoaling to <250 m, and comprise several surface outcrops in the form of island groups, such as the Auckland and Campbell Islands (Neil et al., 2004). Campbell Plateau is separated from Macquarie Ridge to the west by the Solander Trough (Fig. 2.4), a narrow (~100 km) submarine depression that begins at a water depth of about 500 m at 46.5°S and extends southward for ~550 km, ending in depths of 4000 m at 51°S (Bostock et al., 2015). East of Campbell Plateau lies the Bounty Plateau (179°E, 49°S), an isolated, submarine platform ~250 km in diameter (Fig. 2.4). Over much of the Bounty Plateau, water depths are around 1000 m and the plateau it is separated from Campbell Plateau to the west by the ~1400 m deep Pukaki Saddle (Neil et al., 2004).

East of New Zealand, a major topographic feature that influences oceanic circulation is the Chatham Rise - a ridge ~100 km wide that begins at about 174.5°E and stretches in an eastward orientation for more than 1000 km at waters depths of 450-350 m. The northern and southern margins of the Chatham Rise are steep, falling sharply from around 450 m to

more than 3000 m. Chatham Rise is separated from the South Island continental shelf to the west by the ~500 m deep Merno Saddle (174.5°E, 44°S), and from Bounty Plateau to the south by the Bounty Trough, a rift feature that begins at about 1500 m at 173°E and falls away to more than 3000 m east of 180°E (Uenzelmann-Neben et al., 2009).

2.8 Descriptive Physical Oceanography of the study region

Heath (1985) and Chiswell et al. (2015) provide detailed historical reviews on the physical oceanography of seas around New Zealand region. A brief, descriptive overview of the regional water masses, ocean currents and fronts that are relevant to the present work is given below. More expansive reviews of previous work on the position, structure and variability of the STF in the Tasman Sea and around southern New Zealand is provided in Section 2.9 and in the introductions to **Chapter 3**, **5** and **6**, where that information is most relevant.

2.8.1 Water masses

Three main surface waters are identifiable in the New Zealand region (Chiswell et al., 2015): Subtropical Water (STW), Subantarctic Water (SAW) and Antarctic Surface Water (AASW). These surface waters are separated by three major ocean fronts - the Subtropical Front (STF), Subantarctic Front (SAF) and Polar Front (PF) (Fig. 2.5). STW is the warmest and most saline water in the region, with typical temperatures of >18°C (> 14°C) during summer (winter) and salinities higher than 34.5 (Heath, 1985; Sutton, 2001; Chiswell et al., 2015). STW is transported into the New Zealand region by the South Pacific subtropical gyre and the East Australian Current (EAC) (Chiswell et al., 2015). SAW is found between the STF and SAF, and is characterised by cooler temperatures (summer < 14°C; winter <10°C) and lower salinities (<34.6) than STW (Heath, 1985; Sutton, 2001; Chiswell et al., 2015). SAW is driven north and east over the southern Tasman Sea and Campbell Plateau by Ekman transport resulting from the prevailing westerlies (Hamilton, 2006; Chiswell et al., 2015). There is also an ingress of SAW into the Bounty Trough via the Pukaki Saddle (Davis, 1998; Morris et al., 2001). AASW is found south of the PF and extends poleward to the margins of Antarctica (Chiswell et al., 2015). In addition to these three main surface waters, lower salinity (33.8-34.6) neritic waters are also found in the near-coastal waters (Shaw, 1998).

2.8.2 Ocean currents and fronts

Between the latitudes of 30°S and 60°S, hydrographic and remote sensing observations show that there are three main, permanent oceanographic features within the southwest Pacific

(Fig. 2.5) (Chiswell et al., 2015): the EAC system, together with sections of the global STF and SAF.

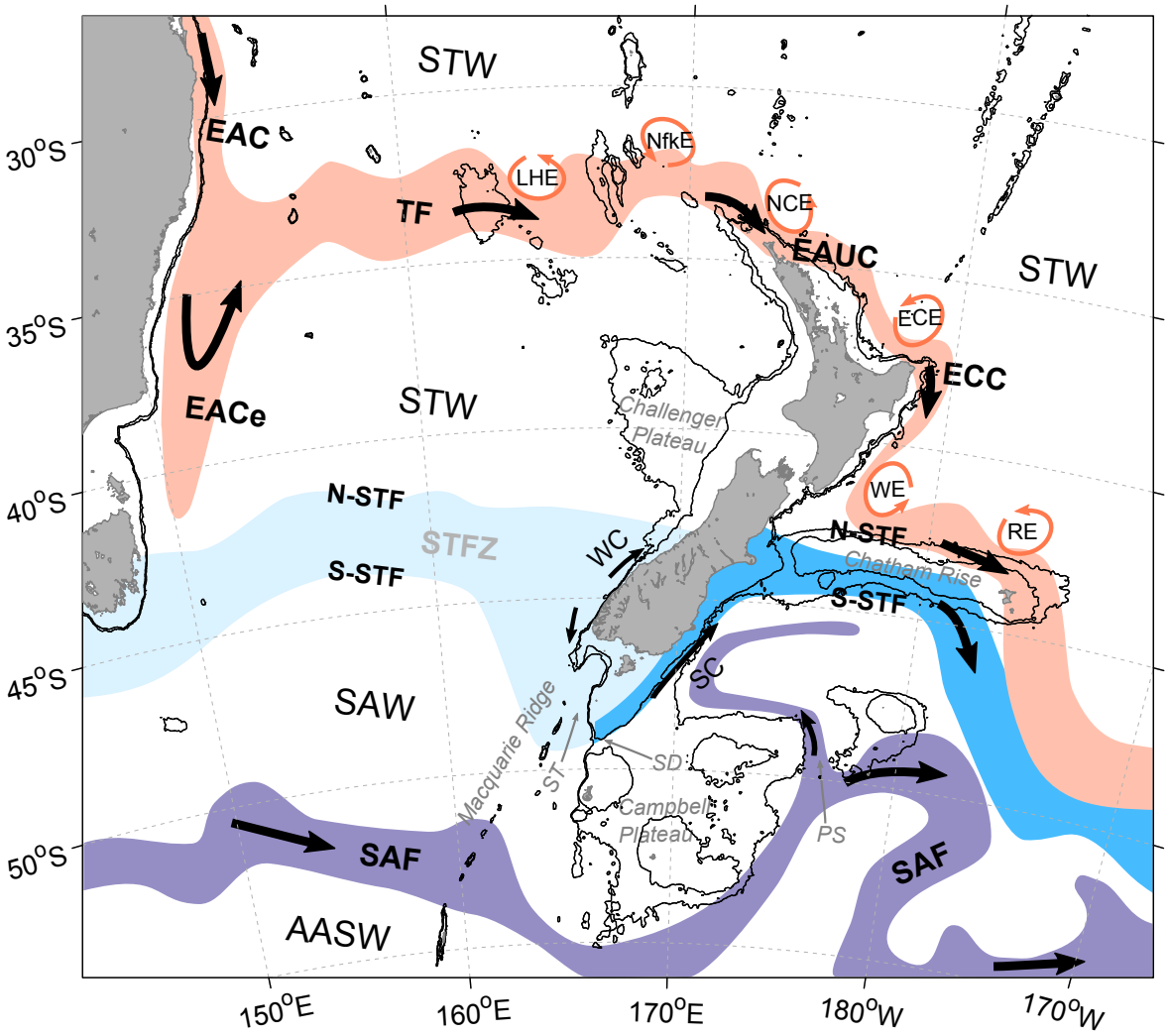

Figure 2.5: Schematic of the major ocean front and current systems in the western South Pacific - adapted from Chiswell et al. (2015) and Sutton (2001). Areas of flow are shown by the coloured bands. The STF in the Tasman Sea is strongly density compensated with little zonal flow, as indicated by the lighter shading. Water masses are: Subtropical Water (STW), Subantarctic Waters (SAW) and Antarctic Surface Water (AASW). Ocean fronts are: Tasman Front (TF), Subtropical Front (STF) and Subantarctic Front (SAF). In this region, the STF can be described as northern and southern subtropical fronts (N-STF and S-STF) that enclose a subtropical frontal zone (STFZ) (Sutton, 2001; Hamilton, 2006). Ocean currents are: East Australian Current (EAC), East Australian Current extension (EACe), East Auckland Current (EAUC), East Cape Current (ECC), Westland Current (WC) and Southland Current (SC). Eddies are: Lord Howe Eddy (LHE), Norfolk Eddy (NfkE), North Cape Eddy (NCE), East Cape Eddy (ECE), Wairarapa Eddy (WE) and Rekohu Eddy (RE). The 500 m and 1000 m depth contours are shown as gray lines. Major bathymetric features are also labeled (ST-Solander Trough, SD-Snares Depression, PS-Pukaki Saddle).

The East Australian Current

The EAC system is the western boundary current of the South Pacific subtropical gyre and flows south (~22 Sv, Mata et al., 2000) along the east Australian shelf break (Boland and Church, 1981). The majority of the EAC flow (~8-13 Sv - Ridgway and Dunn, 2003; Sutton and Bowen, 2014) separates from the coast near 32°S and establishes the Tasman Front (TF, Fig. 2.5), which flows eastward across the Tasman Sea towards northern New Zealand (Stanton, 1981; Ridgway and Dunn, 2003). Around the northern tip of New Zealand (34°S, 173°E), part of the current associated with the TF reattaches to the continental shelf forming the East Auckland Current (EAUC, Fig. 2.5), which flows to the southeast along the east coastline of North Island, New Zealand (Heath, 1980; Stanton et al., 1997; Roemmich and Sutton, 1998; Ridgway and Dunn, 2003). Near 37°S, the EAUC feeds into the southward flowing East Cape Current (ECC, Fig. 2.5) that transports subtropical waters towards the northern side of the STFZ over the Chatham Rise (Sutton, 2001).

In the Tasman Sea, the remainder of the EAC flow (7-10 Sv - Ridgway and Dunn, 2003; Ridgway et al., 2008) continues southward along the Australian coast as an envelope of eddies that can drift as far south as Tasmania (Wyrtki, 1962; Nilsson and Cresswell, 1980) and is referred to as the East Australian Current extension (EACe) (Ridgway and Dunn, 2003; Ridgway et al., 2008). Between 38-43°S, separations from the EACe drive a weak (~3 Sv, Stramma et al., 1995) eastward flow across the Tasman Sea towards South Island, New Zealand (Stanton, 1976; Stanton and Ridgway, 1988; Stramma et al., 1995; Ridgway and Dunn, 2003). This flow bifurcates in the vicinity of Challenger Plateau (Fig. 2.5), with a portion turning to the southeast and forming an intensified southward flow (2.4-3 Sv, Stanton, 1976; Stanton and Moore, 1992) along the coastal boundary near 44°S (Garner, 1969; Stanton, 1976; Heath, 1980, 1982; Rahmstorf, 1992; Ridgway and Dunn, 2003). Analyses of hydrographic data suggest between 1-2 Sv of subtropical water passes around southern New Zealand (Morris et al., 2001; Sutton, 2001), where it contributes to a northeast flowing coastal band inshore of the STF.

The Subtropical Front in the Tasman Sea

Towards the southern border of the Tasman Sea lies the regional expression of the global STF. The STF extends across the southern Tasman Sea from south of Tasmania towards the South Island, New Zealand, at a latitude of approximately 45°S (Fig. 2.6). Within the Tasman Sea, the STF displays a double frontal structure (Jeffrey, 1986; Hamilton, 2006), consisting of a homogenous STFZ that is bordered by two fronts: the N-STF and the S-STF (Hamilton, 2006) (Fig. 2.6). There is only a weak thermohaline contrast between STW and SAW in the Tasman Sea (Hamilton, 2006) and a general, but weak eastward flow of about 3

Sv in the vicinity of the STF (Stramma et al., 1995; Ridgway and Dunn, 2003). As a result, the STF in the Tasman Sea is a relatively diffuse feature, displaying characteristics similar to the STF observed on the central and eastern sides of each basin - such as in the southeast Indian Ocean (James et al., 2002).

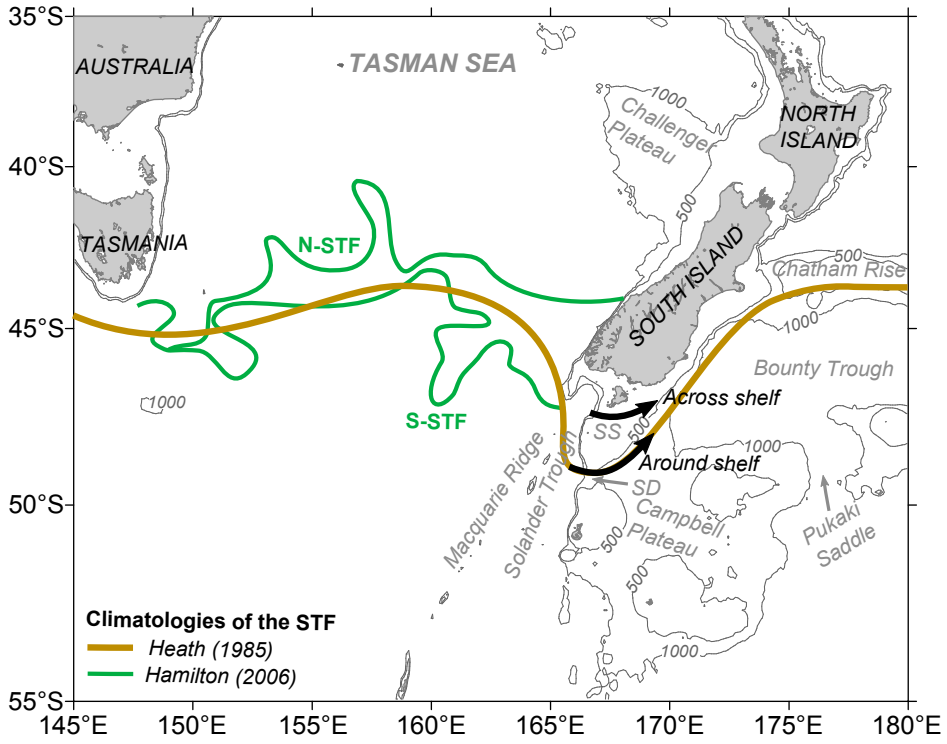

Figure 2.6: Climatological configuration of the STF in the Tasman Sea based on analyses of hydrographic data by Heath (1985), and for the N-STF and S-STF based on analyses by Hamilton (2006). Also shown south of New Zealand are the suggested across shelf and around shelf positions of the main front of the STFZ (the S-STF) described in the literature (see **Chapter 3**). The 500 m and 1000 m depth contours are shown as gray lines. Major bathymetric features are also labeled (SS-Snares Shelf, SD-Snares Depression).

The Subtropical Front around Southern New Zealand

The continental shelf south of New Zealand presents a major topographic barrier to the zonal path of the STF. Here, the bathymetry rises to within less than 200 m of the surface ocean (Fig. 2.4) and the STF deviates south to pass around southern New Zealand, after which it turns northeast to follow the upper continental slope off the southeast coastline of South Island, New Zealand (Fig. 2.5-2.6) (Garner, 1959; Heath, 1981, 1985). In this area, the nature of the STF changes considerably from the Tasman Sea, forming a permanent, quasi-stable and sharply defined front that is known locally as the Southland Front (SLF) (Jillett, 1969; Chiswell, 1996; Uddstrom and Oien, 1999). A strong density field is associated with the SLF, which establishes a local northward flow known as the Southland Current (SC, Fig.

2.5) (Heath, 1985; Chiswell, 1996; Sutton, 2003). The core of this flow lies ~50 km offshore of the Southland Front and primarily transports SAW (Sutton, 2003), fed from an ingress of SAW into the Bounty Trough via the Pukaki Saddle (Fig. 2.5) (Davis, 1998; Morris et al., 2001), with a smaller contribution (1-2 Sv) inshore of the SLF from STW advected zonally across the Tasman Sea (Chiswell, 1996; Sutton, 2003). Analyses of satellite SST images show that the surface expression of the SLF moves further offshore during the austral winter (Shaw and Vennell, 2001; Hopkins et al., 2010) and that its thermal gradients is strongest during the austral summer and winter (Hopkins et al., 2010).

The Subtropical Front east of New Zealand

East of New Zealand, the STF deflects out into the South Pacific ocean along the Chatham Rise at approximately 43-44°S, where a N-STF and S-STF become re-established across a ~150 km wide STFZ (Jeffrey, 1986; Belkin, 1988; Sutton, 2001). At around 180°E, the S-STF extends southward and approaches the strong eastward flow of the SAF that flows along the southern margins of the Campbell Plateau and Bounty Plateau (Fig. 2.5). Here, subtropical and Subantarctic flows come to within about 1° of latitude (Heath, 1985; Uddstrom and Oien, 1999) and form a strong frontal region southeast of Chatham Rise (Fernandez et al., 2014). Following Fernandez et al. (2014), this region is referred to herein as the "confluence region". From this region, the position of the S-STF subsequently extends eastward across the South Pacific (Heath, 1985; Belkin, 1988; Uddstrom and Oien, 1999; Chiswell et al., 2015).

The Subantarctic Front

The SAF lies south of the STF at latitudes of between 50-56°S (Fig. 2.5). The SAF is separated from the STF by the SAZ, consisting of a largely homogenous region of SAW and SAMW that occupies the Campbell Plateau and Bounty Trough (Fig. 2.5) (Morris et al., 2001). The pathway and eastward zonal flow associated with the SAF are strongly constrained by bathymetry and follow the southeast flank of the Campbell Plateau (Morris et al., 2001; Sokolov and Rintoul, 2009a). In this sector, Morris et al. (2001) find some flow associated with the SAF is diverted into a strong cyclonic flow of SAW that develops around the western edge of the Bounty Trough and contributes to the SC (Sutton, 2003) (Fig. 2.5).

2.9 Previous studies of the Subtropical Front in the Tasman Sea

This section reviews previous studies of the position, structure and variability of the STF in the Tasman Sea and south of New Zealand, and provides background information relevant to **Chapters 3**, **5** and **6**.

2.9.1 Position and structure of the STF in the Tasman Sea

To date, studies of the STF within the Tasman Sea and around southern New Zealand have mainly focused on hydrographic surveys of the frontal region (see e.g. Heath (1985), Stramma et al. (1995) and Hamilton (2006) for detailed reviews). Based on these historical data, previous studies have identified the STF these areas using one of two general definitions: (1) a traditional concept of a singular front (e.g. Deacon, 1933, 1982; Garner, 1959; Edwards and Emery, 1982; Heath, 1981, 1985; Szymanska and Tomczak, 1994, and (2) a more detailed description of a double frontal structure (Jeffrey, 1986; Butler et al., 1992; Hamilton, 2006).

Many earlier studies describe the STF in the Tasman Sea in the context of a single front separating STW and SAW (e.g. Deacon, 1982; Garner, 1959; Edwards and Emery, 1982; Heath, 1981, 1985; Szymanska and Tomczak, 1994), and estimated the position of the front using a single isotherm and/or isohaline. Differences between studies in the criteria used to identify the STF in this area has led to historical differences in the reported position of the STF. For instance, Deacon (1937) gave the seminal description of the large-scale water mass structure, properties and frontal distribution over the southwest Pacific, based on analyses of three coarsely-sampled, quasi-synoptic hydrographic sections in the Tasman Sea and east of New Zealand occupied during winter 1932. According to Deacon (1937), the STF stretched northeastward from about 45°S south of Tasmania toward 40°S in the eastern Tasman Sea, approximately following the 34.9 surface isohaline. In a later reanalysis of these data, Garner (1959) examined the characteristics of the STF in the Tasman Sea and east of New Zealand. He concluded that the convergence zone between STW and SAW in the vicinity of New Zealand followed approximately the surface isohalines of 34.7 to 34.8 and the isotherms of 15°C in summer and 10°C in winter, and followed a more zonal path toward 46°S in the eastern Tasman Sea.

These studies were followed by several further hydrographic surveys of the STF in the Tasman Sea and around southern New Zealand (Wyrtki, 1962; Edwards and Emery, 1982; Stanton and Ridgway, 1988; Warmus, 1989; Butler et al., 1992; Morris et al., 2001). Like Deacon (1937) and Garner (1959) before them, these studies gave sometimes conflicting

accounts regarding the properties and position of the STF. An expanded survey of the STF in the Tasman Sea was carried out by Wyrtki (1962), based on a larger data set from 36 hydrographic stations sampled during January 1961. Edwards and Emery (1982) sampled two north-south XBT sections across the STF in the western Tasman Sea during March 1977. In turn, Stanton and Ridgway (1988) completed a synoptic-scale survey of the STF in the Tasman Sea based on hydrographic data sampled during Oct-Nov 1977 and Warmus (1989) carried out a similar CTD survey of the water mass and frontal distribution in the Tasman Sea during December 1988 (reanalysed in Szymanska and Tomczak (1994)).

Heath (1981; 1985) carried out more complete analyses of the general position of the STF in the western South Pacific, based on analyses of composites of hydrographic data collected from different years and surveys. He described the general pathway of the STF over the Tasman Sea and south of New Zealand in the context of a single front that extends across the Tasman Sea from southeast of Tasmania (150°E, 45°S) towards the southern end of the South Island, New Zealand, then passing south of New Zealand (Fig. 2.6), based on composites of *in-situ* data collected from multiple cruises conducted during the summer months between 1963 and 1971. Around southern New Zealand, Butler et al. (1992) described the water masses and frontal structure of the STF by combining data from two CTD surveys, together with underway sampling, conducted during May 1989 and Morris et al. (2001) examined the subsurface distribution of water masses through the Solander Trough based on a north-south CTD survey during May 1998 (nine stations north of 52°S).

Contrasting with these earlier descriptions of a singular-STF within the Tasman Sea, detailed analyses of hydrographic survey data by Jeffrey (1986) and Hamilton (2006) have revealed a double frontal structure. Jeffrey (1986) reviewed reports of front locations in the Tasman Sea and inferred two parallel bands of enhanced salinity gradients generally exist, and thought these were possibly associated with the STF. These frontal zones were centered on the 34.7 and 35.1 surface isohalines. Jeffrey (1986) subsequently inferred the general positions of these frontal zones based on 23 historical hydrographic sections. In the western Tasman Sea, both frontal zones were found to be effectively merged and located near 46°S. The frontal zone centered the 34.7 isohaline was found to extended eastward across the Tasman Sea from south of Tasmania towards southern New Zealand near 46°S, whereas the frontal zone centered on the 35.1 isohaline deviated northward, extending zonally across the Tasman Sea along 44°S. In later work, Stramma et al. (1995) inferred the general positions of the 34.7 and 35.1 surface isotherms using data from 10 historical hydrographic sections in the Tasman Sea and Carter et al. (1998) provided an overview of the configuration of the STFZ in the New Zealand region based on available hydrographic data collected around New Zealand.

Hamilton (2006) subsequently examined the detailed structure and configuration of the STF in the Tasman Sea based on a reanalysis of historical data for 1961-1989. He concluded that the STF in the Tasman Sea manifests as a well-defined zonal band, within which overrides, interleaving and intrusion of STWs and SAWs occur. The zonal band was found to be bounded by a northern and southern front, originally identified by Jeffrey (1986), and typically centered on the 35.1 and 34.7 surface isohalines, respectively. Hamilton (2006) found that the northern front marked the northern limit of (surface) SAWs, which over-ride saltier STWs, whereas the southern front was found to mark the southern limit of (subsurface) STWs. Following Belkin (1988), Hamilton (2006) described these fronts as the N-STF and S-STF and estimated their general position west of New Zealand (Fig. 2.6) based on eight coarsely sampled Nansen surveys conducted over the period 1964-1985 (see Fig. 10 in Hamilton, 2006). The recognition of the double frontal structure for the STF in the Tasman Sea by Hamilton (2006) has been crucial for understanding the origins of the STF and in reconciling past differences in interpretations of its position, and hence, its temporal variability.

2.9.2 Temporal variability of the STF in the Tasman Sea

To date, analyses of hydrographic survey data have provided a limited and somewhat conflicting picture of temporal variability of the STF in the Tasman Sea. Using comparisons of the position of the 35.1 and 34.7 isohalines under different atmospheric conditions, Jeffrey (1986) inferred that the position of the double frontal structure was rather fixed in the western Tasman Sea. In turn, Hamilton (2006) inferred the STF as having a "rather constant" position across the Tasman Sea, based on similarities between its position estimated from (1) a single hydrographic survey (Warmus, 1989) and (2) a composite of historical hydrographic data.

Hamilton's (2006) inference of a rather constant position for the STF in the Tasman Sea has questionable support. Results from Jeffrey (1986) show the position of the S-STF in the central and eastern Tasman Sea shifting by between 0-3.5° of latitude under different atmospheric conditions. Results presented by Hamilton (2006) show the S-STF in the central Tasman Sea meandering by ±2° latitude relative to the position of the S-STF estimated from the Warmus (1989) survey. Furthermore, reported positions of the STF south of New Zealand differ by up to 2° latitude. Several studies suggest that the the STF (or S-STF) might occur near 47°S and over the shallow (< 200 m depth) South Island continental shelf (Garner, 1959; Butler et al., 1992; Orsi et al., 1995; Belkin and Gordon, 1996; Chiswell, 1996; Morris et al., 2001; Carter et al., 2008; Belkin et al., 2009; Hopkins et al., 2010). In contrast, other studies have described the STF deflecting strongly poleward in the eastern Tasman Sea to near 49°S and following a pathway around the continental shelf, lying in water depths of 500-700 m along the upper continental slope (Jillett, 1969; Heath, 1981, 1985; Bradford et al., 1991;

Carter et al., 1998; Uddstrom and Oien, 1999). A more recent study by Belkin and Cornillon (2003) has suggested that the S-STF may exist simultaneously in both locations, across the shelf and around the shelf. The suggested across shelf and around shelf positions of the S-STF in this area described in the literature are illustrated in Figure 2.6 and Figure 3.2.

Contrary to the inference of Hamilton (2006), the above results suggest that the position of the STF might in fact be quite variable in the central and eastern Tasman Sea on some time scales. This raises a number of basic questions about variability of the STF south and west of New Zealand, which motivate this thesis: How much does the position of the STF vary on seasonal and interannual time scales? Is the seasonal and interannual variability in the position of the front of similar magnitude in each part of the basin or does it vary zonally? How reliable are climatological estimates of the position of the STF, based on hydrographic data sampled sparsely in time, in light of potentially large variability in the front position? and what determines seasonal and interannual variability in the positions of the STF in this region?

2.9.3 Remote sensing of the STF in the Tasman Sea

Near the landmass boundaries of Tasmania and New Zealand, hydrographic survey data suggest that the STF may have a strong surface temperature expression (Butler et al., 1992; Hamilton, 2006). As highlighted in Section 2.4, satellite-derived SST data can provide vastly improved spatial and temporal sampling when compared to hydrographic survey data. This raises the possibility that long-term data sets of remotely sensed SST images could be used to better understand the fronts temporal variability in this area. However, there is ongoing uncertainty regarding whether or not surface expressions of the STF in the Tasman Sea are observable using satellite SST images (Tate 1988; Tate et al. 1989; Uddstrom and Oien 1999), a point which further motivates the work presented in this thesis.

Within the western South Pacific, prior satellite-based studies of the spatial and temporal variability of the STF have mostly focused on the area of the upper-continental slope and Chatham Rise to the east of New Zealand (42-50°S, 170°E-160°W) (e.g. Chiswell, 1994; Uddstrom and Oien, 1999; Shaw and Vennell, 2001; Sutton, 2001; Belkin and Cornillon, 2003; Hopkins et al., 2010; Graham and de Boer, 2013; Fernandez et al., 2014). In these areas, the surface expression of the STF is relatively straightforward to identify in satellite SST and SSH data, existing as a persistent and quasi-contiguous region of enhanced SST and SSH gradients (see e.g. Uddstrom and Oien, 1999; Graham and de Boer, 2013).

Over the area studied in this thesis (40-50°S, 150-171°E), the STF is a much more challenging feature to identify and track using satellite-derived SST or SSH data. The STF in the Tasman Sea is strongly density compensated and thus, it is not clearly revealed in satellite-

derived SSH data (Sokolov and Rintoul, 2002, 2007a, 2009a; Graham and de Boer, 2013). A number of studies have analyzed multi-year sequences of satellite-derive SST images covering the Tasman Sea (Tate, 1988; Tate et al., 1989; Butler et al., 1992; Uddstrom and Oien, 1999; Belkin and Cornillon, 2003; Graham and de Boer, 2013). A brief overview of previous work is given here, which will be expanded on in **Chapter 5**.

Studies by Tate (1988), Tate et al. (1989) and Uddstrom and Oien (1999) analyzed the climatological SST distribution in the Tasman Sea but could not clearly identify surface thermal signatures of the STF, leading to the suggestion by Uddstrom and Oien (1999) that the STF in the Tasman Sea might lack a surface thermal expression. Belkin and Cornillon (2003) detected thousands of thermal fronts across the STF and STFZ within the Tasman Sea based on applying an edge detection algorithm to 12 years of AVHRR Pathfinder SST images, but were unsure of their association with the STF identified in hydrographic survey data (i.e. Heath, 1985; Szymanska and Tomczak, 1994). Later work by Graham and de Boer (2013), based on a combination of an 11-year (1999-2009) climatology of satellite SST measurements and satellite SSH measurements, reveals a range of SST gradient maxima in the Tasman Sea, some of which are located along the pathway of the STF in this area described by Deacon (1982) (Fig. 3 in Graham and de Boer, 2013). However, the physical association of these gradients in the annual-mean SST fields with the STF remains unclear. This thesis seeks to shed further light on whether surface expressions of the N-STF and S-STF in the Tasman Sea can be observed within remotely sensed SST images (see **Chapter 3** and **Chapter 5**).

Chapter 3

Hydrographic surveys and remote sensing of the Subtropical Front around southern New Zealand

This Chapter examines a section of the global STFZ that passes around southern New Zealand, using hydrographic sections and remotely sensed SST data collected during the austral autumns of 2007, 2008 and 2011. The contents of this Chapter are published as Smith et al. (2013).

3.1 Introduction

The subtropical front zone (STFZ) is a fundamental feature of the western South Pacific Ocean. It separates waters in the subtropical gyres from Subantarctic waters. South and east of New Zealand the global STF has been found to interact strongly with shallow bathymetry (Shaw and Vennell, 2001; Sutton, 2001; Hopkins et al., 2010). Whilst it has become accepted that a continuous STF passes south of New Zealand (Heath, 1985; Belkin and Cornillon, 2003; Carter et al., 2008), reported positions of the front in this region differ by approximately 1-2° latitude.

Classically, the STF has been depicted as a single, well-defined front separating STW and SAW (e.g. Deacon, 1982). However, Belkin (1988) found a double frontal structure for the STF in the South Pacific and distinguished the STF as a broad (4-5° latitude) STFZ bounded by two sharp temperature-salinity fronts: the N-STF and S-STF. This double frontal structure for the STF has also been identified in the south Atlantic Ocean (Belkin and Gordon, 1996; Smythe-Wright et al., 1998; Burls and Reason, 2006), south Indian Ocean (Belkin and Gordon, 1996; Kostianoy et al., 2004), south Tasman Sea (Hamilton, 2006) and across the Chatham Rise east of New Zealand (Sutton, 2001). The STFZ is typically covered by

a layer in the upper 50–100 m composed of a modified SAW, this being a mixture of SAW and STW (Belkin, 1988; Hamilton, 2006), which is driven north and east over the STFZ by prevailing westerly winds (Hamilton, 2006) and is characterised by a wide range of temperature–salinity (T–S) relationships (Fig. 3.1a). The double front structure of the STFZ extends through the south Tasman Sea, with the N-STF as a shallower feature delimiting the northern extent of modified SAW, whilst the deeper S-STF is the main front of the STFZ and defines the poleward extent of sub-surface STW (Hamilton, 2006). The structure of the STFZ in the Tasman Sea is illustrated in Fig. 3.1b.

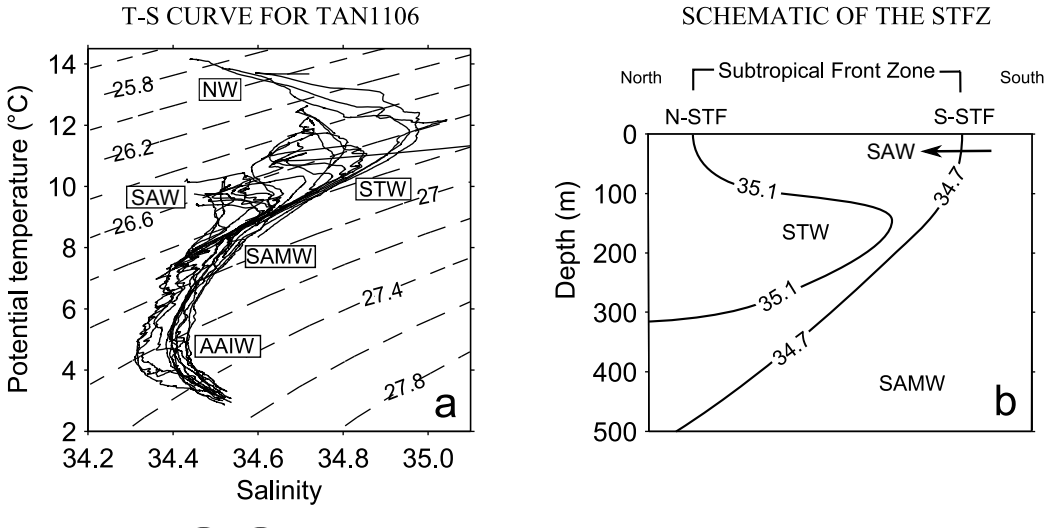

Figure 3.1: (left, a) Potential temperature-salinity diagram of water mass distribution south of New Zealand, based on 0-1000 m CTD casts from all the stations occupied during the TAN1106 cruise. Also shown are selected density contours (grey lines) and water mass labels (Neritic Water NW, Subtropical Water STW, Subantarctic Water SAW, Subantarctic Mode Water SAMW and Antarctic Intermediate Water AAIW). (right, b) Schematic of the STFZ in the Tasman Sea based on Hamilton (2006), with isohalines that approximately delineate the N-STF (35.1) and S-STF (34.7) locations.

In the southern Tasman Sea the S-STF is associated with the poleward limit of a subsurface salinity maximum of STW (at approximately 150m depth), south of which lies SAW overlying the SAMW (Fig. 3.1 b) (Edwards and Emery, 1982; Butler et al., 1992; Szymanska and Tomczak, 1994; Morris et al., 2001; Hamilton, 2006). This tongue-shaped feature of STW extends polewards through the STFZ (Fig. 3.1b) and may be accompanied by strong property gradients in the upper ocean, as the subtropical thermocline outcrops at the 34.7 isohaline (Jeffrey, 1986; Hamilton, 2006). A tongue of high salinity STW is a persistent feature associated with the STF, which has also been observed about the Chatham Rise (Heath, 1976; Sutton, 2001), in the south Pacific Ocean (Belkin, 1988), in the Indian Ocean (Sokolov and Rintoul, 2002; Tomczak et al., 2004) and in the south Atlantic Ocean (Smythe-Wright et al., 1998). There is an intermittent, southward subsurface flow of high salinity STW that maintains the tongue, while flow above the tongue is generally northward (Heath, 1976).

We follow the definition of a breakdown of the tongue of high salinity STW to determine crossings of the S-STF in the hydrographic data presented in Section 3.3.

Traditionally, studies of the STF south of New Zealand have been limited by patchy in-situ data coverage, a challenge in a complex frontal region covering almost 100,000 km^2. Also, remote sensing studies of the STF around New Zealand (Uddstrom and Oien, 1999; Belkin and Cornillon, 2003) have encountered difficulty in identifying the STF unambiguously in the presence of numerous other surface fronts. Using hydrographic and remotely sensed data, we sample the full depth, meridional and zonal extent of a continuous S-STF, interacting with the continental shelf south of New Zealand.

The STF is strongly density compensated in both the southeast Indian Ocean (James et al., 2002) and the south Pacific Ocean (Sutton, 2001) i.e. the effect of temperature and salinity gradients across the front on density largely oppose one-another, resulting in a weak density structure. In the Tasman Sea, there exists only a weak thermohaline contrast between STW and SAW (Hamilton, 2006) and the large amount of density compensation at the STF is associated with a weak, eastward geostrophic transport of around 3 Sv (1 Sv =1×10^6 m^{-3} s^{-1}) (Stramma et al., 1995). In the Tasman Sea, the STF is– composed of a highly variable surface regime (Szymanska and Tomczak, 1994; Uddstrom and Oien, 1999; Belkin and Cornillon, 2003) and a relatively stable, deeper regime (Szymanska and Tomczak, 1994). In-situ surveys of the STFZ discussed by Heath (1985)and Hamilton (2006) also reveal a well-defined subsurface structure and location for the STFZ, with the S-STF found at around 45°S west of New Zealand. Both the surface and deeper regimes exhibit marked meandering of the STF away from regions of steeply shelving bathymetry (i.e. Fig. 10 in Hamilton (2006).

In contrast, along the southeast coastline of the South Island of New Zealand, the STFZ consists of a single, well defined, narrow front which is weakly density compensated and tied to the upper continental slope, following closely the 500 m isobath and displaying limited spatial variability (Shaw and Vennell, 2001; Hopkins et al., 2010). Here it is known locally as the Southland Front. Associated with the front is the Southland Current (Heath, 1985; Chiswell, 1996), an induced geostrophic current that flows to the northeast along the upper continental slope with an estimated transport of 8-10 Sv (Sutton, 2003). East of New Zealand, the STF deflects out into the South Pacific ocean along the Chatham Rise at approximately 43-44°S, where a N-STF and S-STF become re-established across a ~150 km wide STFZ (Jeffrey, 1986; Belkin, 1988; Sutton, 2001). Here, Uddstrom and Oien (1999) and Sutton (2001) show the position of the STF to be topographically guided by the shallow bathymetry of the Chatham Rise.

The continental shelf south of New Zealand presents a barrier to the zonal path of the global STF, which extends to depths of <200 m into the stratified ocean (Hurlburt et al.,

2008), deflecting the STF poleward (Orsi et al., 1995; Carter et al., 1998). In this region differing positions have been given for the STF (Fig. 3.2). Enhanced temperature and salinity gradients in the northern and southern Solander Trough have been attributed to the presence of the STF southwest of New Zealand (Butler et al., 1992; Morris et al., 2001). East of the Solander Trough some studies have positioned the STF directly crossing the Snares Shelf (~47.5°S) south of Stewart Island (across the shelf pathway in Fig. 3.2), turning towards the northeast along the 200-300 m isobath to follow the upper continental slope (Garner, 1959; Orsi et al., 1995; Belkin and Gordon, 1996; Chiswell, 1996; Carter et al., 2008; Belkin et al., 2009; Hopkins et al., 2010).

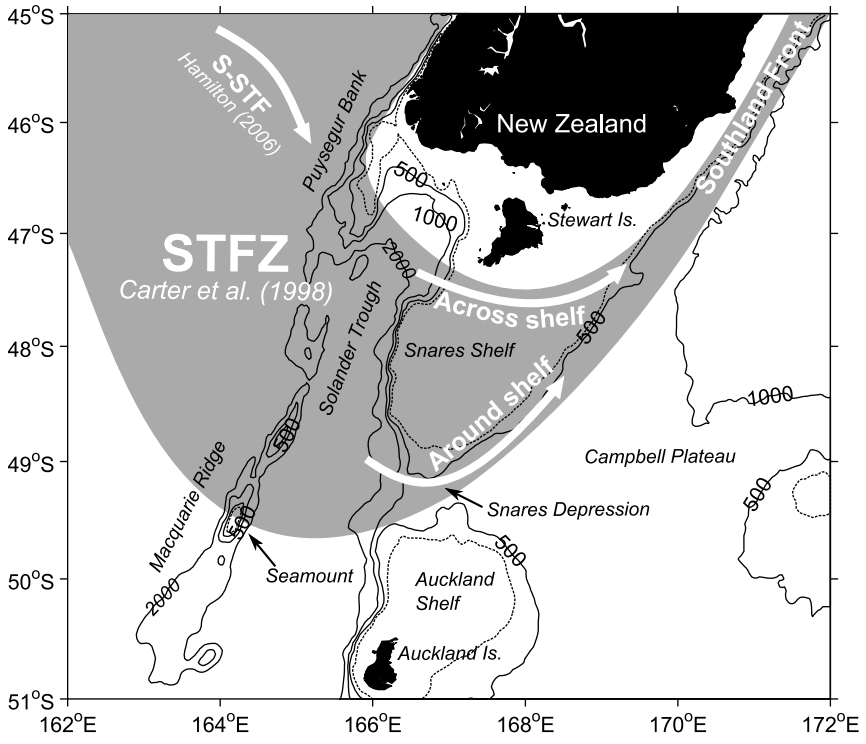

Figure 3.2: Bathymetry south of New Zealand with depth contours at 250 (dashed), 500, 1000 and 2000 m (solid) depth. Also shown is the STFZ position from Carter et al. (1998) (grey shading), the suggested across shelf and around shelf positions of the main front of the STFZ (S-STF) described in the literature, the S-STF position in the Tasman Sea from Hamilton (2006) and the location of the Southland Front from Shaw and Vennell (2001).

In contrast, other studies have described the STF deflecting strongly southward in the eastern Tasman Sea, passing through the Snares Depression at ~49°S before turning towards the northeast to follow the upper continental slope (around the shelf pathway in Fig. 3.2) (Jillett, 1969; Heath, 1981, 1985; Bradford et al., 1991; Carter et al., 1998; Uddstrom and Oien, 1999). More recently, Belkin and Cornillon (2003) applied front detection algorithms to remotely sensed SST data, and suggested that the position of the S-STF south of New Zealand

varies year-to-year. At times the S-STF may pass around or directly cross the Snares Shelf, with the S-STF occasionally splitting into multiple branches upstream of the continental shelf, which may exist simultaneously in the across shelf and around shelf positions.

The differences between the reported positions of the STF imply the position of the front may be highly variable around southern New Zealand. They also raise the question as to whether the front is topographically steered around the Snares Shelf or is largely unaffected by topography and may directly cross the Snares Shelf. The expectation would be for the STF to follow the steeply shelving bathymetry of the upper continental slope, as per the historical view. Here we focus on this dilemma: Can the varying historical locations given for the STF and S-STF south of New Zealand be resolved? Is the front topographically steered or can its position vary?

3.2 Data and methods

3.2.1 Hydrographic data

We use data from three hydrographic surveys undertaken during the austral autumn season in the region of the Macquarie Ridge, Solander Trough and the Campbell Plateau (Fig. 3.3).

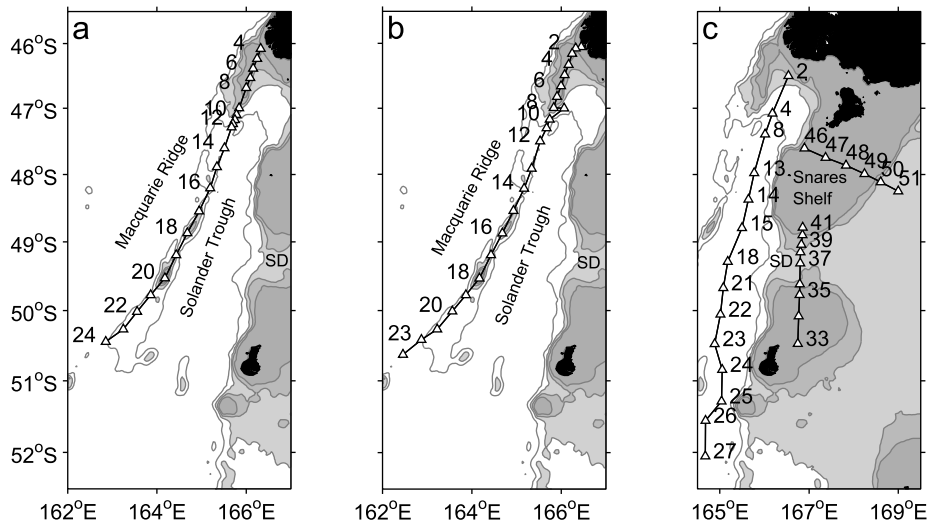

Figure 3.3: Location and station numbers of hydrographic stations used in this study, from the (a) TAN0704, (b) TAN0803 and (c) TAN1106 cruises (triangles). Depth contours are shown at 250, 500, 1000 and 2000 m depth. Major bathymetric features are also labeled (SD - Snares Depression).

The first is a meridional section crossing 164°E during March 2007 along the crest of the Macquarie Ridge on voyage TAN0704 (Fig. 3.3a). This forms the western boundary of our study region. The second is a repeat of the Macquarie Ridge section that was under-

taken during March 2008 during voyage TAN0803 (Fig. 3.3b). Three meridional sections were collected in March and April 2011 during voyage TAN1106, one through the Solander Trough, and two sections crossing the shelf break of the Snares Shelf and the upper continental slope (Fig. 3.3c). These form the eastern boundary of our study region. All three cruises took place on the RV *Tangaroa* where CTD data were collected with a Seabird Electronics SBE-911 CTD and profiles were averaged at 2 dbar intervals for analysis.

To quantify the level of density compensation at the S-STF we estimate the horizontal Turner angle (Tu^h) (James et al., 2002; Soloviev et al., 2002; Tippins and Tomczak, 2003), this being the arctangent of the density ratio ($R\rho = \alpha\Delta T/\beta\Delta S$) given by$Tu^h = atan\,(\alpha\Delta T/\beta\Delta S)$. Here ΔT and ΔS are temperature and salinity differences taken at a specified depth (in the mixed layer at 20 m and at the depth of the STW salinity maximum at 150 m) between stations either side of a frontal interface. Here $\alpha = (1/\rho)\,(\Delta\rho/\Delta T)$and $\beta = (1/\rho)\,(\Delta\rho/\Delta S)$, which are the temperature and salinity expansion coefficients in units of kg m^{-3} $°C^{-1}$ and kg m^{-3} psu^{-1} and are evaluated at the mid-point between station pairs. This quantification categorizes a front as being weakly density compensated (Tu^h = 75-90°), moderately density compensated (Tu^h = 60-74°) or strongly density compensated (Tu^h = 45-60°). Owing to the presence of a seamount that comes within 60 m of the surface along the Macquarie Ridge (clearly evident in Fig. 3.4, 3.6 at ~49.6°S) we do not capture the STW salinity maximum at the S-STF and therefore do not quantify the strength of density compensation below the mixed layer along the ridge.

Absolute geostrophic velocities for each of the meridional sections analysed in this study (Fig. 3.3) are given in Appendix A.

3.2.2 Remote sensing data

We use estimates of SST at 4 km spatial resolution from the Moderate Resolution Imaging Spectroradiometer (MODIS) aboard the Aqua satellite platform, available from the NASA Ocean Color Group (http://oceancolor.gsfc.nasa.gov). Details of how the SST estimates are derived and the data processing steps are given by Minnett et al. (2002). We use the highest MODIS quality flag (QF = 0) so as to eliminate poor quality data where the SST retrieval may have been contaminated by cloud.

To further minimise the contamination of the SST fields by any remaining cloudy-pixels and to reduce the inherent sensor noise, we also apply a 3×3 median filter to the SST fields. We use two single-day MODIS SST fields (covering the 28th and 29th April 2011, respectively), to provide near full coverage of our study region when unusually cloud-free conditions prevailed during cruise TAN1106. Estimates of the SST gradient were made by calculating gradient vectors from adjacent pixels. The gradient vector in the x-direction

(Gx) is given by: $Gx = \partial SST/\partial x$. The gradient vector in the y-direction (Gy) is given by: $Gy = \partial SST/\partial y$. Here ∂SST is the difference in the pixel SST value between pixels adjacent to the pixel being examined (i.e. north-south and east-west) and ∂x and ∂y are the distances between adjacent pixels centres (i.e. ~8 km) in the x and y direction. The gradient magnitude (ΔSST) is then given by: $\Delta SST = \sqrt{Gx^2 + Gy^2}$.

3.3 Locating the Subtropical Front

3.3.1 Macquarie Ridge TAN0704

The S-STF at the Macquarie Ridge transect (Fig. 3.3a) was located from potential temperature and salinity profiles (Fig. 3.4). The ridge itself is composed of undulating bathymetry and a series of seamounts (for instance at 49.6°S in Fig. 3.2, 3.4) that rise from valley floors of around 3000 m depth, to within less than 100 m of the surface ocean (Conway et al., 2012).

Overall TAN0704 captures the position of the S-STF, which is particularly well defined during this voyage. Extending poleward from the Puysegur Bank (47.0°S) is a high salinity tongue of STW (~120 m, salinity > 35.0) capped by a fresher mixed layer composed of modified SAW. South of station 17 the erosion of the tongue of STW locates the poleward extent of the STFZ (close to 49°S), which is also accompanied by sharp meridional property gradients in the S-STF that outcrop into the mixed layer between stations 19 and 20 (Fig. 3.4). Here we see the S-STF consists of a sharp salinity expression (salinity in the top 100 m drops 0.3 over 50 km), which is displaced south of a narrower temperature front (temperature in top 100 m drops 2°C in ~40 km).

We estimate the level of density compensation across the S-STF between stations 19-21, where the front is moderately density compensated in the mixed layer (Tu^h_{20m} = 72.86°). There is a distinct change in the vertical water mass structure that accompanies the strong property gradients at the S-STF (Fig. 3.5a). North of the S-STF water mass properties are distinctly subtropical (salinity > 34.7) with a well-established salinity maximum, whilst to the south of the S-STF the high salinity tongue of STW is strongly eroded and T-S values are more typical of SAW (salinity < 34.5). These findings indicate that during the TAN0704 voyage the S-STF crossed the Macquarie Ridge in water depths of 100-700 m, immediately north of the seamount seen close to 49.6°S (Fig. 3.4). Some remnants of a modified STW are detected south of the seamount, characterised by a weak salinity maximum (salinity ~34.6) at 120 m depth that becomes indistinct at the poleward limit of this transect.

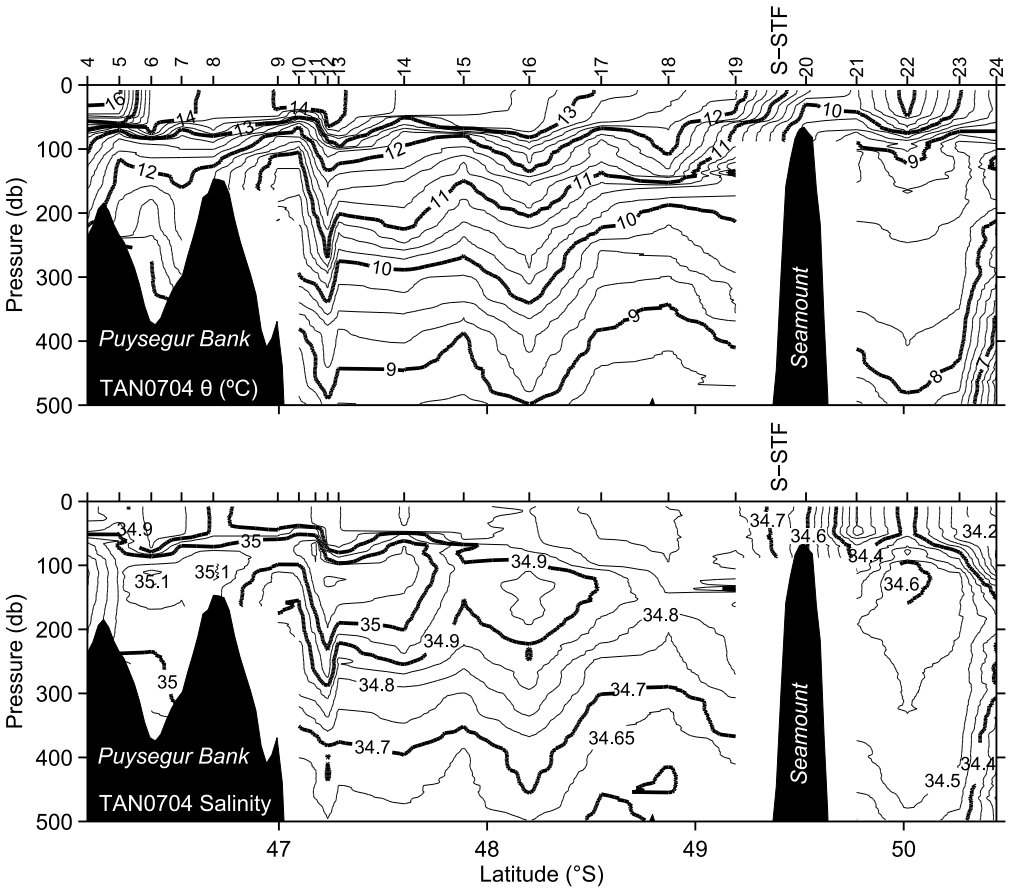

Figure 3.4: (Top) Potential temperature (θ °C) and (bottom) salinity through the upper 500 m along the Macquarie Ridge during cruise TAN0704. Contour intervals are 0.25°C and 0.05 respectively. Station numbers are indicated on the top axis. Also labeled is the approximate position of the crossing of the S-STF. The feature at approximately 49.6°S is a seamount located along the Macquarie Ridge.

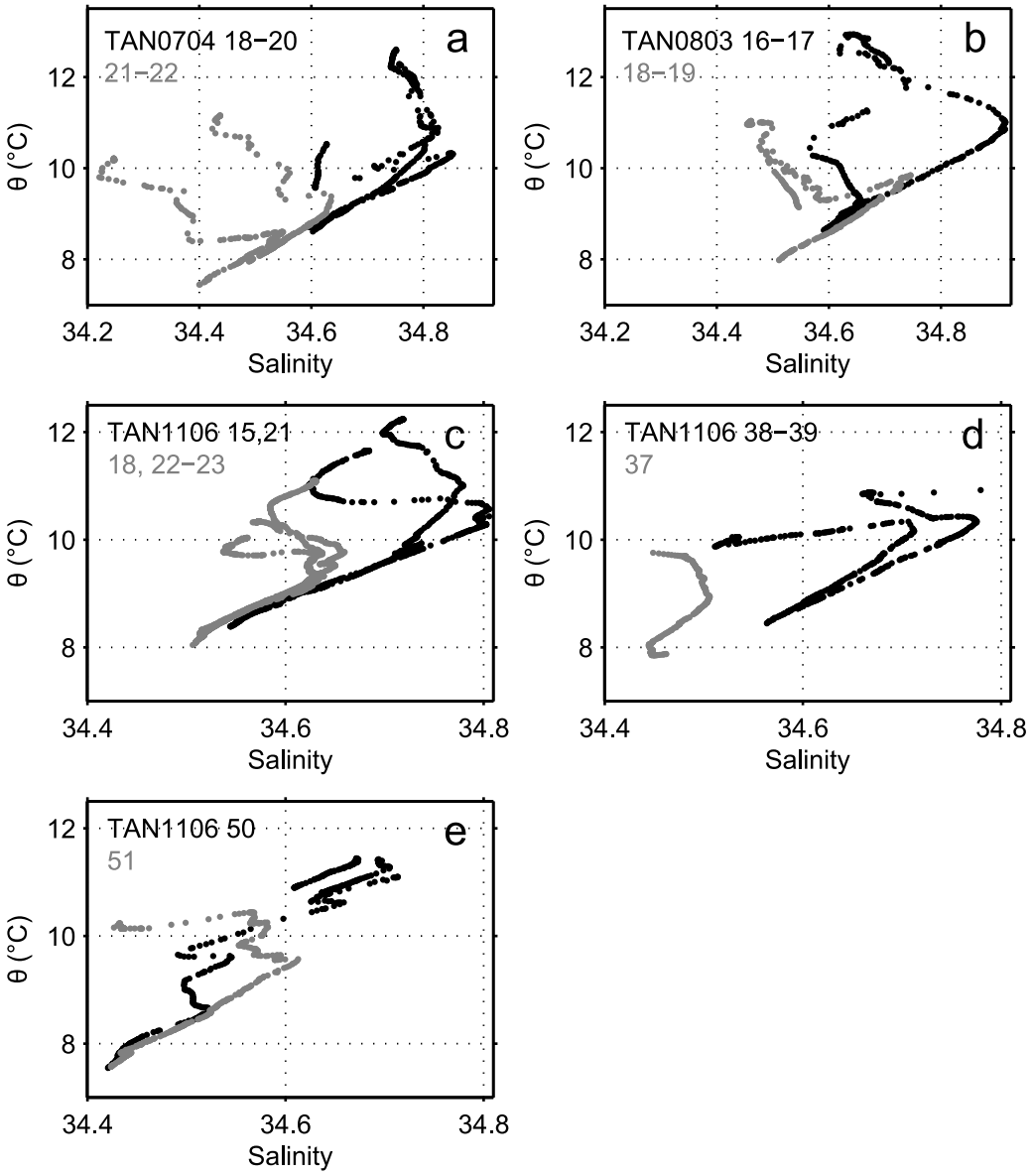

Figure 3.5: Potential temperature-salinity diagrams across the S-STF (a) along the Macquarie Ridge during cruise TAN0704, (b) along the Macquarie Ridge during cruise TAN0803, (c) through the Solander Trough during cruise TAN1106, (d) through the Snares Depression during cruise TAN1106 and (e) across the shelf break of the Snares Shelf and upper continental slope during cruise TAN1106. CTD stations north (south) of the front are marked black (grey).

3.3.2 Macquarie Ridge TAN0803

The potential temperature and salinity profiles (Fig. 3.6) from the TAN0803 voyage (Fig. 3.3b) are comparable to those noted the previous year during the TAN0704 voyage. A core of subsurface STW (salinity > 35.0) extends polewards from the Puysegur Bank at approximately 100 m, with the core becoming fresher and increasing in depth to the south. Overlying the STW is a 50-100 m mixed layer composed of modified SAW and eddy-like features (e.g. stations 11-13 and stations 14-16, Fig. 3.6).

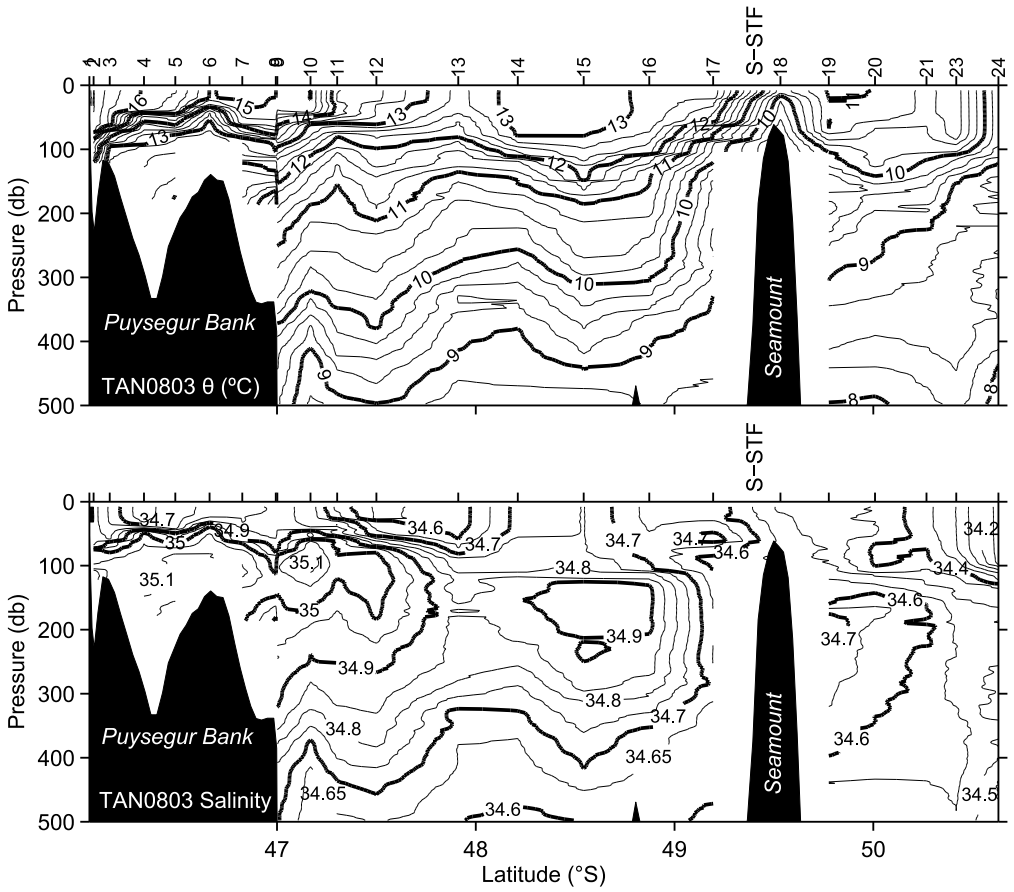

Figure 3.6: (Top) Potential temperature (θ °C) and (bottom) salinity through the upper 500 m along the Macquarie Ridge during cruise TAN0803. Contour intervals are 0.25°C and 0.05 respectively. Station numbers are indicated on the top axis. Also labeled is the approximate position of the crossing of the S-STF. The feature at approximately 49.6°S is a seamount located along the Macquarie Ridge.

The breakdown of the salinity maximum lies north of the seamount between stations 16 and 17 (Fig. 3.5b), with sharp meridional salinity gradients at ~49°S extending between 150-300 m (Fig. 3.6). Poleward of 49°S, the location of the S-STF can be seen in the outcropping of the subtropical thermocline, which extends from approximately 150 m to the surface between stations 17 and 18. This locates the S-STF in a very similar position to that noted in the TAN0704 voyage (compare Fig. 3.4, 3.6), immediately north of the seamount at 49.6°S

and closely coupled with bathymetry shallower than 700 m. The S-STF observed during TAN0803 is again well-defined at the Macquarie Ridge, with the intense temperature and salinity signatures (Fig. 3.6) marking a sharp (~50 km) transition from STW (temperature > 11°C, salinity > 34.7, Fig. 3.5b) to SAW (temperature < 11°C, salinity < 34.6, Fig. 3.5b). We find the S-STF crossing between stations 17 and 18 to be weakly density compensated in the mixed layer (Tu^h_{20m} = 79.85°). A difference between the TAN0704 and TAN0803 voyages is that the low salinity SAW observed south of the surface S-STF expression during TAN0704 (Fig. 3.4) is displaced ~100 km to the south during TAN0803. It lies at the southern edge of an eddy-like feature that is south of both the S-STF and the seamount (Fig. 3.6) and overlaying a tongue of modified subtropical water extending south of the S-STF (at approximately 200 m depth).

3.3.3 Solander Trough TAN1106

The distribution of potential temperature and salinity through the Solander Trough section along 165°E, collected during TAN1106 (Fig. 3.3c), captures distinct transitions in water mass properties associated with two separate frontal regimes (Fig. 3.7). We define these as a neritic front at ~47.5°S and the S-STF, lying between 48.8-49.8°S (Fig. 3.7). The position of the neritic front is evident from compressed isotherms and isohalines at around 75 m depth, lying between stations 4 and 8 at the southern edge of the Puysegur Bank. Warm, low salinity Neritic Waters (NW, T > 13°C, S 34.4-34.6, Fig. 3.1a), derived from STW modified by freshwater outflow from southwest New Zealand (Butler et al., 1992), lie north of the neritic front. The sharp property gradients associated with the neritic front are largely confined to the upper 150 m of the water column and appear to outcrop close to station 8. The inflow of STW from the Tasman Sea around southern New Zealand (Heath, 1985) is clearly seen by a subsurface salinity maximum (S > 34.9 at 100-250 m, Fig. 3.7) that extends polewards, below the neritic front. The poleward limit of this tongue of STW is less distinct in the Solander Trough than seen along the Macquarie Ridge during the TAN0704 and TAN0803 voyages. While water mass properties are more typical of SAW at station 18 (Fig. 3.5c, salinity < 34.65, temperature < 10.5°C), a sub-surface core of high salinity STW is again encountered at station 21 (Fig. 3.5c, salinity > 34.8). This eddy-like feature is evident in Figure 3.7, centered on station 21 and positioned south of the main STW tongue. This complex transition between STW and SAW is accompanied by two temperature fronts (between stations 15-18 and 21-22 respectively) that extend from the depth of the salinity maximum to outcrop into the mixed layer (i.e. 11-12°C and 10-11°C isotherms), in water depths exceeding 2000 m (Fig. 3.7). Property gradients at both fronts are moderately density compensated in the mixed layer (Tu^h_{20m} = 73.06° and Tu^h_{20m} = 71.94° respectively) and at the approximate depth of the salinity maximum (Tu^h_{150m} = 65.81° and Tu^h_{150m} = 62.44° respec-

tively). These observations show that the structure of the S-STF within the Solander Trough during TAN1106 is more diffuse (extending over approximately 144 km (Fig. 3.7)), than the sharp S-STF structure observed while crossing the front along the Macquarie Ridge during TAN0704 and TAN0803 (i.e. Fig. 3.4, 3.6).

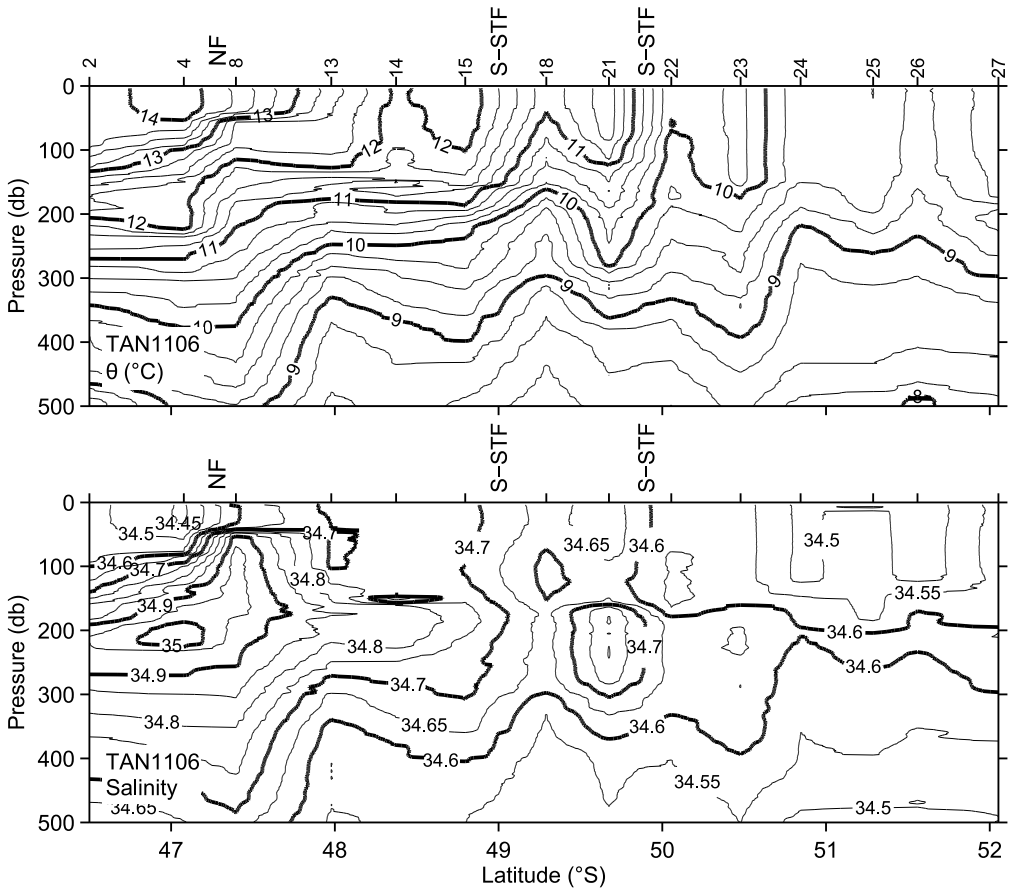

Figure 3.7: (Top) Potential temperature (θ °C) and (bottom) salinity through the upper 500m of the Solander Trough during cruise TAN1106. Contour intervals are 0.25°C and 0.05 respectively. Station numbers are indicated on the top axis. Also labeled are the approximate position of crossings of the neritic front (NF) and S-STF.

3.3.4 Snares Depression TAN1106

A crossing of the S-STF along the transect of the Snares Depression (Fig. 3.3c) is noted in the potential temperature and salinity profiles (Fig. 3.8) at approximately 49.2°S. A well-mixed layer of modified SAW extends over the top 100 m of the Snares Shelf between stations 40 and 42. Moving south across the upper continental slope, moderate stratification develops below the mixed layer as the salinity maximum associated with STW is encountered hugging the shelf edge around 49°S (salinity > 34.8). This high salinity core of STW has a poleward limit between stations 37 and 38 (Fig. 3.5d), where it is seen to be coincident with sharp

meridional property gradients that extend from the depth of the salinity maximum to the surface (Fig. 3.8). These sharp gradients mark the position of the S-STF, outcropping at the surface between stations 38 and 40. The S-STF is more compressed (surface expression is ~28 km wide) and sharply defined in the Snares Depression than we see across the Macquarie Ridge and the Solander Trough (e.g. Fig. 3.4, 3.6, 3.7). While the sharpest salinity gradients associated with the S-STF in the Snares Depression lie close to 150 m depth near the tip of the STW tongue, temperature gradients are strongest in the surface waters, with the front positioned across the upper continental slope in water depths of 300-500 m. The front is characterised by a poleward freshening and cooling of the upper 50 m layer by approximately 2°C and 0.25 respectively (Fig. 3.8). The S-STF within the Snares Depression appears to be weakly density compensated between stations 38 and 40 within the mixed layer (Tu^h_{20m} = 79.11°) and at the depth of the salinity maximum (Tu^h_{150m} = 79.05°). Stations 33-37 south of the S-STF show the presence of a well-mixed fresher (<34.55) and cooler (<10.5°C) SAW, characterised by the absence of a well-defined salinity maximum (e.g. station 37, Fig. 3.5d).

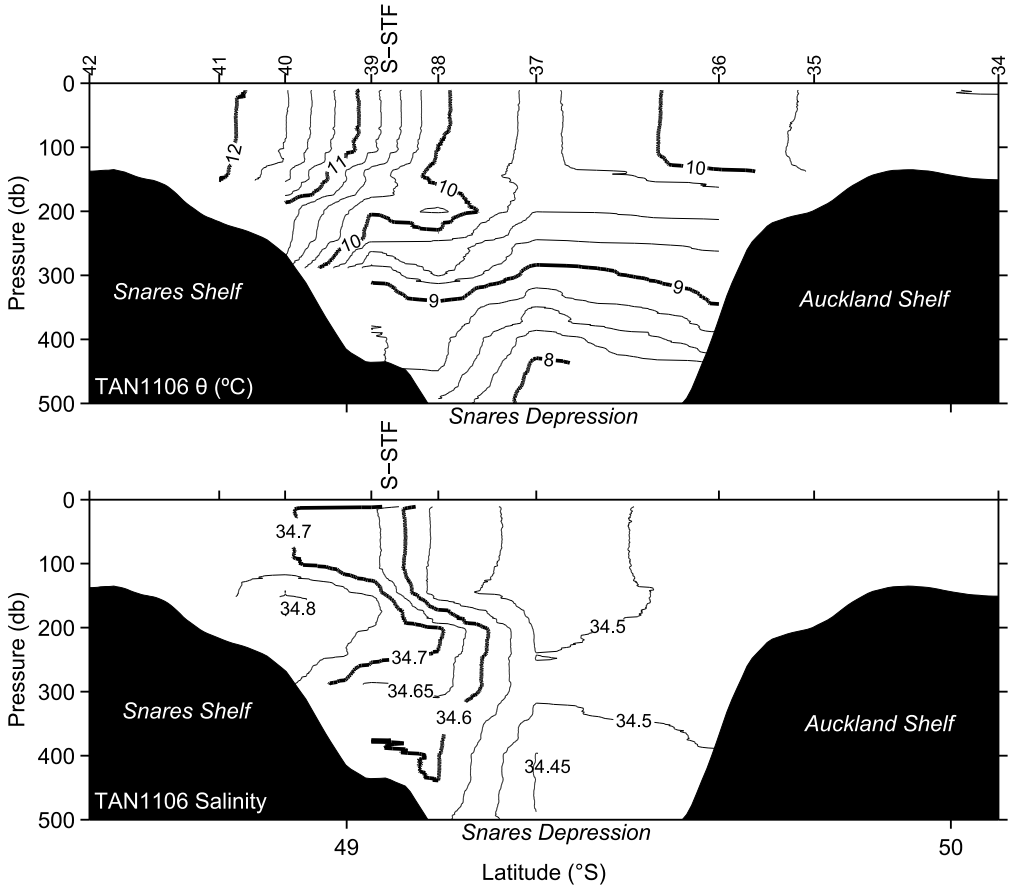

Figure 3.8: (Top) Potential temperature (θ °C) and (bottom) salinity through the upper 500m of the Snares Depression during cruise TAN1106. Contour intervals are 0.25°C and 0.05 respectively. Station numbers are indicated on the top axis. Also labeled is the approximate position of the crossing of the S-STF.

3.3.5 Snares Shelf TAN1106

Well mixed shelf waters extend over the Snares Shelf (Fig. 3.9) in the third transect of the TAN1106 voyage (along 167-169°E, Fig. 3.3c). Approaching the rapidly shelving upper continental slope, moderate stratification develops below the mixed layer due to the presence of a cool, fresh (T < 11.25°C, S ~ 34.6) tongue of SAW encroaching on the shelf (Fig. 3.9). Significant interleaving is evident in Fig. 3.5e (i.e. at salinities between 34.5-34.6), suggestive of mixing between STW and SAW.

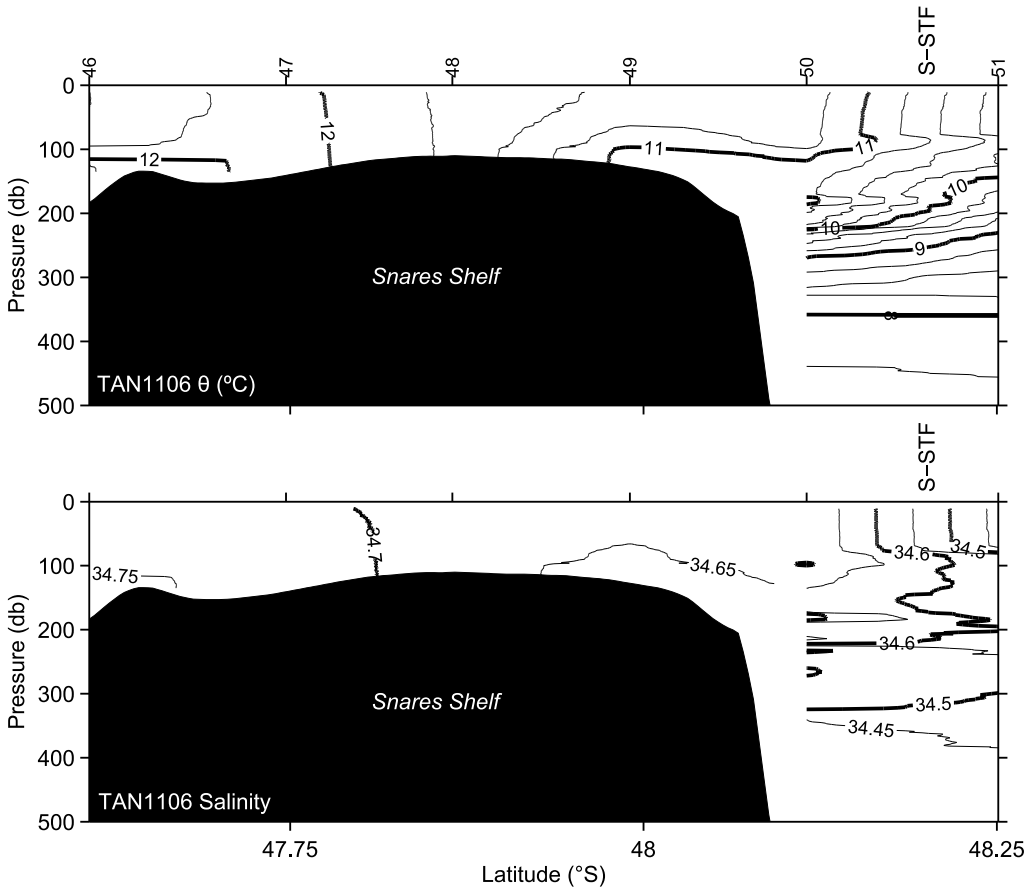

Figure 3.9: (Top) Potential temperature (θ °C) and (bottom) salinity through the upper 500m of the shelf break of the Snares Shelf and upper continental slope during cruise TAN1106. Contour intervals are 0.25°C and 0.05 respectively. Station numbers are indicated on the top axis. Also labeled is the approximate position of the crossing of the S-STF.

Contrary to the four previous descriptions of S-STF crossings, we cannot distinguish the breakdown of a well-defined salinity maximum. The 34.5 isohaline that typically outcrops offshore of the Southland Front (e.g. see Fig. 2.2c in Hopkins et al. (2010)) lies beyond the eastern limit of this transect, suggesting we have only a partial crossing of the S-STF along this section. Sharp drops in the mixed layer temperature and salinity between stations 50 and 51 (1°C and 0.25 respectively, Fig. 3.5e) capture the surface transition into SAW at the

end of the transect. This reveals a sharp surface expression of the S-STF that extends ~15 km offshore of the rapidly shelving continental slope (Fig. 3.9), lying across the 500-600 m isobaths. Between stations 50 and 51 temperature and salinity gradients in the top 100 m largely compensate for one-another in density, as such this partial crossing of the S-STF is strongly density compensated in the mixed layer (Tu^h_{20m} = 47.38°) but moderately density compensated at the level of the salinity maximum (Tu^h_{150m} = 68.70°).

3.3.6 Remote Sensing Observations

While the hydrographic data we have presented provides snapshots of the vertical structure of the S-STF, remotely sensed data is able to provide broader spatial and temporal coverage. With SST observations this is limited to examining surface features. In the previous section we have shown that south of New Zealand the S-STF has a definite surface expression, which during the austral autumn is well coupled with the sub-surface expression of the front. Coupling of S-STF above and below the mixed layer indicates that the position of the front's surface expression provides a reasonable approximation of the location of the S-STF. Similar coupling of surface and sub-surface frontal signatures has been used to approximate the position of the STF south of Australia (James et al., 2002), the S-STF south of New Zealand (Butler et al., 1992), the Southland Front (Shaw and Vennell, 2001; Hopkins et al., 2010), the Subantarctic Front (Luis and Pednekar, 2010; Campanelli et al., 2011)and the Polar Front (Moore et al., 1999; Dong et al., 2006). Here we examine the detailed structure of SST fronts south of New Zealand to estimate the spatial extent of the S-STF, using Aqua MODIS SST estimates collected in April 2011 towards the end of the TAN1106 cruise.

The SST distribution on the 28th and 29th of April 2011 (Fig. 3.10a and 3.10b) reveals a transition from warm surface waters (both STW and modified SAW) that extend from the eastern Tasman Sea (north of 47°S), southeast over the Snares Shelf (>11°C) and along the east coast of the South Island (SST 12-14°C), into cooler SAW (SST < 10°C) south of 49°S. The sharp transition between these two surface regimes marks the surface expression of the S-STF. In places the sea surface is obscured by cloud (white). Previous studies of the S-STF in the Tasman Sea have suggested the position of the 11-12°C surface isotherm in satellite SST fields gives a reasonable approximation of the S-STF position (Tate and Gay, 1986; Butler et al., 1992; Uddstrom and Oien, 1999). Based on the near-surface properties of the S-STF revealed from the hydrographic sections, we use alternative criteria to approximate the position of the front around the South Island. We diagnose the location of the S-STF from a band of high SST gradients (ΔSST 0.08-0.18°C km^{-1}, Fig. 3.10c, d) that are typically enclosed by the 10-11°C isotherms (Fig. 3.10a, b). Using the SST gradient field in this way provides a more definite fix on the S-STF position as opposed to solely examining the

trend in surface isotherms. It also reveals fluctuations in the strength and structure of frontal filaments at the surface.

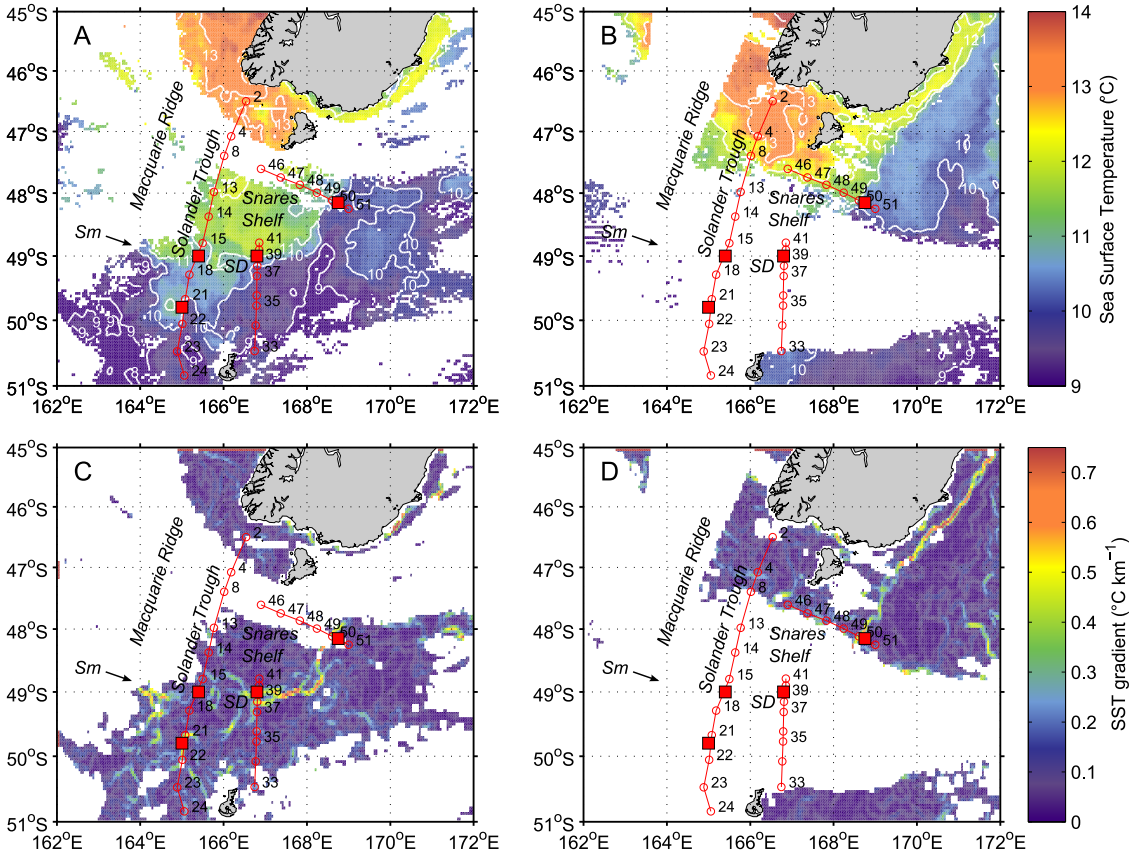

Figure 3.10: Estimates of SST (a-b, °C) and SST gradient (c-d, °C km^{-1}) at the time of the TAN1106 cruise, for the 28th April 2011 (left, a and c) and 29th April 2011 (right, b and d) from the MODIS sensor on the Aqua satellite platform. Also shown are the CTD station locations of the three hydrographic sections from the TAN1106 cruise (red circles) along with the location of S-STF crossings during the TAN1106 cruise (red squares). The location of the seamount (Sm) crossed during the TAN0704 and TAN0803 voyages is also shown, along with the location of the Snares Depression (SD).

Cloud cover west of 165°E obscures our view of the front in the eastern Tasman Sea (Fig. 3.10a, c). The surface expression of the S-STF can be distinguished crossing the Macquarie Ridge (49.4-49.0°S, 164.0°E), where the front has a strong surface expression (ΔSST 0.4-0.6°C km^{-1}, Fig. 3.10c) composed of intense frontal filaments. The position of the S-STF from this satellite image in April 2011 is consistent with the observations from the TAN0704 and TAN0803 hydrographic sections (Fig. 3.4, 3.6), placing the well-defined S-STF in the vicinity of a sharply defined seamount that rises to within 60 m of the surface along the Macquarie Ridge. The stability in the S-STF location at the Macquarie Ridge during the austral autumns of 2007, 2008 and 2011 suggests that the front may be constrained by the sharply defined seamount and valley topography along the ridge.

After crossing the Macquarie Ridge, the S-STF flows eastward into the deep (>2000 m) Solander Trough (164-166°E), where the front meanders to the east-north-east to around 165.5°E, then cuts back to the south forming a backwards 'S' shape that extends across the Solander Trough (i.e. 11°C isotherm in Fig. 3.10a). The surface expression of the S-STF also weakens (ΔSST < 0.3°C km^{-1}, Fig. 3.10c) and becomes fragmented after crossing the Macquarie Ridge. This suggests that the particularly diffuse transition region noted during TAN1106 (Fig. 3.7) spans the full width of the Solander Trough. Although the satellite data were collected 10 days after the S-STF crossing in the Solander Trough during TAN1106, remnants of the eddy-like feature encountered in the hydrographic section (Fig. 3.7) can be seen in the vicinity of 50°S, noted by the closed contour of the 11°C isotherm (Fig. 3.10a).

The surface expression of the S-STF re-intensifies as a distinct, high SST gradient feature west of 166°E, as the front encounters the steep flanks of the Campbell Plateau. There is a marked depression (~600 m deep) in the Campbell Plateau around 49°S (Snares Depression, Fig. 3.2, 3.10), where the S-STF was crossed during the TAN1106 voyage (Fig. 3.8). The satellite data confirms that during TAN1106 the S-STF passed through the northern Snares Depression, hugging the upper continental slope. The detailed structure of the S-STF surface expression reveals a sharp, double temperature front (Fig. 3.10c, ΔSST ~0.6°C km^{-1}). The inshore filament is roughly aligned with the 400 m isobath across the upper continental slope, whilst the second filament lies further south above the 500-600 m isobaths.

Northeast of the Snares Depression the surface expression of the S-STF is well defined, being composed of single or double filaments, which merge and split as the front deflects equatorward, closely following the steep bathymetry of the upper continental slope. The intensity of the surface S-STF expression varies along this path, although SST gradients remain above 0.3°C km^{-1} (Fig. 3.10c). Figure 3.10b shows the SST imagery from the 29th April 2011, which covers a section of the Snares Shelf obscured by cloud the previous day. The surface expression of the S-STF lies close to station 50 (red square in Fig. 3.10b, d), in agreement with the location of the S-STF crossing during TAN1106, across the upper continental slope, east of the Snares Shelf (Fig. 3.9). To the northeast, the S-STF becomes aligned with the 400-500 m isobaths (Fig. 3.2), which the front follows into the climatological position of the Southland Front (Shaw and Vennell, 2001; Hopkins et al., 2010). This finding suggests that during TAN1106, the S-STF position is closely coupled with the upper continental slope between our two crossings of the front seen in the voyage data (Fig. 3.8, 3.9).

The only other feature of note in the satellite SST fields is a fragmented SST front that is observed north of the S-STF in the northern Solander Trough (~47°S), approximately delineated by the 13°C isotherm (Fig. 3.10b) and SST gradients of 0.2-0.4°C km^{-1} (Fig. 3.10d). The proximity of this SST front to the location of the neritic front crossing during

TAN1106 (station 4-8, Fig. 3.7) suggests this is likely the surface manifestation of the neritic front, which is shallower and has a water mass structure distinct from the well-defined S-STF observed following the upper continental slope. Tracing the position of the 13°C isotherm implies the neritic front deflects north towards New Zealand, to the west of Stewart Island (47°S, 168°E).

3.4 Discussion

The interaction of the STF with shallow topography in the southwest Pacific Ocean has been reported in several studies (Uddstrom and Oien, 1999; Shaw and Vennell, 2001; Sutton, 2001; Hopkins et al., 2010). Due to differences between reported pathways of the STF around southern New Zealand (Fig. 3.2), it is unclear whether the position of the front is highly variable in this region or is steered by the shallow topography of the continental shelf and ridge systems. The three hydrographic surveys and largely cloud-free satellite observations allowed us to determine the location of the S-STF and examine how the front responds to shallow topography.

3.4.1 Resolving the position of the Subtropical Front around southern New Zealand

The CTD data show a well-defined S-STF in each of the hydrographic sections. We find the S-STF crossing the Macquarie Ridge (Fig. 3.4, Fig. 3.6) at 49.6°S and the Solander Trough (Fig. 3.7) close to 49.0°S, with eddy-like features migrating to 50.0°S (Fig. 3.7, 3.10), then turning equatorward and following the upper continental slope around southern New Zealand (Fig. 3.8-3.10). These results are consistent with the around the shelf pathway of the S-STF (Fig. 3.2) given in earlier studies that sampled in the same region during both austral summers and winters (Heath, 1981, 1985), as well as in an overview of available hydrographic data collected around New Zealand (Carter et al., 1998), a multi-year remote sensing study of New Zealand waters (Uddstrom and Oien, 1999) and regional ocean simulations of the Campbell Plateau (Tilburg et al., 2002; Hurlburt et al., 2008). Our results place the southerly extent of the semi-permanent S-STF at 49.6°S, further south of New Zealand than some previous authors have suggested (Orsi et al., 1995; Belkin and Gordon, 1996), at what is the most poleward location of the STFZ within the southern hemisphere.

In contrast with our findings, (Butler et al., 1992) located the S-STF at around 47°S within the Solander Trough during the austral autumn. The study by (Butler et al., 1992) noted a subsurface core of STW extended more than 100 km south of their S-STF location to the poleward limit of their survey (48°S), similar to the STW core that extended southward to

the S-STF in our study and that of (Morris et al., 2001). The composite dataset of Hamilton (2006) highlights the strongly meandering nature of the S-STF in this region (see Fig. 10 in Hamilton (2006)). Eddy and meander-like features were also associated with the S-STF during our three voyages (i.e. Fig. 3.6, 3.7, 3.10). Considering the poleward extension of STW beyond Butler et al.'s S-STF location, and the high mesoscale activity associated with the STFZ, the 47°S location reported by Butler et al. (1992) would seem more likely to be a meander or eddy associated with the S-STF, rather than the poleward limit of the front around southern New Zealand.

We do not find evidence for the S-STF passing directly across the Snares Shelf (i.e. across the shelf pathway in Fig. 3.2), which is the pathway for the STF some previous studies have suggested (Garner, 1959; Orsi et al., 1995; Belkin and Gordon, 1996; Chiswell, 1996; Belkin and Cornillon, 2003; Carter et al., 2008; Belkin et al., 2009; Hopkins et al., 2010). The only front-like features we observe north of the S-STF in any of the three voyages are shallow (< 50 m) temperature and salinity fronts within a layer of modified SAW (Fig. 3.4, 3.6, 3.7) along with the neritic front west of Stewart Island (Fig. 3.7, 3.10b, 3.10d), a feature that is typically seen inshore of the S-STF around New Zealand (Heath, 1975; Bradford et al., 1991; Currie et al., 2011). Neither type of front has a water mass structure consistent with the S-STF. The modified SAW occupying the zone between the neritic front and S-STF, which overlies the Snares Shelf, appears to be well mixed and weakly stratified during TAN1106 (e.g. north of the S-STF in Fig. 3.8, 3.9, 3.10a-b). Our findings are in good agreement with Belkin and Cornillon (2003) who suggest it is only the S-STF that is continuous around southern New Zealand. Hamilton (2006) describes the N-STF crossing the Tasman Sea along 44°S in the Tasman Sea, approximately following the 35.1 surface isohaline and terminating offshore of the west coast of New Zealand. We observe a 50-100 m deep mixed layer composed of modified SAW that becomes increasing salty as it extends northward, suggesting the N-STF lies north of our study region.

3.4.2 Response of the S-STF to topography around southern New Zealand

Examining the location of the S-STF revealed that east of 165°E, the S-STF is strongly coupled to the 400-600 m isobaths along the upper continental slope that borders the Snares Shelf (i.e. Fig. 3.8-3.10). This finding is consistent with the study of Shaw and Vennell (2001), which found the Southland Front has an approximate vertical scale of around 500 m, with the front being topographically steered along the upper continental slope by isobaths of a similar depth. It also agrees with earlier studies that show the STF position is closely tied to the upper continental slope along the southeast coastline of New Zealand (Heath, 1975, 1981, 1985; Chiswell, 1996; Sutton, 2003; Hopkins et al., 2010), supporting the view that the S-STF is topographically steered around the Snares Shelf. Our results also reveal a

remarkable consistency between the S-STF position across the Macquarie Ridge during the 3 different years (at approximately 49.6°S, Fig. 3.4, 3.6, 3.10a, c). Although the reason for this consistency is not clear, similar behaviour has been noted in studies of the Polar Front (Moore et al., 1999; Dong et al., 2006) and Subantarctic Front (Sokolov and Rintoul, 2009b), which each follow preferred pathways around bathymetry to conserve potential vorticity (Marshall, 1995). Given the persistent location at which the S-STF crosses the Macquarie Ridge, north of the seamount at 49.6°S (Fig. 3.2), we speculate that the observed S-STF position is one such preferred pathway, with the front being topographically steered by bathymetry of between 100-700 m depth at the ridge.

We find the S-STF is particularly well defined when it crosses the Macquarie Ridge (Fig. 3.4, 3.6), with SST gradients at the front (Fig. 3.10) comparable in magnitude to those observed as the front is topographically steered along the upper continental slope (Fig. 3.8, 3.9, 3.10) and within the Southland Front (Shaw and Vennell, 2001; Hopkins et al., 2010). The strong property gradients at the S-STF as it crosses the Macquarie Ridge are unexpectedly large, given that in the eastern Tasman Sea the STF has historically been considered to be a relatively weak feature (Deacon, 1982; Szymanska and Tomczak, 1994; Stramma et al., 1995) and lacks a strong surface signature (Uddstrom and Oien, 1999). Moore et al. (1999) noted SST gradients at the Polar Front were enhanced in regions of strong topographic steering, a result they contributed to intensification of flow by large topographic features. Although we lack direct measurements of the flow associated with the S-STF, the magnitude of cross-front property gradients provides an indication of the relative flow velocity associated with the front (Shaw and Vennell, 2001). The intense, narrow S-STF observed crossing the Macquarie Ridge implies a localised intensification of flow across the ridge, in keeping with our suggestion that the S-STF is topographically steered not only by the continental shelf around southern New Zealand but also by the Macquarie Ridge. Interestingly, the S-STF interacts with the topography at the Macquarie Ridge for only a relatively short distance, implying the cross-front property gradients rapidly adjust in regions of strong topographic steering.

The topographic intensification of the S-STF across the Macquarie Ridge also indicates an increase in vertical shear. Downstream of topography this makes fronts more prone to the growth of instabilities (Moore et al., 1999). Results presented by Morris et al. (2001) from a hydrographic survey during May 1998 indicated the S-STF spanning an approximate latitudinal range of 49-50°S within the Solander Trough, a result confirmed by our findings from the TAN1106 voyage. However, Morris et al. (2001) could not examine the detailed structure of the front downstream of the Macquarie Ridge as their CTD stations were c. 90 km apart. Our more detailed observations reveal a diffuse and meandering S-STF downstream of the Macquarie Ridge, which is associated with a mesoscale eddy-like feature that

reaches 50.0°S (Fig. 3.7, 3.10). These results resemble the elevated mesoscale variability and reduced front strength downstream of regions of strong topographic steering in the Polar Front (Moore et al., 1999; Dong et al., 2006), Sub-Antarctic Front (Sokolov and Rintoul, 2009b) and Southland Front (Hopkins et al., 2010). Although we have insufficient observations to offer a complete explanation of the front-topography interactions, the presence of meander and eddy-like features in the Solander Trough would seem to be a consequence of the topographic steering and intensification of the S-STF across the Macquarie Ridge, which gives rise to a destabilsation of flow and growth of meander and eddy-like features downstream (Huppert and Bryan, 1976; Moore et al., 1999). The meander-like nature of the S-STF downstream of the Macquarie Ridge offers a possible explanation to the study of Belkin and Cornillon (2003) who found the front position to be particularly variable in the Solander Trough. Following the passage of the S-STF through the Solander Trough, the front reintensifies against the topography of the upper continental slope (Fig. 3.8, 2.10), in line with the behaviour expected from a topographically steered front (Moore et al., 1999).

Topographic steering of the STFZ has also been reported east of New Zealand across the Chatham Rise, where the positions of the N-STF and S-STF are steered by bathymetry of between 250-500 m depth (Chiswell, 1996; Uddstrom and Oien, 1999; Sutton, 2001). West of New Zealand, Rintoul et al. (1997) suggested topographic influence on the STF south of Tasmania may explain the persistence of the front location over the South Tasman Rise, in a region where bathymetry shallows sharply from 3000 m to < 1000 m. In contrast, the description of the S-STF following a pathway across the Snares Shelf (Fig. 3.2) implies the S-STF would be limited to less than 200 m in the vertical by the bathymetry of the continental shelf and therefore be largely unaffected by topographic steering around southern New Zealand. However, this is not consistent with our new observations, which extend the finding of Shaw and Vennell (2001) in the Southland Front, suggesting a depth of approximately 500 m is required for the S-STF to pass around southern New Zealand.

While the neritic front and a series of shallow fronts within a surface layer of modified SAW were observed north of the S-STF around southern New Zealand, we find no evidence supporting the suggestion of multiple S-STF branches around southern New Zealand (Belkin and Cornillon, 2003). However, given that our study is a series of snapshots limited to one season, more observations would be required to understand whether a shallow branch that is unaffected by the topographic steering of the 500 m isobath may at times split from the S-STF and cross the Snares Shelf. The composition and dynamics of the unusually persistent SST front observed lying across the Snares Shelf by Belkin and Cornillon (2003) remains unclear.

3.4.3 Modification of the STFZ around southern New Zealand

A notable finding of our study is that the S-STF is moderately-to-weakly density compensated both above and below the mixed layer around southern New Zealand (with the exception of the incomplete front crossing across the eastern edge of the Snares Shelf, shown in Figure 3.9). In comparison, earlier studies have found property gradients across the STF to be strongly density compensated in the South Atlantic (Stramma and Peterson, 1990; Lutjeharms et al., 1993), southern Indian Ocean (Stramma, 1992; James et al., 2002; Tippins and Tomczak, 2003) and west and east of New Zealand (Hamilton, 2006; Sutton, 2001). An apparent consequence of the increased density contrast at the S-STF as it passes around southern New Zealand, is that the front transitions from being associated with limited transport in the Tasman Sea (Stramma et al., 1995) to larger transports in the Southland Front (Sutton, 2003). Topographic intensification of flow at the Macquarie Ridge and along the upper continental slope offers a possible explanation for the narrow S-STF and sharp property gradients in these locations (i.e. Fig. 3.10). However, an increase in the spatial gradient at the S-STF does not explain why the thermohaline contrast across the front is relatively strong around southern New Zealand (i.e. Fig. 3.5), when compared to the weak thermohaline contrast and strong density compensation at the STF in the Tasman Sea (Hamilton, 2006; Stramma et al., 1995). While our observations do not reveal the mechanism responsible for this enhancement of the density contrast across the S-STF, the 1-2°C drop in SST properties at the S-STF between the Tasman Sea and Southland Front (Uddstrom and Oien, 1999; Shaw and Vennell, 2001) implies the change in density structure of the front may be due to a modification of water mass properties around southern New Zealand. Such water mass modification would be expected given the southerly deflection of the S-STF around southern New Zealand and the exposure of the upper water column to increased heat flux loss from polar westerlies, coupled with the modification of surface waters by freshwater influx around the coastline of southern New Zealand (Butler et al., 1992).

It remains unclear what dynamics in the Tasman Sea control the poleward deflection of the S-STF to its observed poleward limit close to 49.6°S across the Macquarie Ridge and Solander Trough. Previous results have suggested that the S-STF turns poleward to the west of New Zealand in water deeper than 2000 m (Heath, 1985; Carter et al., 1998; Hamilton, 2006), well before we find the S-STF encountering shallow topography around southern New Zealand. Both our observations and those of Stramma et al. (1995) suggest the S-STF is moderately density compensated within the eastern Tasman Sea, implying that topographic influence of the Macquarie Ridge and Puysegur Bank on the S-STF would only extend to the baroclinic Rossby radius of deformation, approximately 20 km around southern New Zealand (Chelton et al., 1998). This would not cause the large-scale poleward deflection noted in the S-STF (e.g. see Fig. 3.2 in Heath (1985)). The poleward deflection of the

front may be driven by an atmospheric mechanism, given that the S-STF has a particularly intense surface signature (Fig. 3.10) and therefore away from regions of strong topographic interaction, the position of the front in the Tasman Sea would be expected to respond strongly to shifts in wind-stress curl (McCartney, 1977; Stramma et al., 1995; Burls and Reason, 2006; Graham et al., 2012). A second mechanism that may contribute to the strong poleward deflection of the S-STF around southern New Zealand is a southward advection of STW along the west coast of New Zealand described by Hamilton (2006), which Butler et al. (1992) found to be around 0.5 m s-1 at 50 m depth. Based on analyses of a high-resolution climatology of the region by Ridgeway and Dunn (2003), a likely source of this STW is zonal eastward flow from the central Tasman Sea that is steered southward by the Challenger Plateau and in turn, by the coastal boundary. Results presented by Heath (1975) who used geopotential topography, show a similar southward flow that deflects the STF across the Macquarie Ridge and Solander Trough north of 49˚S (Heath, 1985), close to the position of the S-STF noted in our study.

Strong changes taking place in the western boundary current of the south Pacific gyre (the East Australian Current), which has intensified and penetrated southward by 350 km since 1944 (Ridgway, 2007; Hill et al., 2008) under increased wind stress curl in the south Pacific (Roemmich et al., 2007), are likely to have implications for the STFZ in the south Pacific Ocean. A recent study by Hill et al. (2011) reveals stronger wind stress curl over the south Pacific favors a southward extension of the south Pacific gyre to envelop New Zealand, and stronger transport through the southern Tasman Sea via the East Australian Current extension, at the expense of the dominant transport pathway north of New Zealand via the Tasman Front (along 32°S). Whether such an increase in the trans-Tasman export of STW to New Zealand affects the structure or transport associated with fronts in the STFZ await further observations and research.

3.5 Conclusions

We conclude that around southern New Zealand the S-STF consists of a single branch, which is topographically steered by the Macquarie Ridge and upper continental slope. A robust feature delineating the surface intensified S-STF around southern New Zealand is the poleward limit of a subsurface tongue of high salinity STW. At the time of our analysis, the surface and subsurface expressions of the S-STF are strongly coupled, showing remotely sensed SST data can provide a good approximation of the front's position. The poleward limit of the S-STF around southern New Zealand is 100-200 km further south than the across-shelf pathway suggested in earlier studies (i.e. Belkin et al. (2009) and Chiswell (1996)) and the S-STF crossing of Butler et al. (1992). The location of the S-STF during the austral autumns

of 2007, 2008 and 2011 is remarkably similar to the around-shelf STF position inferred by Heath (1985) and the southern extent of the STFZ given by Carter et al. (1998), which each draw on data collected at different times of the year to this study. We conclude from this that the around-shelf pathway is the most likely position of the S-STF, rather than just a seasonal deflection during austral autumn. The S-STF is traced around southern New Zealand, crossing the Macquarie Ridge and Solander Trough at 49.6°S, before turning equatorward to follow the upper continental slope around the Snares Shelf (Fig. 3.11).

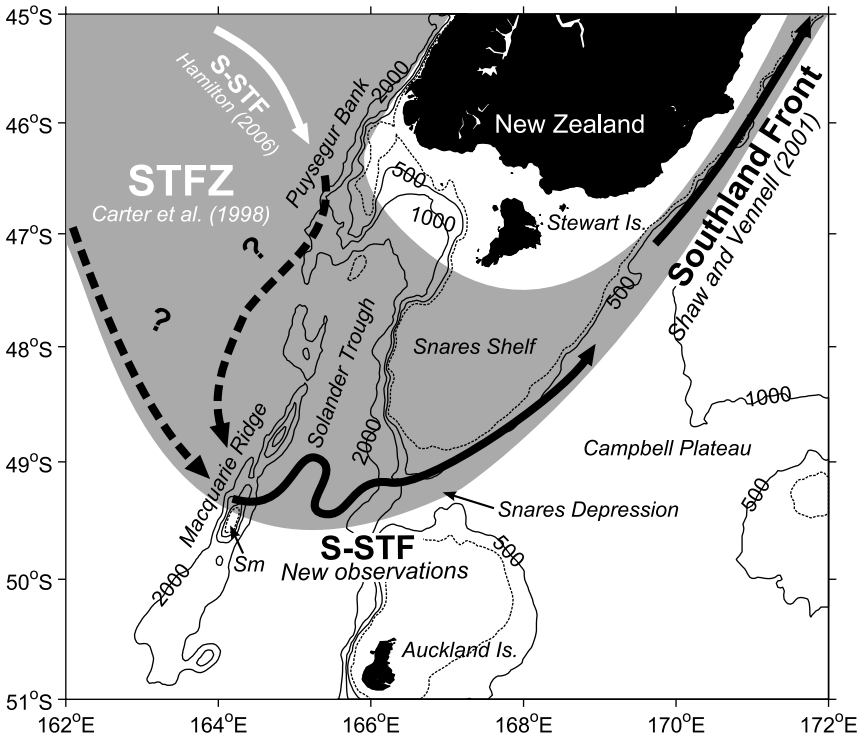

Figure 3.11: Schematic of the S-STF pathway (solid lines) around southern of New Zealand based on Hamilton (2006) and our new observations presented in this study. Also shown is the location of the STFZ from Carter et al. (1998) (grey shading) and the location of the Southland Front from Shaw and Vennell (2001). Dashed lines show where the position of the S-STF is uncertain. The location of the seamount (Sm) crossed during the TAN0704 and TAN0803 voyages is also shown. Depth contours are shown at 250 (dashed), 500, 1000 and 2000 m (solid) depth.

The around-shelf pathway shows that the S-STF is consistently aligned with particular isobaths around southern New Zealand. This pathway is explained in terms of topographic steering of the front by bathymetry at approximately 500 m depth. The S-STF is well-defined in its passage across the Macquarie Ridge and along the upper continental slope. Within the Solander Trough the front is more diffuse and forms a distinct meander (Fig. 3.11). We link this behaviour to topographic intensification of the S-STF across the Macquarie Ridge, giving rise to flow disruption and increased mesoscale variability downstream of the ridge.

The S-STF then reintensifies as it is topographically steered along the upper continental slope. The presence of mesoscale eddies, a meandering S-STF and a series of shallow fronts that lie north of the S-STF, potentially explain the range of reported positions of the STF around southern New Zealand. Around southern New Zealand there is little density compensation in the S-STF, which is in contrast to the strong density compensation in the STF over much of the rest of the Southern Hemisphere. This raises a question as to whether the S-STF around southern New Zealand is associated with significant transport compared to the weak STF in the Tasman Sea, and whether that transport is continuous with the Southland Current. The STF is traditionally considered a relatively weak and highly variable frontal system (Stramma et al., 1995), yet we show that around southern New Zealand the S-STF is particularly well defined and is steered by topography.

Chapter 4

Methodology for studying oceanic front variability from remotely sensed SST images

4.1 Introduction

In **Chapter 3**, two remotely sensed SST images collected during April 2011 enabled estimates of the position of the S-STF south of New Zealand to made. Much longer data sets of remotely sensed SST images are also available - for instance, from the Advanced Very High Resolution Radiometer (AVHRR) Pathfinder Sea Surface Temperature (SST) Program (Casey et al., 2010). The Pathfinder SST program provides remotely sensed SST images that are collected twice-daily, with global coverage and extend over a period exceeding 30 years. The availability of the Pathfinder SST data provided the motivation to go further in this thesis, to investigate variability of the N-STF and S-STF over the wider Tasman Sea, and on much longer time scales, by analyzing their surface expressions using this long term data set remotely sensed SST images. This Chapter develops the methodology and data set that is used in these investigations.

In this Chapter, an existing edge-detection algorithm (Cayula and Cornillon, 1992) is used to detect oceanic fronts in remotely sensed SST images covering the period 1982 through 2011 over the Tasman Sea (30-55°S, 140-180°E). These images are derived from the AVHRR Pathfinder Version 5.2 (herein, PFV5.2) SST data set (Casey et al., 2010). A new algorithm is then developed and implemented in this Chapter to estimate physical properties (including the SST and SST gradient magnitude) of the fronts detected in these images. This new algorithm is an original methodological contribution for the analysis of oceanic fronts that stems from this thesis. The result is a 30 year (1982-2011) data set of oceanic front detections covering the Tasman Sea, together with estimates of the physical properties of each detected

front. This new data set is used in **Chapters 5** and **6** to investigate the existence and the variability of the surface expressions of the N-STF and S-STF in the Tasman Sea and south of New Zealand.

This Chapter is split into eight further sections: The data set of SST imagery is described in Section 4.2. The motivation for developing a data set of thermal fronts from this satellite imagery is presented in Section 4.3. An overview of existing methods to identify and to parameterize the properties of ocean fronts in remotely sensed SST images is then given in Sections 4.4-4.6. The previously developed Single Image Edge Detector (SIED) algorithm (Cayula and Cornillon, 1992) that is used to detect fronts in the remotely sensed SST images of SST is described in Section 4.7. The development of a new algorithm to estimate physical properties of the thermal fronts detected in satellite imagery is discussed in Section 4.8. Results from applying the edge-detection and front-analysis methods to synthetic SST images, in order to test the sensitivity of the methodology, is presented in Section 4.9. A summary of the Chapter is provided in Section 4.10.

4.2 Data

This section begins with a brief overview of the instruments available for the measurement of SST from space. The data set of remotely sensed SST images that is used in this Chapter to produce the new data set of thermal fronts is then discussed.

4.2.1 Remote sensing of SST

Since the late 1970s, several instruments flown on earth-observation satellites have provided the means to determine SST from space. The instruments, known as radiometers, measure the thermal emission of electromagnetic radiation from the sea surface (Minnett, 2009). From these measurements, one is able to derive estimates of the SST using a retrieval algorithm, which corrects for the atmospheric absorption, scattering and re-emission of the sea-leaving signal. There are two types of radiometers for SST measurement from space: infrared radiometers and microwave radiometers. Robinson (2004) and Minnett (2009) provides a basic introduction to these instruments and their measurement principles. The main characteristics of these different instruments for estimating SST are summarised in Table 4.1.

Table 4.1: Characteristics of infrared and microwave radiometers for estimating SST. Adapted from Minnett (2009).

Infrared Radiometers	*Microwave Radiometers*
SST estimates with a spatial resolution of 1-4 km	*Poorer spatial resolution (~50 km)*
Surface can be obscured by cloud	*Through-cloud capability, but measurement sensitive to rain, along with sea-surface roughness*
SST estimates available near coastlines	*SST estimates are not available within ~75 km of coastlines due to side-lobe contamination by microwave emissions from land*
Records extend from 1981 to present	*Records extend from 1997-2014 (TMI) between 2002 to present (AMSR-series)*
Instruments include: the Advanced Very High Resolution Radiometer (AVHRR), the Moderate Resolution Imaging Spectroradiometer (MODIS) and the Along Track Scanning Radiometer (ATSR) series of sensor	*Instruments include: the TRMM Microwave Imager (TMI) (data limited to regions 40°N to 40°S) and the Advanced Microwave Scanning Radiometer (AMSR) series of sensors*

4.2.2 The AVHRR Pathfinder Version 5.2 SST Data Set

This thesis uses remotely sensed SST images from the PFV5.2 SST data set (Kilpatrick et al., 2001; Casey et al., 2010). This is a long term data set of gridded and quality controlled SST estimates that are derived from a reprocessing of more than 30 years (1981 to present) of infrared measurements taken by the AVHRR sensors. A regional subset of the PFV5.2 data set was retrieved from http://pathfinder.nodc.noaa.gov. These data comprised of night-time SST data at ~4.4 km spatial resolution, covering a 30 year period from January 1982 to December 2011 and the geographical region of 30-55°S, 140-180°E. Day-time SST data are also available in the PFV5.2 data set but are not used in this study in order to limit the potential contamination of the remotely sensed SST data due to diurnal warming events (Minnett, 2009).

There are a couple of motivating factors for using the PFV5.2 data set for the detection and analysis of thermal fronts:

1. The spatial resolution of the PFV5.2 data set (~4 km) is adequate to resolve the strong horizontal temperature gradients associated with surface thermal fronts. The high spa-

tial resolution of these remotely sensed images also provide adequate data in the cross-frontal water masses with which to parameterise the physical properties of a detected front.

2. A second reason for using the PFV5.2 data set is the length of the data record. The PFV5.2 data set consists of a reprocessing of all measurements made by the AVHRR instrument, which has flown aboard the NOAA series of polar orbiting satellites from November 1981 to present (Kilpatrick et al., 2001; Casey et al., 2010). The length of this record is of benefit in **Chapter 5** where statistics of occurrence of thermal fronts are examined - this long term data record can potentially provide hundreds of observations of thermal fronts, over three decades, and hence more robust statistics. This long-term, 30 year record is also consistently calibrated (Kilpatrick et al., 2001), making it suitable for studying the seasonal to decadal time scales of SST variability at the S-STF that are of primary interest in **Chapter 6**.

A potential drawback of using a data set of remotely sensed SST images derived from infrared measurements is that the surface expression of thermal fronts in these images may be obscured in regions of frequent cloud (Table 4.1). This potential issue is addressed by deriving the data set of thermal fronts from PFV5.2 SST monthly composite images (Section 4.2.5). Although cloud-free images of SST are available from the AMSR-series of sensors (Chelton and Wentz, 2005), and these cover the study region in the Tasman Sea, the AMSR-derived data have much coarser (c. 50 km) spatial resolution and these are only available for sporadic periods from 2002 onwards (Table 4.1). This makes the AMSR-derived data much less suitable for deriving a data set of thermal fronts, and investigating the variability of the STF, than the PFV5.2 data set.

4.2.3 The Pathfinder algorithm

The PFV5.2 data set utilizes a multi-channel SST retrieval algorithm - the Pathfinder algorithm - to derive SST estimates from the measurements made by the AVHRR instrument. An overview of the Pathfinder algorithm is given here; further details of the data processing and derivation of the Pathfinder algorithm can be found in Kilpatrick et al. (2001).

The AVHRR instrument measures the infrared radiance emitted by the sea surface and reports this as a satellite brightness temperature (Minnett, 2009). The brightness temperature measurements made by the instrument are characteristic of the skin-layer of the ocean (<1 mm depth); however, these measurements will be contaminated by atmospheric effects, including the atmospheric absorption and scattering of infrared radiance (Minnett, 2009). The Pathfinder algorithm utilizes a set of coefficients to correct the brightness temperature measurements for atmospheric effects. These coefficients are derived from a regression of the

satellite brightness temperatures onto coincident *in-situ* SST measurements made by drifting buoys at a depth of ~ 5 m (Kilpatrick et al., 2001; Lumpkin and Pazos, 2007; Minnett, 2009). Consequently, the SST estimates produced by the Pathfinder algorithm correspond to an estimate of SST at ~ 5 m depth (i.e. within the oceans mixed layer), rather than in the 'skin' of the ocean (Minnett, 2009).

The Pathfinder coefficients are updated on a month-by-month basis in order to minimise errors in the SST data due to drifts in the sensor calibration, platform orbit or changes in atmospheric conditions (Kilpatrick et al., 2001; Marullo et al., 2007). As a consequence, SST estimates obtained using the Pathfinder algorithm provide a consistently processed, stable record of global SST that is suitable for studies of interannual climate variability and multi-decadal trends (Marullo et al., 2007; Casey et al., 2010). Kilpatrick et al. (2001) suggest, based on global comparisons with measurements from drifting buoys by latitudinal band, that the global accuracy of the Pathfinder algorithm is around $0.02°C \pm 0.5°C$. The upper bound on the relative error in remotely sensed SST estimates from the AVHRR instrument has been estimated at a similar level of ~0.2°C by Ullman and Cornillon (1999), who deemed this to be of acceptable accuracy to detect the spatial differences in temperature associated with the surface expression of thermal fronts, as is also attempted here.

4.2.4 Pixel-by-pixel science quality levels

Processing errors in the Pathfinder algorithm, along with the presence of cloud contamination, may lead to poor quality SST estimates (Kilpatrick et al., 2001). The processing steps used to derive SST estimates using the Pathfinder algorithm include a set of quality condition tests to help identify pixels that are cloud contaminated, and to assess the overall quality level of the SST estimates. An overall quality level is assigned to each pixel following these tests, varying from 0 (lowest quality) to 7 (highest quality). A technical description of the quality condition tests is given in Kilpatrick et al. (2001) and in Barale et al. (2010).

Before examining SST data from the PFV5.2 data set, user judgement is needed to select data with an appropriate pixel quality level. In general, the higher the quality level, the greater the reliability that can placed on a pixel SST value; however this is at the expense of reducing the spatial coverage of data, due to the removal of lower-quality SST estimates (Kilpatrick et al., 2001). The Pathfinder user guide (Evans et al., 2009) suggests that for most oceanographic applications, the use of pixels between quality levels 4 and 7 is appropriate. In the work presented here, only SST pixels with a PFV5.2 quality level of 4 or above were used. All other pixels were masked as cloud. This quality level was considered to provide the best compromise between maximizing the spatial coverage of valid data in each remotely sensed

SST image and minimising the likelihood of cloud contamination and thus, poor quality SST estimates.

4.2.5 Motivation for using monthly composite images

One of the limitations of using infrared SST images acquired at a daily resolution in the Tasman Sea is the presence of frequent and persistent cloud cover (e.g. Fig. 3.10). It was noted during initial tests with daily resolution PFV 5.2 SST images that cloud cover frequently prevented the observation and detection of thermal fronts in one of at least three ways:

1. Persistent cloud cover was seen to completely obscure the view of particular regions of the Tasman Sea for periods of a few months at a time.

2. There were often periods of several months or more at a time when cloud cover within the daily images was too heavy over wide regions of the Tasman Sea for the front detection algorithm (SIED) used in this study to operate. As described in Section 4.7.2, the SIED performs edge-detection in a sliding 32×32 pixel window, but only provided that at least 65% of the satellite image pixels in that window are cloud free (Cayula and Cornillon, 1992).

3. Scattered cloud cover within the daily images appeared to obstruct the SIED from locating thermal fronts in remotely sensed SST images that could be seen 'by eye', by masking sections of fronts that meandered through a sliding window position. Using the level 4 quality flag, the cloud screening employed by the Pathfinder processing is also known to incorrectly flag satellite pixels within the daily images that lie in the vicinity of intense surface thermal fronts as being cloud contaminated (see e.g. Kilpatrick et al., 2001; Ullman et al., 2007; Hopkins, 2008), further hampering the observation and detection of thermal fronts.

To mitigate for the frequent and large-scale cloud cover over the Tasman Sea in PFV5.2 SST daily resolution images, PFV5.2 SST monthly composite images were used in this study. A monthly composite SST value was calculated at each image pixel using the mean of all of the valid, daily, night-time only SST estimates at that image pixel within a given month. Monthly compositing reduces cloud-contamination within a given geographic region, increasing not only the probability that the SIED can operate, but also the probability that a thermal front that is present within a given part of an image over the course of a month can be observed and detected. Monthly compositing, coupled with changes in the location of ocean fronts and cloud cover within a month, also help to supply valid data for frontal pixels that may be

erroneously flagged as being cloud-contaminated in daily-resolution remotely sensed SST images.

A potential issue with using monthly composite images are false "fronts". As outlined in Section 4.7, the SIED indicates a "front" where the mean SST of adjacent water masses exceeds 0.375°C. For a false "front" to occur, changes in temperature and cloud-coverage within a month need to conspire in such a way that an area of the sea surface is warmed (or cooled) during the month, with half of this area visible at the start of the month and the adjacent area visible later in the month. These conditions would give the impression of a thermal front in a monthly composite image, when none exists in daily images. If the change in temperature exceeds 0.375°C and occurs of a spatial scale greater than about 50 km$\times$50 km, there is a potential the SIED might wrongly identify these compositing artefacts as "fronts". This is a particular issue when examining patterns of occurrence of thermal front detections, as performed in **Chapter 5**, because repeated false front detections may introduce artificial signals in to the frontal statistics. The potential impact of false front detections on the results presented in **Chapter 5** are discussed at the end of Section 5.5.1.

4.3 Motivation for developing a data set of oceanic fronts

This chapter develops a new data set of thermal fronts detected in the AVHRR Pathfinder SST imagery. There are two factors that motivated the development of this data set:

1. Most previous attempts to study the STF in the Tasman Sea based on remotely sensed SST imagery have examined only the climatological mean SST distributions (reviewed in **Chapters 2** and **5**). It is apparent from these studies that neither the position of the N-STF nor the S-STF in the Tasman Sea show up clearly in climatological mean SST distributions. This has led to the suggestion that the STF in the Tasman Sea lacks a classic temperature-front signature at the surface (Uddstrom and Oien, 1999). In contrast, at least in some parts of the Tasman Sea, data from hydrographic surveys suggests that the position of the S-STF is identifiable from strong SST gradients at synoptic time scales (e.g. Butler et al., 1992; Szymanska and Tomczak, 1994; Hamilton, 2006). This provided the motivation to take a different approach in this thesis to study the N-STF and S-STF using remotely sensed SST images. Here, an edge-detection algorithm (Cayula and Cornillon, 1992) is used to objectively locate thermal fonts in 30 years of remotely sensed SST images. **Chapter 5** uses the resulting data set to study the spatial and seasonal variability of thermal fronts in the Tasman Sea. **Chapter 5** then goes on to examine whether any of the thermal fronts detected in the monthly composite SST images are likely to be surface expressions of the N-STF or S-STF, through comparisons with remotely sensed SSS data.

2. The physical properties of thermal fronts, such as their SST gradient and the temperature differential across them, are useful for understanding them. These properties can help to identify oceanographically significant features in synoptic-scale images, which if they are highly variable in position, may show up only weakly in climatological SST distributions. **Chapter 5** focuses on thermal fronts considered to be strong, to investigate surface expressions of the N-STF and S-STF in the Tasman Sea. Where the position of a frontal system is known, and it is persistent, a data set of thermal front properties can also provide information about how the physical state of that frontal system varies in time (e.g. Ullman and Cornillon, 1999; Shaw and Vennell, 2001; Saraceno et al., 2004; Castelao et al., 2006; Ullman et al., 2007; Hopkins et al., 2010). **Chapter 6** uses the data of thermal fronts set developed in this Chapter to investigate variability and trends in the temperature and temperature difference between the water masses that border the S-STF around southern New Zealand, and their possible links with changes in winds over the South Pacific during the last 30 years.

4.4 Overview of methods for detecting oceanic fronts in satellite SST imagery

If an oceanic front influences one of the ocean properties that is measurable from space (i.e. ocean color, sea surface temperature, sea surface salinity, sea surface height), then it potentially can be identified in satellite imagery (Robinson, 2010). Because many ocean fronts have strong gradients in temperature, satellite SST data provides a valuable source of information for their study.

A hierarchy of image processing techniques are available to help identify fronts in satellite imagery (see e.g. Robinson, 2010). At the simplest level are gradient operators. Gradient operators compute the spatial rate of change of brightness in an image (the *gradient magnitude*) (Simpson, 1990). This processing enhances the visibility of image discontinuities, such as the abrupt transition from warmer to cooler waters across a temperature front (Fig. 4.1). These processed images can be used to manually locate the position of particular frontal systems and to study their surface characteristics (see e.g. Burls and Reason, 2006). They can also be combined with an image thresholding step to objectively locate fronts in satellite imagery (see Section 4.4.1). An overview of several gradient operators that are commonly used to compute gradients and to enhance the visibility of fronts in satellite imagery is given by Simpson (1990).

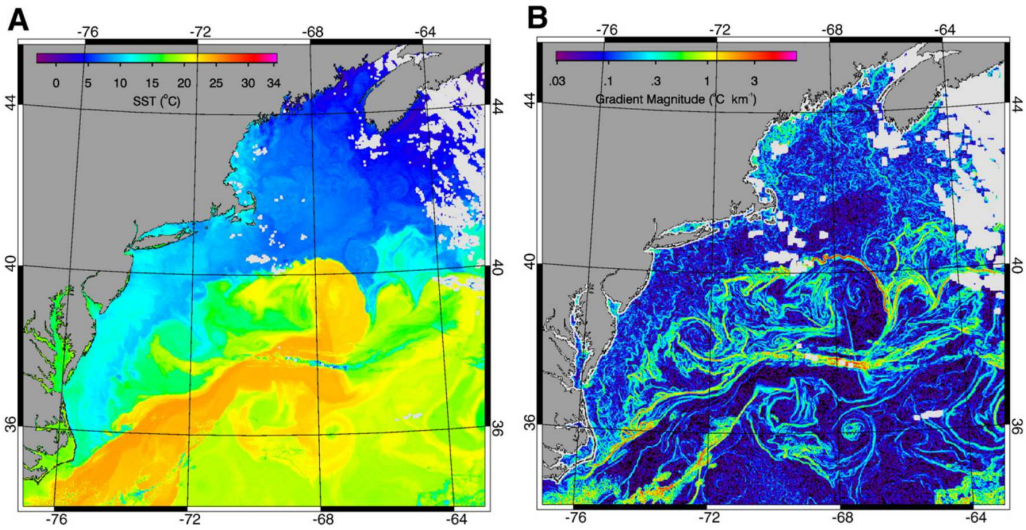

Figure 4.1: Examples of a satellite SST field (A) off the east of the United States (3 May 2001) and the corresponding SST gradient magnitude field (B) computed using a Sobel gradient operator (Simpson, 1990). The SST field has been filtered prior to calculating the image gradient using a contextual median filter to compensate for image noise (Belkin and O'Reilly, 2009). From Belkin and O'Reilly (2009).

At the next level of complexity are edge detection algorithms. Edge detection algorithms are a set of image processing methods that identify discontinuities within a digital image automatically (Jain et al., 1995), and provide the user with a map of the locations of the detected image discontinuities (or 'edges'). There are three main edge detection techniques have been used to identify thermal signatures of fronts in satellite SST imagery: gradient techniques (e.g. Canny, 1986), histogram algorithms (e.g. Cayula and Cornillon, 1992) and the entropic algorithm (Shimada et al., 2005). These techniques have been used extensively to study ocean fronts in coastal and marginal seas (e.g. Ullman and Cornillon, 1999; Hickox et al., 2000; Belkin and Cornillon, 2003; Shimada et al., 2005; Castelao et al., 2006; Chang et al., 2006; Wall et al., 2008; Belkin et al., 2009; Miller, 2009; Nieto et al., 2012). They have also provided new insights into spatial and temporal variability of major current and frontal systems in the open-ocean (see e.g. Moore et al., 1999; Saraceno et al., 2004; Dong et al., 2006; Graham and de Boer, 2013; Miller et al., 2013; Freeman and Lovenduski, 2016). An overview of these three edge detection techniques is given below (Sections 4.4.1-4.4.3). Detail is then provided on their relative performance, which guided the choice of which edge detection technique to use in creating the new data set of thermal fronts (Section 4.4.4).

4.4.1 Gradient-based edge detection

Gradient-based edge detection techniques consist of two main processing steps: (1) a gradient magnitude calculation and (2) the application of image thresholding (Jain et al., 1995). The first processing step applies a gradient operator to an image to compute its gradient

magnitude. The second step applies image thresholding to the gradient magnitude image to objectively locate image discontinuities. Image pixels above a specified gradient magnitude threshold are flagged as edge pixels and their location is recorded in a binary 'edge image'. In the edge image, any pixel flagged that is an edge pixel is set to a value of one, all other (non-edge) pixels are set to a value of zero.

The gradient-based edge detectors used in this application range from a simple thresholding of an image (e.g. Moore et al., 1999; Saraceno et al., 2004), to applying more complex algorithms, such as the Canny (Canny, 1986) edge detector, which localizes individual image discontinuities (fronts) (e.g. Castelao et al., 2006; Wall et al., 2008). The choice of an appropriate gradient-based edge detector depends on level of detail required. For example, a simple image-thresholding can highlight the general position of strong gradients within a remotely sensed SST image (Fig. 4.2), whereas, the Canny method provides a finer level of spatial detail, by narrowing image discontinuities (fronts) down to their local maxima within the gradient image (Fig. 4.3).

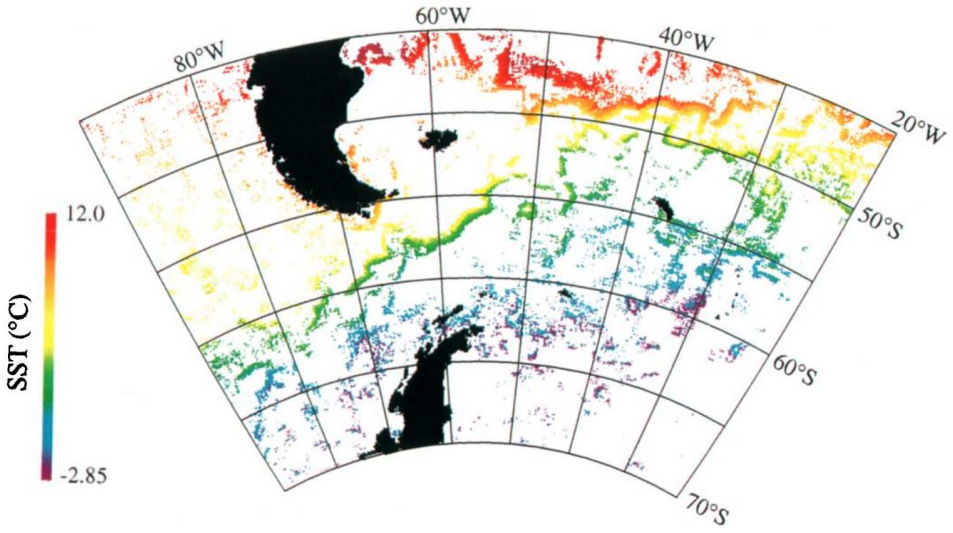

Figure 4.2: An example edge image derived from a simple gradient thresholding. The underlying image consists of a subset of a weekly-composite AVHRR Pathfinder SST images (Jan 1-7th 1987) over Drake Passage, where only pixels with a strong SST gradients (gradient exceeding 1.35°C per 45 km) have been retained. Reproduced from Moore et al. (1997).

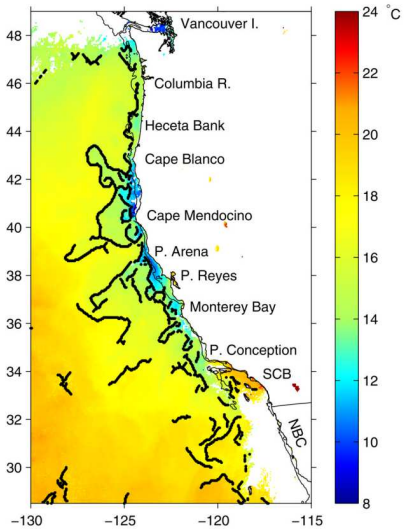

Figure 4.3: Remotely sensed SST image from 25 August 2011 covering the California Current System overlain with the location of thermal fronts found by applying the Canny edge-detection algorithm to the SST image (black dots). Cloud contaminated pixels are shown in white. Reproduced from Castelao et al. (2006).

To objectively identify thermal fronts in remotely sensed SST images, values used to threshold a gradient image also need to be determined subjectively. This is typically performed by examining a cumulative histogram of gradients in an image (Saraceno et al., 2004; Castelao et al., 2006; Oram et al., 2008; Wall et al., 2008; Rivas and Pisoni, 2010). The scientific credibility of the resulting edge image depends on the validity of the detected edges (Oram et al., 2008) and whether the gradient thresholds are set appropriately; set too low, noise will overwhelm frontal signatures in the form of false front detections but set too high, large portions of fronts may be missed.

4.4.2 Histogram-based edge detection

The histogram-based Single Image Edge Detector (SIED) (Cayula and Cornillon, 1992) is an algorithm that has been designed specifically to objectively locate thermal fronts in remotely sensed SST images. The SIED operates on a different premise to gradient algorithms. The SIED locates thermal fronts within a remotely sensed SST image by performing a series of statistical tests on subsets of that image, contained within a sliding window (with nominal dimensions of 32×32 image pixels). The operation of the SIED is described in detail in Section 4.7, a summary is given here.

The SIED employs two statistical tests to objectively locate thermal fronts in satellite SST imagery. The first consists of a histogram-analysis; the bimodality of the temperature distribution within each pixel window is evaluated, in order to determine the statistical likelihood of there being two temperature populations within a window and hence, an edge. The second

is a test for the spatial cohesion of the temperature populations. This test evaluates whether the detected temperature populations form adjacent bodies of water. If the algorithm detects (histogram-analysis) and confirms (cohesion-algorithm) the presence of an edge within a window, the SIED proceeds to a third step. In the third step, the algorithm locates edge pixels within the pixel window (i.e. the pixels that separate the two temperature populations). After the algorithm has processed all pixel-windows within the image, the output of these three steps is an edge image, containing the locations of the detected edge pixels. A final step in the SIED consists of a contour-following procedure, which connects the independent edge pixels in the edge image so that they form continuous front segments. Figure 4.4 shows an example of the SIED algorithm applied to a remotely sensed SST image covering the North Atlantic.

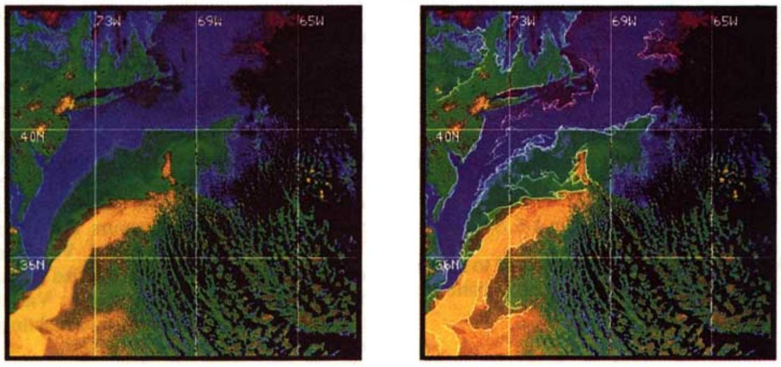

a. SST image of 26 March 1985 at 18:41 local time.

b. Fronts detected by the single-image edge detection algorithm.

Figure 4.4: Example of thermal fronts detected in a remotely sensed SST image by the single-image edge detection (SIED) algorithm. Reproduced from Cayula et al. (1995, Figure 3).

The Multiple Image Edge Detector (MIED) (Cayula and Cornillon, 1995) is set of techniques that improve the accuracy of the SIED, by incorporating a-priori information contained in remotely sensed SST images that are neighbouring in time. The MIED starts by applying the SIED to a daily-resolution image under investigation. Edge pixels detected in the single image are then compared to those detected in images that are neighbouring in time - nominally within ±2.5 days - to identify persistent edge pixels. The location of these persistent edge pixels are then input into two repeat passes of the SIED over the sequence of images. This approach enhances the detection of thermal fronts in cases that are problematic for the SIED, including thermal fronts that are weak and thermal fronts near large areas of cloud cover. Like all edge-detection algorithms, however, the MIED is hampered by regions of persistent cloud cover that block the view of the sea-surface.

The SIED and MIED have been widely used to detect thermal fronts in remotely sensed SST images. They have been successfully applied to infra-red SST images to investigate the distribution and variability of surface thermal fronts over the continental shelf off the east

coast of North America (Ullman and Cornillon, 1999, 2001), marginal sea regions (Hickox et al., 2000; Belkin and Cornillon, 2005), the Gulf of Mexico (Wall et al., 2008) and in upwelling systems in the North Pacific (Kahru et al., 2012) and North Atlantic (Nieto et al., 2012; Miller, 2009; Miller et al., 2013). The MIED algorithm has been used to conduct basin and global-scale surveys of thermal fronts and assess their variability (Belkin and Cornillon, 2003; Ullman et al., 2007; Belkin et al., 2009).

4.4.3 Entropy-based edge detection

The entropic-based edge detection algorithm developed by Shimada et al. (2005) is designed to detect fine-scale (~1 km) thermal fronts in high resolution remotely sensed SST images. Like the SIED, the edge detection is based on the outcome statistical tests applied to subsets of a satellite image.

The edge-detection method is divided into three parts: First, estimates are made of the *Jensen-Shannon divergence* of SST at each image pixel. These estimates are made using SST data located within pairs of filter windows, each window being 5×5 pixels in size (see e.g. Fig. 3 in Shimada et al., 2005). The Jensen-Shannon divergence is a measurement of the inverse cohesion between a set of probability distributions (Lin, 1991). The concept behind using the Jensen-Shannon divergence for edge detection is that a pair of filter windows that contain two discrete temperature populations, and hence a thermal front, will have a higher Jensen-Shannon divergence than a pair of filter windows that contain the same temperature population and hence no front. Second, a thresholding is applied to the image pixels; image pixels with a Jensen-Shannon divergence that exceeds a specified threshold - nominally 0.4 (Shimada et al., 2005) - are designated as edge pixels and their locations are recorded in an edge image. The last step of the algorithm applies a thinning and contour-following algorithm to this edge image, to obtain contiguous front segments. Among other studies, the entropic-based edge detection algorithm has been used to investigate the distribution of fine-scale thermal fronts occurring along the Japanese coastline (Shimada et al., 2005) and over the South China Sea (Chang et al., 2006; Lan et al., 2009).

4.4.4 Validation of edge detection algorithms

Several studies (Cayula and Cornillon, 1992, 1995; Ullman and Cornillon, 2000; Miller, 2009) have assessed the accuracy and relative performance of gradient-based, histogram-based and entropic-based edge detectors when applied to remotely sensed SST images. Results from these studies have shown the histogram algorithms (SIED and MIED) are capable of estimating the position of thermal fronts in remotely sensed SST images with skill close to that of a trained analyst, and above that from using gradient algorithms.

Ullman and Cornillon (2000) assessed the performance of the SIED and MIED algorithms, using as baselines the location of fronts detected using a gradient algorithm applied to (1) remotely sensed SST images and (2) coincident *in-situ* SST estimates collected by ships. Ullman and Cornillon (2000) found the histogram algorithms performed significantly better than the gradient algorithm in terms of having a false-front detection rate (fronts not identified from gradient analyses of coincident in-situ ship-based SST estimates) 50% lower than the more noise sensitive gradient algorithm. The gradient algorithm was found to better detect frontal features with an across-front length scale <10 km, which tend to prevail in coastal waters, in comparison to the histogram algorithms. The histogram algorithms have a missed-front error rate of 10% in cloud-free conditions for fronts with a length exceeding 10 km Ullman and Cornillon (2000).

A recent study by Chang and Cornillon (2015) compared the performance of the histogram-based MIED (Cayula and Cornillon, 1995) and the entropic algorithm (Shimada et al., 2005), when applied to remotely sensed SST images, relative to thermal fronts detected from *in-situ* SST data. They found the entropic algorithm detected more weaker, and likely shorter, thermal fronts that the histogram algorithm. The entropic algorithm was also found to have a higher (~20%) false-front detection rate than the histogram algorithm. Chang and Cornillon (2015) note that the weaker, shorter thermal fronts, together with the false-fronts, identified by the entropic algorithm may mask the occurrences of stronger and longer thermal fronts, such as those separating two large water masses, in statistical analyses of front occurrence.

4.5 Overview of methods for analysing the properties of oceanic fronts in satellite SST imagery

Front-analysis methods can provide additional information about individual thermal fronts, such as their intensity and width. The resulting data sets can be used to derive information about how the properties of a frontal system vary in space and/or time Hopkins et al. (2010, 2011) (Moore et al., 1997, 1999; Ullman and Cornillon, 1999; Shaw and Vennell, 2000, 2001; Ullman et al., 2007; Hopkins et al., 2010, 2011). Below, an overview is provided of two types of front-analysis methods: front-sampling (Section 4.5.1) and functional modelling (4.5.2) techniques. Some brief comments are then provided on the existing front analysis methods that are utilized and adapted in this Chapter (Section 4.5.3).

4.5.1 Front sampling

Front-sampling methods are complementary to the edge-detection algorithms described in Section 4.4. They sample a remotely sensed SST image in the local region that surrounds a

detected thermal front. These data are then used to calculate a set of properties that describe an individual thermal front.

An example of a front sampling method is in the studies of the PF carried out by Moore et al. (1997; 1999). These studies developed a method to estimate the width and the temperature change across the surface expression of the PF seen in remotely sensed SST images. These two frontal parameters are obtained from cross-sections of SST across the PF. Cross-sections are taken starting at the poleward edge of the PF, which is manually digitized from weekly maps of SST gradient using a gradient-based edge-detection algorithm. Cross-sections move up the temperature gradient until reaching the warm temperature plateau that marks the warm side of the front. This is determined at the point at which SST remain steady over a distance of 20-30 km. The length of the cross-section, and temperature change across it, provide estimates of the frontal width and temperature change respectively. A limitation of the method used by Moore et al. (1997; 1999) is the need for user input; since the position of the poleward (cold) side of the PF is unknown, and several other thermal fronts may occur in its vicinity, the location of the fronts surface expression must be determined from manual inspection of SST gradient maps. Such manual inspection is impractical for analysing the properties of large numbers of thermal fronts, like that attempted in this Chapter.

An automated scheme for estimating the intensity of thermal fronts detected in a remotely sensed SST image has also been developed. The "region-averaging" scheme, developed by Ullman et al. (2007), uses a set of three data sampling masks to measure the temperature difference, and temperature gradient, of an individual thermal front. The geometry of the three data sampling masks is illustrated in Figure 4.5.

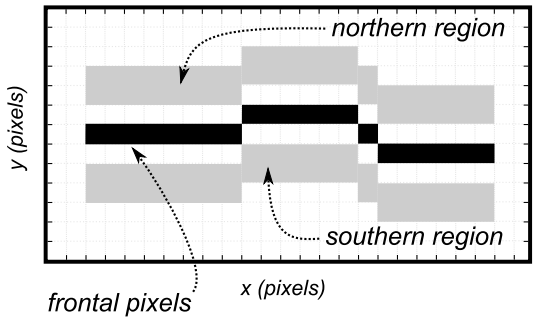

Figure 4.5: Geometry of the data sampling masks used in Ullman et al. (2007). Frontal pixels are marked as black boxes, and their locations are used to calculate the temperature gradient associated with a frontal segment (∇SST_f). Pixels within the 2-pixel wide northern and southern regions (grey shaded boxes) are used to calculate the change in SST across the front ($\triangle SST_f$).

The first mask comprises the 1-pixel band of edge pixels that make up a detected front and are designated as the "frontal pixels". The set of the second and third pixels to north of each frontal pixel are designated as the "northern region". Similarly, the set of the second and

third pixels to south of frontal pixels are designated as the "southern region". The northern and southern region are assumed to be sampling the warm and cold temperature plateaus that border a thermal front. The mean change in SST across a detected front, $\triangle SST_f$ (C), is calculated by subtracting the mean SST of pixels in the southern region from those in the northern region. The SST gradient associated with a detected front, ∇SST_f $(C\ km^{-1})$, is obtained by averaging the SST gradient magnitude of the underlying remotely sensed SST image at the frontal pixels. Where large portions of the "northern" or "southern" region are obscured by cloud, an estimate cannot be made.

The technique is unique in that it functions autonomously, basing the geometry of the data sampling masks on the locations of fronts detected using an edge detection algorithm. A limitation of the "region-averaging" scheme (Ullman et al., 2007) is the fixed geometry of the sampling masks. The method was developed to characterise zonally-orientated fronts in the North Atlantic. The scheme does not adapt to varying frontal orientations or widths, unlike the Moore et al. (1997; 1999) methods. This restricts its application (as is) to regions where the orientation and width of the fronts being targeted are well known and fairly consistent.

4.5.2 Functional modelling

Functional modelling methods are an alternative approach to locate, and parameterise the physical properties of, an ocean front revealed in remotely sensed SST images (Shaw and Vennell, 2000; Hopkins et al., 2011). In contrast with the techniques discussed so far, functional modelling methods operate independent of edge detection techniques (Section 4.4). They instead rely on the users knowledge of the location, dimensions and structure of the specific front being targeted. These techniques fit a functional model of a thermal front, based on a hyperbolic tangent, to remotely sensed SST images that contains a front. The hyperbolic tangent describes the front using a set of parameters, which include the location of the axis of the front within the window and the temperature difference across the front. Details of the functional modelling approach are given in Shaw and Vennell (2000) and Hopkins et al. (2011), and their applications to remotely sensed SST images to investigate spatial and temporal behaviour of the Southland Front are given in Shaw and Vennell (2001) and Hopkins et al. (2010).

An important limitation of functional modelling methods, which makes them unsuitable for developing a data set of thermal fronts, is that they are designed to target a known, persistent and contiguous frontal system; they require prior understanding of that fronts location, properties and configuration. For such a frontal system, these methods can produce high-quality results (see e.g. Shaw and Vennell 2001; Hopkins et al. 2010); however, this thesis is undertaking a more exploratory-based investigation. The location, properties and existence

of surface thermal expressions of the STF in the Tasman Sea remain unclear (**Chapter 5**), making function modelling methods unsuitable for a large part of this thesis.

4.6 Methods utilized and adapted in this Chapter

Based on the findings of the above studies, which identify the histogram-based algorithms (SIED and MIED) as generally being more robust than gradient-based and entropy-based edge-detection algorithms, and thus, likely to produce more reliable statistics of thermal front occurrence, the SIED (Cayula and Cornillon, 1992) was selected for use in the present study. If the focus of this work had been on remotely sensed SST images at a daily-resolution, the MIED might have been used. However, this Chapter works with monthly composite images - for the reasons discussed in Section 4.2.5. The MIED is designed to work with remotely sensed SST images that have daily resolution, and is therefore not appropriate for this study. In this Chapter, the SIED (Cayula and Cornillon, 1992) was applied to PFV5.2 SST monthly composite images. The thermal fronts detected using the SIED form the basis of the data set of thermal fronts that is developed in this Chapter.

To measure the properties of thermal fronts detected using the SIED, a new front-analysis algorithm is developed in Section 4.8. The algorithm builds on the methods developed by Moore et al. (1997; 1999) and Ullman et al. (2007), by using information about the gradient of SST to automatically adapt to the orientation and width of thermal fronts identified in remotely sensed SST images. The new algorithm extracts frontal cross-sections of temperature and gradient magnitude using a region-averaging method, then uses these cross-sections to calculate a set of parameters that describe the physical properties of individual thermal fronts and their surrounding water bodies. The new algorithm circumvents some of the limitations of the methods developed by Moore et al. (1997; 1999) and Ullman et al. (2007); it does not require user intervention (i.e. works from detected thermal fronts themselves) and adapts automatically to the orientation and width of the detected thermal fronts.

The next section describes in detail the edge detection algorithm (Cayula and Cornillon, 1992) that is used in this work to objectively locate thermal fronts in the PFV5.2 SST monthly composite images.

4.7 The Single Image Edge Detection (SIED) algorithm

The SIED (Cayula and Cornillon, 1992) was used to identify thermal fronts in PFV5.2 monthly composite SST images. The SIED was implemented in MATLAB based on original FORTRAN code obtained from Peter Cornillon (P. Cornillon, Pers. Comm., 2012). The

SIED was applied to three hundred and sixty PFV5.2 monthly composite SST images, collected between January 1982 and December 2011. The outcome of this section is a data set of the locations of thermal fronts identified over these 30 years in the Tasman Sea.

The SIED algorithm comprises a set of processing steps that function at the image-level, window-level (a regional subset of the image) and pixel-level. A flowchart of these processing steps is shown in Fig. 4.6. The original SIED algorithm includes a cloud-detection step, to mask potentially cloud-contaminated pixels from the remotely sensed SST image. Because PFV5.2 monthly composite SST images are used in this work, which have already been masked for cloud (Section 4.2), only the formal edge-detection steps of the SIED are used here.

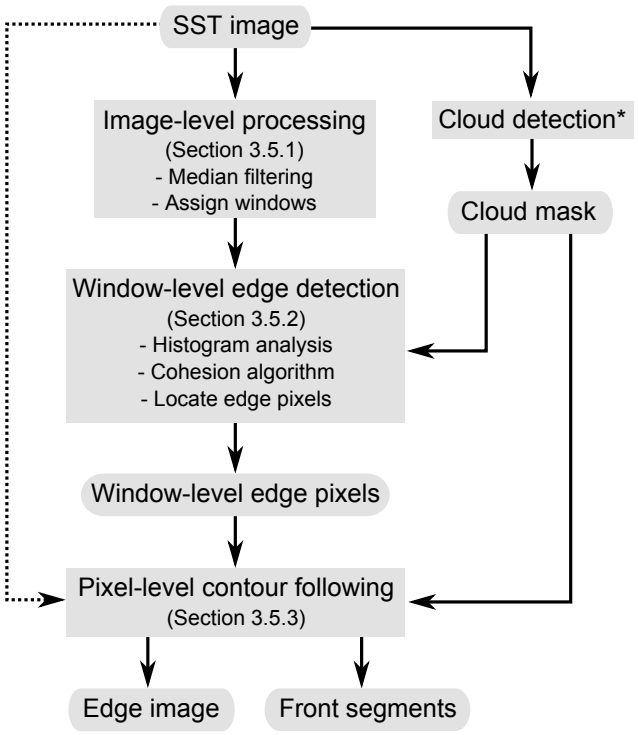

Figure 4.6: Flowchart of the SIED algorithm - adapted from Cayula and Cornillon (1995). *The cloud detection preprocessing steps are not implemented in this work. Instead, this work uses the cloud mask provided with the PFV5.2 SST images.

4.7.1 Image-level

Prior to edge-detection, the SIED filters the remotely sensed SST image with a 3×3 median filter to suppress noise in the image. This filter helps - in a later contour-following step of the SIED – to reduce instances of front segments being broken up artificially by noise in the image.

The remotely sensed image is then subdivided into overlapping pixel windows, which in the configuration used here have the dimensions of 32×32 pixels and a 50% overlap. (Cayula and Cornillon, 1992) find the edge detections obtained using square windows with dimensions of 16×16 pixels or 64×64 pixels to be similar to the default value of 32×32 pixels, which is typically employed in remote sensing studies (see e.g. Ullman et al.,1999; 2001; 2007).

4.7.2 Window-level

In the next step, the SIED moves down to the window-level. Each window is processed in turn to evaluate the probability that it contains a thermal front. The algorithm proceeds with the window-level processing provided that the proportion of window-level pixels with valid data is at least 0.65. The purpose of this threshold is to ensure that the window-level data set is sufficiently large to obtain reliable statistics.

The window-level processing consists of two steps: (1) a histogram analysis and (2) a cohesion analysis. In the first step, the algorithm analyzes the temperature distribution (histogram) in each window to determine the statistical likelihood of an edge. The intention of this step can be understood by the example shown in Fig. 4.7. If an edge is not present, the histogram will likely be unimodal, containing one temperature population (Fig. 4.7a). If an edge is present, the histogram is more likely to be bimodal, containing two temperature populations (Fig. 4.7b).

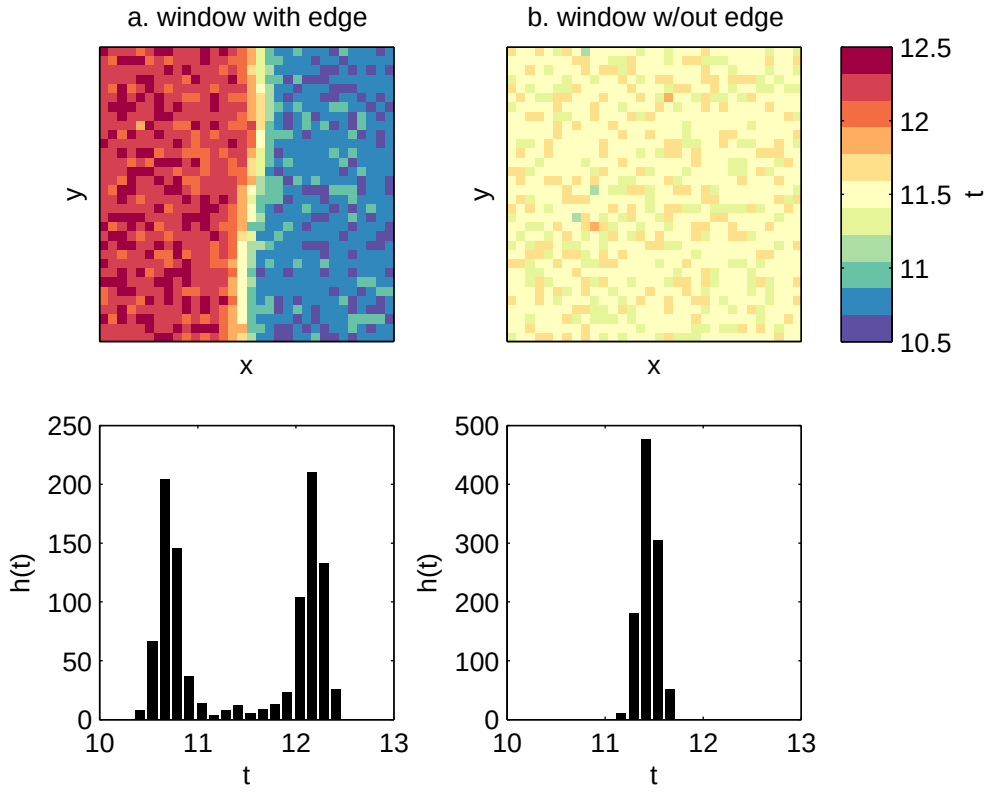

Figure 4.7: Synthetic example of temperature histograms in two 32×32 pixel window containing (a) two well-defined populations (with a thermal front orientated north to south) and an edge and (b) one population, no front and no edge. Here, $h(t)$ is the value of the histogram in temperature bin t.

To test for this bi-modality, the algorithm first assumes that two temperature populations are present in the window (i.e. a cold population and a warm population), and computes a set of parameters that describe the distributions of these populations. These parameters are then used to determine the statistical relevance of segmenting the window into two populations.

A decision on the uni-modality or bi-modality of a temperature histogram is evaluated from a criterion function

$$\theta(\tau) = \frac{J_b(\tau)}{S_{tot}}, \tag{4.1}$$

where S_{tot} is the total variance of the SST data within a window. In the SIED, S_{tot} is partitioned into the sum of two terms dependent on the temperature threshold τ (Cayula, 1990):

$$S_{tot} = J_e(\tau) + J_b(\tau). \tag{4.2}$$

Here $J_e(\tau)$ is referred to as the within-cluster variance and it represents the sum of the variances within each of the two populations that result from segmenting the window with respect to τ. $J_e(\tau)$ is defined as

$$J_e(\tau) = \frac{N_1}{N_1+N_2} S_1(\tau) + \frac{N_2}{N_1+N_2} S_2(\tau), \tag{4.3}$$

where N_1 is the number of data in population 1, N_2 is the number of data in population 2, $S_1(\tau)$ is the variance of population 1, $S_2(\tau)$ is the variance of population 2. The number of data in each population are defined as

$$N_1 = \sum_{t<\tau} h(t), \tag{4.4}$$

and

$$N_2 = \sum_{t\geq\tau} h(t), \tag{4.5}$$

where $h(t)$ is the value of the histogram at temperature t. The variances of the two populations are defined as

$$S_1(\tau) = \frac{\sum_{t<\tau} [t-\mu_1(\tau)]^2 h(t)}{N_1}, \tag{4.6}$$

and

$$S_2(\tau) = \frac{\sum_{t\geq\tau} [t-\mu_2(\tau)]^2 h(t)}{N_2}, \tag{4.7}$$

where $\mu_1(\tau)$ and $\mu_2(\tau)$ are the mean temperatures of population 1 and population 2 respectively, defined as

$$\mu_1(\tau) = \frac{\sum_{t<\tau} t h(t)}{\sum_{t<\tau} h(t)}, \tag{4.8}$$

and

$$\mu_1(\tau) = \frac{\sum_{t\geq\tau} t h(t)}{\sum_{t\geq\tau} h(t)}. \tag{4.9}$$

The second term in eq. 4.2, J_b, is referred to as the between cluster variance. This value represents the contribution to the total variance that comes from the temperature difference between the two populations. It is defined as

$$J_b(\tau) = \frac{N_1 N_2}{(N_1+N_2)^2} [\mu_1(\tau) - \mu_2(\tau)]^2. \tag{4.10}$$

The ratio $\theta(\tau) = \frac{J_b(\tau)}{S_{tot}}$ indicates how good a segmentation is with respect to τ (i.e. the statistical relevance of a bimodal separation) (Cayula 1990). The best temperature segmentation for a window, τ_{opt}, is given by the maximum of $\theta(\tau)$, evaluated over all τ (i.e. histogram

bins). If the criterion function for the best temperature segmentation, $\theta(\tau_{opt})$, exceeds a critical value, and the difference between $\mu_1(\tau)$and $\mu_2(\tau)$ exceeds 0.375°C, then the histogram is flagged as being bimodal and this step of this algorithm is passed. Cayula (1988) and Cayula and Cornillon (1992) examined the behaviour of the criterion function and found values of $\theta(\tau_{opt})$ greater than a critical value 0.70 give a statistically relevant indication of a bimodal histogram, and hence an edge. In light of these experiments, a window was flagged as containing an edge if $\theta(\tau_{opt}) \geq 0.7$.

If a window passes the histogram analysis, the algorithm proceeds to a cohesion analysis. This step incorporates information about the spatial properties of the two temperature populations, and is used to validate or discard an edge detected in the histogram portion of the algorithm. The meaning of this cohesion analysis can be understood from the example distributions of temperature populations shown in Fig. 4.8. For a pixel in a window with high cohesion (Fig. 4.8a), its neighbouring pixels are likely to come from the same temperature population; high cohesion validates the segmentation of the window into two temperature populations, implying that the presence of a front is likely. For a pixel in a window with low cohesion, its neighbouring pixels are likely to come from a different temperature population (Fig. 4.8b), meaning that a front is unlikely to exist in the window.

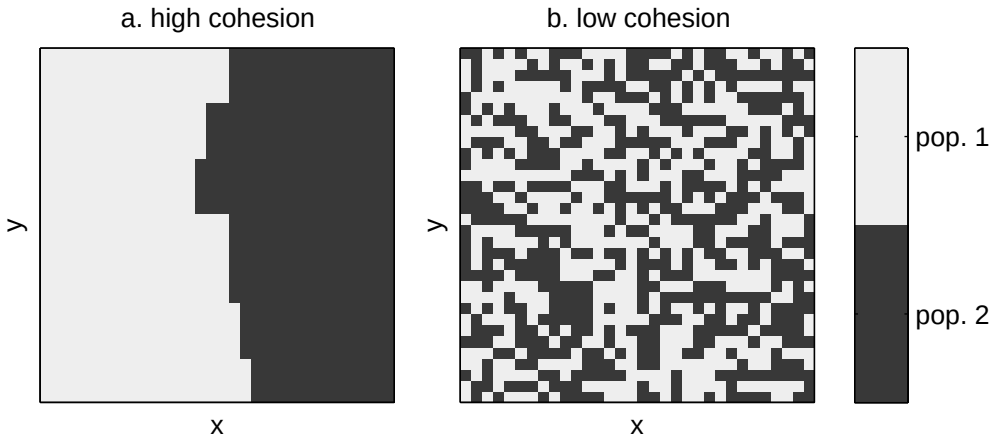

Figure 4.8: Example of the spatial distribution of temperature populations in a 32×32 pixel window containing two populations showing (a) high cohesion (with a front orientated north to south) and (b) low cohesion.

To determine the cohesion of data within a window, the algorithm segments the window into two temperature populations, ω_1' and ω_2', by thresholding data in the window based on τ_{opt} - those data with temperature values less than or equal to τ_{opt} are mapped to ω_1', remaining data are mapped to ω_2'. Next, the algorithm calculates a set of cohesion coefficients, for populations ω_1' (C_1) and ω_2' (C_2), and for the data within the window (C), as follows:

$$C_1 = \frac{R_1}{T_1}, \tag{4.11}$$

$$C_2 = \frac{R_2}{T_2}, \tag{4.12}$$

$$C = \frac{R_1 + R_2}{T_1 + T_2}, \tag{4.13}$$

where R_1 is the total number of times a pixel belonging to ω_1' has neighbouring pixels to the right or above that belong to ω_1' and T_1 is the total number of times a pixel belonging to ω_1' has neighbouring pixels to the right or above that belong to either ω_1' orω_2'. R_2 and T_2 are similarly defined, using the pixels in ω_2'.

Cayula and Cornillon (1992) find that for a window with pixel dimensions of 32×32, threshold values exceeding 0.90 for C_1 and C_2 and exceeding 0.92 for C reliably exclude those windows whose edges likely derive from images with noisy distributions. If the cohesion coefficients for a window exceed these thresholds, the algorithm proceeds down to the pixel-level.

4.7.3 Pixel-level

The pixel-level processing identifies the locations of edge pixels that separate the two temperature populations within the window. Those pixels with a neighbouring pixel to the right or below that belonging to the opposing population are marked as edge pixels in an edge image that is initialized to a digital count of zero. The edge image has the same dimensions as the original remotely sensed SST image. Pixels in the edge image are set to a value of one if they contain an edge pixel. This edge image is then built up from successive iterations of the window-level processing over the remaining windows.

Once the window level processing is complete, a contour-following algorithm is applied to the edge image. This algorithm incorporates information from the edge image with an analysis of the underlying SST gradient, in order to connect edge pixels in the edge image into contiguous front segments. For further details of the contour following algorithm, the reader is directed to Cayula and Cornillon (1992). The SIED produces two outputs: (1) an edge image and (2) a vector containing the coordinates of edge pixels that make up each front segment. Those front segments consisting of fewer than 15 frontal pixels are regarded as isolated edge pixels left over from the window-level processing and are discarded from edge image and the vector.

The SIED, in the configuration described above, was applied to PFV5.2 SST monthly composite images Jan 1982 and Dec 2011 (Section 4.2). The outcome of this processing

was a data set of the locations of oceanic fronts detected over 30 years in the Tasman Sea (Fig. 4.9).

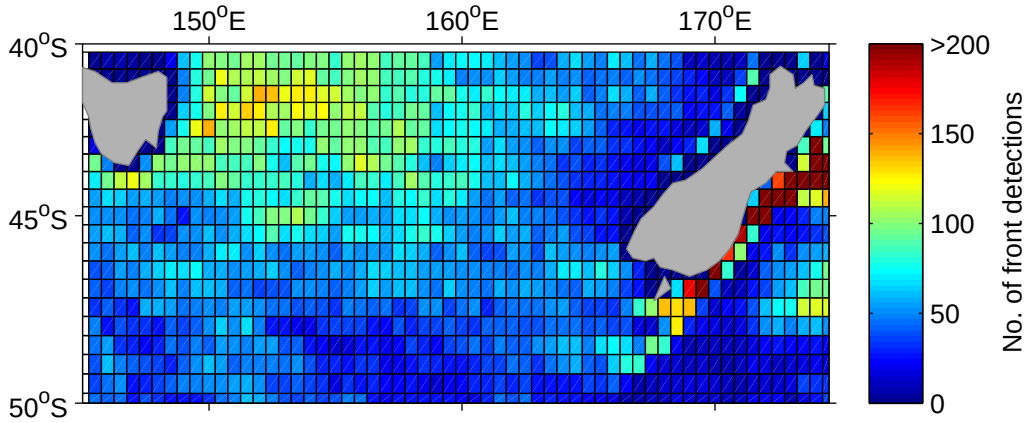

Figure 4.9: Illustration of the 30 year data set of thermal fronts detected in PFV5.2 SST images over the Tasman Sea. Shown are the total number of thermal fronts detected in 0.5° lat-lon bins over the period 1982-2011.

4.8 A new algorithm to parameterise the properties of oceanic fronts

This section provides technical details on a new algorithm that was developed to calculate a set of physical properties for each thermal front detected in the PFV5.2 SST monthly composite images. The objective was to provide further information about the thermal fronts that would be useful for investigating the research questions proposed in **Chapters 5** and **6**.

The new front-analysis algorithm that is developed here adapts and extends the front-analysis methods developed by Moore et al. 1997, 1999 and Ullman et al. (2007) (discussed in Section 4.5.1) in a couple of ways. First, the new algorithm adjusts itself to the orientation of each thermal front detected in a remotely sensed SST image. It does this by using information about the SST gradient; it approximates the orientation of a front segment using the average gradient direction of SST at the front segment. Second, the algorithm extracts frontal cross sections of SST and SST gradient magnitude, using an approach that adapts to the width of a front; it does this by sampling outward from a front segment until it reaches the temperature plateaus that border a front. The algorithm uses the cross-sections of SST and SST gradient magnitude to calculate a set of five parameters that describe the physical properties of individual front segments.

This approach circumvents the limitations of the methods used by Moore et al.(1997; 1999) and Ullman et al. (2007); the method developed by Moore et al.(1997; 1999) method requires manual intervention to locate the cold side of a front, whereas, the method used by Ullman et al. (2007) was designed for thermal fronts detected in remotely sensed SST images that have a fixed orientation (north-south) and width.

4.8.1 Overview of new algorithm

The front analysis algorithm samples data from a remotely sensed SST image at the location of each front identified in that image, as well as in the cross-frontal water masses. The algorithm uses these data to calculate a set of five parameters that describe physical properties of the detected thermal fronts. These properties are: the gradient magnitude at a thermal front, the temperature change across a thermal front, the SST at a thermal front and the SST in the two cross-frontal water masses. The front analysis algorithm is divided into six parts, which are illustrated schematically in Figure 4.10:

1. Input data are provided to the algorithm (Section 4.8.2). The input data consist of (i) a remotely sensed SST image, (ii) an edge image and (iii) the pixel co-ordinates of each front segment detected in the remotely sensed SST image, following application of the SIED to that image (Section 4.7).

2. Calculations of SST gradient magnitude and SST gradient direction are performed on the remotely sensed SST image (Section 4.8.3).

3. One front segment is selected from the pool of fronts detected in the remotely sensed SST image.

4. The algorithm estimates the SST and SST gradient magnitude at the location of the front segment (Section 4.8.5)

5. The algorithm progressively samples in an across-front direction, to obtain frontal cross-sections of SST and SST gradient magnitude (Section 4.8.6).

6. The algorithm uses the frontal cross-sections to calculate a set of five parameters to describe the physical properties (Fig. 4.11) of the front segment (Section 4.8.7). The algorithm terminates once a set of five parameters has been calculated for each front segment detected within the remotely sensed SST image.

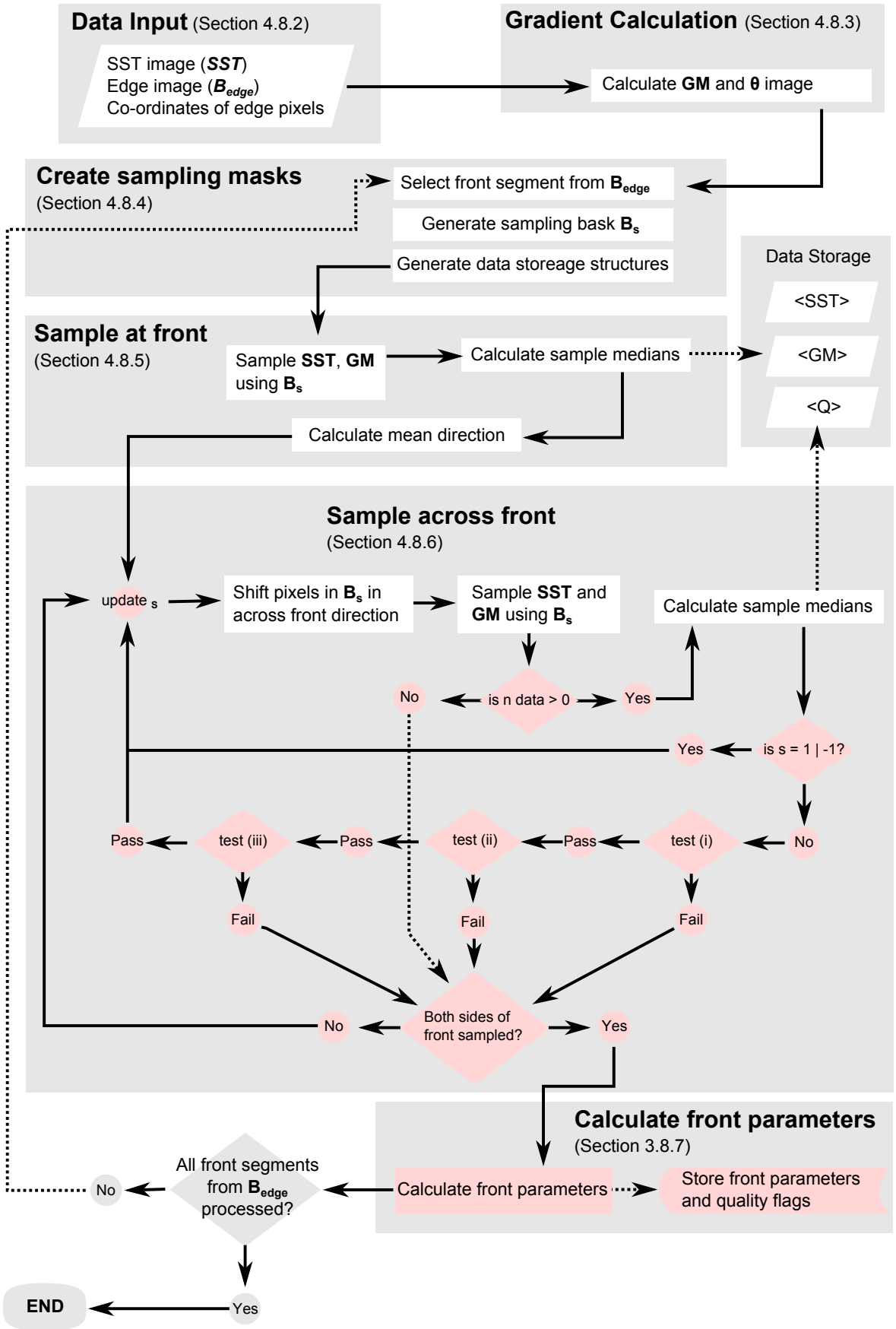

Figure 4.10: Flowchart of the front-analysis algorithm. Also labeled are the Section numbers in this Chapter where each step is described.

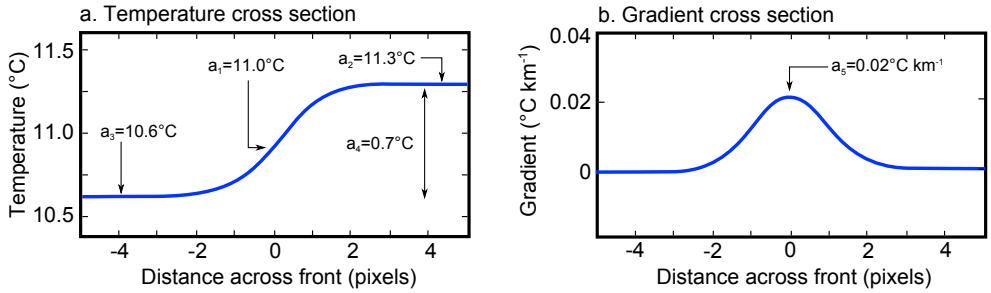

Figure 4.11: Physical meaning of the five front parameters (a_n) calculated by the front-analysis algorithm. Shown are idealised frontal cross-sections of (a) SST and (b) SST gradient magnitude across a thermal front, with the following front parameters labeled: the temperature at the front segment (a_1), the temperature of the warm plateau (a_2), the temperature of the cold plateau (a_3), the temperature change across the front (a_4) and the SST gradient magnitude at the front segment (a_5).

The following Sections (Section 4.8.2-4.8.7) provide a detailed description of each part of the front analysis algorithm.

4.8.2 Data input

Three inputs are provided to the front-analysis algorithm:

1. A remotely sensed SST image, **SST** (Section 4.2).
2. An edge-image, containing the edge pixels of each front segment detected in the remotely sensed SST image, $\mathbf{B}_{edge}$ (Section 4.7).
3. Row vectors of the x and y coordinates for the edge pixels that make up each front segment in $\mathbf{B}_{edge}$ (Section 4.7).

4.8.3 Gradient calculation

The algorithm begins with a pre-processing step that estimates the gradient magnitude, **GM** (°C km^{-1}), and gradient direction , θ (degrees), of **SST** using a Sobel gradient operator. The gradient vector in the x and y directions, $\mathbf{G}x$ and $\mathbf{G}y$ respectively, are calculated by convolving **SST** with the kernels of the Sobel operator, defined by:

$$\mathbf{G}x = \begin{bmatrix} -1 & 0 & +1 \\ -2 & 0 & +2 \\ -1 & 0 & +1 \end{bmatrix} * \mathbf{SST}, \tag{4.14}$$

and

$$\mathbf{G}y = \begin{bmatrix} +1 & +2 & +1 \\ 0 & 0 & 0 \\ -1 & -2 & -1 \end{bmatrix} * \mathbf{SST}. \tag{4.15}$$

The SST gradient magnitude is estimated as

$$\mathbf{GM} = \sqrt{(\mathbf{G}x/R_{zonal})^2 + (\mathbf{G}y/R_{merid})^2}, \tag{4.16}$$

where R_{zonal} and R_{merid} are the zonal and meridional resolutions of **SST** at the image pixel being processed. The SST gradient direction is estimated as

$$\theta = atan2(\mathbf{G}y, \mathbf{G}x), \tag{4.17}$$

where $atan2$ is the arctangent of $\mathbf{G}x$ and $\mathbf{G}y$, with the SST gradient direction pointing from warm to cold.

4.8.4 Creation of sampling masks

The algorithm initiates a front-sampling procedure by selecting a front segment from $\mathbf{B}_{edge}$ and generating four data structures. These data structures are a pixel sampling mask, $\mathbf{B}_s$, which has the same dimensions as the remotely sensed SST image and is initialized to zero (0), and three row vectors $< \mathbf{SST} > (s)$, $< \mathbf{GM} > (s)$ and $< \mathbf{Q} > (s)$. These row vectors are used to store frontal cross sections of temperature, gradient and a measure of data quality, respectively. The algorithm finishes this step by setting the value of pixels in $\mathbf{B}_s$ that correspond to the location of the pixels that make up the selected front segment, to a value of 1. These pixels are referred to herein as the sampling mask pixels. Figure 4.12 illustrates the geometry of a front detected in a remotely sensed SST image using the SIED algorithm, together with the pixel arrangement in $\mathbf{B}_s$ after the algorithm completes this first step.

In subsequent steps, the algorithm uses $\mathbf{B}_s$ to sample data from the **SST** and **GM** images at pixels that are labeled as ones in $\mathbf{B}_s$ (i.e. the mask pixels). The algorithm also uses a morphological procedure to shift the position of the sampling mask pixels, in order to extract frontal cross-sections of temperature and gradient magnitude. Each shift of the sampling mask pixels in $\mathbf{B}_s$ is referred to herein as a mask shift and is indexed by the subscript s: A mask shift of zero corresponds to the sampling mask pixels in $\mathbf{B}_s$ being positioned along the axis of a front segment ($\mathbf{B}_{s=0}$) (as in Fig. 4.12), a positive mask shift corresponds to sampling mask pixels in $\mathbf{B}_s$ being shifted into waters on the warm side of a front ($\mathbf{B}_{s=1,2,\ldots,n}$) by s image pixels, while a negative mask shift corresponds to sampling mask pixels in $\mathbf{B}_s$ being shifted into waters on the cold side of a front ($\mathbf{B}_{s=-1,-2,\ldots,-n}$) by s image pixels.

Indexing, using the subscript s, is used as a frame of reference for row vectors used to store the frontal cross sections. For example, the value of $< \mathbf{SST} > (s = 0)$ corresponds to the average SST along the axis of a front segment (Fig. 4.13b), whereas, the value of $< \mathbf{SST} > (s = 3)$ corresponds to the average SST at pixels in the remotely sensed image

sampled by the algorithm after shifting the sampling mask pixels a distance of three image pixels from the axis of the front segment (Fig. 4.13b).

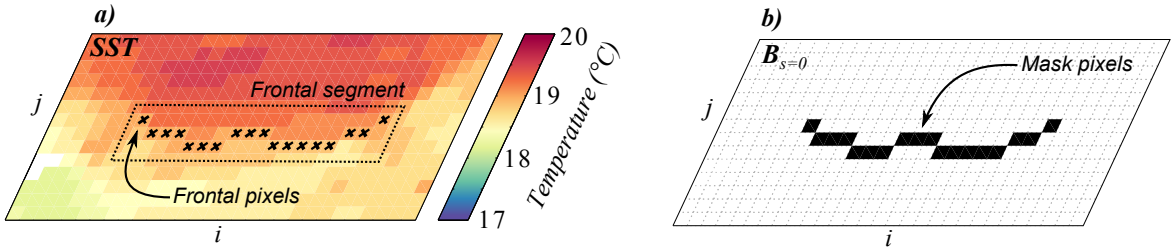

Figure 4.12: Illustration of the algorithm state after setting up the sampling masks (Section 4.8.4). (a) Subset of a remotely sensed SST image in the eastern Tasman Sea, overlaid with the location of a front segment detected using the SIED algorithm. The set of pixels comprising the front segment as shown as black crosses. Also shown (b) is the initial geometry of a sampling mask, $\mathbf{B}_s$, generated by the algorithm and used to sample the underlying **SST** and **GM** images. The location of mask pixels in $\mathbf{B}_s$ are shown as filled black squares and correspond to a value of one (1), white squares signify a pixel value of zero (0).

4.8.5 Method for sampling at a front

In this step, the algorithm samples data from the **SST**, **GM** and θ images at the sampling mask pixels in $\mathbf{B}_s$. The geometry of this procedure is illustrated in Figure 4.13, and proceeds as follows:

- Let $\mathbf{Z_s} = [z_1, z_2, ..., z_n]$ be a sample of n SST data read from **SST** along the set of sampling mask pixels in $\mathbf{B}_s$ that equal one (Fig. 4.13a). Similarly, let $\mathbf{G_s} = [g_1, g_2, ..., g_n]$ be a sample of n SST gradient magnitude data sampled from **GM** using $\mathbf{B}_s$.

- The average temperature at the front axis is estimated from the median of $\mathbf{Z_s}$ and is recorded in $< \mathbf{SST} > (s = 0)$ (Fig. 4.13b). Similarly, the median of $\mathbf{G_s}$ is calculated and recorded in $< \mathbf{GM} > (s = 0)$. The median, rather than the mean, values are used to minimise the sensitivity to anomalously low or high SST or SST gradient values, associated with small-scale geophysical noise or residual cloud contamination of the AVHRR images.

- An estimate of the gradient direction at the front segment, dir, is then calculated. To do so, a sample, $\mathbf{D}$, is read from the θ image using $\mathbf{B}_s$, where $\mathbf{D} = [\theta_1, \theta_2, ..., \theta_n]$, and then computing the sample median. The algorithm uses the value of dir in the next step of the front-sampling procedure to initialize an across-front sampling procedure. The direction of the front should be estimated from the angular median, rather than median value (Nikolaidis and Pitas, 1998), although sensitivity tests performed in Section 4.9.1 do suggest the algorithm, as implemented, is robust to variations in frontal orientation and to a meandering front.

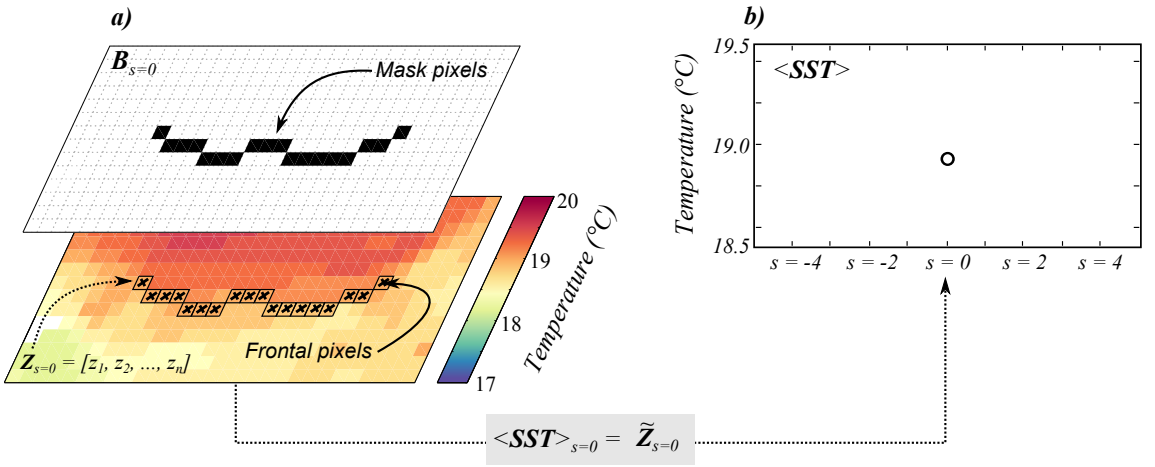

Figure 4.13: Illustration of the algorithm state after sampling at a front. (a) Geometry of the data sampling procedure used to read data from an underlying remotely sensed SST image using $\mathbf{B}_s$. In this example, the position of black pixels in $\mathbf{B}_s$ correspond to a mask shift of 0 ($s = 0$), and are used by the algorithm to sample at the axis of the front segment. The pixel locations being read from the remotely sensed SST image using $\mathbf{B}_{s=0}$ are overlain as black boxes. (b) Temperature cross section of a front after the algorithm has completed sampling at a front.

4.8.6 Method for sampling across a front

Next, the algorithm uses an iterative procedure to extract a SST and SST gradient magnitude cross section across the thermal front. This procedure is divided into four steps:

1. The algorithm shifts the sampling mask pixels in $\mathbf{B}_s$ outward from, and orthogonal to, the front segment, by one image pixel. The algorithm also updates the index value s (Section 4.8.6.1).

2. The algorithm samples from the **SST** and **GM** images using $\mathbf{B}_s$, then averages the sampled data and records the sample average in $<\mathbf{SST}>(s)$ and $<\mathbf{GM}>(s)$ respectively (Section 4.8.6.2).

3. The algorithm performs a set of threshold tests (Section 4.8.6.3). These are designed to evaluate whether the algorithm is likely to be sampling the temperature change across the thermal front, or has moved out of the frontal region, and on to one of the temperature plateaus that border the front.

4. The algorithm evaluates the outcome of thresholds tests and uses this to adapt or terminate the sampling procedure (Section 4.8.6.4)

Figure 4.14 shows an example of this sampling procedure applied to the front segment shown in Fig. 4.12. The sections below provide technical detail on each of these four steps.

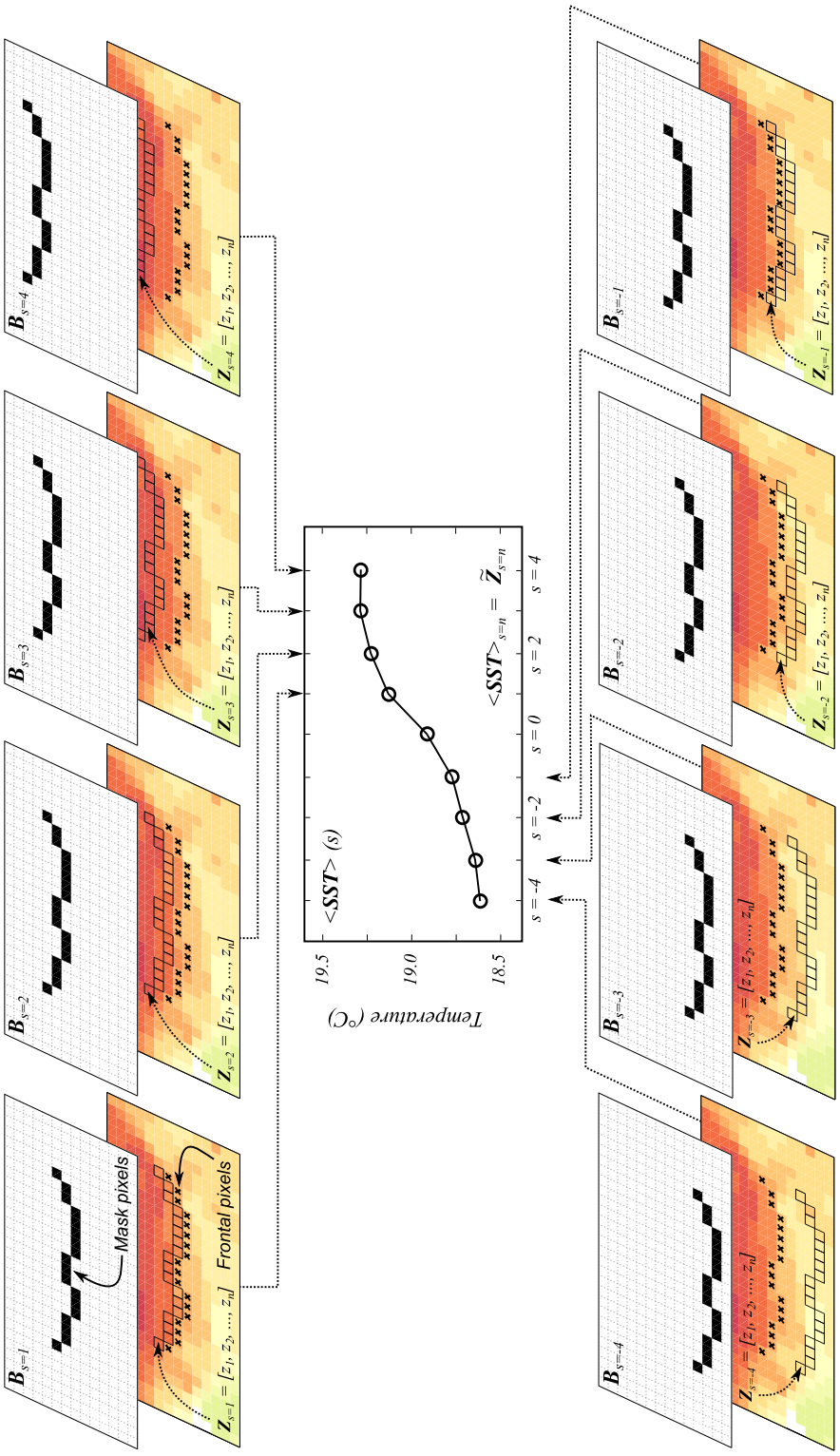

Figure 4.14: Illustration of the algorithm state as it samples across a front. The resulting across-front temperature profile that is extracted is also shown.

4.8.6.1 Method for shifting the sampling masks

In order to sample across the front, the algorithm shifts the sampling pixels in $\mathbf{B}_s$, using an image morphology procedure. Fig. 4.16 illustrates the geometry of this procedure, with sampling pixels in $\mathbf{B}_s$ being moved up the temperature gradient, into the warm side of a front. The principle behind the image morphology procedure used in this part of the algorithm are discussed in Appendix B. The procedure followed by the algorithm is divided into three steps:

- The algorithm flags the front segment as belonging to one of eight directional bins, k, based on the gradient direction of the front segment (dir). These eight direction bins are expressed using the four cardinal and four ordinal directions: N-S ($k = 1$), NE-SW ($k = 2$), E-W ($k = 3$), SE-NW ($k = 4$), S-N ($k = 5$), SW-NE ($k = 6$), W-E ($k = 7$) and NW-SE ($k = 8$).

- The algorithm then selects one structuring element from a pool of 32 structuring elements. The neighbourhood structures for this pool of 32 structuring elements are illustrated in Figure 4.15. The pool of structuring elements is divided into two sets: set 1 and set 2, into two temperatures: warm ($\mathbf{S}_k^{warm}$) and cold ($\mathbf{S}_k^{cold}$), and into eight directions ($k = 1 - 8$). The algorithm selects a structuring element based on the following logic:

  - The algorithm selects a structuring element from set 1 if $s = 0$ and from set 2 if $s \neq 0$.
  - The algorithm selects a structuring element from $\mathbf{S}_k^{warm}$ if it is processing the warm side of the front, and from $\mathbf{S}_k^{cold}$ if it is processing the cold side of the front.
  - The algorithm selects a structuring element from the directional-bin that corresponds to the direction flag (k) assigned to the front it is processing. The structuring elements in Set 1 and in Set 2 are designed to dilate the sampling pixels either up or down the frontal temperature gradient, orthogonal to the orientation of the front segment, by way of the image morphology calculation described in step (iii).
  - Eight of the structuring elements in Set 1 (k = 2, 4, 6, 8, warm and cold) are designed to perform an additional task: these structuring elements will also adapt the arrangement of the sampling pixels in the image dilation from $\mathbf{B}_s$ to $\mathbf{B}_{s=1}$ and in $\mathbf{B}_s$ to $\mathbf{B}_{s=-1}$. For a front segment with an ordinal gradient direction (i.e. NW-SE, k = 8), these structuring elements add off-diagonal pixels to the sampling pixels. This fills in sampling gaps that would otherwise appear in the sampling masks at the off-diagonal pixels.

- The algorithm shifts the sampling pixels in $\mathbf{B}_s$a distance of 1 image pixel along the temperature gradient, outward from the front segment. The algorithm shifts the sampling pixels by first dilating $\mathbf{B}_s$ with the structuring element selected above, then applying a pixel subtraction. If the algorithm is processing the warm side of a frontal segment, this procedure is expressed as

$$\mathbf{B}_{s+1} = (B_s \oplus S_k^{warm}) - \mathbf{B}_s. \tag{4.18}$$

If the algorithm is processing the cold side of a frontal segment, the procedure is expressed as

$$\mathbf{B}_{s-1} = (B_s \oplus S_k^{cold}) - \mathbf{B}_s. \tag{4.19}$$

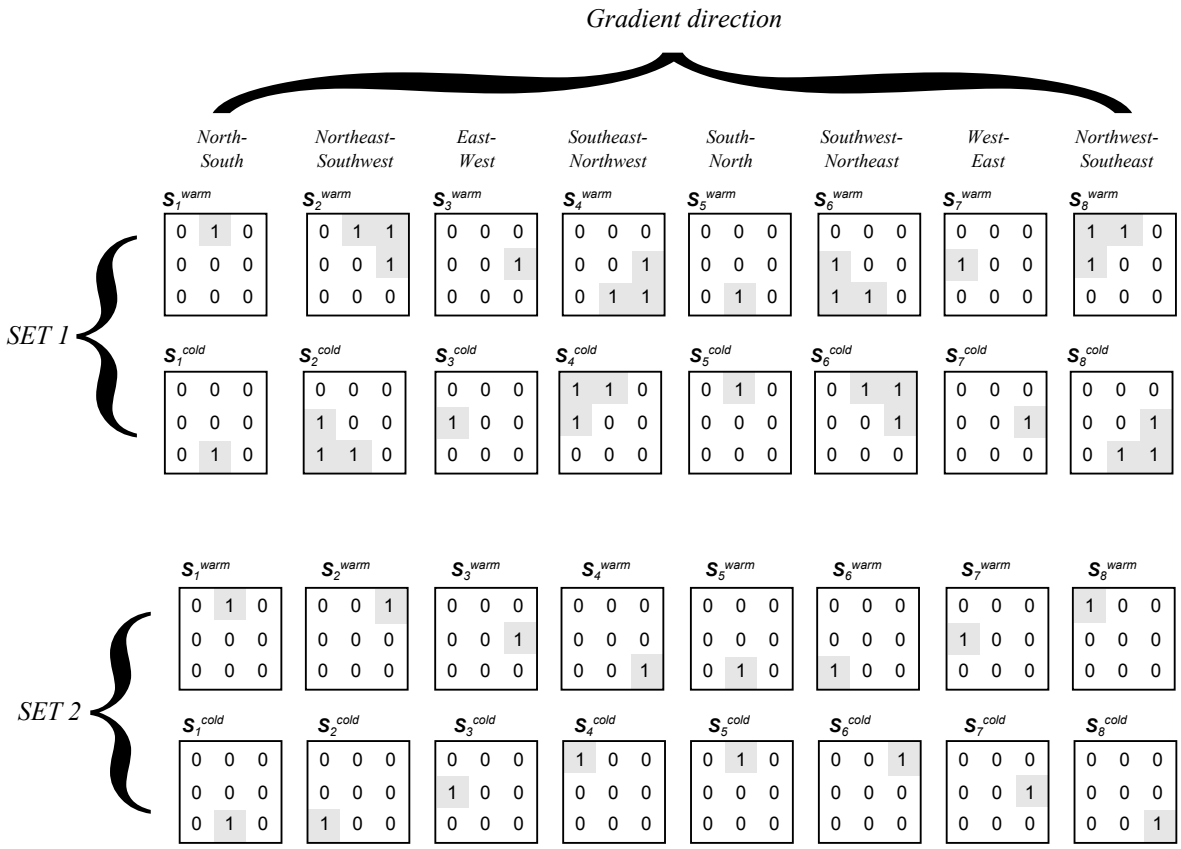

Figure 4.15: The neighbourhood structure of the two sets of structuring elements for dilating the binary sampling mask ($\mathbf{B}_s$) using eq. 4.18-4.19.

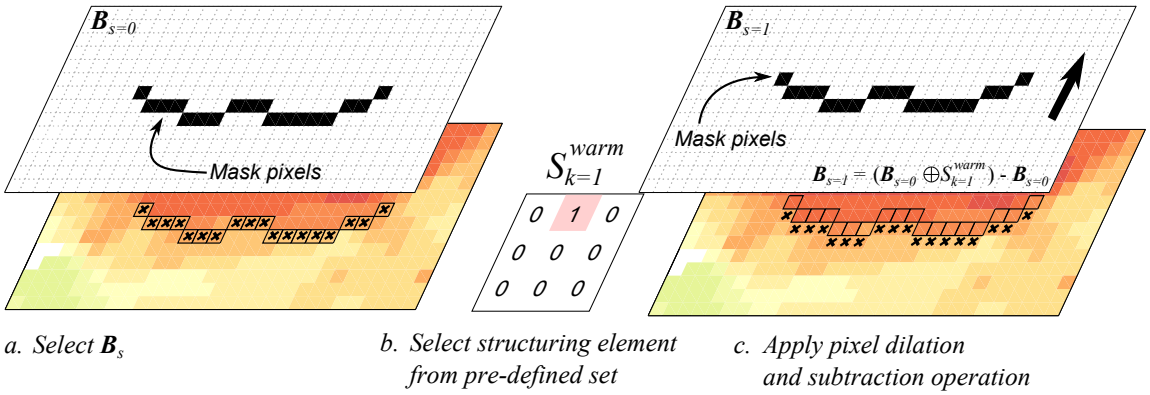

a. Select $\mathbf{B}_s$

b. Select structuring element from pre-defined set

c. Apply pixel dilation and subtraction operation

Figure 4.16: Example of shifting the binary sampling mask, $\mathbf{B}_{s=0}$, towards the warm side of a front by one-pixel using eq. 4.18.

4.8.6.2 Method for sampling from satellite images

Next, the algorithm samples data from **SST** and **GM** along the set of sampling pixels in $\mathbf{B_s}$ as follows:

- Let $\mathbf{Z}_s = [z_1, z_2, \ldots, z_n]$ be a sample of SST data drawn from **SST** using $\mathbf{B}_s$. Similarly, let $\mathbf{G}_s = [g_1, g_2, ..., g_n]$ be a sample of SST gradient magnitude data drawn from **GM** field using $\mathbf{B}_s$.

- Any sample members in $\mathbf{Z}_s$ deemed to have be drawn from the opposing side of the frontal segment are discarded from the sample. The corresponding SST gradient sample member, $\mathbf{G}_s(i)$, is also discarded. Sample members are examined using a logical test, based on the mean temperature of the front segment along its axis ($<\mathbf{SST}>(0)$):

  - If the algorithm is processing the warm side of a front, the procedure discards a sample member if $\mathbf{Z}_s(i) << \mathbf{SST} > (0)$, where i is the linear index to the sampled member.
  - If the algorithm is processing the cold side of a front, the procedure discards a sample member from $\mathbf{Z}_s$ if $\mathbf{Z}_s(i) >< \mathbf{SST} > (0)$.
  - The above tests were found necessary to account for occasions when the contour of a front segment meandered strongly, causing occasional pixels in $\mathbf{B}_s$ to overlap parts of the frontal segment onto an opposing side of a front, resulting in dubious spikes in the temperature and gradient cross sections ($<\mathbf{SST}>(s)$ and $<\mathbf{GM}>(s)$).

- The algorithm then checks the percentage of SST pixels being sampled using $\mathbf{B}_s$ that contain valid data and records this value in the row vector $<\mathbf{Q}>(s)$. There are two outcomes from this test:

- If there is at least 1 valid SST pixel being sampled by the algorithm, it proceeds to the step below.
- If there are no valid SST pixels being sampled by the algorithm, the sampling processes for the warm side of the front is terminated at this step. These conditions will occur when all image pixels being sampled using $\mathbf{B}_s$ are cloud-contaminated or where land is encountered. The algorithm then proceeds to sample across the cold side of the front (see Section 4.8.6.4 below).

- The median values of $\mathbf{Z}_s$ and $\mathbf{G}_s$ ($\widetilde{\mathbf{Z}}_s$ and $\widetilde{\mathbf{G}}_s$ respectively), are calculated using the remaining sample members and recorded as new cross section values $<\mathbf{SST}>(s)$ and $<\mathbf{GM}>(s)$ respectively.

4.8.6.3 Description of threshold tests

The algorithm next performs three threshold tests:

- First, the algorithm tests whether it has reached one of the temperature plateaus that border the thermal front. This test examines the gradient of SST. It is based on a similar technique implemented by Moore et al. (1997; 1999) (see Section 4.5.1) and one suggested by Shaw (1998). It uses the idea that the gradient of SST will decay as one moves outward from a front, and will approach a background temperature gradient, typical of the region under examination (see e.g. Ullman and Cornillon, 1999; Ullman et al., 2007). On the temperature plateaus that border a front segment, the gradient will approach this background temperature gradient. The plateau detection procedure proceeds as follows:

  1. The algorithm computes the horizontal change in SST as it samples outward from the front segment, using adjacent values in $<\mathbf{SST}>(s)$. It compares this to a pre-specified threshold value, $\mathbf{T}_{crit}$, which is based on the background SST gradient - defined here as the SST gradient at image pixels not adjacent to fronts. The test is failed if the difference between adjacent values in $<\mathbf{SST}>(s)$ falls below $\mathbf{T}_{crit}$ (i.e. the horizontal temperature gradient approaches the background gradient, and thus, a temperature plateau that borders the front). If processing the warm side of the front ($s = 1, 2, \ldots, n$) this test is expressed as:

$$<\mathbf{SST}>(s=n) - <\mathbf{SST}>(s=n-2) < \mathbf{T}_{crit}. \tag{4.20}$$

  If processing the cold side of the front (s = -1, -2, . . . , n) this test is expressed as

$$<\mathbf{SST}>(s=n) - <\mathbf{SST}>(s=n+2) < \mathbf{T}_{crit}. \tag{4.21}$$

The value of $\mathbf{T}_{crit}$ determines how steady the SST needs to remain, over a 3-pixel distance, for the algorithm to determine that it has reached a temperature plateaus, and should therefore stop sampling across the front. In the Tasman Sea, where the algorithm is utilised in this thesis a value of 0.15 was selected as an appropriate value for $\mathbf{T}_{crit}$ (see Section 4.8.8 below).

- The algorithm next checks whether it is encountering a secondary thermal front. This test assumes that the SST gradient magnitude will decay moving away from a thermal front, unless a secondary front is encountered. The presence of a secondary thermal front can degrade the accuracy of front parameter estimates made by the algorithm because the algorithm will begin, unknowingly, to sample across the secondary front. The algorithm performs this test by checking whether the temperature gradient has increased over consecutive values in $< \mathbf{GM} > (s)$. The test will fail if $< \mathbf{GM} > (s)$ increases relative to the value in the prior iteration of the procedure. If processing the warm side of the front ($s = 1, 2, \ldots, n$), this test is expressed as

$$< \mathbf{GM} > (s = n) >< \mathbf{GM} > (s = n - 1). \tag{4.22}$$

  Similarly, if the algorithm is processing the cold side of the front, the threshold test is expressed as

$$< \mathbf{GM} > (s = n) >< \mathbf{GM} > (s = n + 1). \tag{4.23}$$

  Testing of the SIED algorithm revealed that the location of detected thermal fronts were occasionally positioned 1 pixel away from corresponding gradient maxima estimated using a Sobel operator. This appeared to be attributable to the design of the SIED contour following algorithm. As a result, neither of the threshold checks (i-ii) are applied when s = 1 or s= -1, in order to prevent the algorithm terminating too early.

- Third, the algorithm checks how many loops it has made through the iterative procedure. During development, it was noted that the algorithm might endlessly sample across a front if the horizontal temperature change never falls below $\mathbf{T}_{crit}$ (i.e. if the front encounters a steady background temperature gradient that is above $\mathbf{T}_{crit}$). This test fails if the algorithm makes 10 iterations through the across-front sampling procedure.

4.8.6.4 Evaluation of threshold tests

Next, the algorithm evaluates the results of the three threshold tests (Section 4.8.6.3). Until one of these threshold tests fails, the algorithm iterates through steps 1 to 3 (described above in Sections 4.8.6.1-4.8.6.3) to extract one half of the frontal cross section, which covers the

warm side of the front (top row of Fig. 4.14). Once one of the threshold tests fail, the algorithm halts the sampling procedure for the warm side of a front. It then proceeds to sample across the cold side of the front. The algorithm initiates processing the cold side of the front segment by resetting $\mathbf{B}_s$ to $\mathbf{B}_s = 0$, so that the mask pixels are arranged along the frontal axis. The algorithm then iterates through steps 1 to 3 (described above in Sections 4.8.6.1-4.8.6.3) to extract the second half of the frontal cross section, which covers the cold side of the front (bottom row of Fig. 3.14). At the point at which the threshold tests fail for the cold side of the front, the complete frontal temperature cross section $< \mathbf{SST} > (s)$ has been extracted.

4.8.7 Calculation of front parameters

The final processing step calculates a set of five front parameters, shown schematically earlier in Fig. 4.11. An estimate of the average temperature of the front segment (a_1) is obtained from $< \mathbf{SST} > (s = 0)$ and recorded. The temperature of the warm plateau, a_2, is obtained from $< \mathbf{SST} > max(s)$. Similarly, the temperature of the cold plateau, a_3, is obtained as $< SST > min(s)$. The temperature change across the thermal front, a_4, is calculated as the difference between the warm and cold population temperatures, $a_2 - a_3$. An estimate of the gradient magnitude at the thermal front, a_5, is obtained from $< \mathbf{GM} > (s = 0)$. The algorithm amends these parameters to the corresponding front segment in the data set of thermal fronts. The algorithm then selects a new front segment from $\mathbf{B}_{edge}$ for processing, and creates a new sampling mask for that front (Section 4.8.4). The algorithm terminates once all front segments within $\mathbf{B}_{edge}$ have been processed.

4.8.8 Deriving an appropriate value for $\mathbf{T}_{thresh}$

An estimate of the background SST gradient magnitude in the Tasman Sea was used to set the algorithm plateau detection parameter, $\mathbf{T}_{thresh}$ (Section 4.8.6.3). SST gradient magnitude images were calculated by applying a Sobel gradient operator (Section 4.8.3) to PFV5.2 SST monthly composite images covering the period 1982 through 2011 in the Tasman Sea (Section 4.2). The locations of thermal fronts identified in these images using the SIED (Section 4.7) were then acquired. Following Ullman et al. (2007), the background SST gradient was defined as the average SST gradient magnitude at image pixels not adjacent to thermal fronts. This was calculated on a monthly basis as the median SST gradient magnitude of all image pixels excluding those within a 3-pixel mask surrounding a thermal front detected using the SIED.

To confirm the background gradient is distinguishable from the gradient of frontal features, a frontal temperature gradient, was also calculated as the median SST gradient mag-

nitude at frontal pixels. Fig. 4.17 compares the distribution of the monthly-median background and frontal temperature gradients. Not unexpectedly, comparison of the distributions shows the background gradient is distinct from the frontal gradients; the median frontal SST gradient is $0.043°C\ km^{-1}$, more than twice that of the median background SST gradient of $0.019°C\ km^{-1}$. Estimates of the background gradient using 5 and 7 pixel masks around fronts identified using the SIED yielded similar results, therefore, $0.019°C\ km^{-1}$ was deemed to be representative of the background SST gradient. Converting the background gradient to an equivalent change over 3 image pixels in the PFV5.2 data set (~4.4 km resolution), T_{thresh} was set to a slightly less conservative value of 0.15°C.

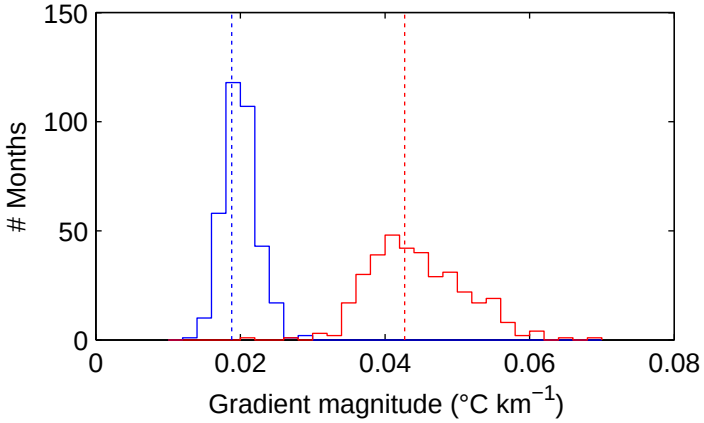

Figure 4.17: Distribution of monthly median SST gradient magnitude in the Tasman Sea at frontal pixels (red) and at background pixels (blue) for the period 1982 to 2011.

Using a value for $\mathbf{T}_{thresh}$ defined above, the front-analysis algorithm (Section 4.8) was applied to the thermal fronts detected in PFV5.2 monthly composite SST images using the SIED (Section 4.7). The resulting data set consists of the locations of thermal fronts identified in each remotely sensed SST image, together with their five corresponding properties determined from the front-analysis algorithm.

4.9 Sensitivity testing of the methodology

In this section, a Monte-Carlo analysis is used to assess the robustness of the front detection and analysis algorithms to variations in front configuration. Synthetic remotely sensed SST images that contain a thermal front - that has known properties - and that have similar noise characteristics to the PFV5.2 SST data were generated. The synthetic images contain a front modelled on a hyperbolic tangent function that emulates the steep gradient of a thermal front. This approach has also been utilised in several earlier studies, to evaluate the performance of front-analysis algorithms based on functional modelling (Shaw, 1998; Shaw and Vennell,

2000; Hopkins, 2008; Hopkins et al., 2011). Following Shaw (1998), synthetic images containing two types are fronts were generated. Synthetic images containing a straight front were generated using the following function:

$$SST_{X,Y} = x_1 + x_2 \times \tanh\left(\left(-X\cos\left(\theta\right) - Y\sin\left(\theta\right)\right)/x_3\right) + \eta, \tag{4.24}$$

where x_1 is the temperature of the frontal axis (°C), x_2 is half the total temperature difference across the front (°C), x_3 is the horizontal distance over which the temperature change is 76.2% of x_2, defined here as the cross frontal length scale (km), X is the distance (east-west) across the front (km), Y is the distance (north-south) along the front (km), θ is a rotation parameter (°) and η is noise with mean zero and standard deviation σ (°C). Synthetic images containing a meandering front that is orientated north-south were generated using the following function:

$$SST_{X,Y} = x_1 + x_2 \times \tanh\left(\left(X + C\right)/x_3\right) + \eta, \tag{4.25}$$

$$C = A \times \sin\left(\left(2\pi Y\right)/L\right),$$

where A is the meander amplitude (east-west) (km) and L is the meander wave length (north-south) (km).

Synthetic images were generated with the dimensions 32 x 32 pixels and with a pixel resolution of 4.634 km - to simulate the resolution of PFV5.2 data set. The default values used to generate the synthetic images were: x_1 = 11.5°C, x_2 = 0.5°C, x_3 = 7 km, θ = 0° (gradient lies west-east). These parameters yield a synthetic image containing a front that is representative of the fronts typically detected in remotely sensed SST images in the Tasman Sea; this front has a SST at the front axis (a_1) of 11.5°C, a warm plateau with a SST (a_2) of 12°C, a cold plateau with a SST (a_3) of 11°C, an across-front temperature difference (a_4) of 1°C, a cross frontal length scale of 14 km (width) and a temperature gradient (a_5) of 0.07°C km^{-1}. A synthetic image containing a front generated using eq. 4.24 is shown in Figure 4.18. Examples of synthetic fronts generated using eq. 4.25 are shown in Figure 4.19.

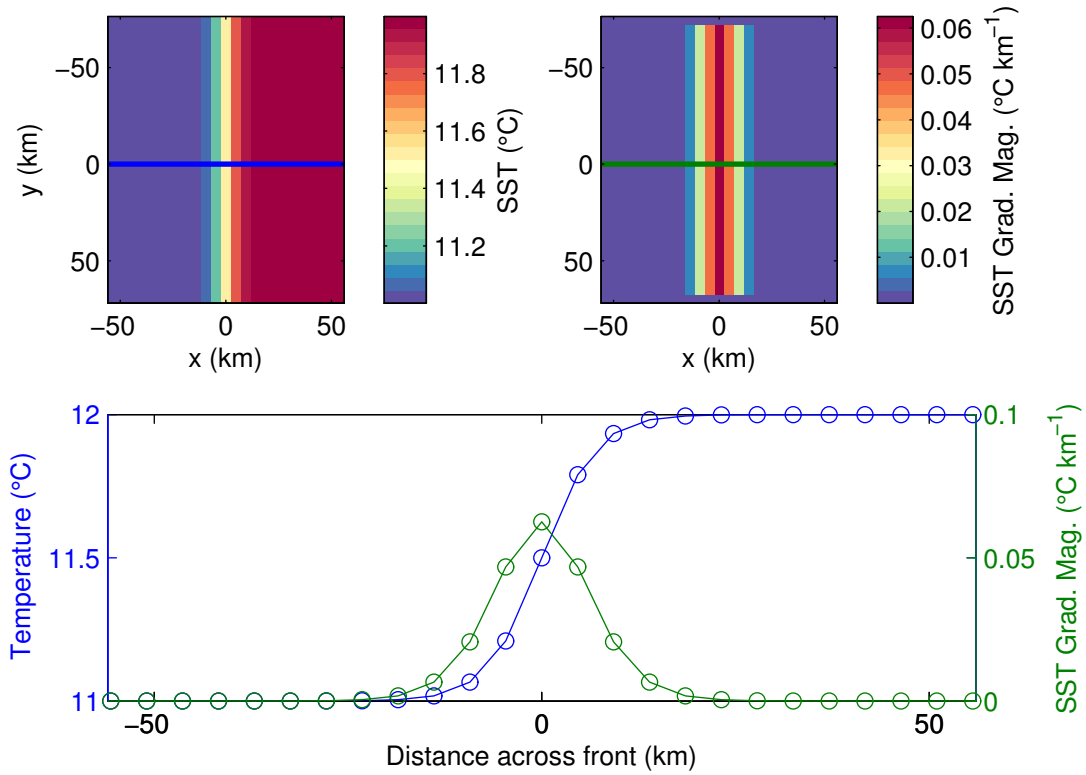

Figure 4.18: (a) Example of a synthetic 32×32 pixel remotely sensed SST image containing a front generated using eq. 4.24. (b) SST gradient magnitude of the synthetic image. (c) Across front profiles of SST (blue) and SST gradient magnitude (green) data extracted across the synthetic data sets. The locations of the across-front profiles are shown in (a) and (b) by the horizontal lines.

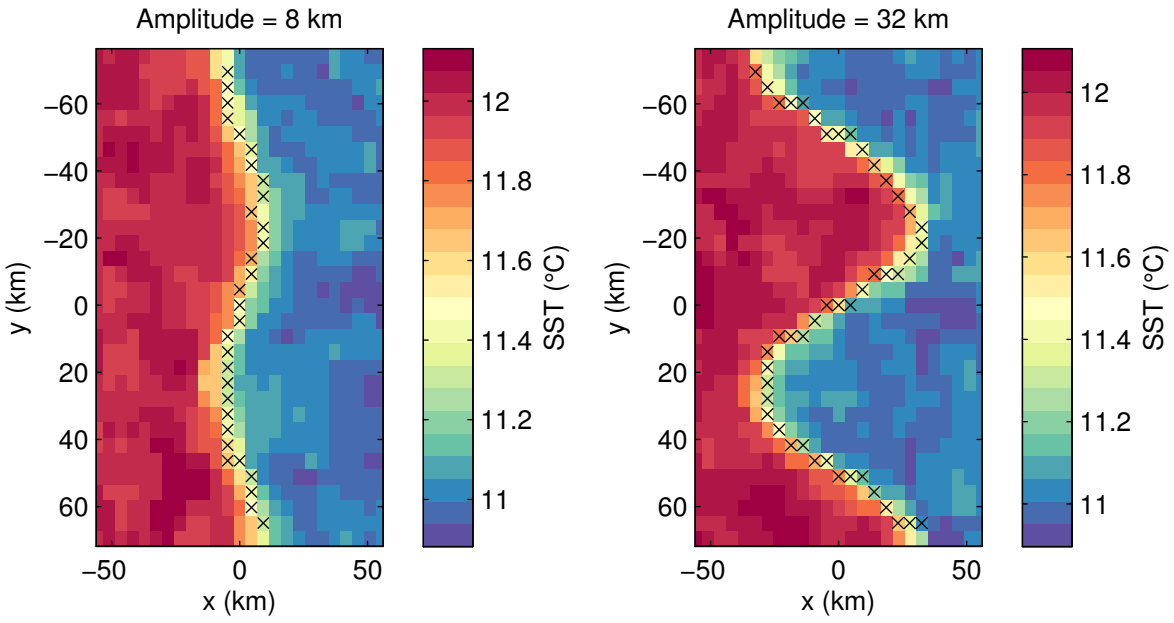

Figure 4.19: Examples of synthetic remotely sensed SST images containing a front generated using eq. 4.25 with a meander amplitude of (a) 8 km and (b) 32 km overlain with the location of edges detected using the SIED algorithm (black crosses).

Four experiments (A-D) were performed to test the robustness of the front analysis algorithm. In each experiment, synthetic images were generated using the hyperbolic tangent functions (eq 3.24 and 3.25), and one of the functions parameters was permutated across a physically realistic range at fixed intervals. Remaining parameters of the hyperbolic tangent function were maintained at the default values.

The permutations of the frontal parameters in each experiment are shown in Table 4.2. 1000 synthetic images were produced for each interval. Normally distributed noise with mean zero and σ = 0.1°C was added to each synthetic image, in order to simulate errors on the Pathfinder SST retrievals, where 0.1°C is the approximate accuracy of the Pathfinder SST retrievals assessed from co-located satellite-buoy match ups (Section 4.2.3).

In each experiment, the SIED (Section 4.7) was applied to a synthetic image, and then the front analysis algorithm (Section 4.8) was applied to detected front. The relative accuracy of the algorithm front parameter estimates was evaluated from the mean difference $\pm 2\sigma$ between the estimated and known parameters of the fronts in the synthetic images, calculated over the 1000 synthetic images generated for each interval. In these experiments, the $\mathbf{T}_{crit}$ parameter of the front analysis algorithm was set to a value 0.15°C, to simulate the application of the front analysis algorithm to fronts detected in remotely sensed SST images covering the Tasman Sea.

Table 4.2: Range (interval) across which parameter values were permutated in the four algorithm performance experiments.

Experiment	Synthetic eq.	Synthetic parameter	Range (interval)
A (orientation)	eq. 4.24	θ	0-360° (30°)
B (cross frontal length scale)	eq. 4.24	x_3	4-14 km (1 km)
C (temperature difference)	eq. 4.24	x_2	0.25-1.375°C (0.125°C)
D (meander)	eq. 4.25	A	0-40 km (2 km)

4.9.1 Results of Monte-Carlo analysis

Figure 4.20 shows the mean difference and variance (± 2 standard deviations of the difference) between the algorithm estimate of a front parameter, and the known front parameter of a synthetic front, in each experiment.

Across the four experiments, the absolute difference (variance) between the temperature of the front estimated from the front analysis algorithm and the temperature of the synthetic front ($\hat{a}_1 - a_1$) was less than 0.02°C (±0.08°C). The estimate of the temperature of the front from the front analysis algorithm depends on where in the synthetic image the SIED detects the front. This relatively small difference provides some confidence that the SIED is accurately detecting the location of the synthetic fronts.

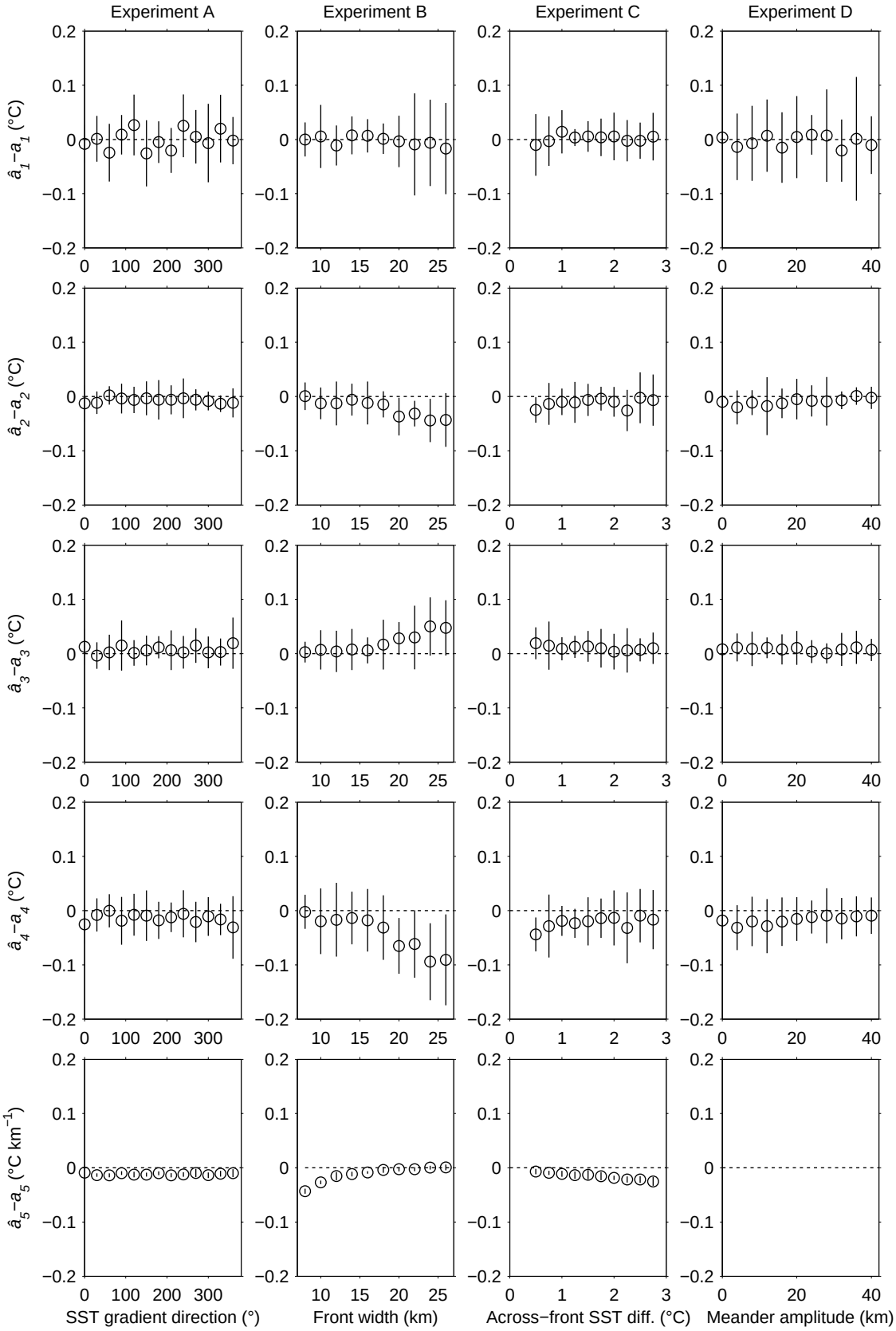

Figure 4.20: Mean difference between estimated ($\hat{a}$) and known (a) parameters of synthetic thermal fronts averaged over the 1000 Monte-Carlo experiments at each interval (circles) for experiments A-D (Table 4.2). Vertical black bars indicate ± 2 standard deviations of the difference.

In experiment A, synthetic images with fronts that have different orientations were generated (Table 4.2). Results from this experiment (Fig. 4.20a) show that the absolute differences between the algorithm-based estimates of the front parameters a_2, a_3 and a_4, and those of the fronts in the synthetic images, are generally <0.02±0.04°C, under different frontal orientations. The algorithm-based estimate of the across-front temperature difference (a_4), and frontal-gradient (a_5) are under-estimated by up to 3% and 14%, respectively, compared to the front in the synthetic images.

In experiment B, synthetic images with fronts that have different cross-frontal length scales were generated (Table 4.2). The results of this experiment (Figure 4.20b) show that with increasing cross frontal length scale, the algorithm-based estimates of the temperatures of the bordering water masses, and across-front temperature difference (a_4), deviate from those of the fronts in the synthetic images. a_4 is under-estimated by <1% for a cross frontal length scale of 4 km, which increases to an underestimate of -0.1±0.08°C (10%±8%) for a front with a cross frontal length scale of 13 km. For synthetic images that contain a front with a cross frontal length scale exceeding 18 km, the algorithm underestimates the temperature gradient of that front by up to 9% of the known value, which increases to 30% for fronts with a cross frontal length scale of 4 km.

In experiment C, synthetic images with fronts that have different across-front temperature differences were generated (Table 4.2). The results of this experiment (Figure 4.20c) show that the front-analysis algorithm under-estimates the temperature difference across fronts in the synthetic images by no more than -0.03°C±0.05°C, equivalent to a percentage error relative to the known value of between 1- 6%. Absolute errors on the algorithm-based estimates of the gradient of the front are between 12-18% of the known value.

In experiment D, synthetic images containing a meandering front were generated (Table 4.2). Differences between the algorithm-based estimates of the front parameters and those of the fronts in the synthetic images are similar to the results noted in experiments A-C (Fig. 4.20). This suggests that the presence of a meander does not impose any significantly greater loss in accuracy of the front-analysis algorithm. In experiment D, comparisons were not made between the algorithm-based estimates of the front gradient and those of the meandering, synthetic fronts, because the gradient of fronts in the synthetic images does not have a fixed value; it varies along the frontal axis as isotherms are spatially compressed or stretched by the meander.

The Monte-Carlo experiments suggest the main limitation of the front analysis algorithm is in making accurate estimates of the frontal gradient as the cross frontal length scale approaches the ~4 km resolution of the PFV5.2 data set (Experiment B). This is a natural consequence of the analysis resolution; the ~4 km resolution of the synthetic Pathfinder images inherently limits the scales that can be resolved from pixel-differencing to scales greater than

4 km. In addition, the resolution of the 3×3 pixel Sobel operator implemented in the front analysis algorithm is twice the resolution of the image it is convolving and thus, inherently smooth's image gradients.

It is also apparent from the Monte-Carlo experiments that the new front-analysis algorithm underestimates the frontal temperature difference of fronts in the synthetic images by up to 10%. These underestimates arise from the combined effects of the algorithm underestimating a_2 (warm plateau) and overestimating a_3 (cold plateau). These offsets are not unexpected. They arise when the spatial decay in SST moving away from a frontal axis drops below the value of the $\mathbf{T}_{crit}$ parameter (0.15°C over 3-pixels), and the algorithms across-front sampling procedure is terminated. The offset becomes more pronounced with an increasing cross frontal length scale (Fig. 4.20c) because the frontal temperature profile of the synthetic fronts becomes smoother and mimics the typical background temperature gradients that $\mathbf{T}_{crit}$ is designed to monitor.

Nonetheless, the overall evidence from the Monte-Carlo experiments suggests the front analysis algorithm is robust to realistic variations in frontal configurations. For a range of configurations of fronts in synthetic remotely sensed SST images, in the presence of image noise with $\sigma = 0.1$°C, the upper bounds on the absolute biases in estimation of frontal properties (a_1,a_2,a_3,a_4) is 0.1°C. This is regarded here as an acceptable level of error when considering the Monte-Carlo error-estimates are comparable to or less than the approximately 0.1°C uncertainties on the Pathfinder SST retrievals themselves (Ullman and Cornillon, 1999; Kearns et al., 2000; Kilpatrick et al., 2001; Marullo et al., 2007).

4.10 Summary

- A new data set of thermal fronts identified over a 30 year period (1982-2011) in the Tasman Sea has been developed.
- The data set of thermal fronts was derived from PFV5.2 SST monthly composite images covering the period Jan 1982 through Dec 2011 (Section 4.2).
- Thermal fronts were detected in each of the PFV5.2 SST monthly composite images using the SIED (Cayula and Cornillon, 1992) (Section 4.7).
- A new algorithm was developed to parameterize the properties of thermal fronts (Section 4.8). The algorithm extracts a cross-section of SST and SST gradient magnitude across a thermal front detected using the SIED. It then uses this cross section to calculate a set of five parameters that describe physical properties of the front. This

algorithm was applied to each thermal front detected in the PFV5.2 SST monthly composite images.

- The resulting data set comprises 30 years (1982-2011) of the locations (Fig. 4.21) and physical properties of thermal fronts detected in the Tasman Sea at monthly resolution. This data set is used in the remainder of this thesis to investigate surface temperature expressions of the N-STF and S-STF in the Tasman Sea and south of New Zealand (**Chapters 5**), and to examine interannual variability of SST at the S-STF around southern New Zealand (**Chapter 6**).

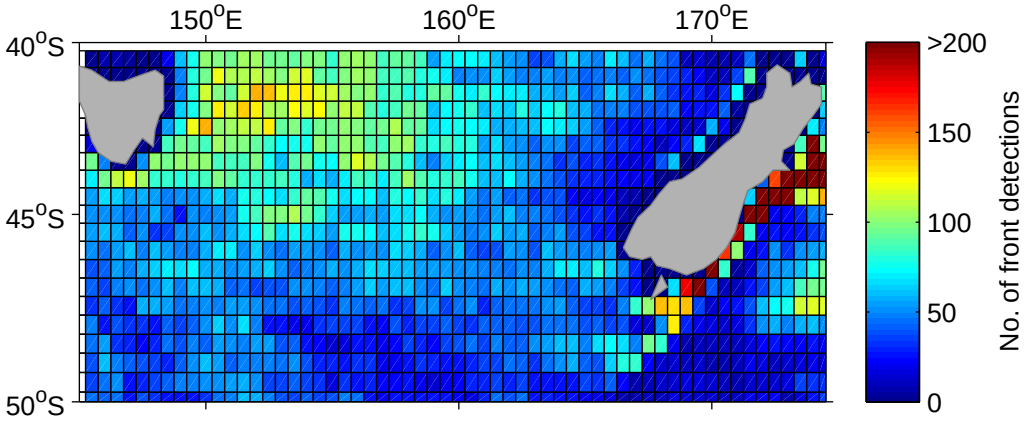

Figure 4.21: Illustration of the 30 year data set of thermal fronts detected in PFV5.2 SST images over the Tasman Sea. Shown are the total number of thermal fronts detected in 0.5° lat-lon bins over the period 1982-2011.

Chapter 5

Remote sensing of the surface expression of the Subtropical Front in the Tasman Sea

5.1 Introduction

Temporal variability in the position of the STF in the Tasman Sea has not been described in detail. To date, the position and structure of the STF in this region has been determined largely from analyses of historical hydrographic survey data. Only a rudimentary picture exists about the fronts temporal variability, mainly due to the scarcity of repeat observations (**Chapter 2**). This Chapter aims to discover whether surface expressions of the N-STF and S-STF in the Tasman Sea can be observed in a long term data set of remotely sensed SST images. By attempting to identify and locate surface expressions of the N-STF and S-STF in the remotely sensed SST data, this work also seeks to provide new detail to the hydrographic-based understanding of the position and variability of the STF in the Tasman Sea.

5.1.1 The Subtropical Front in the Tasman Sea

Historically, there have been considerable differences in interpretation of the properties and position of the STF in the Tasman Sea (reviewed by Jeffrey (1986), Stramma et al. (1995), Hamilton (2006) and in **Chapter 2**). More recent work by Hamilton (2006) has reconciled the various historical definitions and positions reported for the STF in this area. Hamilton (2006) found that the STF in the Tasman Sea can be described as two fronts - the N-STF and S-STF - that generally coincide with the 35.1 (N-STF) and 34.7 (S-STF) surface isohalines. These fronts enclose a broader, more homogenous STFZ. Hamilton (2006) used historical hydrographic survey data collected west of New Zealand to estimate the general position of

the N-STF, S-STF and STFZ (Fig. 5.1). These data however were relatively poorly sampled, consisting of eight Nansen surveys from the period 1964-1985 (see Fig. 10 in Hamilton (2006)).

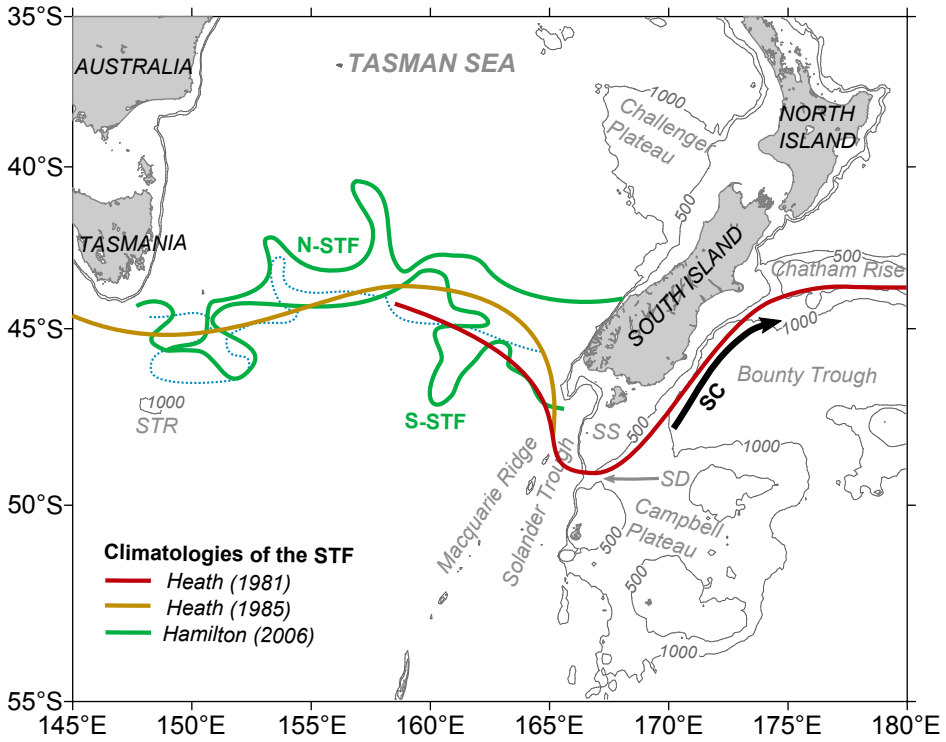

Figure 5.1: Schematic of the climatological position of the STF in the Tasman Sea from Heath (1981; 1985) and the N-STF and S-STF from Hamilton (2006). A 'synoptic' position of the STF derived by Hamilton (2006) from a hydrographic survey of the Tasman Sea during December 1988 (Warmus, 1989) is also shown (blue dotted line). The position of the Southland Current (SC) is shown by the black arrow. Also shown is the regional bathymetry with depth contours at 500 and 1000 m depth (grey lines). Major bathymetric features referred to in the text are also labeled (STR – South Tasman Rise, SD – Snares Depression, SS – Snares Shelf).

5.1.2 Temporal variability of the STF

Whilst hydrographic survey data have provided valuable information about the spatial characteristics of the N-STF and S-STF in the Tasman Sea, there is still not much known about their temporal variability, mainly due to the paucity of observational data.

To date, analyses of hydrographic survey data have provided a limited and inconsistent picture of temporal variability of the N-STF and S-STF in this area. For instance, using a composite of 21 hydrographic sections spread across the Tasman Sea, Jeffrey (1986) investigated latitudinal variability of the 35.1 (N-STF) and 34.7 (S-STF) frontal zones in response to atmospheric forcing. Jeffrey (1986) found that the position of the 35.1 frontal zone was strongly influenced by the latitudinal position of the subtropical high pressure belt, whereas

the 34.7 frontal zone was much less sensitive to this forcing. From similarities in the latitudinal position of the 35.1 and 34.7 isohalines under different forcing scenarios, Jeffrey (1986) inferred that the N-STF and S-STF in the western Tasman Sea (145-150°E) were somewhat fixed in position, possibly due to the topographic influence of the Tasmanian continental shelf. Hamilton (2006) inferred a similar picture of temporal variability in the position of the STF, based on a comparison between the position of the STF in a composite of Nansen data and an earlier quasi-synoptic CTD survey of the Tasman Sea from December 1988 (Warmus, 1989). These frontal positions are shown in Fig. 4.1. Hamilton (2006) noted similarities between the general position of the STF (S-STF) in both data sets and, on the basis of this limited data, suggested that the STF has a "rather constant position" in the Tasman Sea.

There is limited support in the literature, and in Hamilton's (2006) own results, for the STF in the Tasman Sea having a relatively constant position. For instance, results presented by Hamilton (2006) show the position of the S-STF in the central and eastern Tasman Sea meandering by ±2° latitude relative to the position of the S-STF estimated from the Warmus (1989) survey (Fig. 5.1). This meandering suggests that the position of the S-STF (and hence the width of the STFZ) might in fact be quite variable in the central and eastern Tasman Sea on some times scales.

Similarly, results presented by Jeffrey (1986) show the position of the S-STF in the central and eastern Tasman Sea shifting by between 0-3.5° of latitude under different atmospheric conditions, and hydrographic survey data collected in the eastern Tasman Sea (164-166°E) show the S-STF might occur near 47°S (Heath, 1981, 1985; Jeffrey, 1986; Butler et al., 1992; Morris et al., 2001; Hamilton, 2006) and between 49-49.6°S (**Chapter 3**). Contrary to the inference of Hamilton (2006), these differences in the reported position of the S-STF suggest the position of the Front in the central and eastern Tasman Sea might be highly variable over some time scales.

At the western border of the Tasman Sea, the N-STF and S-STF are merged (Jeffrey, 1986; Hamilton, 2006). Here, a couple of studies have used repeat hydrographic survey data to sample interannual variability in the position of the STF (Rintoul et al., 1997; Sokolov and Rintoul, 2002). The most recent of these studies, based on seven years of austral summer repeat XBT sections collected south of Tasmania (144-146°E), shows the latitudinal position of STF varies by about ±1° around its mean latitude (45.2°S) at interannual time scales (Sokolov and Rintoul, 2002). Nevertheless, at present, the available hydrographic survey data within the Tasman Sea are too sparse and infrequent to say much confidently about time scales of variability in the positions of the N-STF and S-STF.

This raises a number of basic questions about the position of the S-STF and its temporal variability south and west of New Zealand, such as: How much does the position of the S-STF vary on seasonal and interannual time scales? Is the seasonal and interannual variability

in their position of similar magnitude in each part of the basin or does it vary zonally? and how reliable are climatological estimates of the position of the S-STF (e.g. Hamilton, 2006), based on hydrographic data sampled sparsely in time, in light of potentially large variability in the front's positions?

5.1.3 Remote sensing of the STF

The availability of remotely sensed SST products since the 1980s, and the recent development of global remotely sensed SSS products (Lagerloef et al., 2008), now provide surface observations of SST and SSS on spatial scales of 10s to 100s of km, covering timescales from daily to multi-decadal. These data present new opportunities for studying both the spatial and temporal variability of the surface expressions of the N-STF and S-STF in the Tasman Sea, and in assessing some of the ideas about the frontal variability gleaned from the limited hydrographic data.

Within the Tasman Sea, a number of previous studies have already analyzed climatological mean SST distributions (Tate, 1988; Tate et al., 1989; Uddstrom and Oien, 1999; Graham and de Boer, 2013), while Butler et al. (1992) analyzed ten remotely sensed SST images covering the waters around southern New Zealand. However, there is ongoing uncertainty regarding whether or not surface expressions of the STF in the Tasman Sea can be observed within remotely sensed SST images. Tate (1988) analysed five years (Jun 1979 to May 1984) of AVHRR-derived SST data to estimate the climatological monthly mean SSTs with a 1° spatial resolution. In turn, Tate et al. (1989) used five years of remotely sensed SST data to examine the time and space scales of SST variability associated with the surface expressions of the EAC and TF in the Tasman Sea. Neither study was able to identify any features in these fairly coarse, mean SST fields that might indicate surface temperature expressions of the STF.

In a later study, Uddstrom and Oien (1999) utilized a five year time series (Jan 1993 to April 1998) of bias-corrected and cloud-cleared AVHRR SST images to produce a higher ~17.8 km spatial resolution analysis of the climatological SST field for the New Zealand region. They found that the location of the STF defined by Heath (1985) in the Tasman Sea was not clearly revealed in their five-year mean SST field, and inferred that the STF in the Tasman Sea might therefore lack a classic temperature-front signature at the surface. In contrast, at least in some parts of the Tasman Sea, data from hydrographic surveys suggests that the position of the S-STF is identifiable from strong SST gradients at synoptic time scales (e.g. Butler et al., 1992; Szymanska and Tomczak, 1994; Hamilton, 2006). A recent study of the global STF by Graham and de Boer (2013), based on a combination of an 11-year (1999-2009) climatology of remotely sensed SST measurements and remotely sensed SSH

measurements, reveals a range of SST gradient maxima across the STFZ in the Tasman Sea (Fig. 3 in Graham and de Boer (2013)). Some of these gradient maxima are located along the pathway of the STF defined by Deacon (1982) (Fig. 3 in Graham and de Boer (2013)). However, their physical association with the N-STF and S-STF water mass boundaries is as yet unclear. Taking a different approach, Belkin and Cornillon (2003) examined annual-mean and seasonal-mean statistics of occurrence of thermal fronts over the Pacific Ocean by applying an edge detection algorithm to 12 years of 9 km resolution AVHRR Pathfinder SST images. Their analyses reveals hundreds of thermal fronts located across the STFZ in the Tasman Sea defined by Hamilton (2006). However, much like the studies that preceded them (Tate, 1988; Tate et al., 1989; Uddstrom and Oien, 1999), Belkin and Cornillon (2003) could not identify a dominant pathway for surface expressions of the STF in this area from the remotely sensed SST images.

5.2 Focus of this study

This Chapter will examine whether surface expressions of the N-STF and S-STF in the Tasman Sea can be observed within a long-term data set of remotely sensed SST images. An automated edge-detection algorithm (Cayula and Cornillon, 1992) is used to locate thermal fronts in 30 years (1982-2011) of PFV5.2 monthly composite SST images (**Chapter 4**). Thermal fronts detected in four regions of the Tasman Sea are then statistically analysed to determine their annual-mean and seasonal-mean frequency of occurrence. This study then looks for connections between spatial patterns of thermal front occurrence and the occurrences of the N-STF and S-STF, based on isohaline definitions. This connection is made using three years (2013-2015) of remotely sensed SSS data, in combination with newly reconciled, isohaline-based definitions of the N-STF and S-STF (Hamilton, 2006). Ultimately, surface expressions of the S-STF are identified in the remotely sensed SST images, allowing spatial and seasonal variability of surface expressions of the S-STF to be investigated.

5.2.1 Contributions of this study

Whilst this study explores some similar threads to some previous work, it has several aspects that contribute to an improved regional and global understanding of the S-STF:

1. An edge detection algorithm is utilized to identify thermal fronts in monthly composite remotely sensed SST images (Cayula and Cornillon, 1992), potentially resolving surface temperature expressions of the S-STF rather than trying to identify smooth and weak signatures of the S-STF in annual-mean SST distributions (e.g. Tate, 1988; Tate et al., 1989; Uddstrom and Oien, 1999; Graham and De Boer, 2013).

2. Results from remotely sensed SST images are integrated with results derived from analyses of remotely sensed SSS images using the historical, salinity-based definitions of the N-STF and S-STF of earlier investigators (Hamilton, 2006). This enables this study to identify surface expression of the S-STF in remotely sensed SST images with greater confidence than previous remote sensing studies that covered the Tasman Sea.

3. The data set of remotely sensed SST images used in this study consists of 4-km resolution, monthly composite images, over a 30 year period (1982-2011) (**Chapter 4**). These data provide greatly improved temporal coverage of surface observations, compared with both the scattered historical hydrographic survey data available in Tasman Sea and with data sets of remotely sensed images used in earlier satellite-based studies.

4. The length of the remotely sensed SST record also enables this study to develop a statistical view of the position of surface expressions of the S-STF over 30 years (1982-2011), which the historical hydrographic survey data cannot provide. This final aspect is particularly valuable because it allows this study to infer the 30-year typical locations and seasonal migrations of surface expressions of the S-STF in the Tasman Sea and south of New Zealand. This information can also potentially provide new insight to the drivers of temporal variability of the S-STF.

5.2.2 Outline of this study

This Chapter is organised as follows. Section 5.3 presents the data sets used in this study. Section 5.4 describes the approaches used to generate spatial histograms. In Section 5.5, spatial histograms are used to describe the mean spatial patterns in the frequency of occurrence of (i) surface thermal fronts and (ii), the SSS indicators of the N-STF and S-STF, in four regions of the Tasman Sea. In Section 5.6, comparisons are performed between the distributions of thermal fronts and the N-STF and S-STF based on their SSS definitions, to assesses whether any of the thermal fronts are likely to be surface thermal signatures of the N-STF or S-STF. Here, it is apparent that spatial patterns in the occurrence of the S-STF near the landmass boundaries of Australia and New Zealand are reflected in the pattern of occurrence of thermal fronts. The implication is that the spatial histograms of thermal fronts provide distributions of the position of hundreds of surface expressions of the S-STF over 30 years (1982-2011). The remainder of Section 5.6 discusses the implications of these findings for knowledge of the typical position and seasonal migration of the S-STF, and their links with seafloor topography and atmospheric forcing. Section 5.7 presents conclusions from the study.

5.3 Data

5.3.1 The AVHRR Pathfinder Version 5.2 SST Data Set

The primary data set used in this study is the Level 3 remotely sensed estimates of SST from the PFV5.2 data set (**Chapter 4**). These data consist of gridded 4 km daily SST fields, which span the 30 year period January 1982 to December 2011. To eliminate thermal front detections that might arise from diurnal warming events, only the night-time SST retrievals are used in this work. To reduce the inclusion of poor quality SST retrievals, where the satellite view of the sea surface is likely to have been obscured by cloud cover, only SST pixels with a Pathfinder quality flag of 4 or above are used in this work (as discussed in **Chapter 4**). To assist the detection of thermal fronts in the PFV5.2 data, which is greatly restricted in this area due to persistent cloud cover (Uddstrom and Oien, 1999), the daily data were averaged into 360 monthly composite SST images (covering Jan 1982 to Dec 2011). These monthly composite images form the primary data used in this study.

5.3.2 Thermal front data set

The SIED (Cayula and Cornillon, 1992) was used to detect thermal fronts in the PFV5.2 SST monthly composite SST images. The application of the SIED to the SST images was described previously in **Chapter 4**. The gradient magnitude of the detected thermal fronts was determined by applying the front analysis procedure also described in **Chapter 4**.

This Chapter uses a subset of strong, thermal fronts detected in the monthly composite SST images (Fig. 5.2). A threshold on the frontal SST gradient magnitude of >2.5°C 100 $km^{-1}$is used to define a strong, thermal front. This value was selected in order to confirm that the edges (fronts) detected by the SIED have the properties expected of an ocean thermal front, i.e., they have an SST gradient magnitude that is significantly greater than the ambient meridional SST gradient magnitude. In the Tasman Sea, the ambient meridional SST gradient magnitude is approximately 0.8°C 100 km^{-1} (Uddstrom and Oien, 1999).

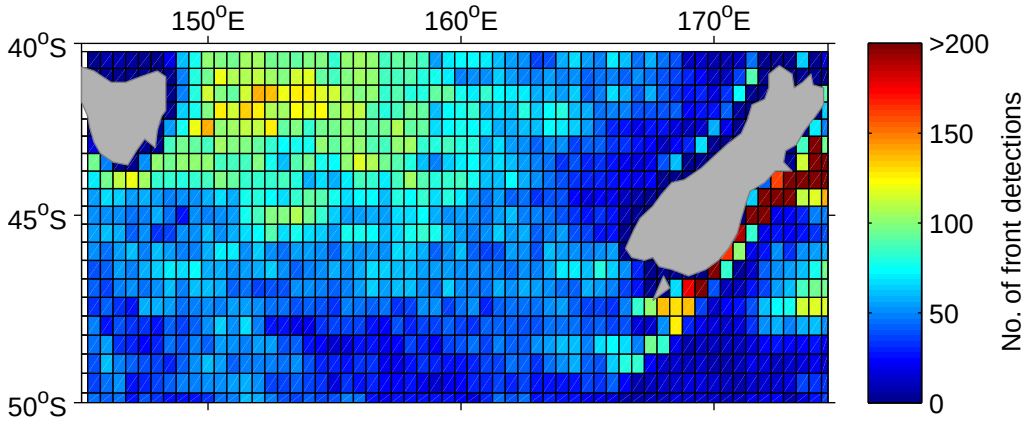

Figure 5.2: Illustration of the 30 year data set of thermal fronts detected in monthly-composite PFV5.2 SST images over the Tasman Sea that is used in this study. Shown are the total number of thermal fronts detected in 0.5° lat-lon bins over the period 1982-2011.

5.3.3 AVHRR Pathfinder climatology

A long term (1982-2011) annual mean SST climatology was also derived from the PFV5.2 dataset. To generate this climatology, monthly gridded SST (4 km) from January 1982 to December 2011 were binned into 0.5° lat-lon bins (145°-180°E, 40°-50°S). For example, all 4 km monthly mean SST estimates within ±0.25° of 150°E, 45.25°S were assigned to the bin centered on 150°E, 45.25°S bin. The binned data were then averaged into annual means on a per-bin basis. The climatological SST estimate in each bin is:

$$ANMSST_{i,j} = \frac{\sum_{y=1982}^{2011} \sum_{m=1}^{12} SST_{y,m,i,j}}{N_{i,j}} \tag{5.1}$$

where *ANMSST* is the climatological mean, *SST* is a 4 km satellite pixel, y is the year of observation, m is the month of observation, and i and j are subscripts to which bin observation falls into. Due to the problem of cloud contamination in the satellite SST images, the monthly gridded SST data will contain missing values in some 4 km satellite pixels. Because of this, the sample used to estimate the annual mean SST in each bin is likely to be skewed towards the summer months, when mean cloud cover is lower (see e.g. ISCCP, 2009). As such, the annual mean SST estimates that are reported in this study should be interpreted as being biased towards the summer (warm) months.

5.3.4 Aquarius sea surface salinity

To accompany the remotely sensed SST images, a secondary data set of remotely sensed SSS images is examined. The SSS images used here fall within a 36 month period between December 2011 and November 2014. The salinity data used in this study are the Version 4.0 Level-3 (gridded 1-degree monthly) remotely sensed estimates of SSS from the Aquarius remote sensing mission (Lagerloef et al., 2008). The Aquarius mission produces monthly SSS estimates with global root-mean-square-error less than 0.2 psu on 150 km spatial scale (Lagerloef et al., 2015). The Aquarius data used here consist of monthly, version 4 (V4.0), SSS estimates that are gridded at $1^\circ \times 1^\circ$ spatial resolution, and generated using a local polynomial gridding technique (Lilly and Lagerloef, 2008). The Aquarius data were acquired from http://podaac.jpl.nasa.gov/SeaSurfaceSalinity/Aquarius.

A statistical error analyses, based on a 36 month (September 2011 to August 2014 (inclusive)) comparison of (Level-3) Aquarius with surface *in-situ* (Argo buoy) and ocean model (HYCOM) data, show that the average Aquarius root-mean-square error for V4.0 monthly Level-3 gridded data over the southern Tasman Sea range between approximately 0.05-0.2 psu. (see Fig. 21 in Lagerloef et al., 2015). The complete Level-3 monthly Aquarius V4.0 data set spans the period September 2011 to May 2015 (inclusive), following which a hardware failure in early June 2015 caused the end of the mission (Lagerloef et al., 2015).

Ideally, this study would have used data for the full 36 month period between December 2011 and November 2014. However, due to a residual seasonal bias in the Aquarius V4.0 Level-3 monthly SSS maps that is discussed below, this study instead uses a reduced 27 month subset of these data. This subsets consists of the monthly SSS images from three consecutive seasons of Dec-Jan-Feb, Mar-Apr-May and Jun-Jul-Aug between 2011 to 2014 (e.g. Dec 2011-Aug 2012, Dec 2012-Aug 2013 and Dec 2013-Aug 2014).

An error analyses of the Aquarius V4.0 data set conducted by Lagerloef et al. (2015), based on comparisons between gridded 1-degree seasonal Aquarius SSS maps and collocated in-situ buoys SSS measurements, indicate a seasonally varying bias in the Aquarius data over the latitudinal range 40-50°S: there is positive bias in the Aquarius data of 0.17 psu during the austral spring (Sep-Oct-Nov), which is nearly double the maximum bias observed in any of the other seasons (Table 4 in Lagerloef et al., 2015). This bias is relevant to the analyses conducted here because SSS contours in the Aquarius data are used to infer positions of the N-STF and S-STF over the southern Tasman Sea; a positive bias during the austral spring would be expected to result in unusually poleward positions of SSS contours used to infer positions of the N-STF and S-STF during this season. To reduce the possibility that these positive biases during the austral spring are interpreted as oceanographic signals, the monthly SSS images covering the austral spring were excluded from these analyses.

5.4 Analysis Procedure

5.4.1 Statistical analysis of thermal front occurrence

Subsets of the 30 years of thermal front detections were aggregated into spatial histograms of frequency of occurrence. These histograms were used to determine the spatial and seasonal variability in the occurrence of thermal fronts within the Tasman Sea and south of New Zealand. A procedure, described below, was developed to calculate these histograms. This procedure is based on an earlier method described by Ullman and Cornillon (1999), and was modified in this study to use subsets of thermal fronts detected in portions of relatively clear (cloud free) PFV5.2 monthly composite SST images.

Spatial histograms of the frequency of occurrence of thermal fronts, or front frequency, were calculated for consecutive, 0.5° wide latitudinal strips in the Tasman Sea. These strips started at 145°E and ran eastward to 175°E. Each strip extended from 40°S to 50°S. To calculate the histograms of front frequency, each strip was subdivided into 0.5° lat-long bins. In the histograms of front frequency that are presented later, front frequency describes the ratio, calculated within these 0.5° lat-long bins, of the total number of thermal front segments observed in a bin, when the bin was also clearly viewed, to the total number of months a bin was clearly viewed, over the period 1982 to 2011.

Annual mean (1982-2011) histograms of front frequency were obtained for each latitudinal strip, using the following procedure (illustrated in Fig. 5.3):

(a) First, a 0.5° latitudinal strip between 145°E and 175°E was selected and then subdivided into 0.5° lat-lon bins (Fig. 5.3a).

(b) A monthly composite remotely sensed SST image, and the set of lat-long positions of thermal front segments detected in that monthly image, was then extracted from the input data sets, starting with January 1982 (Fig. 5.3b).

(c) Strong thermal front segments that cross the selected strip during that month were identified and their mean latitudinal position within the region was calculated (Fig. 5.3c).

(d) Each of the front segments was assigned to one of the 0.5° lat-long bins within the strip, based on the mean latitudinal position of the front segment (Fig. 5.3d).

(e) Each bin was then analysed based on (i) whether the bin could be 'clearly viewed' and (ii) the total number of front segments assigned to the bin. A bin was considered to be clearly viewed provided the following criteria were met: the ratio between the total number of clear (cloud free) satellite image pixels within each bin to the total number

of satellite image pixels within each bin was greater than 0.90 (e.g. a bin that is more than 90% clear of cloud obscured pixels). The use of this criteria greatly reduces the influence that spatial and temporal variability in cloud cover may have on estimates of the frequency of occurrence of thermal fronts and is explained in more detail at the end of this section. If a bin could be clearly viewed, this was recorded in an array (clearly viewed + 1, cloud obscured + 0). Provided a bin was clearly viewed, the number of front segments within the bin was also recorded in a separate array (Fig. 5.3e).

(f) Steps b-e were then repeated for all monthly composite SST images and accompanying sets of thermal fronts (e.g. Jan 1982 to Dec 2011). In doing so, the number of front segments in each bin was aggregated into the array described above. This resulted in a 'front-count' histogram, recording the total number of strong frontal segments within each bin, in months when the bin was clearly viewed, over the 30 year period. Using an analogous procedure, a second 'clear-count' histogram was obtained, which records the total number of months each bin was clearly viewed over the 30 year period (Fig. 5.3f).

(g) By dividing the front-count histogram by the clear-count histogram, an estimate of the average frequency of occurrence of thermal fronts (front frequency) is obtained as a function of latitude, within the selected strip (Fig. 5.3g). Several features are apparent in the example histogram centered on 165°E, most notably, the increased frequency of occurrence of thermal fronts southwest of New Zealand (between 47°-50°S).

Seasonal mean (1982-2011) histograms of front frequency were also obtained for each latitudinal strip. The procedure used is analogous to that described above, but using two seasonal subsets of PFV5.2 monthly composite SST images and their associated thermal front detections, with the subsets corresponding to the austral summer (Dec-Jan-Feb, 1982-2011) and austral winter (Jun-Jul-Aug, 1982-2011), respectively.

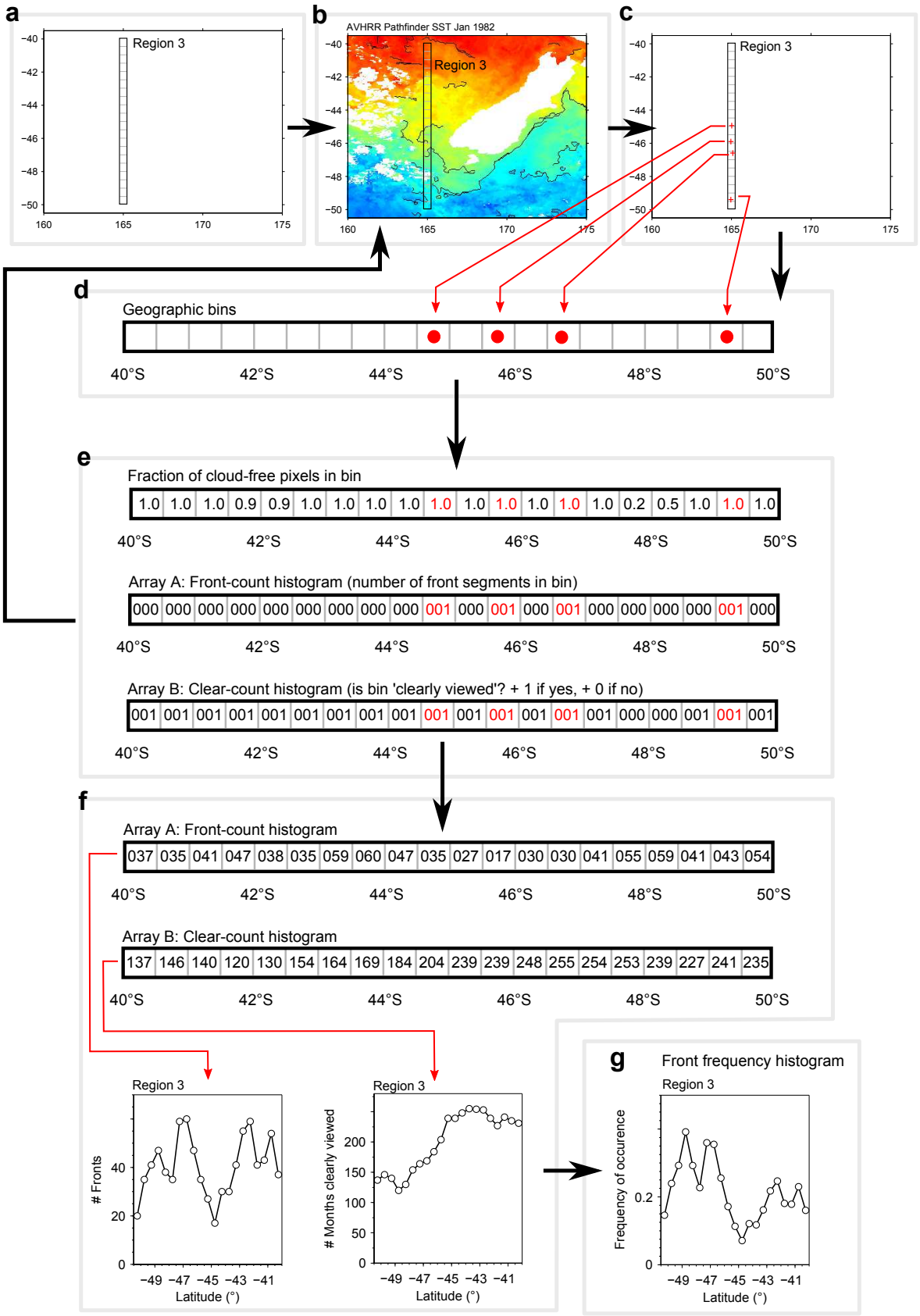

Figure 5.3: Illustration of the procedure used for calculating histograms of the frequency of occurrence of strong thermal fronts. The example given is for Region 3 (Fig. 5.4). See text in Section 5.4.1 for details of each labeled step.

As discussed below (Section 5.5.1), this study focuses in detail on the spatial and seasonal histograms of thermal front occurrence along four particular latitudinal strips, denoted as Region 1-4 (Fig. 5.4). The positions of these strips are bounded by: 40°-50°S and 152.75°-153.25°E (Region 1), 159.75°-160.25°E (Region 2), 164.75°-165.25°E (Region 3) and 167.75°-168.25°E (Region 4). The possibility that thermal fronts were randomly distributed throughout each of these regions, as opposed to occurring preferentially in particular locations, was also tested. The approach used to assess the statistical significance of the frequency of occurrence of thermal fronts in each bin is described in Appendix C.

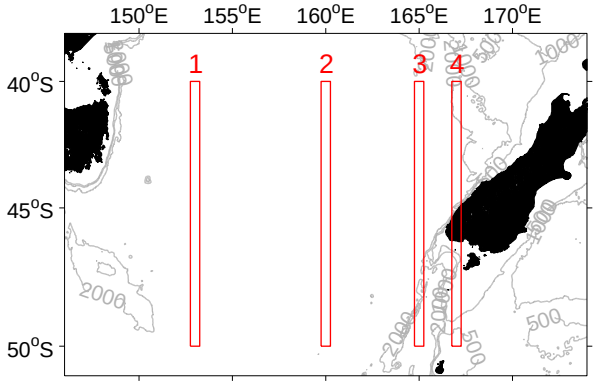

Figure 5.4: Latitudinal strips from which histograms of thermal front occurrence are examined in detail (solid red lines). These strips are referred to as Region 1 (western Tasman Sea), Region 2 (central Tasman Sea), Region 3 (eastern Tasman Sea) and Region 4 (southern New Zealand).

Before concluding this section, some brief comments on the use of largely cloud-free observations for generating the histograms of front frequency are necessary. Firstly, the detection of thermal fronts in an infrared SST image using the SIED is conditional on thermal fronts not being obscured by cloud (Cayula and Cornillon, 1992; Ullman and Cornillon, 1999). Secondly, due to the large spatial and temporal variability in cloudiness over the Tasman Sea (Uddstrom and Oien, 1999), the number of front segments that are observed in a particular bin will be strongly related to variability in cloud cover within that bin. Because the spatial and temporal variability in cloud cover will differ between bins, comparisons of front-counts between bins are difficult unless the influence of between-bin variability in cloud cover on front occurrences is taken into account.

For these reasons, the front occurrence statistics used in this study were computed using a subset of thermal fronts detected when a bin was largely cloud-free (i.e. when the ratio of clear to cloud-obscured satellite image pixels within each bin exceeded 0.9). The use of this strict criteria helps to greatly reduce the influence that between-bin variability in cloud cover has on estimates of the frequency of occurrence of thermal fronts and thus facilitates a like-for-like comparison of front frequency between bins. Nonetheless, the estimates of the

frequency of occurrence of thermal fronts that are reported here are presumably underestimates of the 'true' rate of front frequency because any remaining cloud obscured pixels in the bins, or surrounding region, will influence the detection of thermal fronts by the SIED and thus bias low the observed front counts.

5.4.2 Analysis of sea surface salinity

Ancillary information about the N-STF and S-STF was developed to investigate the connection between thermal fronts detected in the PFV5.2 monthly composite SST images and the traditional, hydrographic definition of the N-STF and S-STF, which uses surface isohalines (Hamilton, 2006). Monthly estimates of the latitudinal position of the frontal isohalines corresponding to the N-STF and S-STF (Hamilton, 2006) were obtained, using the 27-month sequence of Aquarius remotely sensed SSS data (Section 5.3.4). The latitudinal positions of the frontal isohalines were then aggregated into spatial histograms. These provide estimates of the frequency of occurrence of a particular surface isohaline, corresponding to the N-STF or S-STF, at each grid point along a meridian for the period 2013-2015. The histograms were constructed along the following four meridians: 152.5°E, 159.5°E, 164.5°E and 166.5°E (Fig. 5.5). These meridians correspond to the western borders of the study regions used for examining the histograms of thermal fronts in detail (Fig. 5.4). The surface isohalines examined in this study, together with the procedure used for calculating histograms of their positions, are described below.

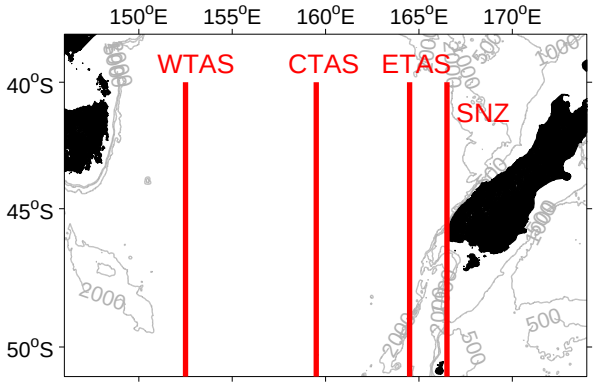

Figure 5.5: Bathymetry of the Tasman Sea with the four meridians along which histograms of the frequency of occurrence of SSS contours corresponding to the N-STF and S-STF were calculated (solid red lines). Meridians are as follows: WTAS, western Tasman Sea (152.5°E); CTAS, central Tasman Sea (159.5°E); ETAS, eastern Tasman Sea (164.5°E); SNZ, southern New Zealand (166.5°E).

This study examines the position of surface isohalines that Hamilton (2006) has previously found to generally coincide with the positions of the N-STF and S-STF in the Tasman Sea. Results and discussion from Hamilton (2006) indicate the surface isohaline that corresponds

to the approximate position of the S-STF (N-STF) changes zonally from 34.9 (35.2) in the western Tasman Sea (near 152°E) to 34.7 (35.1) east of 152-159°E. With this in mind, the position of the following SSS contours, corresponding to the N-STF and S-STF, are examined in this study: in the western Tasman Sea (152.5°E) the position of the 35.2 (N-STF) and 34.9 (S-STF) SSS contours are examined, whilst in the remainder of the Tasman Sea and about southern New Zealand, the position of the 35.1 (N-STF) and 34.7 (S-STF) SSS contours are examined.

The position of the SSS contour corresponding to the N-STF and the S-STF was obtained, along each of the four meridians (Fig. 5.5), on a month-by-month basis, using a four step process:

1. The SSS contour corresponding to a particular front and meridian were specified (e.g. 34.7 for the S-STF on the 164.5°E meridian).

2. The gridded profile of monthly SSS between 30°-60°S along the specified meridian was examined. The following grid points were identified: (i) the southernmost grid point at which the SSS remains above that of the specified SSS contour and (ii) the grid point immediately to the south, where SSS falls below that of the specified SSS contour.

3. The difference between SSS estimates at these grid points and the specified SSS contour was calculated.

4. The position of the SSS contour along the selected meridian was determined by the grid point (of the two above) with the smallest absolute difference relative to the specified SSS contour.

Along each of the four meridians (Fig. 5.5), the positions of the SSS contours identified in this way were aggregated over the full 27 month period. This produced a histogram for each meridian, of the number of months for which the SSS contours corresponding to the N-STF and the S-STF occurred at a particular grid point. Finally, the histograms were divided by the total number of months in the data set (n = 27). This produced four normalized histograms, one for each meridian (Fig. 5.5), showing the frequency of occurrence of the SSS contours corresponding to the N-STF and S-STF at particular grid points.

5.5 Results

This results section is divided into three parts. First, the annual-mean frequency of occurrence of thermal fronts within the Tasman Sea and south of New Zealand is described (Section 5.5.1). Second, the seasonal-mean frequency of occurrence of thermal fronts in these regions is described (Section 5.5.2). Third, the Aquarius SSS data set is used to develop some ancillary information about the spatial and temporal variability of the N-STF and S-STF in these regions (Section 5.5.3).

5.5.1 Spatial variability in thermal front occurrence

The annual-mean histogram of front frequency for the whole Tasman Sea (Fig. 5.6) reveals that thermal fronts are ubiquitous throughout the Tasman Sea; however, they occur more frequently in the western Tasman Sea (west of 160°E), compared to the eastern Tasman Sea. The highest front frequency is found south of New Zealand and along the southeast coast of the South Island, New Zealand, along the path of the Subtropical Front (Fig. 5.1). Examining the spatial histogram (Fig. 5.6) in further detail reveals several 'bands' of locally high front frequency, in the western Tasman Sea (along about i.e. along 153°E near 45°S and 42°S), eastern Tasman Sea (i.e. along 165°E near 49°S and 47°S) and south of New Zealand (i.e. at 167°E near 48°S). No such features are immediately apparent in the central Tasman Sea (i.e. 155-165°E).

Interestingly, the position of these 'bands' of higher front frequency at the borders of the Tasman Sea are similar to the positions of the N-STF and S-STF located by previous studies from hydrographic survey data (e.g. Jeffrey, 1986; Heath, 1985; Butler et al., 1992; Hamilton, 2006; Smith et al., 2013). In the central Tasman Sea, where Hamilton (2006) positioned the N-STF near 42°S and S-STF as lying anywhere between 43°S and 47°S (Fig. 5.1), no similar bands of high front frequency are immediately apparent in Figure 5.6. To study the frontal structure of these areas in more detail, this study next examines histograms of thermal front occurrence along four latitudinal strips, that bisect the western, central and eastern Tasman Sea (Fig. 5.4).

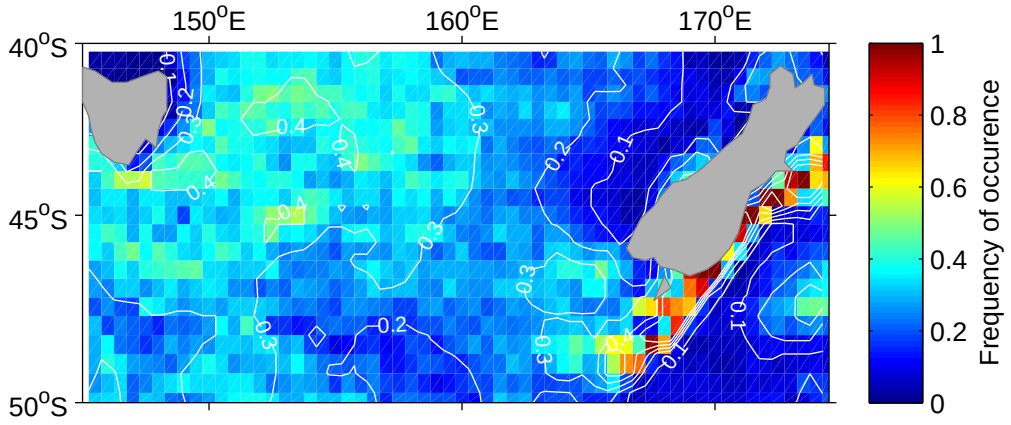

Figure 5.6: Spatial histogram of the annual-mean (1982-2011) frequency of occurrence of strong thermal fronts in the Tasman Sea. Frequency of occurrence is calculated from binning front detections on to a 0.5° lat-long grid (Section 5.4.1).

The long-term mean histogram of front frequency for Region 1 (western Tasman Sea) (Fig. 5.7) reveals that thermal fronts occur more frequently in two particular latitudinal bands. There is an increase in the frequency of occurrence of thermal fronts between about 46°S and 44°S, with a peak in the histogram of front frequency centered near 45°S (front frequency of ~0.5 fronts per month). A second band of increased front frequency is observed further north between about 43° and 41°S, with a histogram peak located around 42°S (front frequency of ~0.45 fronts per month). In both of these latitudinal bands, the maximum front frequency is significantly higher ($p < 0.05$) than the front frequency expected from a random distribution of thermal fronts throughout the region. South of 47°S, the front frequency is relatively stable (c. 0.2-0.3). An examination of the annual mean (1982-2011) SST within this region (Fig. 5.7c) reveals that the two identifiable peaks in the histogram of front frequency, described above, approximately coincide with the latitudinal position of the 12°C and 15°C annual mean SST contour, respectively.

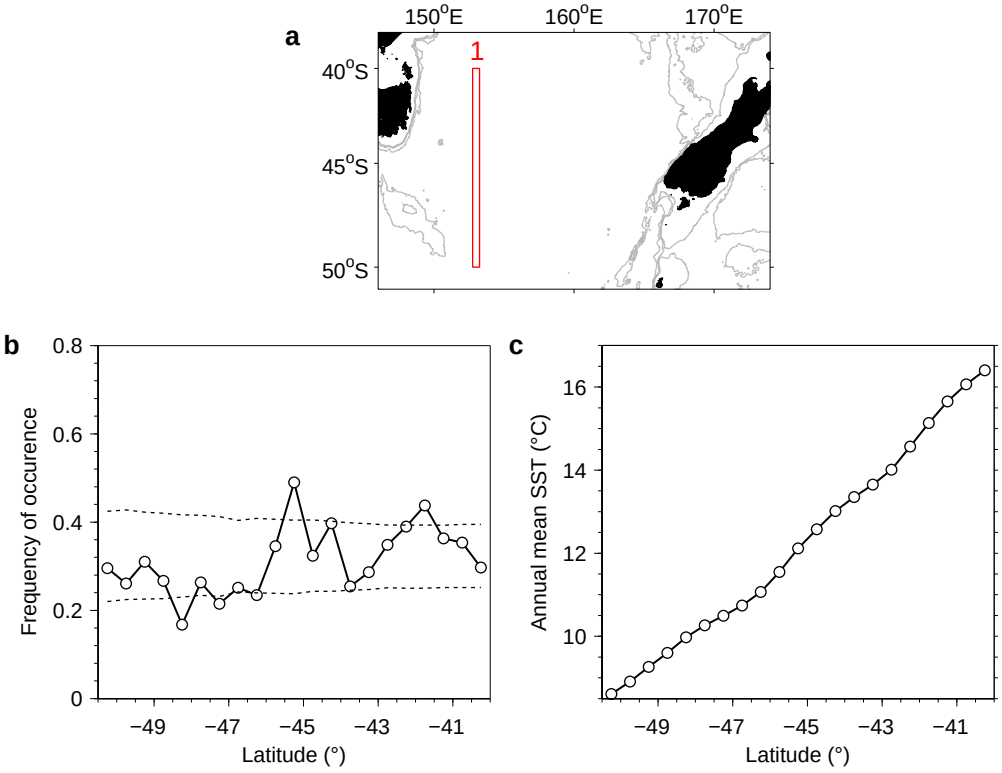

Figure 5.7: (a) Bathymetry of the Tasman Sea with the boundaries of Region 1 (western Tasman Sea) highlighted (red line). (b) Histogram of the annual-mean (1982-2011) frequency of occurrence of strong thermal fronts across Region 1. The dashed lines represent the critical values, outside which the number of thermal fronts found within a bin is significantly different (at the 0.05 level) compared to that which would be expected if the thermal fronts were distributed randomly throughout the bins, in proportion to the number of months each bin was clearly viewed (see Appendix C). (c) Annual mean SST (1982-2011) within each bin across Region 1.

The pattern of occurrence of thermal fronts within Region 2 (central Tasman Sea) (Fig. 5.8), which encompasses waters >4000 m deep in the central Tasman Sea, is noticeably different to that noted in the Region 1 (western Tasman Sea). Although thermal fronts appear to be ubiquitous in this region, there are no well-defined bands of higher or lower frequency in the histogram of front frequency (Fig. 5.8b). The main characteristic of the distribution of thermal fronts in this region is the difference in the front frequency to the north and south of 45°S: thermal fronts occur less frequently (generally < 0.3) south of 45°S, whilst they appear to occur more frequently within a broad region between about 44.5°S and 42°S. In this northern sector, there is a significant peak in the histogram of front frequency near 44°S, but this is much less pronounced than the peaks observed in the histogram of front frequency in the western Tasman Sea (Fig. 5.7).

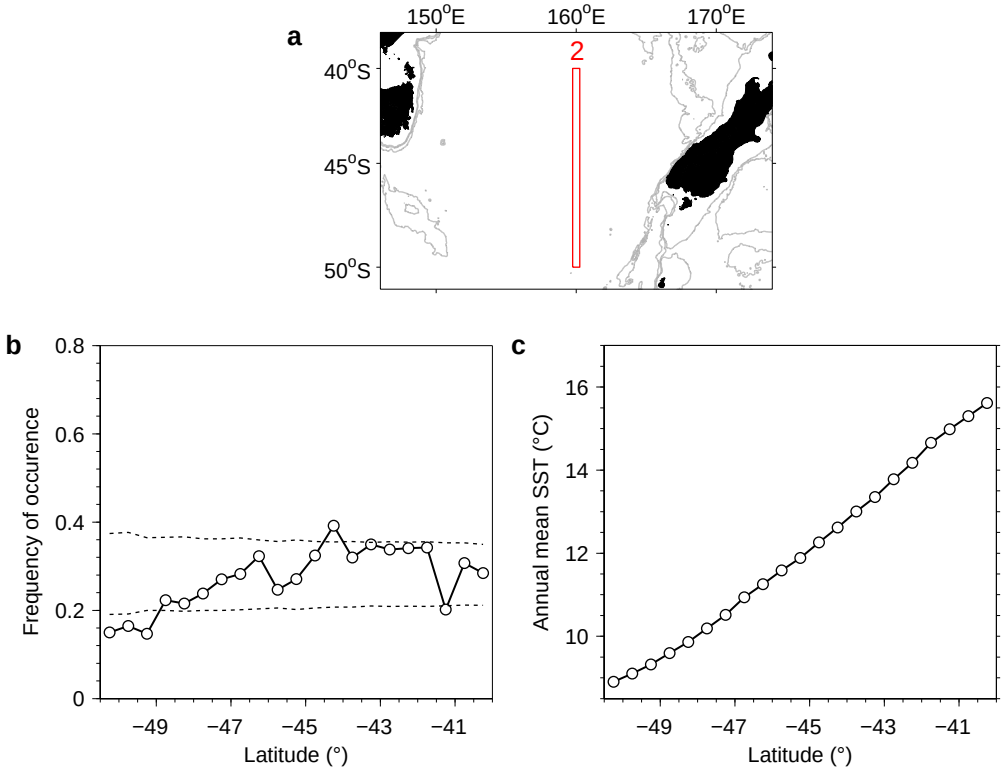

Figure 5.8: Same as Fig. 5.7, for Region 2 (central Tasman Sea).

The spatial variability in the occurrence of thermal fronts in Region 3 (eastern Tasman Sea) is best described by dividing the histogram of front frequency for this region (Fig. 5.9) into two sectors: a northern sector between 40-45°S and a southern sector from 45-50°S. This region encompasses several complex bathymetric features (Fig. 5.9a); water depths exceed 3000 m depth to the west of New Zealand, while, to the southwest of New Zealand, there are a series of shallower bathymetric features including the Puysegur Bank (depths < 500m, 46-47°S) and Macquarie Ridge (a series of seamounts that shallow to <500 m depth near 48.5°S and 49.5°S), together with the deeper and elongated (>2000 m) Solander Trough.

In the northern sector, there appear to be two local maxima in front frequency near 42°S and 41°S, respectively, although neither of these histogram peaks are distinguishable from a random distribution of fronts (Fig. 5.9b). There is a local minima in front frequency near 45°S, which is significantly lower ($p < 0.05$) than that expected from a random distribution of thermal fronts throughout this region (Fig. 5.9b). In the southern sector (e.g. 45-50°S), there are two well-defined latitudinal bands where thermal fronts appear to occur more frequently. This results in a bimodal pattern in the histogram of front frequency (Fig. 5.9b). The first of these bands is observed between about 46-48°S and is centered west of the Puysegur Bank (c. 47°S. 166°E) in water depths exceeding 2000 m (Fig. 5.9a). The second band,

located between about 48-50°S, is centered near, or lies immediately east of, a series of seamounts along the Macquarie Ridge, in water depths of between 500 and 2000 m (Fig. 5.9a). Examination of the histogram of front frequency for this region (Fig. 5.9b) shows that the maxima in front frequency within these bands, which are located near 47°S and 49°S respectively, are both significantly higher ($p < 0.05$) than the front frequency expected from a random distribution of fronts. These two histogram peaks are centered on the approximate latitudinal position of the 12°C and 10.5°C annual-mean isotherms, respectively (Fig. 5.9c).

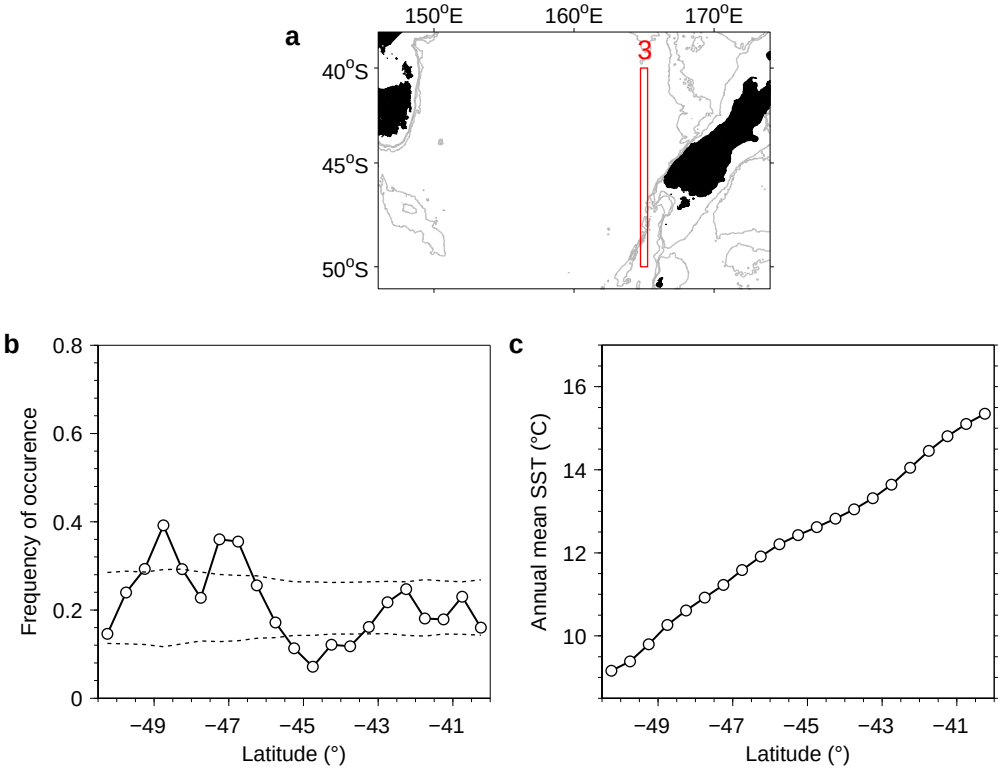

Figure 5.9: Same as Fig. 5.7, for Region 3 (eastern Tasman Sea).

The histogram of front frequency from Region 4 (Fig. 5.10b) shows similarities to that described for Region 3 (eastern Tasman Sea). Region 4 encompasses a sector of the south-west Pacific that consists of complex bathymetry, with seafloor depths exceeding 1000 m over the region poleward of the Challenger Plateau and, after crossing South Island, New Zealand (45-46°S), an area of sharply defined bathymetry south of New Zealand (47-50°S) (Fig. 5.10a). The most prominent features of the distribution of fronts within this region are two latitudinal bands south of New Zealand, where thermal fronts appear to occur more frequently (Fig. 5.10b). The first of these bands can be identified from a sharply defined peak in the histogram of front frequency between 47°S and 48°S, located in a region of relatively shallow (< 200-300 m) and flat bathymetry over the Snares Shelf (Fig. 5.10a). The second

band is evident from a peak in the front frequency histogram identifiable immediately to the south, located between about 48-49.5°S along the upper continental slope (200-500 m slope), in the Snares Depression (49°S). The maximum front frequency within both these latitudinal bands is significantly greater ($p < 0.05$) than that for a random distribution of thermal fronts throughout Region 4. An examination of the annual mean (1982-2011) SST within the region (Fig. 5.10c) shows the band of thermal fronts centered around 47.5°S (49°S) coincides with the 11.7°C (10.3°C) surface isotherm. The pattern of occurrence of thermal fronts to the north of the South Island, New Zealand is comparable to the pattern observed over similar latitudinal bounds in Region 3; front frequency is uniformly low between 43-45°S (front frequency <0.2), with a small increase north of 43°S (front frequency ~0.2).

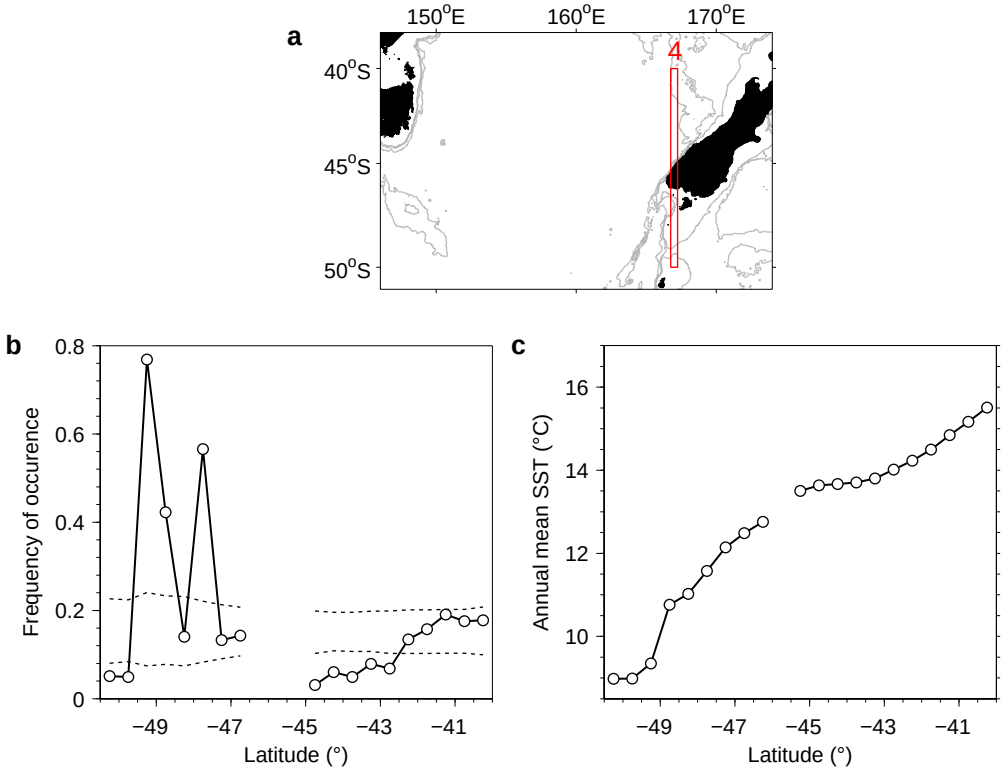

Figure 5.10: Same as Fig. 5.7, for Region 4 (southern New Zealand).

The sensitivity of the patterns of annual-mean (1982-2011) thermal front occurrence (Fig. 5.7-5.10) with respect to the definition of a strong, thermal front was also tested (Appendix D), though this revealed that the threshold chosen to define a strong thermal front had little influence on the results obtained.

A note of caution is due here since this study has examined "fronts" detected in monthly composites of SST images (Section 5.3.1). It is possible that some of these "fronts" are detections of artefacts of the monthly compositing process (see e.g. Section 4.2.5). As a

result, it is also possible that some of the "peaks" observed in the patterns of thermal front occurrence above are caused by repeated detections of image compositing artefacts, rather than real oceanographic signals; however, there are several reasons to suspect this is unlikely to be the case. Like the present study, two previous studies have also analysed long-term patterns of thermal front occurrence in the Tasman Sea (Belkin and Cornillon, 2003; Morato et al., 2016). In contrast to the present study, both of these earlier studies examined "fronts" detected in daily SST "snapshots". These data are not subject to any compositing. The results presented in these earlier studies also show "peaks" in the long-term occurrence of thermal fronts at very similar latitudes to those described above, in the western Tasman Sea, eastern Tasman Sea and south of New Zealand (see e.g. Fig. 1 and Fig. 4 in Belkin and Cornillon (2003) and Fig. 1 in Morato et al., 2016). In addition, there is a strong indication of frequently occurring SST fronts in the Tasman Sea at the same latitudes and longitudes to those reported above in a recent analysis of the gradient of annual mean SST (1999-2009) over the Southern Ocean by Graham and De Boer (2013) (see Fig. 3 in Graham and De Boer, 2013). The fact that these previous studies were conducted on different data sets, which are not susceptible to the same image compositing artefacts described here (Section 4.2.5), and identify similar features to those observed here, suggests that the "peaks" that are observed here in the patterns of thermal front occurrence (this Section) are more likely to be real oceanographic signals, than artefacts of monthly compositing.

5.5.2 Seasonal variability in thermal front occurrence

In the previous section, the 30 year data set (1982-2011) of thermal front detection allowed a detailed examination of the spatial variability in the occurrence of thermal fronts within three regions of the Tasman Sea and one region south of New Zealand. In this section, the thermal front detections are aggregated into seasonal histograms of front frequency. These seasonal histograms are used to describe the seasonal variability of occurrence of thermal fronts in the same four regions of the Tasman Sea (Fig. 5.4). The focus is on the patterns of thermal front frequency present during the austral summer (Dec-Jan-Feb) and winter (Jun-Jul-Aug) seasons.

The seasonal variability in the occurrence of thermal fronts within regions 1-4 (Fig. 5.4) is illustrated in Figure 5.11, using histograms of the seasonal mean (1982-2011) front frequency. Also shown for reference in this figure are the histograms of the annual-mean (1982-2011) front frequency across each region. These seasonal histograms show a couple of noteworthy aspects. First, in Regions 1, 3 and 4, the patterns of front occurrence for the austral summer and winter (Fig. 5.11) are remarkably consistent with those observed for the year as a whole (Fig. 5.7-5.10). From examining the annual mean histograms of front frequency (Section 5.5.1), it was observed that thermal fronts appear to occur more frequently around

42.5°S and 45.5°S in Region 1 (Fig. 5.7b), around 47.5°S and 49.5°S in Region 3 (Fig. 5.9b) and around 47.5°S and 49.5°S in Region 4 (Fig. 5.10b), and a similar distribution of thermal fronts appears to be present in these areas when inspecting the seasonal mean histograms of front frequency (Fig. 5.11a, c-d). Region 2 is the exception to this. In Region 2, there is little consistency between the patterns of annual mean and seasonal mean front frequency; thermal fronts seem to occur more frequently in several scattered locations during the austral summer (e.g. near 46.5°S, 44.5°S, 43°S, 41.5°S) compared to during the austral winter (Fig. 5.11b) or for the year as a whole (Fig. 5.8b).

A second feature to note is that in Regions 1, 3 and 4, the latitudes at which thermal fronts occur most frequently are similar during the austral summer and winter (Fig. 5.11a, c, d). For example, in Region 1 (western Tasman Sea), there appears to be a band of higher front frequency centered around 45°S during both seasons (Fig. 5.11a). Likewise, in Region 4 (eastern Tasman Sea and south of New Zealand), there seem to be two bands of higher front frequency centered on 47.5°S and 49.5°S during the austral summer and winter, respectively (Fig. 5.11d). In Region 3, there seems to be a small seasonal migration in the latitudes at which thermal fronts occur more frequently; the peak in the histogram of front frequency observed near 47°S (49°S) during the austral summer seems to shift northward (southward) by about 0.5° (1.0°S) to nearer 46.5°S (50°S) in austral winter (Fig. 5.11c). It is also noteworthy that at most the locations noted above, the seasonal-mean front frequencies are significantly higher ($p < 0.05$) than would be expected if the thermal fronts were distributed randomly throughout each region. The exception to this is in Region 3; during the austral winter, the peak in the histogram of front frequency near 49°S does not quite meet the criteria set for being considered significant when compared to a random distribution of thermal fronts throughout the region (Fig. 5.11c).

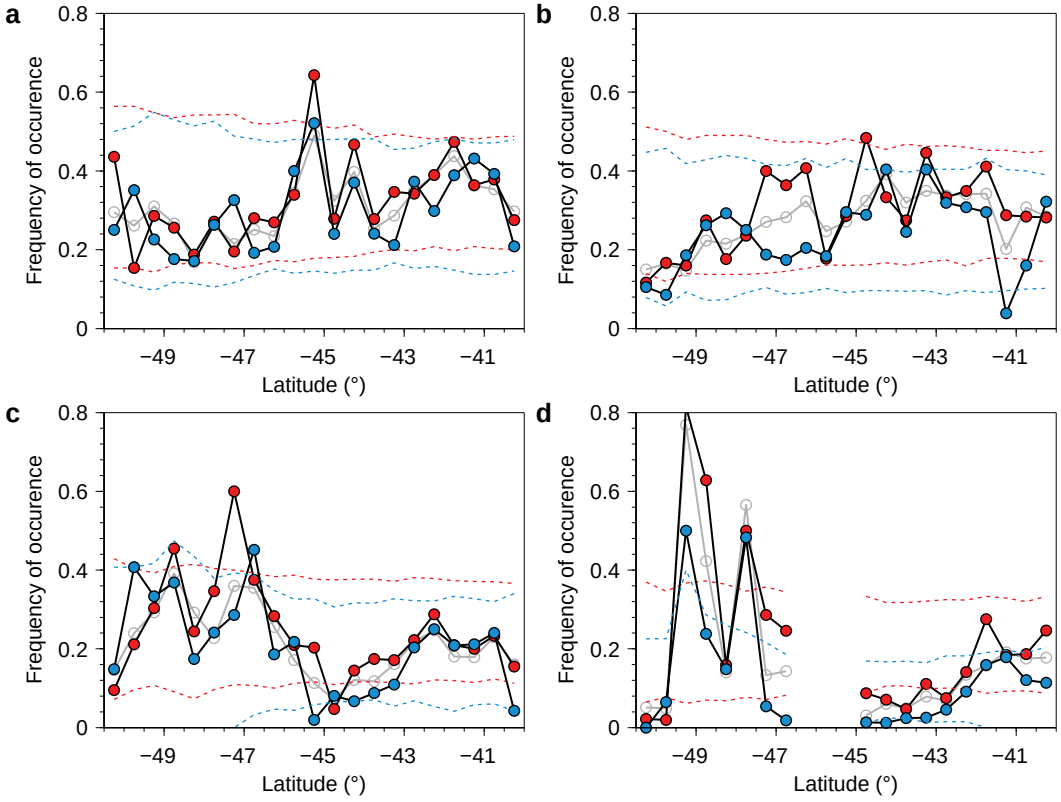

Figure 5.11: Histograms of the seasonal-mean (1982-2011) frequency of occurrence of strong thermal fronts across (a) Region 1 (western Tasman Sea), (b) Region 2 (central Tasman Sea), (c) Region 3 (eastern Tasman Sea) and (d) Region 4 (southern New Zealand) for the austral summer (Dec-Jan-Feb) (red) and austral winter (Jun-Jul-Aug) (blue). The dashed lines represent the critical values, outside which the number of thermal fronts found within a bin is significantly different (at the 0.05 level), compared to that which would be expected if the thermal fronts were distributed randomly throughout the bins, in proportion to the number of months each bin was clearly viewed (see Appendix C). Also shown for reference are the histograms of the annual-mean (1982-2011) front frequency across each region (grey) (Fig. 5.7-5.10).

5.5.3 Analysis of SSS contours

In this section, the 27-month sequence (2013-2015) of monthly Aquarius remotely sensed SSS images (Section 5.3.4) is used to develop ancillary information about the spatial and temporal variability of the N-STF and S-STF. This information will be used to interpret the thermal fronts in terms of the traditional, isohaline-based definitions of the N-STF and S-STF.

Figure 5.12 shows histograms of the frequency of occurrence of the SSS contours corresponding to the N-STF and S-STF along four meridians in the southwest Pacific (Fig. 5.5). For reference, the 27-month mean location (2013-2015) of each SSS contour is also shown.

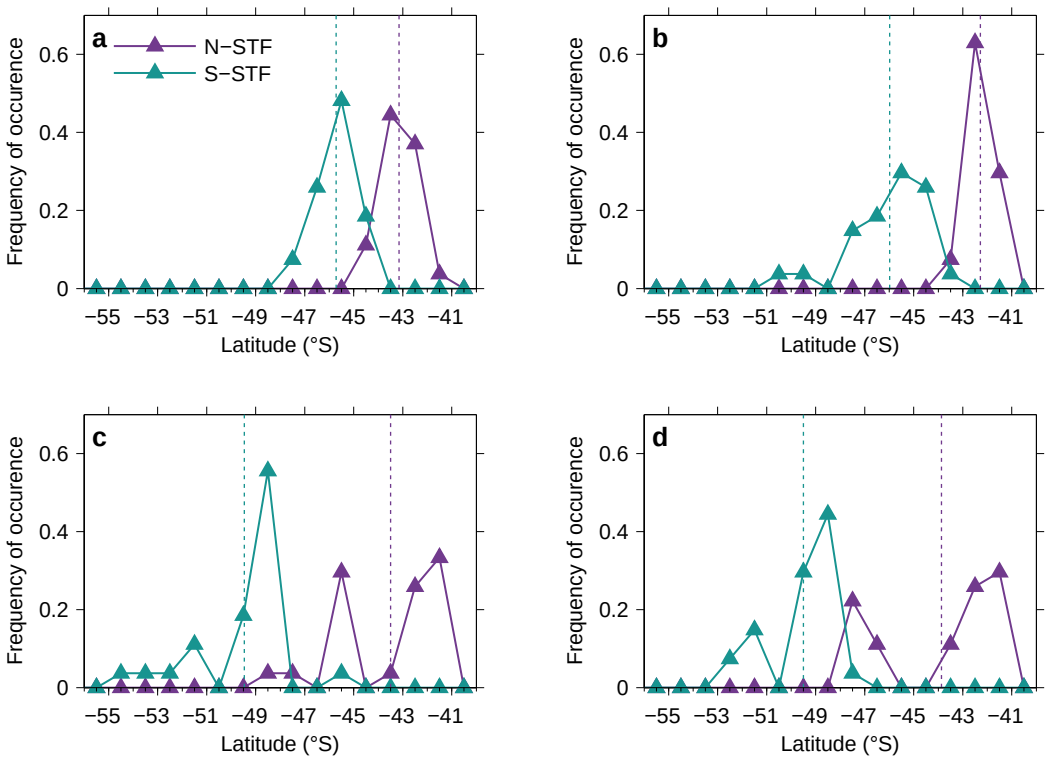

Figure 5.12: Histograms of the 27-month mean (2013-2015) frequency of occurrence of the SSS contour corresponding to the N-STF (purple) and S-STF (green), derived from the Aquarius SSS data, at latitudinal grid points along the (a) 152.5°E, (b) 159.5°E, (c) 164.5°E and (d) 167.5°E meridians (Fig. 5.5). Also shown are the 27-month mean position of the SSS contours corresponding to the N-STF and S-STF along each meridian (dashed lines). The analysis procedure used to calculate these histograms is described in Section 5.4.2.

There are two noteworthy aspects of these histograms. First, the mean positions of the SSS contours corresponding to the N-STF and S-STF are similar to the frontal positions obtained by Hamilton (2006) using a composite of hydrographic survey data (Fig. 5.1). These lay out the general positions of the N-STF and S-STF over the Tasman Sea for the 2013-2015 period. The mean positions of the SSS contour corresponding to the N-STF (Fig. 5.12a-d) suggest that the Front migrates northward from around 43°S in the western Tasman Sea (Fig. 5.12a) to nearer 42°S in the central Tasman Sea (Fig. 5.12b). The SSS contour corresponding to the N-STF then trends southeast to near 44°S approaching New Zealand (Fig. 5.12c). The mean positions of the SSS contour associated with the S-STF (blue lines in Fig. 5.12a-d) place the front near 45.5°S in the western and central Tasman Sea (Fig. 5.12a-b), with the S-STF then migrating poleward toward 49.5°S in the eastern Tasman Sea and around southern New Zealand (Fig. 5.12c-d), where it lies approximately 1.5° poleward of the general location of the S-STF inferred by Hamilton (2006).

The second feature of these histograms is that the distribution of occurrences of the SSS

contours corresponding to the N-STF and S-STF appear to cluster around particular latitudinal positions. In the case of the SSS contours corresponding to the S-STF (blue lines in Fig. 5.12a-d), each histogram appears to have a single, sharply defined 'peak' in the frequency of occurrence, which represents the modal latitudinal position for the frontal SSS contour. In the western Tasman Sea, occurrences of the SSS contour corresponding with the S-STF are spread among grid points between 43.5-49.5°S and most frequently occur at 45.5°S (Fig. 5.12a). In the central Tasman Sea, the distribution of positions of the SSS contour corresponding to the S-STF has a mode near 44.5°S (Fig. 5.12b), which shifts poleward to 48.5°S in the eastern Tasman Sea (Fig. 5.12c) and is also located at 48.5°S south of New Zealand (Fig. 5.12d). The histograms of the frequency of occurrences of the SSS contour corresponding to the N-STF (Fig. 5.12a-d) show similar characteristics, but these histograms can be separated into two sets. Those in the western and central Tasman Sea are characterized by a unimodal distribution (Fig. 5.12a-b), with a band of occurrences of the frontal SSS contour clustered around a single histogram peak centered near 42-43°S. In contrast, in the eastern Tasman Sea and around southern New Zealand, the histograms show a bimodal distribution (Fig. 5.12c-d). In these regions, occurrences of the frontal SSS contour are clustered around two histogram peaks that have a similar frequency of occurrence: in the eastern Tasman Sea (164°E) these peaks are located near 41.5°S and 45.5°S (Fig. 5.12c) and south of New Zealand (167°E), are located near 41.5 °S and near 47.5 °S (Fig. 5.12d).

Occurrences of the SSS contour corresponding to the N-STF (35.1) near 45.5-47.5°S both in the eastern Tasman Sea (Fig. 5.12c) and south of New Zealand (Fig. 5.12d) are somewhat unexpected. Heath (1985) shows the SSS distribution west and south of New Zealand from a composite of hydrographic data collected between 1963 and 1971. This SSS map indicates a surfacing of the 35.1 isohaline north of 43-44°S in the eastern Tasman Sea, with the 35.1 SSS contour not passing south of New Zealand. A similar position for the 35.1 SSS contour is also seen in hydrographic sections in the eastern Tasman Sea (Deacon, 1937; Heath, 1981; Jeffrey, 1986; Stanton and Ridgway, 1988; Szymanska and Tomczak, 1994). The discrepancy between the Aquarius data and hydrographic data suggests there is likely to be a positive bias in the Aquarius SSS data immediately south of New Zealand, and that occurrences of the 35.1 SSS contour near 45-47S°S based on the Aquarius data are likely an artifact of this positive bias.

To examine this positive bias further, a crude comparison was carried out in this region between a mean SSS field calculated from the Aquarius SSS data and data from several hydrographic surveys. At a grid point centered on 47.5°S, 164.5°E, the 27-month (2013-2015) mean SSS from the Aquarius data is ~35.0. This value is ~0.3 saltier than the results from several hydrographic surveys near this position, taken at different times of year, and which consistently show SSS of ~34.7 or less (Heath, 1981; 1985; Jeffrey, 1986; Butler et

al., 1992; Morris et al., 2001; **Chapter 3**). At grid points to the north and to the east of 47.5°S, 164.5°E (e.g. closer to the coastline), mean SSS values were found to be between 34.9-35.5 from Aquarius, which also seem anomalously high compared to the historical hydrographic data measurements south of New Zealand. To the south and west of 47.5°S, 164.5°E, the 27-month mean SSS values from the Aquarius data set, between 40-50°S, are much closer to those of the historical hydrographic data collected at comparable latitudes and would appear more realistic.

5.6 Discussion

5.6.1 Histogram comparisons

The next step of this analysis is to try and understand whether any of the strong thermal fronts identified in the remotely sensed SST images are likely to be surface expressions of the N-STF or S-STF. To do so, qualitative comparisons are performed in this section between the annual-mean histograms of the frequency of occurrence of (1) thermal fronts (Section 5.5.1) and (2) SSS contours corresponding to the N-STF and S-STF (Section 5.5.3). This provides a comparison between the thermal fronts that have been detected and the traditional, hydrographic definitions of the N-STF and S-STF.

It can now be seen that the patterns of occurrence of (1) thermal fronts and (2) the SSS contours corresponding to the S-STF, exhibit several similar characteristics. These characteristics are clearly seen by comparing the histograms of annual-mean thermal front frequency (Fig. 5.7-5.10) with the histograms of 27-month mean (2013-2015) frequency of occurrence of the SSS contour corresponding to the S-STF (Fig. 5.12). For clarity, these histograms are reproduced together in Fig. 5.13. First, note that in each of the four regions, thermal fronts occur within the latitudinal bands where the SSS contour corresponding to the S-STF also occurs. Second, both the thermal fronts and the SSS contour corresponding to the S-STF appear to occur more frequently around particular latitudinal positions. This is indicated by peaks in the histograms of the frequency of occurrence of thermal fronts and frontal SSS contours. Third, in Regions 1, 3 and 4 (Fig. 5.4), there is good qualitative agreement in the locations where (1) thermal fronts and (2) the SSS contour corresponding to the S-STF occur more frequently (Fig. 5.13, a, c-d). For example, in Region 3 (eastern Tasman Sea, Fig. 5.4) the SSS contour corresponding to the S-STF occurs most frequently near 48.5°S and the distribution of thermal fronts show a qualitatively similar pattern, with thermal fronts occurring more frequently around 48.75°S (Fig. 5.13c). In these regions there is also a similar decrease in the frequency of occurrence of thermal fronts and the S-STF frontal SSS contour around these histogram peaks; that is, both histograms of frequency of occurrence

have a similar shape. In Region 2 (central Tasman Sea), there is little qualitative agreement between the frequency of occurrences of strong, thermal fronts, which occur with a similar frequency throughout the region, and occurrences of the SSS contour corresponding to the S-STF, which form a histogram centered around a modal location of 45.5°S (Fig. 5.13b).

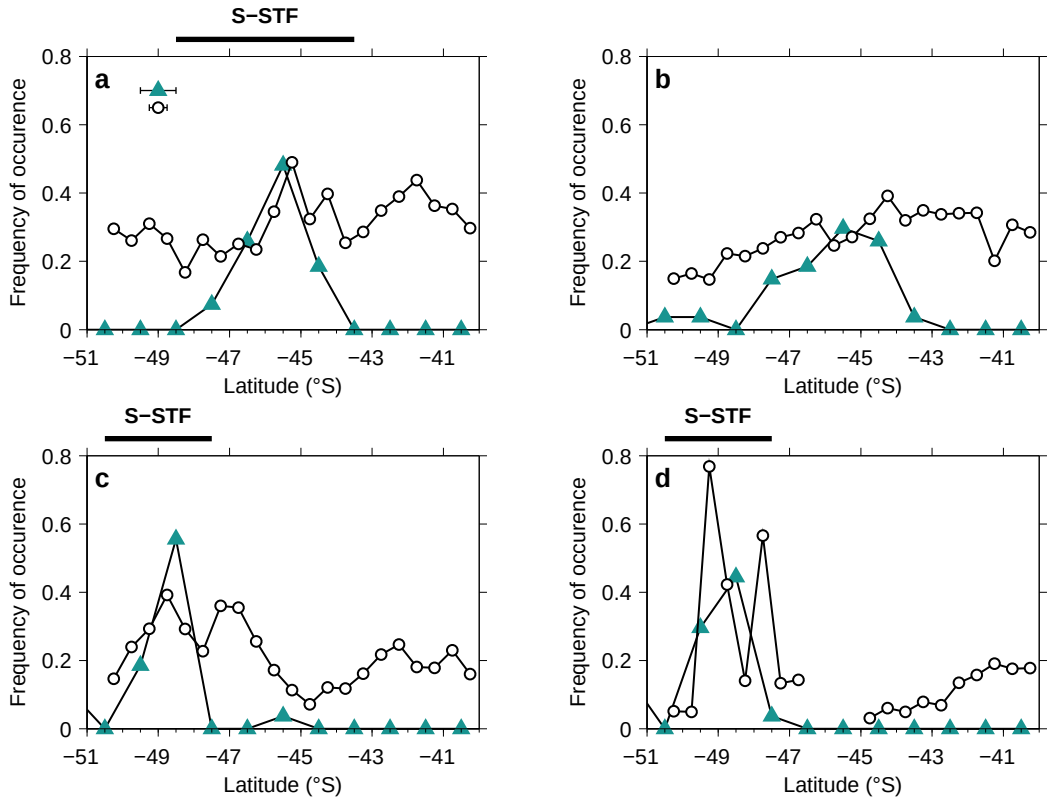

Figure 5.13: Reproduction of panel b in Fig. 5.7-5.10: Histograms of annual-mean (1982-2011) frequency of occurrence of strong, thermal fronts (black solid line), detected in PFV5.2 monthly composite SST images, for (a) Region 1, (b) Region 2, (c) Region 3 and (d) Region 4 over the southwest Pacific (Fig. 5.4). For comparative purposes, over plotted is a reproduction of Fig. 5.12: Histograms of the annual-mean (2013-2015) frequency of occurrence of the salinity indicator of the S-STF, derived from the Aquarius SSS data, along (a) 152.5°E, (b) 159.5°E, (c) 164.5°E and (d) 167.5°E (green solid line). Note that the longitudinal position of each SSS histogram approximately corresponds to the western edge of each of the regions used to calculate the thermal front histograms (Fig. 5.4-5.5). The resolution of the grid spacing for the SST data (black) and SSS data (green) is indicated by the horizontal error bars in the top left of panel a. The locations of thermal fronts likely to be surface expressions of the S-STF, as inferred in the text, are highlighted by black horizontal lines.

The frequency of occurrence of thermal fronts and the SSS contour corresponding to the N-STF are compared in Fig. 5.14. There is little qualitative agreement in the Tasman Sea between the respective patterns of frequency of occurrence. In the western and central Tasman Sea, thermal fronts occur within the distribution of N-STF locations, but there are no coherent peaks in the frequency of occurrence of thermal fronts and the N-STF frontal SSS contour (Fig. 5.14 a-b). In the eastern Tasman Sea, strong, thermal fronts also co-occur within the distribution of locations of the N-STF frontal SSS contour and there is a some-

what similar pattern in their respective frequency of occurrences between about 41S-44°S (Fig. 5.14 c-d). Around southern New Zealand, strong, thermal fronts co-occur within the distribution of locations of the N-STF frontal SSS contour and both occur more frequently over the Snares Shelf near 47.5°S (Fig. 5.14d); however, as discussed in Section 5.5.3, occurrences of the SSS contour corresponding to the N-STF south of New Zealand (35.1) are somewhat suspect, given the apparent positive bias in the Aquarius SSS data in this region.

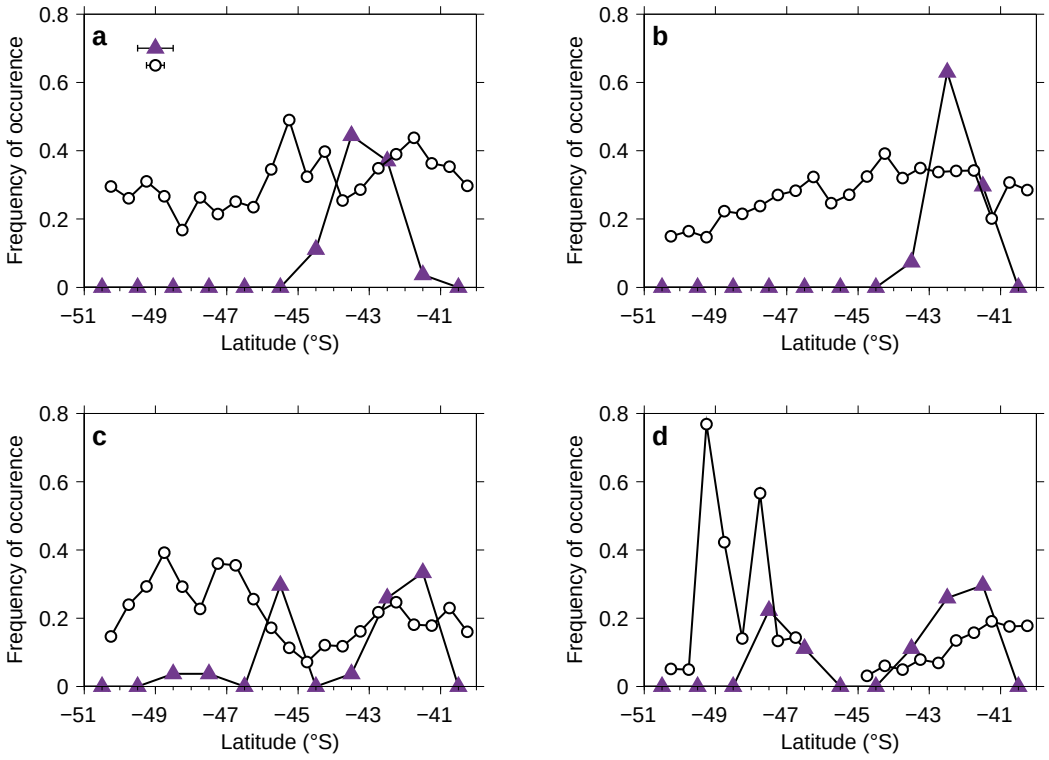

Figure 5.14: Same as Fig. 5.13, for the N-STF (purple solid line).

5.6.2 Can surface expressions of the STFs be identified in the thermal front distributions?

So, what do these comparisons potentially tell us about whether surface expressions of the N-STF or S-STF in the Tasman Sea can be identified from the thermal front distributions? The analyses of thermal fronts detected in the PFV5.2 monthly composite SST images (Section 5.5.1) describe variability in the occurrence of thermal fronts for a 30 year time period (1982-2011) over four regions of the Tasman Sea. The analyses of the Aquarius satellite SSS product (Section 5.5.3) describe variability in the position of the N-STF and S-STF within a more limited 27-month time period (2013-2015) in these same areas. Although these two analyses span different time periods, the results presented in Figure 5.13 reveal strong qual-

itative agreement between the spatial patterns of occurrence of thermal fronts and the SSS contour corresponding to the S-STF. This agreement is apparent in three sectors of the south-west Pacific: in the western Tasman Sea between approximately 43.5-48.5°S (Fig. 5.13a), in the eastern Tasman Sea, between approximately 47.5-50.5°S (Fig. 5.13c) and about southern New Zealand, between approximately 47.5-50.5°S (Fig. 5.13d). In other words, the patterns of occurrence of thermal fronts observed across these latitudinal bands, within Regions 1, 3 and 4, appear to reflect those of the temporal variability in the position of the S-STF, as inferred using contours of SSS. This qualitative agreement strongly suggests that the strong, thermal fronts detected within these latitudinal bands, highlighted subjectively in Fig 4.11, are likely to be surface expressions of the S-STF.

In contrast, surface expressions of the S-STF in the central Tasman Sea are not readily identifiable from the analyses conducted here; patterns of occurrence of thermal fronts and the surface isohaline corresponding to the S-STF show poor qualitative agreement in this region (Fig. 5.13b). The same is true of surface expressions of the N-STF in the Tasman Sea; there is little qualitative agreement between the frequency of occurrence of thermal fronts and the SSS contour corresponding to the N-STF in any of the four study regions (Fig. 5.14). This implies either that the N-STF and S-STF lack a strong (i.e. SST gradient magnitude > 2.5°C 100 km^{-1}) surface thermal signature in these regions, or that there are shortcomings in the approach taken here that prevent these surface thermal signatures from being identified. A high-resolution hydrographic survey of N-STF and S-STF in the Tasman Sea based on a towed CTD system (SeaSoar), similar to that undertaken by James et al. (2002) in the SE Indian Ocean, could provide further insight characteristics of surface expressions of the N-STF and S-STF in these regions, but is beyond the scope of the current study.

Given the results discussed above, it seems reasonable to infer that the thermal fronts detected within the latitudinal bands highlighted in Fig. 4.13 are surface expressions of the S-STF. There is, like other works that seek to observe surface expressions of the N-STF and S-STF in satellite SST imagery (e.g. Uddstrom and Oien, 1999; Belkin and Cornillon, 2003; Burls and Reason, 2006; Graham and de Boer, 2013), a limitation in that although the thermal fronts that have been identified are likely to be surface expressions of the S-STF, it is not possible to say whether every one of these fronts is a surface expression of the S-STF. This study examined histograms of the frequency of occurrence of (1) thermal fronts and of (2) SSS contours corresponding to the historical definitions of the N-STF and S-STF. So, though likely, this study cannot be 100% confident that *all* the thermal fronts identified within the latitudinal bands highlighted in Fig. 4.13 are surface expressions of the S-STF. Some maybe the surface expressions of other oceanographic features that are independent of the S-STF, yet have a pattern of occurrence that is similar to that of the SSS contour corresponding to the historical definition of the S-STF.

One alternative possibility is that the peaks in the histograms of the frequency of occurrence of thermal fronts result from detecting the edges of mesoscale eddies, rather than the S-STF, in the southwest Pacific. In a recent study, Buckingham et al. (2014) identified zonally-elongated bands of repeated thermal fronts (e.g. 'peaks' in frontal occurrence, somewhat similar to those observed here) throughout the subtropics, using 10 years (2002-2011) of remotely sensed SST images. Evidence suggests that these so-called 'quasi-zonal striations' arise at the interface between pairs of propagating mesoscale eddies (Schlax and Chelton, 2008; Buckingham et al., 2014). With the data in hand, there is not enough information to say whether or not these mesoscale eddies exist along the S-STF in the Tasman Sea, and therefore, might contribute to the patterns of thermal front occurrence observed in the present study.

This study could be more confident about the association between each individual thermal front and the S-STF with extra salinity information: in particular, the axial-isohaline of individual thermal fronts. However, the in-situ or remotely sensed salinity SSS data that would be required to go into the PFV5.2 monthly composite SST images and attempt to identify the temperature expressions of the S-STF is not available pre-2013. The remotely sensed SSS data that is available post-2013 has too coarser spatial resolution to attempt to associate thermal fronts detected in remotely sensed SST images with the S-STF on a one to one basis. Such a one-to-one comparison is not feasible with the current generation of remotely sensed SSS products. In the future, coincident remotely sensed SST and SSS data, with comparable spatial resolution, would help circumvent this limitation.

One further question that remains is how the surface expressions of the S-STF that are identified here are produced. According to Tomczack et al. (2004), the STF may produce thermal fronts at the sea surface through at least two mechanisms. Outside of the summer months, the STF can reach through the mixed layer to the surface, resulting in a surface thermal front (Fig. 5.15a). In contrast, during the summer months, the STF can become isolated from the sea surface by a shallow (< 50 m), warm mixed layer (Fig. 5.15b). Summer observations of the STF south of Australia (James et al., 2002) show that surface temperature fronts, at a higher temperature but the same salinity, are often evident above the subsurface expression of the STF, which remains unchanged (i.e. the conditions in Fig. 5.15b). It is thought that these surface temperature fronts are produced via heating of the mixed layer overlying the STF (Tomczack et al., 2004) and subsequent entrainment of water into the mixed layer from the warm and cold sides of the STF below (James et al., 2002). In these summer conditions, the surface front is a consequence of the deeper expression of the STF, rather than an outcropping of the STF. As the present study is limited to examining surface observations, it is not possible to say which of these two types of surface expression might have been detected; however, given that the satellite SST data analysed here are spread

throughout the year, it seems likely that it is some mixture of the two. In future work, high-resolution hydrographic surveys across the S-STF in multiple seasons could be used to better understand the nature of the front's surface expressions, and their connection to the front's deeper expression (see e.g. James et al., 2002).

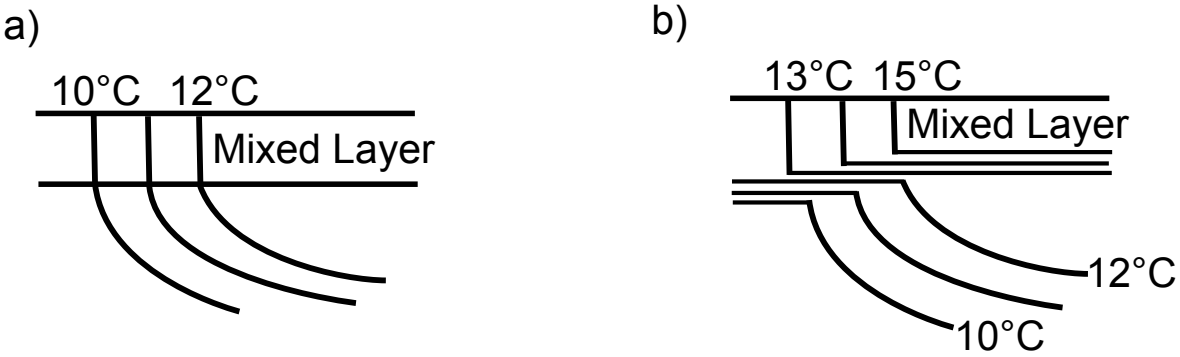

Figure 5.15: Sketch of TS-diagrams and coupling between the surface and sub-surface expressions of the STF south of Australia during (a) winter and (b) summer. Adapted from Tomczack et al. (2004).

In summary, it is possible that not all of the thermal fronts detected in this study, within the latitudinal bands highlighted in Fig. 5.13, are surface expressions of the S-STF; collectively, however, their locations and the spatial patterns in their frequency of occurrence are consistent with those found for the SSS contours historically associated with the S-STF. Thus, for the remainder of this discussion, the thermal fronts detected within the latitudinal bands highlighted in Fig. 5.13 are interpreted as being surface expressions of the S-STF.

5.6.3 Modal positions of the S-STF in the Tasman Sea

Several most-frequent positions for the surface expressions of the S-STF are apparent in Fig. 5.13. In the western Tasman Sea, the surface expressions of the S-STF seem to occur most frequently in the bin positioned between 45.0-45.5°S (Fig. 5.13a). In the eastern Tasman Sea (at 165°E), it is apparent that the surface expressions of the S-STF shift poleward and occur most frequently in the bin located between 48.5-49.0°S (Fig. 5.13c). A similar situation is apparent south of New Zealand, where the surface expressions of the S-STF seem to occur most frequently in the bin between 48.5-49.0°S (Fig. 5.13d).

The most frequent positions of the surface expressions of the S-STF during the period 1982-2011 can be compared with the climatological maps of the S-STF in the southwest Pacific produced in earlier studies. Figure 5.1 shows the climatological location of the STF as found by Heath (1981; 1985) and the S-STF identified by Hamilton (2006), based on composites of hydrographic survey data. In the western Tasman Sea (153°E) and south of New Zealand (167°E), results from the present study corroborate these earlier interpretations

of the general position of the S-STF. Surface expressions of the S-STF in these regions are found to occur most frequently at grid point between 45-45.5°S and 48.5-49.0°S, respectively (Fig. 5.13), much like the climatological positions of the STF found by Heath (1981; 1985) and the S-STF by Hamilton (2006). This agreement provides greater confidence that the present study is likely to be detecting surface expressions of the S-STF in the remotely sensed SST images in these regions.

In the eastern Tasman Sea (165°E), there are some differences between the results presented here and the front locations found by earlier investigators. Heath (1981; 1985) shows the STF as being orientated almost north to south along 165°E, where it lies between about 47 and 49°S (Fig. 5.1). Hamilton (2006) shows the S-STF making a deflection to the east in this region, crossing 165°E further north near 47.5°S (Fig. 5.1). The results presented here suggest that the surface expressions of the S-STF along 165°E occur most frequently between 48.5-49°S (Fig. 5.13c). This position agrees reasonably well with the poleward limit of the STF pathway shown by Heath (1981; 1985) but is more than 150 km south of the position of the S-STF suggested by Hamilton (2006). The reasons for these differences are not immediately apparent; however, the eastern Tasman Sea is a poorly sampled region where there are relatively few historical data to constrain the location and variability of the S-STF, and where there are also some intriguing patterns are apparent in the distribution of thermal fronts and SSS contours associated with the S-STF. Therefore, greater detail is devoted to this region at the end of this discussion (Section 5.6.7).

5.6.4 Seasonal migration of the S-STF in the Tasman Sea

The next feature to consider is the degree of seasonal variability in the patterns observed in the thermal front frequency (Section 5.5.2). Fig. 5.11 shows seasonal-means of the frequency of occurrence of thermal fronts detected over the Tasman Sea and south of New Zealand. During the austral summer (Dec-Jan-Feb) and winter (Jun-Jul-Aug), the histograms of the seasonal-mean frequency distribution of thermal fronts in Regions 1, 3 and 4 are remarkably similar to the distributions of thermal fronts observed in these regions during the year as a whole (Fig. 5.11). There is little seasonal variability in the spatial patterns, and the location of histogram peaks appears to change little with season (Fig. 5.11). These results suggest that if the there is any seasonal migration in the modal position of the surface expressions of the S-STF, as identified from the annual-mean data (Section 5.6.2), then it is within the resolution of the analysis (0.5° latitude) and thus not resolved. One possible exception is in Region 3. Here, there is some suggestion from the distribution of thermal fronts that surface expressions of the S-STF might frequently occur over a broader latitudinal range between 48.5-50.0°S, with the poleward limit of the S-STF possibly shifting to between 49.5-50.0°S (Fig. 5.11c).

The lack of an obvious seasonal shift of the S-STF at the borders of the Tasman Sea is intriguing. The coverage of in-situ data available to earlier investigators was insufficient to compare positions of the N-STF and S-STF in the Tasman Sea on a seasonal time scale (see e.g. Jeffrey, 1986). As discussed in Section 5.1.2, previous studies have also suggested that the positions of the N-STF and S-STF in Tasman Sea are rather constant (Jeffrey, 1986; Hamilton, 2006), but do not distinguish a time scale associated with this supposed stability (e.g. week-to-week, season-to-season). The results presented here are more definitive. The present study has been able to place constraints of 0.5° and 1° latitude on any seasonal migration of the surface expressions of the S-STF in the western and eastern Tasman Sea, respectively. In Section 5.1.2, differences exceeding 2° latitude between reported positions of the S-STF in the central and eastern Tasman Sea were discussed. Given the new constraints that can now be placed on seasonal variability of the S-STF, these differences in frontal position exceeding 2° seem unlikely to be occurring on a seasonal timescale. This issue is explored further in Section 5.6.7.

To the south of New Zealand (167°E), where the climatological position of the S-STF follows the upper-continental slope (Fig. 5.1), the results presented here suggest that if there is any seasonal migration in the position of the surface expressions of the S-STF, then this is within the resolution of the analysis (0.5° latitude) and is not resolved. This is consistent with results by Hopkins et al. (2010), based on 23 years of AVHRR Pathfinder Version 4 SST data, which indicate the average seasonal migration of the Southland Front to be about 30 km.

The picture that emerges from these analyses is that at the borders of the Tasman Sea (153°E, 165°E), and south of New Zealand (167°E), any seasonal migration of the surface expressions of the S-STF does not exceed about 1° latitude. According to previous investigators, the seasonal migration of the S-STF in the southeast of the Atlantic Ocean (0°E) and Indian Ocean (120-140°E) has a comparable range - for example, Burls and Reason (2006) found seasonal shifts of SST gradients in the STF region in the southeast of the South Atlantic (0°E) were rather indistinct. Their results, based on three years of remotely sensed SST images, indicate gradients of SST at the S-STF near 40°S, 0°E migrate by <1° latitude between austral summer and winter (Fig. 3 in Burls and Reason, 2006). Similarly, James et al. (2002) found the location of the STF south of Australia (120-140°E) did not change much during the year, with the STF located between 38-39°S from synoptic surveys in austral summer and winter 2002, with no consistent migration of the S-STF to the north or south. The results of these three studies are intriguing because they show good agreement with the relatively limited seasonal migration observed in the present study for the surface expressions of the S-STF at the borders of the Tasman Sea. This suggests that the seasonal

migration of the S-STF indicated by in the present study, of its lack thereof, may not be unique to the S-STF in the Tasman Sea.

In contrast with the seasonal analyses presented here, recent work by Graham and de Boer (2013) suggest that the STFZ undergoes a larger seasonal migration in each ocean basin, with a latitudinal shift of 5-7° between the austral summer and winter. The study of Graham and de Boer (2013) noted a seasonal shift of a broad region of high SST gradients that bisect the climatological position of the STF and STFZ given by earlier investigators (Deacon, 1982; Orsi et al., 1995; Belkin and Gordon, 1996). It is on the basis of these gradients that Graham and de Boer (2013) inferred a seasonal migration of the STFZ. The results of the present study do not support the suggestion for such a large seasonal shift in the STFZ in the Tasman Sea.

The STFZ is traditionally said to be enclosed by the N-STF and S-STF water mass boundaries (Belkin, 1988; Belkin and Gordon, 1996; Smythe-Wright et al., 1998; Hamilton, 2006). The present study finds evidence that in the Tasman Sea, the southern limit of the STFZ, the S-STF, migrates by no more than 1° latitude between austral summer and winter. Examination of the mean annual location of the STFZ in the Tasman Sea given by Graham and de Boer (2013) (their Fig. 3) shows it to be centered approximately 4° north of both the STFZ found by Hamilton (2006) and the annual mode positions of the S-STF found in the present study. This decoupling raises some doubt that the study by Graham and de Boer (2013) observed seasonal migration of the STFZ traditionally identified from hydrographic data (e.g. Hamilton (2006)). Examining in greater detail the results of Graham and de Boer (2013) in the Tasman Sea (their Fig. 8), it is noted that there are high SST gradients positioned along the climatological position of the STF found by Deacon (1982) and the S-STF found by Hamilton (2006) throughout the whole year. This is consistent with the results presented here that suggest any seasonal shift in the surface expressions of the S-STF in the western and eastern Tasman Sea does not exceed about 1° latitude.

5.6.5 Response of the S-STF to atmospheric variability

The similarities observed in the typical positions of surface expressions of the S-STF at the borders of the Tasman Sea between austral summer and winter, and in the range of this seasonal migration compared with that previously observed in ocean basins, are intriguing. As discussed in detail earlier (Section 2.5.2 and 5.1.2), Jeffrey (1986) has previously linked the latitudinal position of the S-STF to variations in the latitudinal position of the subtropical high pressure belt north of the STFZ. In turn, Streten (1980) reveals that the mean seasonal meridional shift of the subtropical high-pressure belt is smallest in the southeast South Atlantic and southeast Indian Ocean (<0.5° and ~2.5°, respectively) and considerably higher in

the western and eastern Tasman Sea (~3.0° and ~9°, respectively). Interestingly, a comparison of the seasonal results obtained here with the seasonal migration of the S-STF reported by previous investigators in ocean basins indicates that the relatively large seasonal migration of the subtropical high pressure belt in the Tasman Sea does not translate into an increased seasonal migration of the S-STF.

In the southeast Indian Ocean, James et al. (2002) suggested that the position of the STF might be determined by atmospheric forcing during the austral winter. They found that the STF was in contact with the atmosphere during the austral winter, but appeared to be decoupled from the atmosphere during the austral summer by a shallow mixed layer, with the Front retaining its winter time position beneath the surface mixed layer, and thus displaying limited seasonal migration, during the austral summer. The new seasonal observations of the S-STF in the Tasman Sea lend weight to the suggestion of James et al. (2002), based on data from the SE Indian Ocean, that links between the latitudinal position of the STF and atmospheric variability may be dependent on season, with the S-STF in the Tasman Sea also found here to occur at about the same latitude during austral summer and winter seasons, despite large seasonal variability in the overlying atmosphere (Streten, 1980).

5.6.6 Response of the S-STF to topography around southern New Zealand

In the eastern Tasman Sea (165°E), evidence for a topographic influence on the S-STF is vague. Surface expressions of the S-STF in the eastern Tasman Sea appear to have some preference to occur at between 48.5-49°S on annual (Fig. 5.13c) and seasonal time scales (Fig. 5.11c). Examining the bathymetry of this region in Fig. 5.1 shows that the bin between 48.5-49°S (located between 164.75-165.25°E) overlies steeply shelving topography, which shoals from 3000 m to near 350 m depth at a sea mount along the Macquarie Ridge. This suggests a possible influence of the steeply shelving topography of the Macquarie Ridge on the tendency for the S-STF to occur between 48.5-49°S along 165°E, but it seems difficult to make further inferences from the composite data alone.

South of New Zealand (167°E), evidence from the histograms of thermal front frequency suggest that the surface expressions of the S-STF are most frequently located between 48.5-49°S, at annual (Fig. 5.13d) and seasonal time scales (Fig. 5.11c). These positions are consistent with the location of the S-STF in the Snares Depression observed in the April 2011 survey described in **Chapter 3** (e.g. Fig. 3.8 and Fig. 3.10). This agreement, and the consistency observed here in the position of the S-STF seasonally, hints that the S-STF has a relatively stable position south of New Zealand throughout the year. This supports the conclusions in **Chapter 3**, and the earlier inferences of Heath (1981; 1985) based on more

rudimentary data, that south of New Zealand the S-STF is typically positioned along the upper continental slope that borders the Snares Shelf (Fig. 5.1).

Although the results presented here do not explain why the front might have a relatively stable position in the Snares Depression, there are several lines of evidence that topographic steering may play an important role in constraining the position of the S-STF south of New Zealand (e.g. Heath, 1981; 1985; Shaw and Vennell, 2001; Hopkins et al., 2010; **Chapter 3**), by directing the S-STF around steeply shelving bathymetry of about 500 m depth, in order to conserve potential vorticity. In the present study, surface expressions of the S-STF appear to be consistently positioned above the 200-600 m isobaths of the upper continental slope in the Snares Depression (Fig. 5.1), lending further weight to the suggestion that the position of the front is constrained by bathymetry of about 500 m as it passes around southern New Zealand (**Chapter 3**).

5.6.7 Possible bimodality of the S-STF in the eastern Tasman Sea

This discussion is closed with some remarks on an intriguing pattern observed in the distributions of thermal fronts in the eastern Tasman Sea. Figure 5.9 displays the annual mean frequency of occurrence of thermal fronts along 165°E. One notes that south of about 45°S, the distribution of thermal fronts is clearly bimodal, with one mode near 47°S and a second mode further south near 49°S. This is intriguing because the limited in-situ data collected in the region of the Macquarie Ridge-Solander Trough suggest that the S-STF might also have a tendency to occur near 47°S and/or 49°S. To date, four analyses of hydrographic survey data have located the STF, the S-STF, or the 34.7 frontal SSS contour, between 47°S and 47.5°S along about 165°E (Jeffrey, 1986; Butler et al., 1992; Morris et al., 2001; Hamilton, 2006). Conversely, the study presented in **Chapter 3** located the S-STF between 49.0 and 49.6°S in three hydrographic surveys in the region of the Macquarie Ridge-Solander Trough, conducted during the austral autumn of 2007, 2008 and 2011, respectively. Similarly, Heath (1981, 1985) located the southern limit of the STF near 49°S in the vicinity of the Macquarie Ridge based on hydrographic survey data. These differences in the reported latitudinal position of the S-STF in the vicinity of the Macquarie Ridge and Solander Trough suggest that the bimodality observed in thermal fronts might be indicative of a bimodality in the position of the S-STF.

There is further supporting evidence for a bimodality in the position of the S-STF in the eastern Tasman Sea from the Aquarius SSS data set. Before discussing this evidence it must be remembered, as discussed at the end of Section 5.5.3, that the Aquarius SSS data appear to be biased high in the region immediately south of New Zealand (to the north and east of 47.5°S, 164.5°E, inclusive). Along 164.5°E, the distribution of occurrences of the

SSS contour corresponding to the S-STF (34.7) show a clear mode centered on 48.5°S (Fig. 5.13c). Since the Aquarius SSS data appear to be biased high immediately south of New Zealand, it is reasonable to assume this bias has prevented the detection of a second mode in the S-STF, based on the frontal SSS contour, near 47°S.

Figure 5.16 shows histograms of the frequency of occurrence of the SSS contours corresponding to S-STF at four meridians, along the Macquarie Ridge (164.5°E, Fig. 5.16a) and immediately west of the Macquarie Ridge in the eastern Tasman Sea (Fig. 5.16b-d).

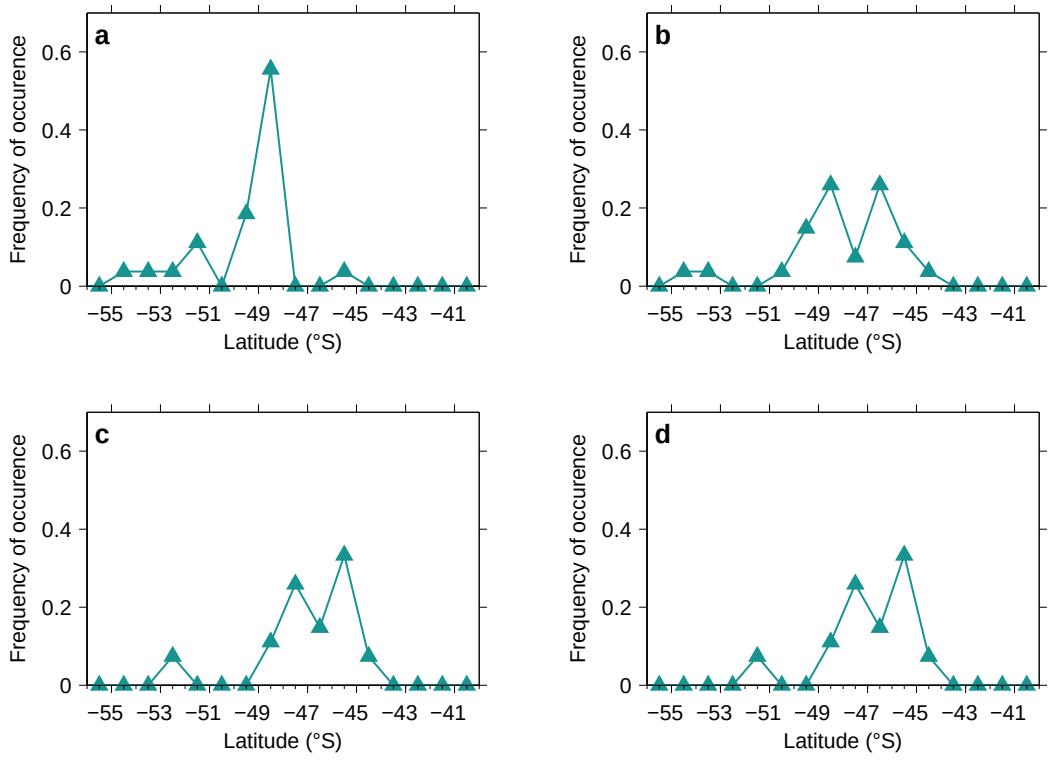

Figure 5.16: Histograms of the annual-mean (2013-2015) frequency of occurrence of the salinity indicator of the S-STF (34.7 surface isohaline), derived from the Aquarius SSS data, along (a) 164.5°E, (b) 163.5°E, (c) 162.5°E and (d) 161.5°E.

It is apparent moving west of 164.5°E (i.e. off the Macquarie Ridge) that the position of the S-STF defined using the Aquarius SSS data becomes bimodal (Fig. 5.16b-d). This bimodality of the 34.7 SSS contour is much like the bimodality seen in thermal fronts, although with modes in the distribution of positions of the 34.7 SS contour shifted slightly north at 46.5°S and 48.5°S. This bimodal pattern in SSS gives weight to the suggestion that the bimodality observed in thermal fronts (Fig. 5.9b, 5.13c) is indicative of a bimodality in the S-STF in the eastern Tasman Sea.

These observations open a question about the timescale of a possible bimodality in the S-STF in the eastern Tasman Sea. With this in mind, it is notable that a bimodal pattern is found to exist in the distribution of thermal fronts in this region during both the austral summer and winter (Fig. 5.11c). This suggests bimodality in the S-STF might exist across seasons, rather than being an interannual feature. This raises the possibility of a bimodality of the S-STF on a sub-seasonal timescale, with the S-STF moving rather quickly (i.e. within a season) between a northern and a southern mode. Unfortunately, the present study does not have sufficient information from the analysis of thermal fronts and SSS to speculate any further on the possible bimodality in the S-STF in the eastern Tasman Sea. A time series of the location of the S-STF along the Macquarie Ridge, with sub-seasonal resolution, will be needed to better constrain the fronts temporal variability, and verify whether the S-STF behaves bimodally, in this region of complex bathymetry.

5.7 Conclusions

The comparison of thermal fronts detected in satellite temperature data with information from satellite salinity data have shed new light on the annual- and seasonal-mean positions of the S-STF in the Tasman Sea. It is evident that the annual-mean patterns of the occurrence of the S-STF at the borders of the Tasman Sea, as inferred using 3 years (2013-2015) of satellite salinity data and historical, salinity-based definitions for the S-STF (Hamilton, 2006), are reflected in annual-mean patterns of occurrence of thermal fronts, detected in 30 years (1982-2011) of satellite temperature data. Both thermal fronts and the S-STF defined using satellite salinity data show bands of higher frequency of occurrence, which extend across similar latitudinal ranges in the western and eastern Tasman Sea. This strong correspondence leads us to infer that the bands of frequently occurring thermal fronts detected in the satellite temperature are surface expressions of the S-STF. Ideally, one requires the salinity of each thermal front detected in these bands to assess their relationship with the S-STF, but such data is not available; nonetheless, the comparisons performed in this study suggest that these bands of frequent thermal fronts are indeed likely to be surface expressions of the S-STF. By examining the patterns of occurrence of these thermal fronts, a statistical view of the S-STF position is developed, which is not possible from the historical hydrographic survey data.

In the western Tasman Sea (153°E), it is apparent that surface expressions of the S-STF most frequently occur between 45.0-45.5°S. This corroborates the interpretations of the general position of the STF, or S-STF, made by earlier investigators using the sparse historical data (Deacon, 1982; Heath, 1985; Hamilton, 2006).

In the eastern Tasman Sea (165°E), the surface expressions of the S-STF are most frequently located between 48.5-49.0°S. These results differ from Hamilton (2006), who lo-

cates the S-STF in this region near 47.5°S, but are consistent with the southern limit of the STF inferred from CTD data by Heath (1981; 1985). This suggests that 47.5°S may be an unusually northward position for the S-STF in the eastern Tasman Sea. However, the existence of a bimodal distribution of thermal fronts in this region, as well as a bimodal distribution in the position of the S-STF derived from SSS, is intriguing and contains the tentative suggestion that the S-STF might be bimodal in this region, with modes near 47°S and 49°S. The bimodality in thermal fronts also exists seasonally, raising the possibility of a transition between these two modes on a sub-seasonal timescale. Further work is needed to verify whether the S-STF behaves bimodally in this region of complex topography.

South of New Zealand (167°E), it is apparent that the positions of the surface expressions of the S-STF are consistently coupled with the 200-600 m isobaths over time, occurring most frequently between 48.5-49.0°S. These findings strengthen the existing evidence that south of New Zealand, steeply shelving bathymetry of approximately 500 m depth constrains the position of the S-STF, possibly due to topographic steering.

A first attempt to quantify seasonal migration of the S-STF in the Tasman Sea has indicated that if there is any seasonal variation in the position of the surface expressions of the S-STF on the western side of the basin, then it is to within the 0.5° latitude resolution of the analysis of thermal fronts and is thus not resolved. A similar situation is found south of New Zealand. On the eastern side of the basin, there is some evidence for a 1.0° southward shift of the S-STF during austral winter. The new constraints that can now be placed on the seasonal migration of the S-STF in the Tasman Sea do not support the inference of Graham and de Boer (2013) that the STFZ undergoes a global seasonal migration of 5-7° latitude , rather, any seasonal migration of the S-STF in the Tasman Sea would appear to be of a similar range to that found by previous studies in the eastern South Atlantic (Burls and Reason, 2006) and southeast Indian Ocean (James et al., 2002). Seasonal observations of the S-STF in the Tasman Sea lend further support to the suggestion of James et al. (2002) that any links between the latitudinal position of the S-STF and wind forcing are likely to be seasonally dependent.

In the Tasman Sea and south of New Zealand, analyses of remotely sensed SST and SSS data sets have revealed new detail on the location and variability of the surface expressions of the S-STF. This study demonstrates that remotely sensed SST images are useful for identifying surface expressions of the S-STF, when used in conjunction with remotely sensed SSS images. The combination of these data enabled this study to connect thermal fronts seen in remotely sensed images with the traditional, hydrographic-based definitions of the N-STF and the S-STF. Due to the limited duration (three years) and spatial resolution (1° latitude) of the Aquarius satellite SSS product available at present, these SSS data were only used to provide ancillary information about the position of the S-STF in this study. At 1° spatial

resolution, the salinity data are likely to be too coarse to resolve the high salinity gradients of the S-STF (Hamilton, 2006). However, in future work focused on temporal variability of the N-STF and S-STF, a satellite SSS product might form a primary data set. By using isohaline-based definitions as a proxy for the positions of the N-STF and S-STF (Hamilton, 2006), one may be able to estimate the location and variability of the fronts on sub-seasonal timescales from maps of satellite SSS data, and to investigate further the possible causes of their variability.

Chapter 6

SST variability at the topographically steered Subtropical Front south of New Zealand and its links to South Pacific winds

In this Chapter interannual SST variations across the STF south of New Zealand are studied in relation to variability of surface winds over the South Pacific, using the data set of thermal fronts developed in **Chapter 4**.

Understanding the drivers of interannual SST variability in the New Zealand region is of considerable practical interest. For instance, interannual SST variations in the waters bordering the STF in the western South Pacific have been found to strongly affect the New Zealand regional climate, in terms of both air temperature (Sutton et al., 2005) and precipitation (Ummenhofer et al., 2009). In turn, variations in the abundance and recruitment of several commercially important fish populations in New Zealand waters have been shown to be related to regional SSTs around New Zealand (Dunn et al., 2009). Variations in the SST differential across the STF in the New Zealand sector may have implications for tropospheric circulation (e.g. Nakamura et al., 2008), as well as providing some indication of changes in the relative geostrophic flow associated with Front (e.g. Shaw and Vennell, 2001; Hopkins et al., 2010), which in turn influences the larger-scale oceanography of the region by transporting water northward into the highly productive STF zone over the Chatham Rise (Sutton, 2001, 2003). Recent work (e.g. Hill et al., 2008, 2011; Ridgway et al., 2008; Wu et al., 2012; Fernandez et al., 2014; Oliver and Holbrook, 2014) has identified basin-wide wind field changes in the South Pacific as contributing significantly to interannual to decadal scale variations in SST, SSS and poleward transport in the western boundary current system

of the South Pacific gyre. This Chapter explores whether similar wind-driven influences are evident in another part of the subtropical gyres system, at the STF south of New Zealand.

6.1 Introduction

Atmospheric observations, reanalysis products and climate model simulations show marked changes in the Southern Hemisphere atmospheric circulation since the 1970s (Thompson and Solomon, 2002; Marshall, 2003; Swart and Fyfe, 2012). These changes include a significant strengthening of the Southern Hemisphere surface westerly winds (Thompson and Solomon, 2002; Gillett and Thompson, 2003; Swart and Fyfe, 2012) and in turn, an increase in positive wind stress curl in the southern mid-latitudes (between about 30-50°S) (Cai, 2006). These changes have had significant impacts on ocean circulation, leading to a strengthening and poleward shift of the subtropical gyre circulations in the South Pacific Ocean, southern Indian Ocean and South Atlantic Ocean (see e.g. Cai, 2006; Hill et al., 2008; Wu et al., 2012), and have significantly affected the water mass distribution in the Southern Ocean, where the main fronts of the ACC have been observed to have shifted poleward over the last 50-70 years (see e.g. Gille, 2008; Sokolov and Rintoul, 2009b).

It is well documented that the basin-wide wind stress curl over the South Pacific plays an important role in driving variations in the temperature and circulation of the South Pacific subtropical gyre and its western boundary current system (Cai, 2006; Roemmich et al., 2007; Hill et al., 2008, 2011; Wu et al., 2012). For example, Roemmich et al. (2007) observed an increase in SSH of 12 cm with large spatial scale over the western South Pacific between 1993 and 2004, representing a strengthening of the circulation of the South Pacific gyre. They diagnose this "spin-up" of South Pacific gyre as a response to a decadal intensification of wind stress curl over the South Pacific east of New Zealand. A subsequent analysis by Ridgway (2007) of observations collected between 1944 and 2002 from the waters off eastern Tasmania, in the poleward extension of the EAC (see Section 2.8), revealed significant interannual to decadal-scale variability in the T and S properties of STW, superimposed on longer term positive trends of 2.28°C century^{-1} and 0.34 psu century. These property changes have in turn been related to variations in the poleward EAC flow through the Tasman Sea, which are forced remotely by changes in the basin-wide wind stress curl east of New Zealand approximately 36 months prior (Hill et al., 2008; 2011).

Basin-wide variations in wind stress curl over the South Pacific have also been found to drive interannual to decadal-scale variability in the strength of major current and frontal systems north and east of New Zealand. Based on 15 years of XBT observations and two 60-year ocean-state estimates, Hill et al. (2011) found the strength of the two outflow pathways from the Tasman Sea – the EAC extension and the Tasman Front (**Chapter 2**) - were anti-

correlated on decadal time-scales. They related this behaviour to changes in wind stress curl east of New Zealand; periods of enhanced wind stress curl appear to strengthen the poleward flow of subtropical waters through the Tasman Sea – via the EAC extension - while circulation north of New Zealand – via the Tasman Front – weakens. Similar anti-correlation in the strength of these two current systems has been observed in numerical experiments with a general circulation model, forced by idealized wind stress curl anomalies east of New Zealand (Hill et al., 2010). More recently, Fernandez et al. (2014) documented a multi-decadal intensification of the confluence region between subtropical and Subantarctic boundary currents southeast of New Zealand between 1992-2012 (l80-200°E, Fig. 2.5). They linked this intensification to increased southward wind-driven flows of STW into the confluence region, coupled with a warming of STW north of the confluence (0.42°C decade^{-1}), resulting from increased basin-wide South Pacific wind stress curl (Hill et al., 2008).

The demonstrable influence of wind field changes on the western boundary current system of the South Pacific gyre raises the question: do these wind-driven influences extend to other parts of the subtropical gyre system? Much like in the EAC extension (e.g. Hill et al., 2008) and in the western boundary currents east of New Zealand (e.g. Fernandez et al., 2014), SSTs at the STF around southern New Zealand show considerable variability on inter-annual and longer time scales (Shaw et al., 1999; Shaw and Vennell, 2001; Hopkins et al., 2010). Whilst the relation of SST variability in the area south of New Zealand to basin-wide changes in the South Pacific wind field has not yet been explored, there are reasons to suspect that there may be a significant wind-driven influence in this region.

Modeling studies show that variations in the basin-wide South Pacific wind stress curl likely impact on various components of the South Pacific gyre through the generation and propagation of baroclinic Rossby waves (e.g. Qiu and Chen, 2006; Sasaki et al., 2008; Hill et al., 2010; Holbrook et al., 2011). In particular, Sasaki et al. (2008) investigated variability in sea level and upper ocean circulation in the South Pacific on the basis of a linear baroclinic Rossby wave model. They show that a large part of interannual sea level variations in the Tasman Sea between 1970 to 2003 can be explained by the westward propagation of baroclinic Rossby waves generated by wind stress curl anomalies over the South Pacific, east of New Zealand.

Later work by Hill et al. (2010), based on idealized model experiments, demonstrates that wind stress curl anomalies over the central South Pacific can generate baroclinic Rossby waves that also pass around southern New Zealand as they propagate westward from the South Pacific. In doing, so these baroclinic waves introduce westward propagating sea level variability over both the STF and the Campbell Plateau (see e.g. Fig. 5 in Hill et al., 2010). Sea level variability can impact on geostrophic flow through modifying the sea surface slope and pressure gradient (e.g. Brown et al., 2001), which in turn can lead to SST anomalies

through horizontal advection (e.g. Deser et al., 2010). Baroclinic Rossby waves generated by wind stress curl in the ocean interior will also cause displacements of the thermocline as they propagate westward (see e.g. Chelton and Schlax, 1996; Schneider et al., 2002; Tomczak and Godfrey, 2003; Fedorov and Brown, 2009). These can lead to SST anomalies if subsurface temperature anomalies caused by fluctuations in the depth of the thermocline are subsequently entrained into the upper ocean through vertical mixing (see e.g. Schneider and Miller, 2001; Schneider et al., 2002; Zhang and Wu, 2010). Taking this all into account leads to the questions: do variations in wind stress curl over the South Pacific introduce SST variability around southern New Zealand? and what impact does this have on the temperature differential across the S-STF in this area? This Chapter examines these questions, using 30 years of remotely sensed SST data and atmospheric reanalysis data.

Although several studies have previously examined intra-annual and inter-annual variability of the S-STF around southern New Zealand (Chiswell, 1994, 1996; Uddstrom and Oien, 1999; Shaw and Vennell, 2001; Hopkins et al., 2010), these studies have focused on the role that local-scale wind stress (Chiswell, 1996) and variability related to the El Niño–Southern Oscillation (ENSO) (Uddstrom and Oien, 1999; Shaw and Vennell, 2001; Hopkins et al., 2010) may play in this variability. Based on data from a 13-month deployment of current meter moorings, (Chiswell, 1996) found that variations in the velocity of the Southland Current – the induced geostrophic flow associated the Southland Current located off the south east coast of the South Island, New Zealand (**Chapter 2**) - were likely linked to variations in zonal (east-west) wind stress over southern New Zealand. Later, Shaw and Vennell (2001) found a decrease in the mean temperature and temperature gradient of the Southland Front between 1989-1992. These changes coincided with a decrease in the Southern Oscillation Index (SOI) – leading the authors to suggest that the SST gradient along the Southland Front, and hence northward flow, might have decreased in response to El Niño conditions that developed between 1991-1994. In turn, Hopkins et al. (2010) examined a longer 21 year (1985-2009) record of the properties of the Southland Front and demonstrated that interannual changes in the temperature and thermal gradient in the Southland Front are significantly correlated with ENSO variability. ENSO variability strongly influences large-scale wind patterns in the South Pacific (e.g. L'Heureux and Thompson, 2006). Thus, the links identified by Shaw and Vennell (2001) and Hopkins et al. (2010) lend further weight to the hypothesis that large-scale changes in wind field over the South Pacific might play an important role in variations in SST around southern New Zealand. Nevertheless, previous studies have not addressed this possibility in any detail.

In summary, there is considerable evidence of links between changes in the oceanography of the southwest Pacific and variations in the basin-scale South Pacific wind stress curl. It is therefore of interest to investigate whether the oceanography of the STF in this region is

linked to the wind field in a similar way. This study examines whether interannual variations in SST across the S-STF around southern New Zealand are indeed correlated with changes in wind stress curl across the South Pacific. It should be noted that a range of processes govern variations in SST, for example, air-sea heat fluxes, Ekman advection, geostrophic advection and entrainment processes at the base of the mixed layer (Dong et al., 2007). At least a couple of recent studies have used a mixed layer heat balance to investigate the relative contribution of these processes in causing interannual variations of SST in the southwest Pacific Ocean, and have also explored the underlying drivers (Ciasto and England, 2011; Bowen et al., 2017). However, carrying out an investigation of the mixed layer heat balance in the waters south of New Zealand lies beyond the scope of this correlative study, and remains a challenge for future work (Section 6.9).

In this study, three, 30 year frontal times series are derived from remotely sensed SST data: SSTs on the subtropical side of the S-STF, SSTs on the Subantarctic side of the S-STF, and the temperature differential across the S-STF (i.e. STW minus SAW). The frontal time series are analysed in conjunction with time series of wind stress and wind stress curl data from an atmospheric reanalysis product. Lagged correlations are used to investigate the relation between variability in winds over the South Pacific and interannual variations in SST across the S-STF. As part of this processes, linear trends from the frontal time series and wind time series are also examined over periods of 20 to 30 years. Multi-decadal changes in SST across the S-STF around southern New Zealand have not, until now, been examined in any detail. This aspect of the present study enables this Chapter to not only quantify and assess the statistical significance of multi-decadal SST trends across the S-STF south of New Zealand for the first time, but also to compare any multi-decadal changes in SST at the S-STF with those observed in the South Pacific wind field.

This Chapter is organized as follows: Section 6.2 presents the data sets used in this study. Section 6.3 describes the statistical methods. In Section 6.4, the influence of changes in the South Pacific wind field on interannual variability of SST at the S-STF is investigated using cross-correlation. Section 6.5 discusses these results, and the potential physical mechanisms behind them. In Section 6.6 multi-decadal trends in SST at the S-STF are analyzed. Section 6.7 discusses these longer term changes and evaluates their possible origins. A sensitivity analysis of the main results of the study is performed in Section 6.8. Suggestions for further research are provided in Section 6.9 and Section 6.10 summarises the study findings.

6.2 Data sets

6.2.1 Thermal fronts

The primary data source for this study is the data set of thermal fronts detected in 30 years (1982-2011) of PFV5.2 monthly composite SST images (**Chapter 4**). This Chapter focus on the properties of front segments within a geographic region that encloses the S-STF around southern New Zealand, which is shown in Figure 6.1. The boundaries for this region were chosen using a plot of the frequency of occurrence of thermal fronts around southern New Zealand (Figure 6.1). Frequency of occurrence is a statistical measure of frontal activity, calculated as the total number of front segments detected at a satellite pixel normalized for variability in cloud cover (Ullman et al., 2007). Around southern New Zealand, the S-STF is well-defined and forms a quasi-stable frontal zone, following the ~500 m isobath along the upper continental slope that borders the Snares Shelf (**Chapter 3**). The mean location of surface expressions of the S-STF is evident from the band of relatively high front frequency (greater than ~10 %) that approximately follows the 500 m isobath (Heath, 1985; Belkin and Cornillon, 2003). Boundaries for the S-STF region were drawn so that they enclosed this band of high front frequency, and were defined by the following latitude-longitude points: (1) 49.4°S, 167.0°E, (2) 48.8°S, 167.0°E, (3) 48.0°S, 168.4°E, (4) 47.0°S, 169.0°E, (5) 45.7°S, 170.9°E, (6) 45.7°S, 171.7°E, (7) 47.5°S, 169.5°E, (8) 48.4°S, 169.0°E.

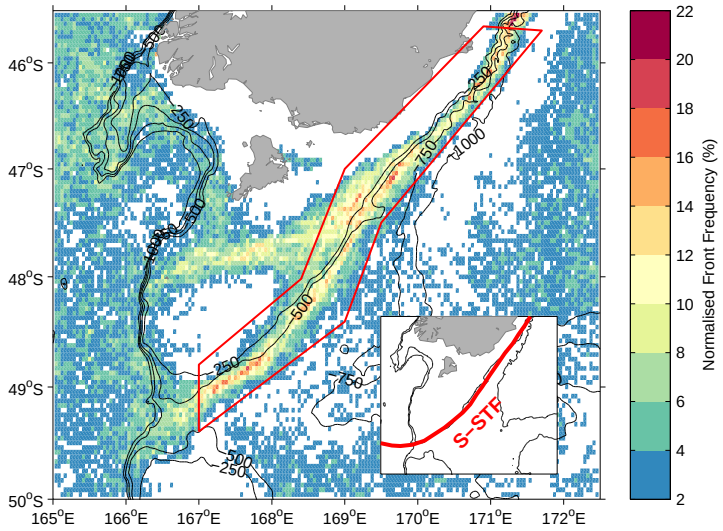

Figure 6.1: Annual-mean (1982-2011) frequency of occurrence of thermal fronts around southern New Zealand between 1982 and 2011, derived from the data set of thermal fronts developed in **Chapter 4**. Locations where the frequency of occurrence is less than 3% have been masked to aid clarity. The geographic region over which front segment properties were averaged for creating the frontal time series are shown by the red box. The black lines are the 250, 500, 750 and 1000 m isobaths. Also shown is a schematic of position of the S-STF based on results from **Chapter 3**.

6.2.2 Frontal time series

Three, 30 year (1982-2011) frontal time series were derived by averaging the thermal properties of front segments over the S-STF region around southern New Zealand (Fig. 6.1). The first time series is the SST on warm side of thermal fronts (T_{warm}) and the second is the SST on the cold side of thermal fronts (T_{cold}). These time series are used to infer SSTs in the near-frontal subtropical (warm) and Subantarctic (cold) waters that border the S-STF. The third time series is the temperature differential across thermal fronts (T_{step}), which is used to infer the temperature differential across the S-STF (i.e. the STW minus SAW temperature differential). The temperature differential across an ocean front – together with the salinity differential - plays an important role in determining the change in density across the front and hence, the velocity of the induced geostrophic flow (e.g. Brown et al., 2001). Since the section of the S-STF around southern New Zealand is weakly density compensated **(Chapter 3)**, and associated with relatively strong (c. 10 Sv) geostrophic flow (see e.g. Chiswell, 1996; Morris et al., 2001; Sutton, 2003; Graham and de Boer, 2013), variability in T_{step} can be thought of as a crude indicator of changes in geostrophic flow associated with the S-STF. The assumption that the properties of thermal front segments are representative of SSTs across the S-STF around southern New Zealand is tested in Section 6.8.

Monthly averaged values of T_{warm}, T_{cold} and T_{step} were computed as the weighted mean of each front property averaged over all front segments in the S-STF region (Fig. 6.1), with weights equal to the length of each front segment in terms of satellite image pixels:

$$T_{property} = \frac{\sum_{i=1}^{N} Segment_{property}(i) \times Segment_{length}(i)}{\sum_{i=1}^{N} Segment_{length}(i)} \tag{6.1}$$

where $T_{property}$ is the monthly average value of a given front segment property (i.e. T_{warm}, T_{cold} and T_{step}), *segment* is a front segment,*property* is the value of a property of a front segment *i*, *length* is the length of a segment in pixels and the sums are over all front segments within the S-STF region. Weighting by front segment length is appropriate here because the surface expression of the S-STF around southern New Zealand typically forms a long, spatially contiguous front (see e.g. Fig. 3.10 and Uddstrom and Oien, 1999). In contrast, surface expressions of non-S-STF fronts (e.g. neritic fronts, filaments split off from the S-STF), which can also occur in this region but are not of interest in this study, are typically much shorter. Calculations were carried out on a month-by-month basis to produce a 30-year time series of T_{warm}, T_{cold} and T_{step} at monthly resolution (Fig. 6.2). The monthly time series were then de-seasoned into anomaly time series by the 30-year (1982-2011) monthly mean for that time series.

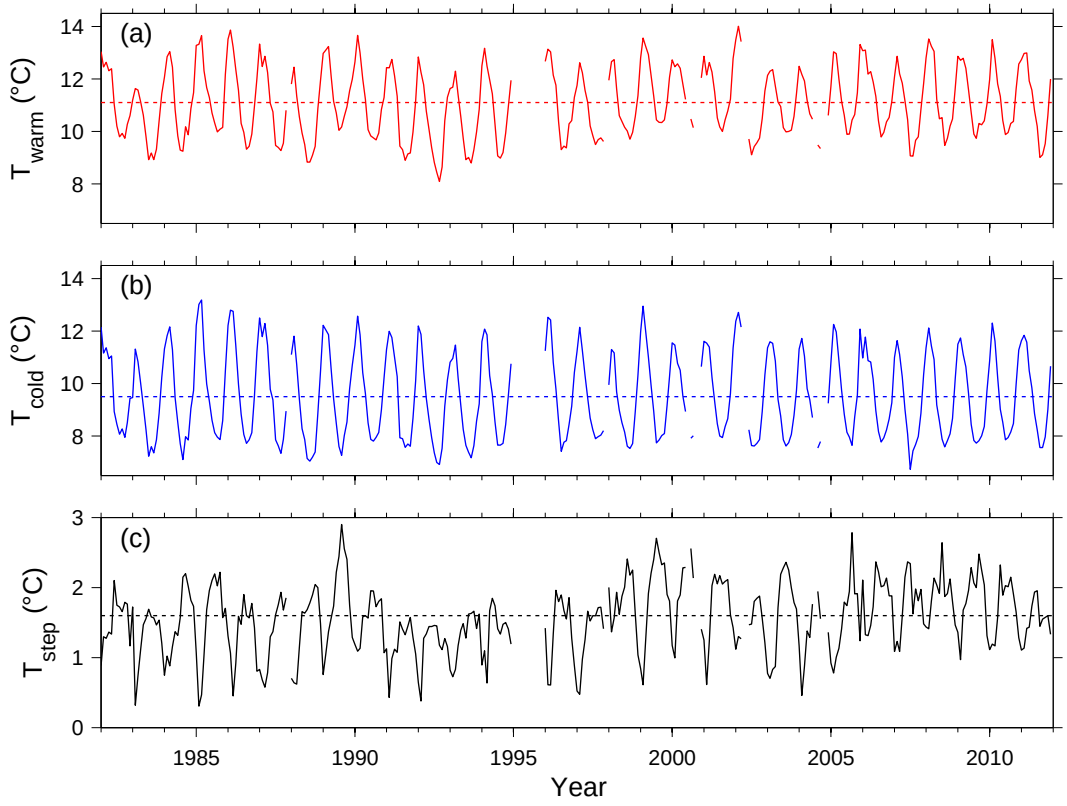

Figure 6.2: Monthly-resolution frontal time series around southern New Zealand. Shown are the time series of (a) subtropical SSTs (T_{warm}), (b) Subantarctic SSTs (T_{cold}) and (c) the temperature differential across the S-STF (T_{step}). Dashed lines show the 30 year (1982-2011) annual mean value of each time series ($T_{warm} = 11.1C$, $T_{cold} = 9.5C$ and $T_{step} = 1.6C$).

The number of front segments that contribute to the monthly average values is shown in Figure 6.3. Note, that each 30-year time series contains a 12 month data gap during 1995, together with nine, month-long gaps, shown by the drop in the number of front segments contributing to the S-STF records. The data gap during 1995 is likely related to a digitizer error in NOAA-14 SST data that resulted in data being flagged as unusually poor quality (Hopkins, 2008). The remaining month-long gaps appear to be due to cloud coverage that obscured the study region. The data gaps create an analysis issue, because standard techniques to compute the cross-correlation function and assess the statistical significance of linear trends (Section 6.3) require gap-free records. In this study, all of these short data gaps in the three frontal time series are filled using a Singular Spectrum Analysis (SSA) gap-filling method (Kondrashov and Ghil, 2006). Details of this gap-filling procedure are given in Appendix E. The frontal time series following this infilling procedure are shown in Figure 6.4.

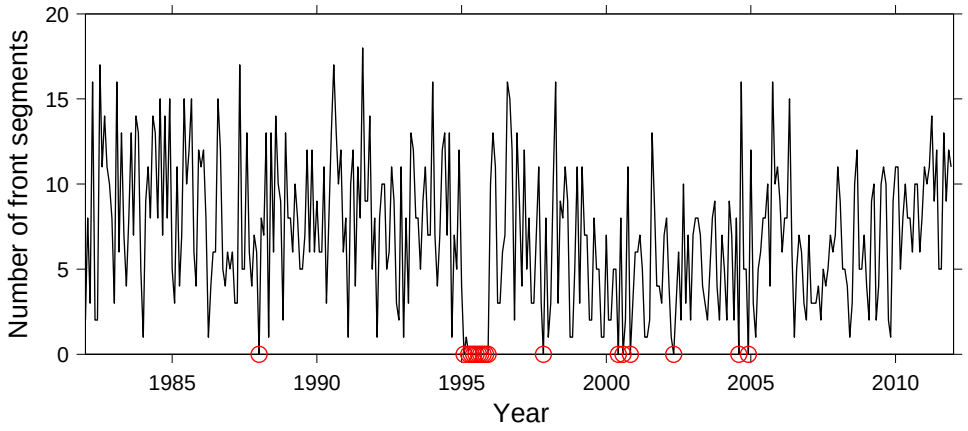

Figure 6.3: The number of front segments that contribute in a weighted fashion to the frontal time series. Months where no front segments were detected within the S-STF region (Fig. 6.1) are highlighted with red circles.

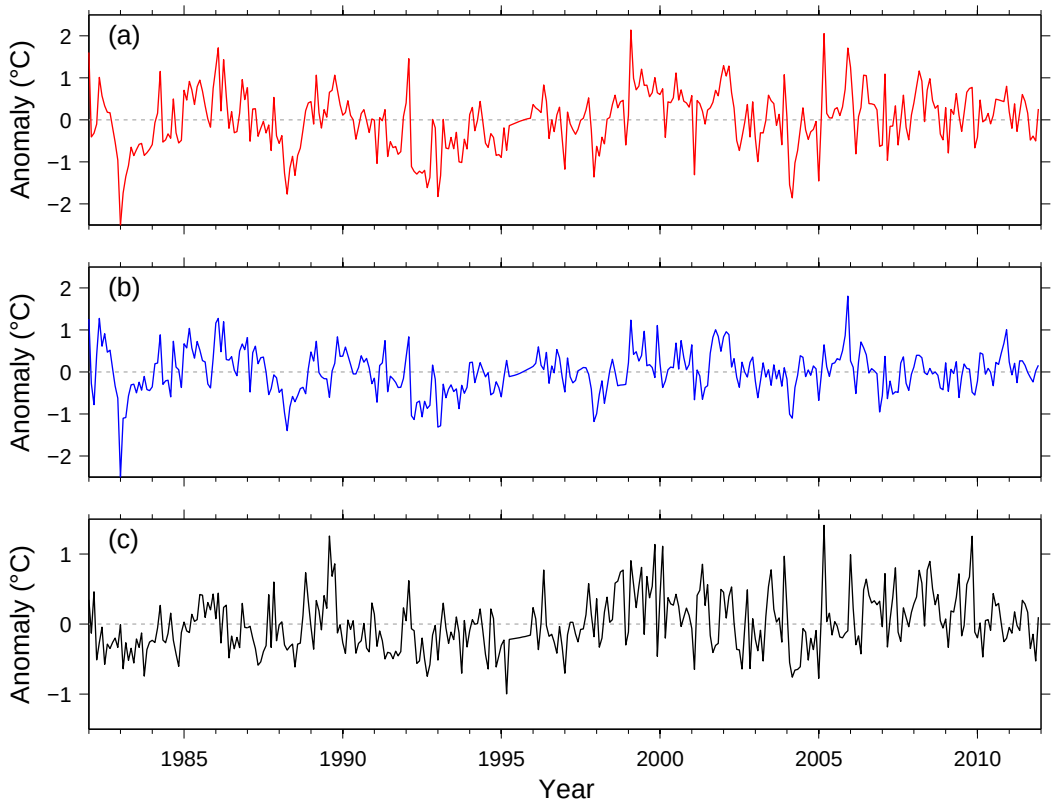

Figure 6.4: Monthly-resolution frontal time series around southern New Zealand. Shown are the time series of (a) subtropical SST anomalies (T_{warm}), (b) Subantarctic SST anomalies (T_{cold}) and (c) the temperature differential across the S-STF (T_{step}). Values in each frontal time series are anomalies relative to the long-term monthly means of each time series computed over 1982-2011.

6.2.3 NCEP-1 Reanalysis

Wind stress data from the National Centre for Environmental Protection (NCEP) and National Centre for Atmospheric Research (NCAR) atmospheric reanalysis product (NCEP-1 reanalysis) (Kalnay et al., 1996) were used to examine changes in surface winds over the South Pacific. The NCEP-1 reanalysis is a observationally-constrained estimate of the time-varying state of the atmosphere that extends from 1948 to the present, on a 2.5° latitude-longitude grid (Kalnay et al., 1996; Kistler et al., 2001; Dee et al., 2016). The NCEP-1 reanalysis is created through inputting millions of in-situ and remotely sensed atmospheric observations collected since 1948 into a data assimilation system, which uses a consistent numerical climate model throughout the entire reanalysis period (Kistler et al., 2001).

The main advantages of using wind stress data from the NCEP-1 reanalysis, rather than purely in-situ or satellite based observations, are that the reanalysis fields are spatially and temporally complete - in-situ data are not - and that they span the complete 30 year length of the S-STF time series – systematic remote sensing measurements of near-surface winds by satellite did not begin until 1991 (e.g. NSIDC, 2008). One limitation of using reanalysis products is that the time-varying mixture of the underlying observations, biases in the underlying model and changes in observational coverage can introduce spurious variability and trends into reanalysis output (Dee et al., 2016). However, Marshall and Harangozo (2000) have demonstrated that the monthly mean sea level pressures data from the NCEP-1 reanalysis over the extra tropical South Pacific – which contribute to the model-derived estimates of the wind-stress fields – can be considered to be reliable from the early 1970s onwards. Hines et al. (2000) have also shown that interannual variations in NCEP-1 fields are reasonably reliable after the 1970s, covering the period examined in the present study. Several recent studies have also investigated SST and circulation variability of the South Pacific subtropical gyre in the context of wind fields from the NCEP-1 reanalysis product (see e.g. (Roemmich et al., 2007; Sasaki et al., 2008; Hill et al., 2008, 2011; Fernandez et al., 2014)) and thus, the use of data from the NCEP-1 reanalysis in the present study simplifies the comparison of results presented in the present study with these earlier studies.

Monthly mean fields of the zonal, τ_x, and the meridional, τ_y, components of wind stress were obtained for the period 1982 through 2011 from the NCEP-1 reanalysis project website http://www.esrl.noaa.gov/. These data were used in turn to construct monthly mean fields of wind stress curl, $curl(\tau)$, using a centered finite difference approach: $curl(\tau) = \frac{\partial \tau_y}{\partial x} - \frac{\partial \tau_x}{\partial y}$, where $\frac{\partial \tau_y}{\partial x}$ is the rate of change of meridional wind stress with longitude and $\frac{\partial \tau_x}{\partial y}$ is the rate of change of zonal wind stress with latitude. The partial derivatives were computed over a distance of one grid point east-west and north-south from the grid point at which the wind

stress curl was evaluated. The monthly grid-point data were converted into anomalies by subtracting the 30 year mean (1982 through 2011) annual cycle at that grid point.

Given the apparent link between changes in basin-wide South Pacific wind stress curl and changes subsequently observed in the EAC system and the Tasman Sea (Section 6.1), the primary focus of this study is to investigate whether similar links exist between the basin-wide South Pacific wind stress curl and SST variability across the S-STF around southern New Zealand. If these links exist, then there are at least two possibilities: (1) a direct link with changes in the basin-wide South Pacific wind stress curl or (2) a direct link with the local-scale - i.e. New Zealand – wind stress or winds stress curl that co-vary with the basin-wide wind stress curl. To help separate these two possibilities, this Chapter investigates SST variability across the S-STF in relation to changes in both the basin-wide and the local-scale wind field, in the cross-correlation and trend analyses performed later. Cross-correlation is also used to examine co-variation between the basin-wide and local-scale winds.

6.2.4 Wind time series

Changes in the basin-wide and local-scale wind fields over the South Pacific are examined using the gridded wind stress and wind stress curl anomalies. Data from two geographic regions (Fig. 6.5) are examined. The first region is a basin-scale region, defined as 20-50°S, 180-280°E. This region was selected following analysis of Hill et al. (2008) and Sasaki et al. (2008), which reveal SSTs and SSH within the Tasman Sea are highly correlated with wind stress curl over this region. The second region is a local-scale region, defined as 40-50°S, 155-180°E. This region was chosen for two reasons. The primary reason was to provide information on wind forcing in the frontal region, which may generate SST anomalies "locally", for example, through Ekman advection and/or vertical entrainment (Dong et al., 2007). The secondary reason was to take into account the winds adjacent to the frontal region (i.e. over the Tasman Sea, Campbell Plateau and Bounty Trough), which may generate SST anomalies in a similar manner, that are subsequently advected into the frontal region by the prevailing surface currents (see e.g. Fig. 3.5). Examining winds over the narrow, frontal region in isolation could miss this important possibility.

From these two regions, the reanalysis wind data were averaged into three 30-year (1982-2011) time series consisting of: (1) the basin-average wind stress curl for the South Pacific (20-50°S, 180-280°E), (2) the regional-mean zonal wind stress and (3) the regional-mean wind stress curl for the area around southern New Zealand (40-50°S, 155-180°E). The area-averaged time series of wind data are shown in Figure 6.6. To explore the sensitivity of the correlations to the geographic regions that have been selected, the spatial structure of the

correlations between interannual SST variability across the S-STF and South Pacific winds are also examined, using lag-correlations maps (Section 6.3.3, Section 6.4.1-6.4.2).

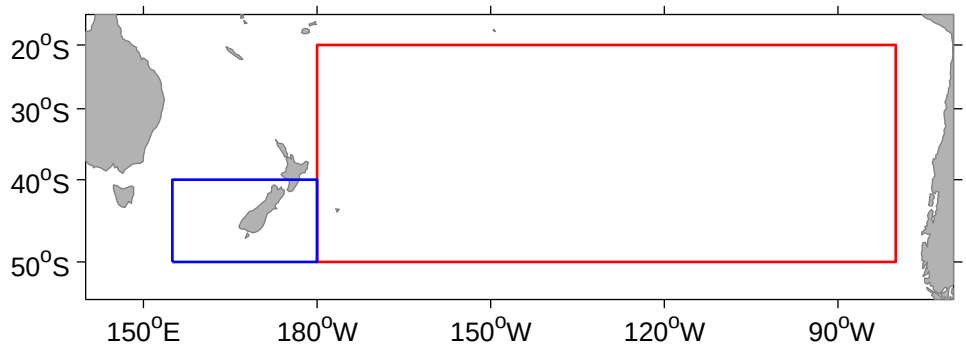

Figure 6.5: Regions over which area-averages of wind stress curl and wind stress were calculated. Coloured boxes are for basin-wide South Pacific (red) and local-scale New Zealand (blue) area-averages.

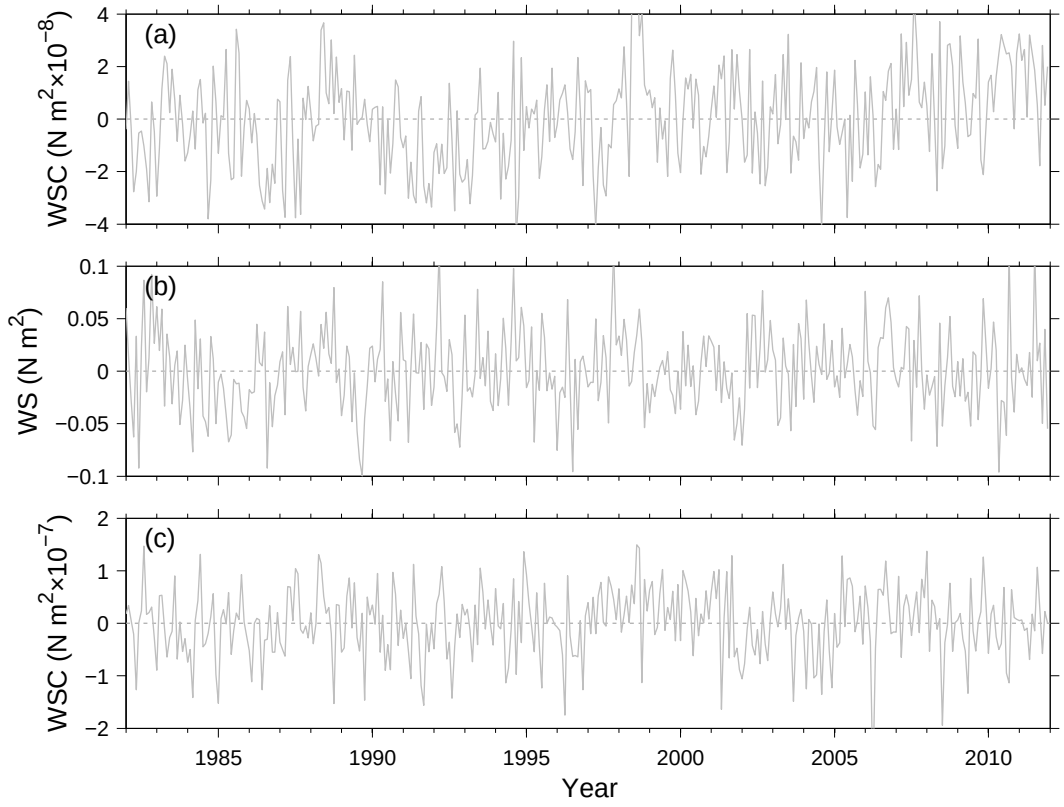

Figure 6.6: Monthly-resolution time series of South Pacific winds. Shown are the time series of (a) the basin-wide South Pacific wind stress curl, (b) the local-scale southern New Zealand zonal wind stress and (c) the local-scale southern New Zealand wind stress curl. Values in each wind time series are anomalies relative to the long-term monthly means of each time series computed over 1982-2011.

6.3 Statistics

6.3.1 Cross-correlation

Cross-correlations were calculated between pairs of time series using the cross-correlation function (Fuller, 1995), $r_{XY}(\tau)$, which is defined as:

$$r_{XY}(\tau) = \begin{cases} \frac{\sum_{i=0}^{N-|\tau|-1}\left[X_{i+|\tau|}-\bar{X}\right][Y_i-\bar{Y}]}{\sqrt{\left[\sum_{i=0}^{N-1}(X_i-\bar{X})^2\right]\left[\sum_{i=0}^{N-1}(Y_i-\bar{Y})^2\right]}} & For\,\tau < 0 \\ \frac{\sum_{i=0}^{N-\tau-1}[X_i-\bar{X}][Y_{i+\tau}-\bar{Y}]}{\sqrt{\left[\sum_{i=0}^{N-1}(X_i-\bar{X})^2\right]\left[\sum_{i=0}^{N-1}(Y_i-\bar{Y})^2\right]}} & For\,\tau \geq 0 \end{cases} \quad (6.2)$$

where $X = (X_0, X_1, X_2..., X_{N-1})$ is the first time series vector, containing a sequence of N observations , $Y = (Y_0, Y_1, Y_2..., Y_{N-1})$ is the second time series vector, with the same number of observations as X, $\bar{X}$ and $\bar{Y}$ are the sample means of X and Y, respectively, τ is the lag time between X and Y and $r_{XY}(\tau)$ is the cross-correlation coefficient between X and Y at lag τ (Fuller, 2008). The lag-lead relationship between X and Y is as follows: for $\tau < 0$, X lags$Y$ by τ, for $\tau > 0$, X leads$Y$ by τ.

Cross-correlations were calculated between seasonally averaged versions of the monthly resolution frontal time series and wind time series (Section 6.2). Seasonally averaged data are used for the cross-correlations in this Chapter for a couple of reasons. First, seasonal averaging removes sub-seasonal variability (i.e. periods < 3 months) from the time series that is not relevant to the interannual time scales (1-10 year) of variability that this Chapter is mostly interested in. Second, a recent model study has suggested that there might be an oceanic response in the New Zealand region - in terms of sea level - to changes in wind stress curl east of New Zealand at a time-lag of between 6 and 18 months (Hill et al., 2010). Retaining at least seasonal resolution in the cross-correlations enables this study to examine whether a similar signal is present in SST variability across the S-STF around southern New Zealand. The use of interannual averages - i.e. one value per year or longer - was also considered, which would have placed a greater emphasis on lower frequency variability in the frontal and wind time series. Seasonally averaged data were used in this study as they appeared to provide the most appropriate balance between emphasizing interannual variability in the time series and providing temporal detail in the cross-correlations.

Seasonally-averaged versions of the frontal time series and wind time series were obtained by block-averaging the monthly-resolution versions of these time series by season (Section 6.2). The seasonal blocks used were 3 months long and were Sep-Oct-Nov, Dec-Jan-Feb, Mar-Apr-May, Jun-Jul-Aug. A linear trend was calculated for each seasonal time series using Eqs. 6.7-6.9 (see below) and then removed prior to calculating cross correlation coefficients. This detrending step is necessary as the methods used to adjust the correlation significance

testing (Section 6.3.2) may have excessive error rates when a time series contains a strong linear trend (Pyper and Peterman, 1998).

6.3.2 Significance testing of cross-correlations

6.3.2.1 Classical hypothesis testing

In this Chapter, the statistical significance of the cross-correlation between two time series was assessed using a Student's t test at the 95% confidence level ($\alpha = 0.05$). Under the assumption that the time series X and Y each consist of N observations that are serially independent, a critical value, r_{crit} for testing the null hypothesis that $r_{XY}(\tau) = 0$ can be derived using the t distribution for two-tailed tests:

$$r_{crit} = \sqrt{\frac{t^2_{\alpha/2,N-2}}{t^2_{\alpha/2,N-2} + (N-2)}} \tag{6.3}$$

where N is the number of degrees of freedoms (Pyper and Peterman, 1998), t is the t distribution and α is the significance level. The null hypothesis (H_0) is no correlation between the two time series ($r_{XY}(\tau) = 0$) and the alternative hypothesis (H_1) is that there is a correlation between the two time series ($r_{XY}(\tau) \neq 0$), at the $100(1-\alpha)\%$ confidence level. The critical values can be understood by the following example: if $r_{XY}(\tau)$ exceeds the critical value r_{crit}, H_0 is rejected and the correlation $r_{XY}(\tau)$ (at lag τ) is considered significantly different from zero at the $100(1-\alpha)\%$ confidence level, else, H_0 is accepted.

6.3.2.2 Influence of autocorrelation

Many oceanographic time series display strong levels of persistence, or autocorrelation, meaning that values at a given time step are highly correlated to values in previous time steps (Emery and Thomson, 2001). SST anomalies, for example, display strong persistence on monthly to seasonal time scales as a result of the thermal inertia of the upper ocean (Frankignoul and Hasselmann, 1977). Autocorrelation presents a challenge when assessing the statistical significance of correlations between a pair of time series. Strong autocorrelation violates the assumption that observations in a time series are serially independent (Pyper and Peterman, 1998), which is required for the hypothesis testing procedure described above. Essentially, this means that the number of degrees of freedom for assessing the significance of correlations is smaller than the $N-2$ assumed in the method described above (Emery and Thomson, 2001; Pyper and Peterman, 1998). If unaccounted for, this increases the likelihood of concluding that a correlation between two time series is statistically significant, when in reality no significant correlation exists (Pyper and Peterman, 1998; Mudelsee, 2010).

The autocorrelation function, $r_{XX}(\tau)$, measures the correlation of a time series with time lagged versions of itself, and is defined as:

$$r_{XX}(\tau) = \frac{\sum_{i=1}^{N-\tau} [X_i - \bar{X}] [X_{i+\tau} - \bar{X}]}{\sum_{i=1}^{N} [X_i - \bar{X}]^2}, \tag{6.4}$$

where $\tau = 0, 1, ..., M$ is the time lag, $\bar{X}$ is the sample mean of X and $r_{XX}(\tau)$ is the autocorrelation coefficient between time series values separated by τ lags (Box and Jenkins, 1976). The two main properties of the autocorrelation function are that $r_{XX}(\tau = 0) = 1$ (i.e. a time series is highly correlated with itself at zero lag) and $|r_{XX}|(\tau) \leq 1$, with large r_{XX} implying that neighbouring values in a time series are highly correlated (Emery and Thomson, 2001).

The time series being considered in this study display relatively strong autocorrelation. Figure 6.7 shows the autocorrelation functions of the seasonally-averaged frontal time series and wind time series used in the correlation analyses in this Chapter (calculated using Eq. 6.4). The frontal time series exhibit moderate levels of auto-correlation with lag-1 autocorrelation coefficients of between 0.34-0.49, whilst the wind time series show lower, but non-negligible levels of autocorrelation with lag-1 autocorrelation coefficients of between 0.06-0.39 (Fig. 6.7). Such autocorrelation means that in order to assess the statistical significance of the correlations between these time series, the hypothesis testing procedure described above needs to be adjusted, to account for the reduced number of degrees of freedom (Emery and Thomson, 2001).

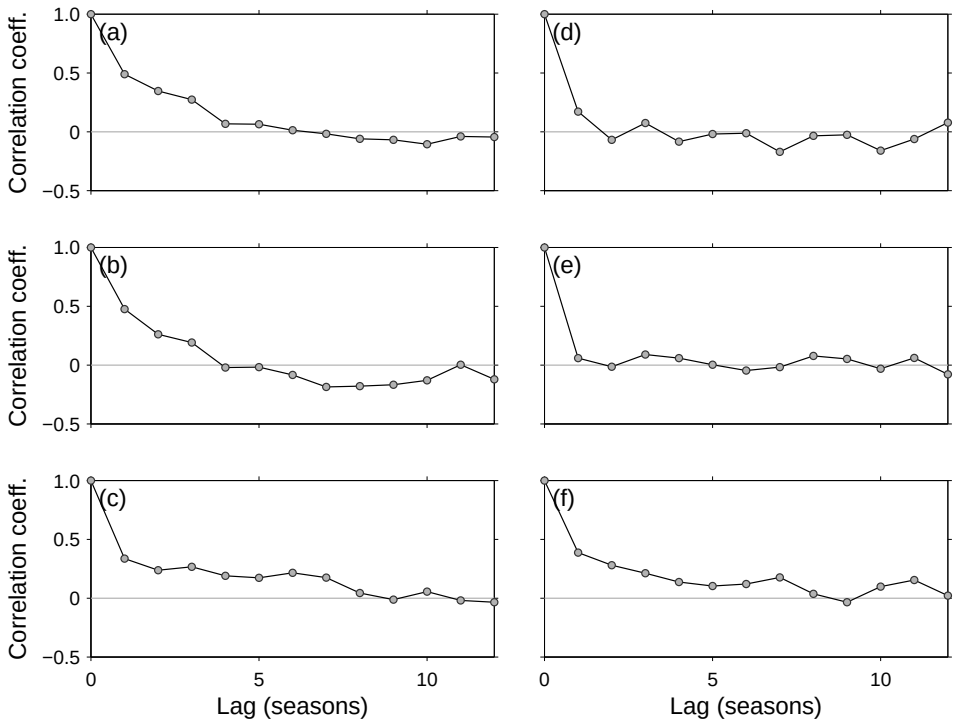

Figure 6.7: Autocorrelation functions for seasonally-averaged time series of (a) subtropical SST anomalies, (b) Subantarctic SST anomalies, (c) the temperature differential across the S-STF, (d) the basin-wide South Pacific wind stress curl, (e) the local-scale southern New Zealand zonal wind stress and (f) the local-scale southern New Zealand wind stress curl.

6.3.2.3 The Modified Chelton method

In this Chapter, the hypothesis test (i.e. the derivation of r_{crit} in Eq. 6.3) is adjusted using an effective number of degrees of freedom, N_*, estimated by the modified Chelton method (Pyper and Peterman, 1998). The modified Chelton method adjusts the null hypothesis test of correlations between two autocorrelated time series (Eq. 6.3) through estimating the effective number of degrees of freedom (N_*) (rather than N in eq. 6.3). The modified Chelton method has been successfully applied in numerous analyses of oceanic and climate time series that are similar to those conducted in the present study (see e.g. Beaugrand and Reid, 2003; Richardson and Schoeman, 2004; Li et al., 2012, 2013, 2015; Boehme et al., 2014).

Using the modified Chelton method (Pyper and Peterman, 1998), the effective number of degrees of freedom, N_*, was calculated using the following estimator:

$$\frac{1}{N_*} \approx \frac{1}{N} + \frac{2}{N} \sum_{j=1}^{\infty} r_{XX}(j) r_{YY}(j), \tag{6.5}$$

where N is the sample size and $r_{XX}(j)$ and $r_{YY}(j)$ are the autocorrelation estimators of the two time series being correlated (i.e. $\mathbf{X}_t$ and $\mathbf{Y}_t$). The autocorrelation estimators were evaluated over the first $N/5$ lags (i.e. $j = 1$ to $N/5$) using the estimator

$$r_{XX}(\tau) = \frac{N}{N-\tau} \times eq.2. \tag{6.6}$$

Monte Carlo experiments undertaken by Pyper and Peterman (1998) demonstrate that evaluating the autocorrelation function over the first $N/5$ lags offers accurate error rates on the null hypothesis test across a broad range of autoregressive time series models. Here, "error rate" refers to the probability of incorrectly rejecting (type-I error) or accepting (type-II error) the null hypothesis - of no statistically significant correlation between two time series - being greater than the specified α (Pyper and Peterman, 1998). The autocorrelation estimator in Eq. 6.6 is used in this study because it is less biased for (i) shorter time series, (ii) longer autocorrelations and (iii) produces slightly more conservative values of N_* relative to the standard estimator (Eq. 6.4), thus further reducing error rates (Pyper and Peterman, 1998).

Given N_*, the critical value r_{crit} for the null hypothesis of no correlation between two autocorrelated time series at all lags, at the α significance level, is derived using the t distribution for a two tailed test (Zar, 1998) using $N_* - 2$ degrees of freedom (Pyper and Peterman, 1998).

To summarize, cross-correlations were computed between detrended, seasonally-averaged time series using Eq. 6.2. The statistical significance of the cross-correlation between two time series is assessed using a Student's t test at the 95% confidence level ($\alpha = 0.05$). To account for autocorrelation in the time series, an effective number of degrees of freedom (N_*) at each τ is calculated following the modified Chelton method (Pyper and Peterman, 1998) (Eqs. 6.5-6.6), with critical values derived using Eq. 6.3 to test the significance of cross-correlations. Correlations were considered statistically significant if they exceed critical values evaluated at the $\alpha = 0.05$ (i.e. 95%) confidence interval.

6.3.3 Lag-correlation maps

To investigate further the relationship between the SST variability across the S-STF and South Pacific winds, lag-correlation maps were calculated. To create a lag-correlation map, 30 year (1982-2011) seasonally-averaged time series of wind stress data were calculated at each grid point from the NCEP reanalysis. The long term seasonal means were then removed and the time series were detrended. Cross-correlation and significance testing was then performed between the frontal time series and the each grid point time series of wind data, following the procedures described above. Each lag-correlation map shows the correlation coefficients between the frontal time series and each grid point time series of wind data for one time lag.

6.3.4 Linear trends

Linear trends were estimated for time series data using the slope of a straight line fit to time series data using the method of least squares linear regression (Emery and Thomson, 2001). For a time series $y_i (i = 1,2,...,N)$, with data collected at times $x_i (i = 1,2,...,N)$, the least squares estimate of the linear trend in y_i minimizes the squared differences between y_i and the regression line $\hat{y}_i$,

$$\hat{y}_i = b_0 + b_1 x_i, \tag{6.7}$$

where b_0 is the intercept of the regression line with the y axis and b_1 is the slope of the regression line. Estimates of b_0 and b_1 ($\hat{b}_0$ and $\hat{b}_1$, respectively) are found using the least squares estimators:

$$\hat{b_1} = \frac{\sum_{i=1}^{N}(x_i - \bar{x})(y_i - \bar{y})}{\sum_{i=1}^{N}(x_i - \bar{x})^2}, \tag{6.8}$$

$$\hat{b_0} = \bar{y} - \hat{b_1}\bar{x}. \tag{6.9}$$

The statistical significance of linear trends in the monthly-resolution time series (Section 6.2.2, 6.2.4) was assessed using a technique described by Santer et al. (2000) that compensates for temporal autocorrelation. Below, a classical method to assess the statistical significance of the trend is described. Then, the modifications made to compensate for temporal autocorrelation are described.

The regression residuals, e_i, from $\hat{y}_i$ are defined as:

$$e_i = y_i - \hat{y}_i. \tag{6.10}$$

Assuming values of e_i are statistically independent, the standard error of $\hat{b}_1$ is defined as:

$$s_b = \frac{s_e}{\left[\sum_{i=1}^{N}(x_i - \bar{x})^2\right]^{1/2}} \tag{6.11}$$

where s_e^2 is the variance of the residuals about the regression line, which is given by:

$$s_e^2 = \frac{1}{N-2}\sum_{i=1}^{N} {e_i}^2. \tag{6.12}$$

To test whether a trend in y_i ($\hat{b}_1$) is significantly different from zero, the t ratio, t_b, between the estimated trend and its standard error is computed:

$$t_b = \hat{b}_1 / s_b. \tag{6.13}$$

Assuming that t_b is distributed as Student's t, t_b is then compared with a critical t value, t_{crit}, derived using the t distribution for two-tailed tests for a given significance level α and degrees of freedom $N-2$:

$$t_{crit} = t_{\alpha/2,N-2}. \tag{6.14}$$

If t_b exceeds t_{crit}, the null hypothesis $b = 0$ is rejected and the trend is considered significant from zero ($b \neq 0$) at the α significance level. Confidence intervals for $\hat{b}_1$ at the $100(1-\alpha)\%$ confidence level were derived as:

$$\hat{b} \pm t_{\alpha/2,N-2} \frac{s_e}{\sum_{i=1}^{N}(x_i - \bar{x})^2}. \tag{6.15}$$

In subsequent sections, confidence intervals obtained using Eq. 6.15 are presented. The interpretation of these confidence intervals is that if the confidence intervals include zero, then the trend cannot be considered significantly different from zero at the $100(1-\alpha)\%$ confidence level (i.e. the null hypothesis that $b_1 = 0$ is accepted). If the confidence intervals do not include zero, there is evidence that a linear trend is significantly different from zero at the $100(1-\alpha)\%$ confidence level (i.e. the alternative hypothesis that $b_1 \neq 0$ is accepted).

The significance testing approach described above assumes that values of e_i are statistically independent. To test this assumption, linear trends were calculated for each of the monthly-resolution time series (Section 6.2.2, 6.2.4) using Eqs. 6.7-6.9, and their regression residuals (e_i) from $\hat{y}_i$ were obtained (Eq. 6.10). The autocorrelation coefficients of the regression residuals were then obtained using Eq. 6.4, and are shown in Fig. 6.8. The lag-1 autocorrelation coefficients of the regression residuals exhibit moderate levels of autocorrelation (persistence) (Fig. 6.8), indicating that the regression residuals are not statistically independent - as is assumed when calculating the variance and standard error in Eqs. 6.11-6.12 above. For the purposes of this study, the hypothesis testing procedure described above needs to therefore be modified, else the significance testing procedure described above will yield too frequent rejection of the null hypothesis $b = 0$ (Santer et al., 2000) - i.e. the confidence intervals will be too small.

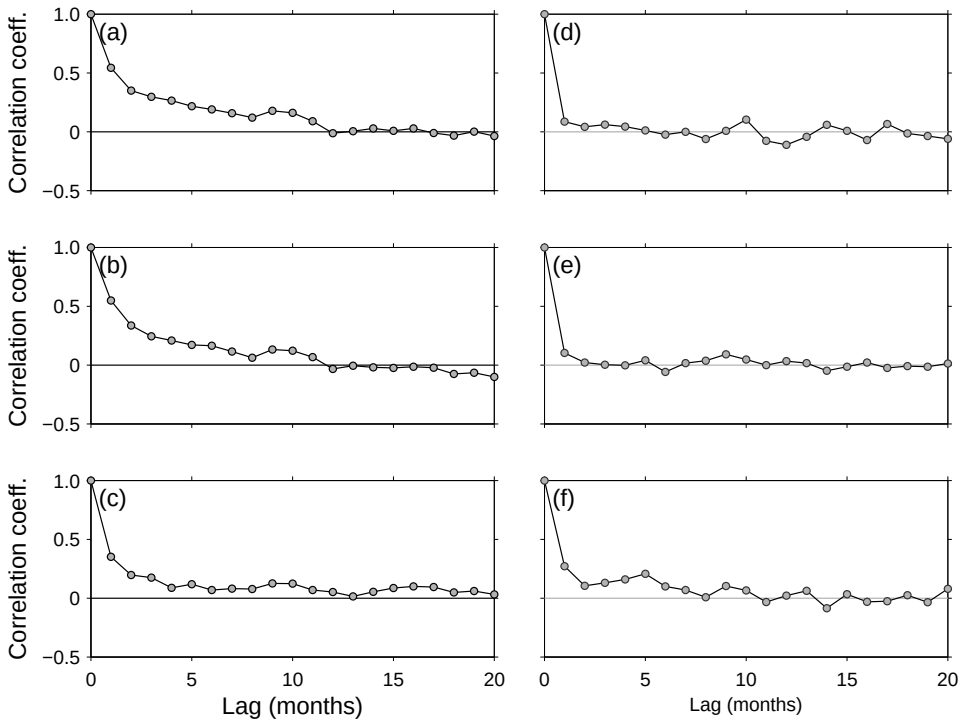

Figure 6.8: Autocorrelation functions for monthly-averaged time series of (a) subtropical SST anomalies (Fig. 6.4a), (b) Subantarctic SST anomalies (Fig. 6.4b), (c) the temperature differential across the S-STF (Fig. 6.4c), (d) the basin-wide South Pacific wind stress curl (Fig. 6.6a), (e) the local-scale New Zealand zonal wind stress (Fig. 6.6b) and (f) the local-scale New Zealand wind stress curl (Fig. 6.6c).

A common technique in the meteorological and oceanographic literature for compensating for the presence of autocorrelation in trend analysis (see e.g. Bartlett, 1935; Mitchell et al., 1966; Bretherton et al., 1999; Santer et al., 2000) is to treat the residuals from the regression line as an AR(1) process and substitute N in the above approach with an effective number of degrees of freedom, N_{eff}, based on r_1, the lag-1 autocorrelation coefficient of e_i:

$$N_{eff} \approx N \times \frac{1-r_1}{1+r_1}. \tag{6.16}$$

In this study, linear trends were estimated for monthly-resolution time series using Eq. 6.7-6.9, then the lag-1 autocorrelation coefficient of e_i was obtained using Eq. 6.4. The hypothesis testing procedure described above was then modified by substituting the effective number of degrees of freedom (N_{eff}) (Eq. 6.16) for N in Eq. 6.12, to obtain 'adjusted' estimates of the standard deviation of regression residuals (s'_e), standard error (s'_b) and t ratio (t'_b). Critical values and confidence intervals were then obtained using Eqs. 6.14-6.15 with $N_{eff}-2$ degrees of freedom.

6.4 Results Part 1: Influence of South Pacific winds

In order to understand whether changes in basin-wide South Pacific wind stress curl contribute to interannual SST variability south of New Zealand, the relationships between frontal time series and wind time series are now evaluated using cross correlations. Several recent studies have found that changes in wind stress curl over the South Pacific can significantly modulate SSTs in the western boundary current system of the South Pacific subtropical gyre (e.g. Hill et al., 2008, 2011; Wu et al., 2012; Fernandez et al., 2014; Oliver and Holbrook, 2014). The focus here is to investigate whether similar links exist around southern New Zealand.

6.4.1 Basin-scale wind stress curl

Statistically significant cross-correlations are observed between subtropical SST anomalies and basin-wide South Pacific wind stress curl (Fig. 6.9a).

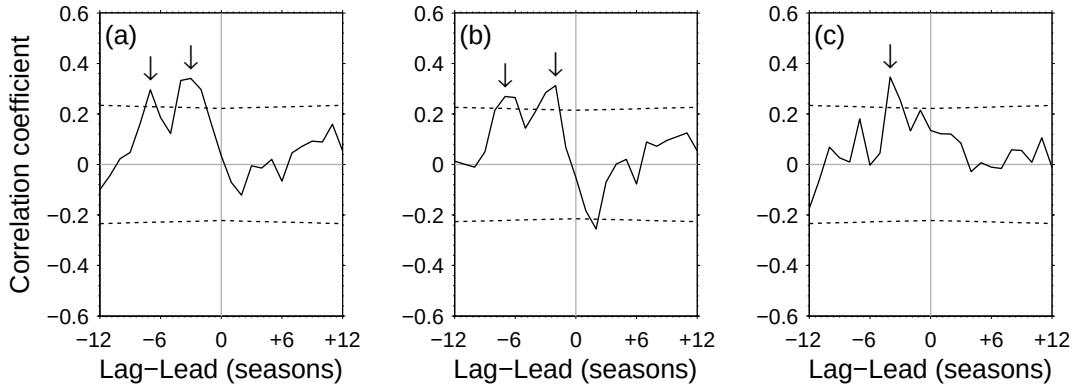

Figure 6.9: The cross-correlation function between the seasonally-averaged frontal time series and the basin-wide South Pacific wind stress curl. Shown are the cross-correlations between (a) subtropical SST anomalies and the basin-wide wind stress curl, (b) Subantarctic SST anomalies and the basin-wide wind stress curl and (c) the temperature differential across the S-STF and the basin-wide wind stress curl. A negative (positive) time-lag indicates the frontal time series lagging (leading) the wind time series. The dashed lines correspond to the 95% confidence levels assessed using the modified Chelton method (Section 6.3.2). Arrows highlight significant peak correlations that are referred to in the text.

The maximum cross-correlations occur at a time lag of three seasons ($r = 0.35$, $p < 0.05$) and at a time-lag of seven seasons ($r = 0.30$, $p < 0.05$). Similarly, the cross-correlation between Subantarctic SST anomalies and basin-wide wind stress curl (Fig. 6.9b) show two statistical significant peaks. Here, maximum correlation coefficients are observed at a time lag of two seasons ($r = 0.31$, $p < 0.05$) and at a time lag of seven seasons ($r = 0.27$, $p < 0.05$). A statistically significant cross-correlation is also observed between the temperature differential across the S-STF and the wind stress curl, with a maximum correlation coefficient at a time lag of four seasons (Fig. 6.9c, $r = 0.35$, $p < 0.05$). The positive sign of

the cross-correlation coefficients indicate that positive wind stress curl anomalies over the South Pacific are followed approximately 9 and 21 months later by positive subtropical SST anomalies, and approximately 6 and 21 months later by positive Subantarctic SST anomalies. Similarly, positive wind stress curl anomalies over the South Pacific are followed approximately 12 months later by an increase in the temperature differential across the S-STF.

To investigate further the relationship between SST variability across the S-STF around southern New Zealand and the wind stress curl over the South Pacific, lagged-correlation maps were calculated. Figure 6.10 show the correlation coefficients between the frontal time series and gridded wind stress curl anomalies from the NCEP reanalysis at time-lags when peak cross-correlations were observed (Fig. 6.9).

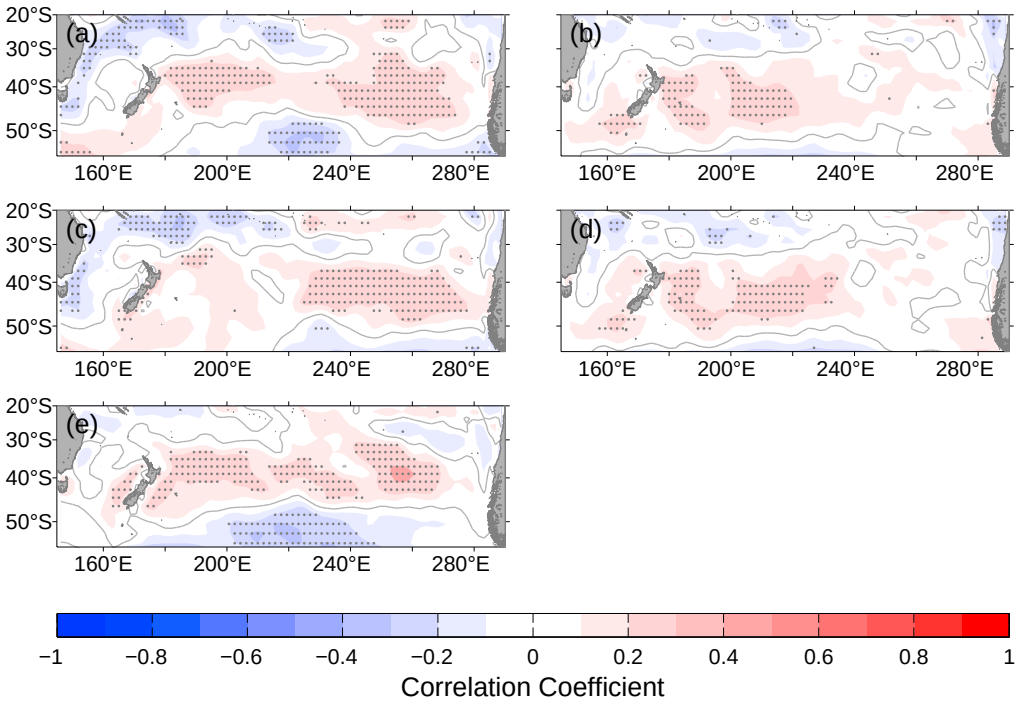

Figure 6.10: Lag correlation map of wind stress curl onto the frontal time series of (a-b) subtropical SST anomalies, (c-d) Subantarctic SST anomalies and (e) the temperature differential across the S-STF using seasonally-averaged time series. The lag in (a) is three seasons, the lag in (b) is seven seasons, the lag in (c) is two seasons, the lag in (d) is seven seasons and the lag in (e) is four seasons, with the wind stress curl leading. The lag-times in (a-e) correspond to the locations of significant peaks in the cross-correlation functions shown in Fig. 6.8 that are highlighted by arrows. Correlations that are statistically significant at the 0.05 level are plotted as black dots, and are assessed using the modified Chelton method (Section 6.3.2).

All of the lag correlation maps show bands of positive and statistically significant correlation coefficients that extend well east of New Zealand, between the latitudes of approximately 30-50°S. The lag-correlation maps also show marked spatial structure. In the three season lag-correlation map between subtropical SST anomalies and wind stress curl, the

highest, and statistically significant, positive correlations ($r > 0.3$, $p < 0.05$) are observed over a broad region to the east of New Zealand (190-200°E) and also in the eastern South Pacific (260°E) (Fig. 6.10a). The two-season lag-correlation map between Subantarctic SST anomalies and wind stress curl show a similar region of significant correlation in the eastern South Pacific, but the band of significant positive correlations immediately east of New Zealand is markedly smaller and contracted toward the equator (Fig. 6.10b). The seven season lag-correlation maps between subtropical SST anomalies, Subantarctic SST anomalies and wind stress curl (Fig. 6.10c-d) show highest positive correlations immediately east of New Zealand (180-190°E) and over the eastern South Pacific (250-270°E) ($r = 0.2$-0.3, $p < 0.05$). Correlations are generally weaker and not statistically significant, at the 95% confidence level, over the remainder of the South Pacific (Fig. 6.10c-d). In the four-season lag correlation map between the temperature differential across the S-STF and wind stress curl, the highest statistically significant positive correlations ($r > 0.2$, $p < 0.05$) are observed over an approximately 15 degree latitudinal band (30-45°S) of the South Pacific to the east of New Zealand.

Overall, these findings show that SST variability across the S-STF around southern New Zealand is significantly lag-correlated with wind stress curl over the South Pacific, east of New Zealand. In the following sections, further cross-correlation analyses are conducted to help understand whether these correlations more likely to be the result of a direct relationship or an indirect relationship involving the 'local' wind field. Cross-correlations are used to examine the relation between SST variability across the S-STF around southern New Zealand and the local-scale southern New Zealand zonal wind stress (Section 6.4.2) and the local-scale southern New Zealand wind stress curl (Section 6.4.3).

6.4.2 Local-scale zonal wind stress

Cross correlations between the SST variability across the S-STF around southern New Zealand and local-scale New Zealand zonal wind stress are shown in Figure 6.11. Statistically significant negative cross-correlations are found for subtropical SST anomalies, Subantarctic SST anomalies and the temperature differential across the S-STF, with zonal wind stress. The maximum cross-correlations are observed when subtropical SST anomalies ($r = -0.49$, $p < 0.05$), Subantarctic SST anomalies ($r = -0.43$, $p < 0.05$) and the temperature differential across the S-STF ($r = -0.34$, $p < 0.05$) lag the zonal wind stress by one season (Fig. 6.11). Westerly (easterly) wind stress anomalies around southern New Zealand are followed one season later by negative (positive) subtropical and Subantarctic SST anomalies, and by a decrease in the temperature differential across the S-STF.

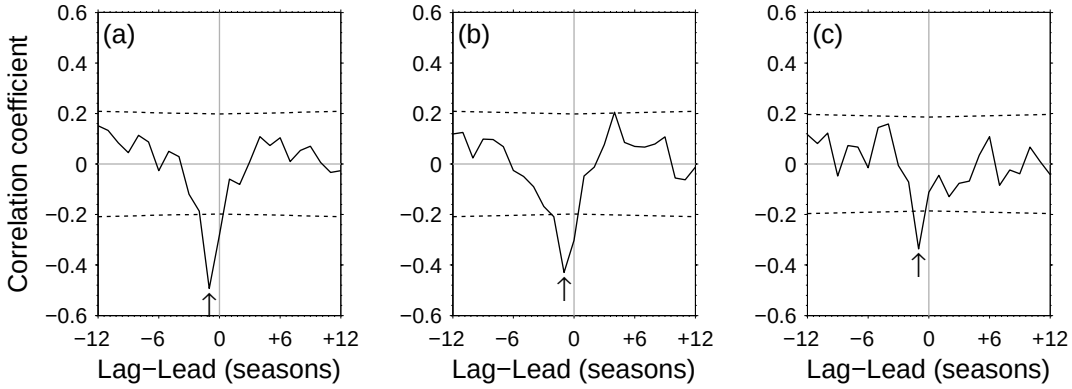

Figure 6.11: The cross-correlation function between the seasonally-averaged frontal time series and the local-scale New Zealand zonal wind stress. Shown are the cross-correlations between (a) subtropical SST anomalies and zonal wind stress, (b) Subantarctic SST anomalies and zonal wind stress and (c) the temperature differential across the S-STF and the zonal wind stress. A negative (positive) time-lag indicates the frontal time series lagging (leading) the wind time series. The dashed lines correspond to the 95% confidence levels assessed using the modified Chelton method (Section 6.3.2). Arrows highlight significant peak correlations that are referred to in the text.

The strength of the cross-correlations between SST variability across the S-STF around southern New Zealand and the local-scale New Zealand zonal wind stress are intriguing. Variability of subtropical and Subantarctic SSTs is more strongly correlated with local-scale New Zealand zonal wind stress (correlation coefficients of -0.43 to -0.49), than with the basin-wide South Pacific wind stress curl (correlation coefficients of 0.31-0.35) (Section 6.4.1), which was the original focus of this study. To investigate further the correlations between the SST variability across the S-STF and zonal wind stress around southern New Zealand, one-season lag-correlation maps were calculated between the frontal time series and gridded zonal wind stress from the NCEP reanalysis over the New Zealand region (Fig. 6.12).

The lag-correlation maps between subtropical SST anomalies and Subantarctic SST anomalies with zonal wind stress show similar spatial patterns, with statistically significant negative correlations ($r < -0.4$) observed around southern New Zealand and extending to the west of New Zealand over Tasman Sea between about 42-48°S. The correlations between subtropical and Subantarctic SST anomalies with zonal wind stress are also locally stronger in the New Zealand region. Subtropical SST anomalies are most strongly negatively correlated with zonal wind stress along, and to north of, the STFZ in the Tasman Sea (Hamilton, 2006), with a maxima in the eastern Tasman Sea (correlation coefficient greater than 0.5, centered on 44°S, 166°E).

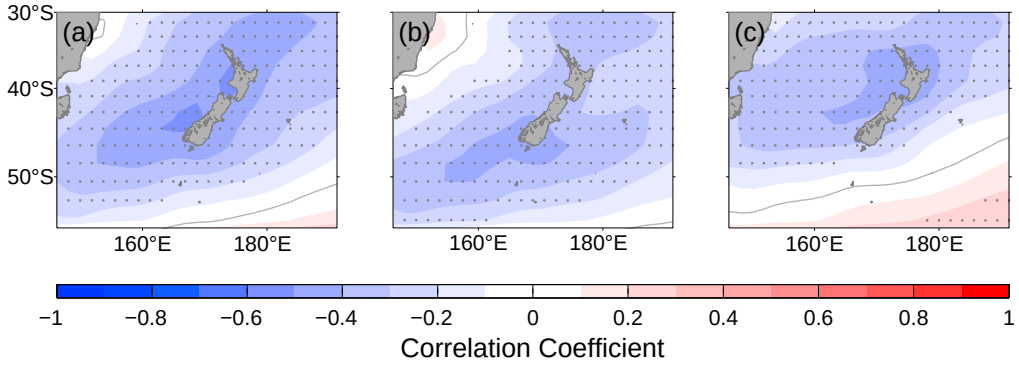

Figure 6.12: Lag correlation map of zonal wind stress onto the frontal time series of (a) subtropical SST anomalies (b) Subantarctic SST anomalies and (c) the temperature differential across the S-STF using seasonally-averaged time series. The lag in (a-c) is one season with the zonal wind stress leading. Correlations that are statistically significant at the 0.05 level are plotted as black dots, and are assessed using the modified Chelton method (Section 6.3.2).

In contrast, Subantarctic SST anomalies are most strongly negatively correlated (correlation coefficient 0.3 to 0.4) with zonal wind stress within and south of the STFZ in the Tasman Sea and around southern New Zealand (between approximately 44-50°S, 155-173°E). The lag-correlation map between the temperature differential across the S-STF and zonal wind stress show a similar spatial pattern to that noted between subtropical SST anomalies and zonal wind stress, with the area of strongest negative correlations (correlation coefficient greater than 0.4) observed over STW in the eastern Tasman Sea, north of the S-STF (centered on approximately 40°S, 170°E).

These results suggest that both changes of wind stress in the southern Tasman Sea (this Section) and wind stress curl over the central and eastern South Pacific (Section 6.4.1) may be contributing to interannual SST variations around southern New Zealand. These possibilities are explored further in Section 6.5.

6.4.3 Local-scale wind stress curl

Cross correlations between SST variability across the S-STF around southern New Zealand and local-scale New Zealand wind stress curl are shown in Figure 6.13.

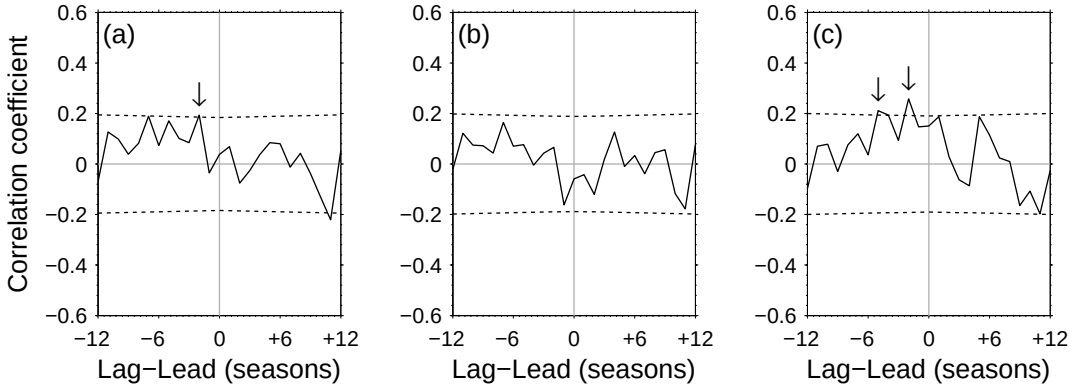

Figure 6.13: The cross-correlation function between the seasonally-averaged frontal time series and the local-scale southern New Zealand wind stress curl. Shown are the cross-correlations between (a) subtropical SST anomalies and the wind stress curl, (b) Subantarctic SST anomalies and the wind stress curl and (c) the temperature differential across the S-STF and the wind stress curl. A negative (positive) time-lag indicates the frontal time series lagging (leading) the wind time series. The dashed lines correspond to the 95% confidence levels assessed using the modified Chelton method (Section 6.3.2). Arrows highlight significant peak correlations that are referred to in the text.

Overall, the cross-correlations are weaker than those noted between SST variability across the S-STF and both the basin-average South Pacific wind stress curl (Section 6.4.1) and the local-scale southern New Zealand zonal wind stress (Section 6.4.2). Statistically significant positive cross-correlations are observed between subtropical SST anomalies and the S-STF temperature differential with the local-scale New Zealand wind stress curl. The maximum cross-correlation between subtropical SST anomalies and wind stress curl (Fig. 6.13a) are observed when the subtropical SST anomalies lag the wind stress curl by two seasons ($r = 0.19$, $p < 0.05$). The maximum cross-correlations between the temperature differential across the S-STF and wind stress curl (Fig. 6.13c) are observed when the S-STF temperature differential lags the wind stress curl by two seasons ($r = 0.26$, $p < 0.05$) and by five season ($r = 0.21$, $p < 0.05$). No statistically significant lag-correlations are identified between Subantarctic SST anomalies and the wind stress curl around southern New Zealand. (Fig. 6.13b). These results suggest that variations in wind stress curl around southern New Zealand do not contribute significantly to the interannual variations of SST in this area.

6.4.4 Co-variability of wind stress and wind stress curl

Cross-correlation is now used to examine the strength and direction of the relationship between variability in the local-scale southern New Zealand wind stress and wind stress curl, and the basin-wide South Pacific wind stress curl. Figure 6.14 shows the cross-correlation between the local-scale southern New Zealand zonal wind stress (Fig. 6.6b) and wind stress curl (Fig. 6.6c), with the basin-wide South Pacific wind stress curl (Fig. 6.6a).

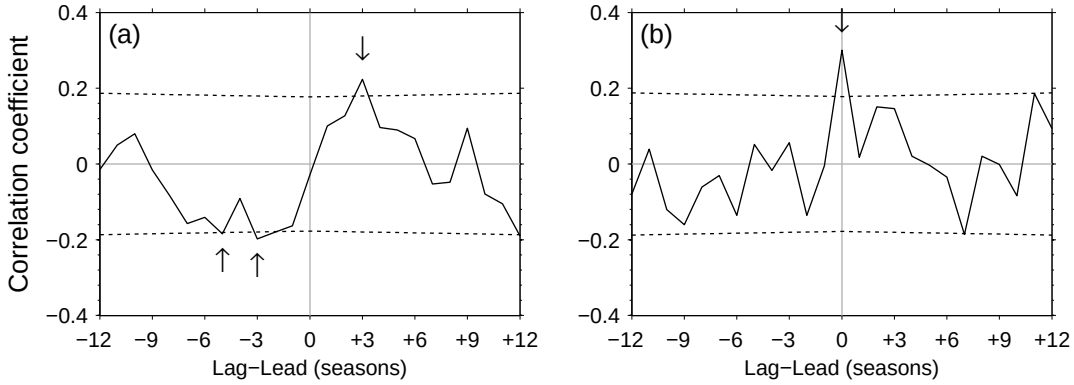

Figure 6.14: (a) The cross-correlation function between the time series of the seasonally-averaged local-scale southern New Zealand zonal wind stress and the basin-wide South Pacific wind stress curl. (b) The cross-correlation function between the time series of the seasonally-averaged local-scale southern New Zealand wind stress curl and the basin-wide South Pacific wind stress curl. The dashed lines correspond to the 95% confidence levels assessed using the modified Chelton method (Section 6.3.2). Arrows highlight significant peak correlations that are referred to in the text.

Statistically significant cross-correlations are observed between the zonal wind stress around southern New Zealand and the basin-wide South Pacific wind stress curl at a lag of three seasons ($r = -0.20$, $p < 0.05$) and at a lead of three seasons ($r = 0.22$, $p < 0.05$) (Fig. 6.14a). A statistically significant cross-correlation is also observed between the wind stress curl around southern New Zealand and the basin-wide South Pacific wind stress curl at zero lag ($r = 0.3$, $p < 0.05$) (Fig. 6.14b). These results indicate that there is an element of co-variability between the basin-wide South Pacific wind stress curl and the local-scale southern New Zealand wind stress and wind stress curl. The results of these cross-correlations are used below in Section 6.5 to help interpret the relationships observed between SST variability across the S-STF around southern New Zealand and the basin-wide South Pacific wind stress curl.

6.4.5 A stronger wind-driven influence on subtropical waters?

It is interesting to note that the temperature differential across the S-STF, like subtropical and Subantarctic SST anomalies, is correlated with variations in both the local and basin-wide winds over the South Pacific (Sections 6.4.1, 6.4.2). To help understand why, lag-regressions were used to examine further the relationship between subtropical and Subantarctic SST anomalies with the local and basin-wide South Pacific winds.

Linear (1st order) regressions were performed for the time series of seasonally-averaged (a) local-scale southern New Zealand zonal wind stress anomalies and (b) basin-wide South Pacific wind stress curl onto the time series of seasonally-averaged subtropical and Subantarctic SST anomalies. In (a), the frontal time series were lagged from the wind time series by one season to match the time-scale of the peak cross-correlations (Fig. 6.11) and in (b) the frontal time series were lagged from the wind time series by three seasons (Fig. 6.9).

For a 1 standard deviation positive zonal wind stress anomaly around southern New Zealand, subtropical SST anomalies decrease by 0.26°C, while Subantarctic SST anomalies decrease by 0.17°C. For a one standard deviation positive basin-wide South Pacific wind stress curl anomaly, subtropical SST anomalies increase by 0.22°C, while Subantarctic SST anomalies increase by 0.11°C. In other words, there appears to be a stronger change in subtropical as opposed to Subantarctic SST anomalies, given the same variability in winds over the South Pacific. Variability in the temperature differential across the S-STF will depend on the relative difference between subtropical and Subantarctic SST anomalies. Thus, these results suggest that correlations between variability in S-STF temperature differential and winds over the South Pacific reflect a stronger influence of winds over the South Pacific on subtropical SSTs, as opposed to Subantarctic SSTs.

6.5 Wind-driven influences on SSTs around southern New Zealand

A growing body of evidence suggests that changes in basin-wide wind stress curl over the South Pacific have a pronounced impact on SSTs and circulation in the South Pacific subtropical gyre (see e.g. Cai, 2006; Roemmich et al., 2007; Hill et al., 2008, 2011; Sasaki et al., 2008; Holbrook et al., 2011; Wu et al., 2012; Fernandez et al., 2014; Oliver and Holbrook, 2014). However, to date studies have mainly focused on the western boundary current system, and have not examined in detail the possibility of similar wind-driven influences on the hydrographic conditions at the STF in the Tasman Sea. The 30 year time series (1982-2011) of remotely sensed SST data, together with reanalysis wind data, enabled an investigation as to whether SST variability across the S-STF around southern New Zealand is influenced by basin-wide South Pacific wind stress curl in a similar manner.

Overall, the results in Section 6.4 suggest that basin-wide South Pacific wind stress curl and zonal wind stress around southern New Zealand play a significant role in SST variability across the S-STF around southern New Zealand. Using cross-correlations, the strongest correlations were found between SST variability across the S-STF and zonal wind stress around southern New Zealand, and the second strongest with variability in basin-wide South Pacific wind stress curl. Although correlations were also identified with variability in wind stress curl around southern New Zealand, these were markedly weaker, suggesting any role local wind stress curl might play in SST variability across the S-STF in this area is more minor and therefore, this aspect is not discussed further.

6.5.1 Relation to local-scale wind stress

Using cross-correlations, statistically significant negative lag-correlations were found between SST variability across the S-STF and the zonal wind stress in the southern Tasman Sea and around southern New Zealand (40-50°S, 155-180°E, Fig. 6.11). Peak correlations occur when the frontal time series lag zonal wind stress anomalies by one season. The zonal wind stress over the southern Tasman Sea and Campbell Plateau is predominantly westerly, thus, surface temperatures in the waters bordering the S-STF around southern New Zealand are anomalously warm (cold), and the temperature differential across the S-STF is anomalously strong (weak), following easterly (westerly) wind stress anomalies.

These results are consistent with previous studies that examined variability in Southern Hemisphere ocean circulation and SST anomalies in relation to variability of the Southern Annular Mode (Hall and Visbeck, 2002; Lovenduski and Gruber, 2005; Sen Gupta and England, 2006). For instance, Hall and Visbeck (2002) show results based on numerical model experiments that indicate positive phases of the SAM - which are also characterised by positive westerly wind anomalies over the Southern Hemisphere between 45-70°S – are negatively correlated with SST anomalies at the approximate latitudes (46-49°S) of S-STF around southern New Zealand (see Fig. 9 in Hall and Visbeck, 2002), similar to the relationships observed in the present study. The observational findings from the present study also agree with results from an earlier study by Rintoul and England (2002), which focused on the role played by Ekman transport caused by anomalous zonal wind stress in driving T-S variability in SAMW. Rintoul and England (2002) show results based on output from 1000 years of coupled climate model simulations that indicate statistically significant negative correlations between variability in modelled, annual-mean SSTs at model grid points between 35-60°S and zonal wind stress 2° south of these grid points, consistent with the sign of the correlations reported in the present study around southern New Zealand (46-49°S).

6.5.2 A link through Ekman transport?

The significant correlations found between subtropical and Subantarctic SST anomalies with variations in zonal wind stress around southern New Zealand raises the question of what might have caused them? A possibility is that the SST variability is driven by variations in zonal wind stress via meridional Ekman transport. Rintoul and England (2002) suggest that in regions where strong winds blow parallel to an ocean front, the resulting cross-frontal Ekman transport of cooler (or warmer) waters might be anticipated to make a significant contribution to the upper ocean temperature and salinity variability. Conditions similar to those described by Rintoul and England (2002) are present within the STFZ in the southern Tasman Sea and around southern New Zealand; at 40-50°S, the prevailing westerly winds

drive a northward Ekman transport of cool Subantarctic surface waters across the S-STF and into the STFZ over the southern Tasman Sea (Hamilton, 2006).

The results from this study also suggest the occurrence of negative (positive) subtropical and Subantarctic SST anomalies around southern New Zealand following positive (negative) zonal (westerly) wind stress anomalies (Fig. 6.11a-b). This is consistent with the cooling (warming) that one would expect to result from an increase (decrease or reversal) in the northward transport of cooler surface waters into the STFZ via an Ekman mechanism (Rintoul and England, 2002). It is further noted that the mean-meridional gradients of SST in the Tasman Sea are nearly twice as strong on the subtropical side of the STF (0.76°C 100 km^{-1}) than on the Subantarctic side of the STF (0.44°C 100 km^{-1}) (Uddstrom and Oien, 1999). Stronger meridional gradients of SST on the subtropical side of the STF would be expected to enhance the effect of wind-driven Ekman transport on subtropical SST anomalies compared to those in Subantarctic waters (Hall and Visbeck, 2002). In line with this expectation, for a one-sigma positive anomaly in zonal wind around southern New Zealand, subtropical SST anomalies were found to decrease more strongly (-0.26°C) than Subantarctic SST anomalies (-0.17°C) (Section 6.4.5), further suggestive that Ekman transport may play an important role in the correlations observed between zonal wind stress and SST variability around southern New Zealand.

Another interesting finding from this study is that the peak cross-correlation between subtropical and Subantarctic SST anomalies with regionally-averaged zonal wind stress occur at a time lag of one season (Fig. 6.11). Although the reason for this time lag is not clear, a similar time lag of one season has previously been noted by Hopkins et al. (2010) between SST variability in the Southland Front and ENSO indices. ENSO variability is known to be linked to the occurrence of large SST anomalies in the Coral Sea and northern Tasman Sea (Mullan, 1998), and Hopkins et al. (2010) speculated that a southward advection of SST anomalies in these regions towards New Zealand might play a role in the lagged correlations they observed between ENSO variability and the temperature of the Southland Front.

The results presented here demonstrate that SST variability across the S-STF around southern New Zealand is negatively correlated with the previous seasons zonal wind stress both around southern New Zealand and to west of New Zealand over the STFZ in the southern Tasman Sea (Fig. 6.12a-b). Given that these regions of strong correlation extend west of New Zealand, over a region of predominantly eastward zonal surface currents (Stramma et al., 1995; Mullan, 1998; Ridgway and Dunn, 2003), it seems plausible that advection of SST anomalies generated by zonal wind stress anomalies over the Tasman Sea may play a role in the one season time lags observed between wind and frontal variability in the present study.

6.5.3 Relation to basin-wide wind stress curl

Similar to the findings of previous studies of wind-driven variability in the EAC extension and the wider south Pacific gyre (e.g. Qiu and Chen, 2006; Roemmich et al., 2007; Hill et al., 2008, 2011; Holbrook et al., 2011; Fernandez et al., 2014; Oliver and Holbrook, 2014), results from this study suggest that wind stress curl forcing east of New Zealand may also play a significant role in SST variability across the S-STF around southern New Zealand. Subtropical and Subantarctic SST anomalies are statistically significantly positively lag-correlated with basin-wide South Pacific wind stress curl, with peak correlations at a time-lag of two and three seasons, respectively. Weaker, secondary peak correlations are also evident at a time lag of seven seasons (Fig. 6.9a-b). In turn, variability in the temperature differential across the S-STF is also statistically significantly positively correlated with basin-wide South Pacific wind stress curl at a time-lag of four seasons (Fig. 6.9c).

The South Pacific is an area of positive wind stress curl (see e.g. Figure 2 in Cai, 2006) hence, the results in Figure 6.9 imply that subtropical and Subantarctic SSTs are anomalously warm, and the temperature differential across the S-STF is anomalously strong, two-to-four seasons following a strengthening of the basin-average positive wind stress curl. A similar thermal response in subtropical and Subantarctic SSTs is also implied at a time lag of seven seasons. However, these temperature changes at a lag of seven months are not accompanied by a change in the temperature differential across the S-STF, and their relation to changes in South Pacific wind stress curl are weaker than those noted at shorter time lags. The remainder of this section of the discussion focuses on the stronger coupling evident between the frontal time series and the South Pacific wind stress curl at a time lag of between two and four seasons.

6.5.4 A direct or indirect relationship?

It seems plausible that the correlations observed between SST anomalies at the S-STF around southern New Zealand and variations in the basin-wide South Pacific wind stress curl could arise in at least three ways:

- Scenario 1: they could be the result of a direct relationship to the basin-wide wind stress curl.
- Scenario 2: they could be the result of an indirect relationship, involving local-scale wind stress curl (i.e. the SST anomalies being related directly to variability in wind stress curl around southern New Zealand, which in turn, is co-varying with the basin-wide wind stress curl).

- Scenario 3: they could be the result of an indirect relationship, involving local-scale zonal wind stress (i.e. the SST anomalies being related directly to variability in zonal wind stress around southern New Zealand, which in turn, is co-varying with the basin-wide wind stress curl).

To assess the plausibility of these three scenarios, results from the cross-correlation analyses (Sections 6.4.1-6.4.4) are now briefly compared.

In terms of the likelihood of Scenario 2, there is significant co-variability between the basin-wide and local-scale wind stress curl at zero lag (r = 0.3, Fig. 6.14b). However, the correlations between subtropical and Subantarctic SST anomalies at the S-STF with variability of the basin-wide wind stress curl (r = 0.31 and 0.35, respectively; Section 6.4.1) are stronger compared to those with the local-scale wind stress curl (r = 0.19 and 0.26, respectively; Section 6.4.3). Thus, a direct relationship between the SST anomalies and the basin-wide wind stress curl (Scenario 1) seems more plausible than an indirect relationship involving local-scale wind stress curl (Scenario 2).

In terms of the likelihood of Scenario 3, there is also significant co-variability between the basin-wide wind stress curl and local-scale zonal wind stress at a time lag of three seasons (r = -0.2, Fig. 6.14a), with the basin-wide winds leading. It is further noted that the peak cross-correlations between SST anomalies at the S-STF and the local-scale winds occur at a time lag of one season (Fig. 6.11a-b), with the local winds leading. This together implies that the minimum time-scale for the conditions set out in Scenario 3 would be four seasons (i.e. local-winds co-varying with the basin-scale winds at a lag of three seasons and, in turn, influencing SSTs south of New Zealand with a lead of one season). Scenario 1, on the other hand, has time scales of between two and three seasons; SST anomalies at the S-STF are most strongly lag-correlated with the basin-wide wind stress curl at lags of two (Subantarctic waters) and three seasons (subtropical waters). Given that the minimum time scale of Scenario 3 exceeds that of Scenario 1, it seems more plausible that SST anomalies south of New Zealand are affected directly by variations in the basin-wide wind stress curl (Scenario 1), than through an indirect relationship involving variations in the local-scale wind stress (Scenario 3).

Taken together, these comparisons suggest that SST anomalies at the S-STF around southern New Zealand are more likely to be directly related to variations in the basin-wide South Pacific wind stress curl than through an indirect relationship, involving changes in the local wind field that co-vary with the basin-scale winds. In the next section, physical mechanisms that might be behind the lag-correlation observed between SST anomalies and variations in the basin-wide South Pacific wind stress curl are discussed.

6.5.5 A link through barotropic and baroclinic Rossby waves?

Links between SSTs and interannual variability in South Pacific wind stress curl have previously been reported in the western Tasman Sea (Hill et al., 2008, 2011). Hill et al. (2008) demonstrated that SSTs and SSSs observed in the EAC extension – approximately 1700 km west of the geographic region examined in the present study - are positively lag-correlated with interannual variations in South Pacific wind stress curl east of New Zealand at a lag of ~36 months. The results presented here show that a similar relationship between temporal variability in SSTs and South Pacific wind stress curl east of New Zealand exists around southern New Zealand. Intriguingly, this relationship exists at a shorter time lag than that observed in the EAC extension, at between 6-months (SAW) and 9-months (STW) months (Fig. 6.9-6.10). This suggests SSTs around southern New Zealand are responding to the wind-forcing prior to SSTs off the east coast of Tasmania.

Evidence from previous studies also suggests that the ~36-month lagged relationship between T and S anomalies in the western Tasman Sea with wind stress curl east of New Zealand reflects ocean adjustment (i.e. sea level, thermocline, transport) at the western boundary to changes in wind stress curl forcing (Hill et al., 2008; Ridgway et al., 2008), due to the arrival of baroclinic and/or barotropic Rossby waves (Hill et al., 2008, 2010; Ridgway et al., 2008). The possibility that SST variations south of New Zealand are also linked to ocean adjustments due to arrival of barotropic and/or baroclinic Rossby waves is examined below.

To explore possible links between SST around southern New Zealand and an ocean adjustment to wind forcing, the peak cross-correlations between South Pacific winds stress curl and temperatures in STW and SAW are first compared to the expected (theoretical) arrival time of barotropic and baroclinic Rossby waves at New Zealand. The areas of highest correlations between wind stress curl and temperatures in STW, SAW are found in the eastern South Pacific between 30-50°S, 240-280°E (Fig. 6.10). At 40°S, the predicted speeds for barotropic Rossby waves are of the order 2 ms^{-1} (Pedlosky, 1996) and for baroclinic Rossby waves, between 0.5-2 cms^{-1} (Killworth et al., 1997). From the centre of the area of highest correlations in the eastern South Pacific, the time required for these waves to propagate westward to reach the east coast of New Zealand (6740 km away) are 39 days (barotropic) and > 10.5 years (baroclinic) respectively. In comparison, the peak cross-correlations between temperatures in STW and SAW occur at 6 months and 9 months respectively (Fig. 6.9). The considerable mismatch between the time lag of peak cross-correlations and theoretical travel time of barotropic and baroclinic Rossby waves from the eastern South Pacific suggests that any connection between SST around southern New Zealand and ocean adjustment to wind stress curl forcing from the east of the basin is likely to be more complex than simply adjustment via barotropic or baroclinic Rossby waves alone.

To explore the causes behind the correlations between SST variations around southern New Zealand and wind forcing in the waters east of New Zealand further, the results of this study are next compared to the results from numerical model experiments by Hill et al. (2010). Hill et al. (2010) explored the mechanism responsible for the observed three year time lag between changes in South Pacific wind stress curl and property and transport changes in the EAC extension (Hill et al., 2008). Their numerical model experiments involved forcing an ocean general circulation model with an idealized, year long, positive anomaly of wind stress curl positioned east of New Zealand between approximately 35-50°S and 210-240°E. One the main reasons for examining the results of Hill et al. (2010) in this thesis is that this idealized anomaly is located within the area that was used in the present study to calculate the time series of the basin-average wind stress curl (Fig. 6.5). The forcing used by Hill et al. (2010) is also positioned immediately west of the areas where the highest correlations between subtropical (Subantarctic) SSTs and wind stress curl are found (Fig. 6.10a, c). Thus, results from Hill et al. (2010) can potentially provide additional insights into the oceanic adjustment of the South Pacific Ocean to variations of wind stress curl from the eastern South Pacific that are of interest here.

The idealized wind stress curl anomaly examined by Hill et al. (2010) produces barotropic and baroclinic Rossby waves. The barotropic waves propagate rapidly (< one month) to the western boundary at New Zealand (180°E) as a positive sea level anomaly. This sea level anomaly stalls offshore of the continental shelf of New Zealand for a period of approximately six months, during which time there is a conversion from barotropic energy to baroclinic energy at the topography, initiating a baroclinic wave. This baroclinic wave subsequently propagates anticlockwise around the coast of New Zealand as a coastally-trapped (Kelvin) wave and further to the south, crosses the Campbell Plateau. A positive sea level anomaly associated with the baroclinic wave subsequently builds along the west coast of the South Island of New Zealand and south of New Zealand, over the Campbell Plateau, 7 to 9 months after the peak wind stress curl forcing anomaly (see Fig. 7 of Hill et al., 2010). In turn, these sea level anomalies propagate westward across the Tasman Sea as a baroclinic Rossby wave, which takes approximately three years to reach Australia.

Interestingly, the timing of the oceanic adjustment around southern New Zealand (i.e. 7 to 9 months) to wind forcing in the central South Pacific, seen in the numerical model results of Hill et al. (2010), compares favorably with the peak lag-correlations observed here between variations of basin-wide South Pacific wind stress curl and temperatures in STW and SAW around southern New Zealand and (i.e. 6 to 9 months). Therefore, it seems possible that the links between subtropical and Subantarctic SSTs around southern New Zealand and basin-wide South Pacific wind stress curl involve a similar mechanism to that proposed by Hill et al. (2010), with ocean adjustment to the wind forcing via the propagation of

barotropic and baroclinic Rossby waves towards New Zealand, and the subsequent spawning of coastal Kelvin waves. Ideally, existing wave theory would also be used to predict the expected lag between wind forcing and subsequent ocean adjustment through the combined barotropic-baroclinic mechanism proposed by Hill et al. (2010); however, to best of the authors knowledge, a theoretical means of estimating the time delay in conversion between barotropic Rossby waves and baroclinic Rossby waves at sloping topography (as seen in model results of Hill et al., 2010) is not available at present.

The possibility described above opens a further question: how might an ocean adjustment around southern New Zealand to wind forcing impact on SSTs? Given that propagating barotropic and baroclinic waves will impact on gradients of sea level along their westward propagation pathway (e.g. Chelton and Schlax, 1996) and hence, geostrophic flow (e.g. Brown et al., 2001), one possibility is that there may be changes in the horizontal advection of heat around southern New Zealand. Another way in which an ocean adjustment to wind forcing may influence SSTs is through displacements of isotherm depths. Barotropic and baroclinic waves forced by positive (negative) wind stress curl anomalies lead to a deepening (shoaling) of the thermocline (e.g. Chelton and Schlax, 1996; Tomczak and Godfrey, 2003; Fedorov and Brown, 2009) and subsequently, a warming (cooling) of the subsurface layer as they propagate westward. In turn, the entrainment of these subsurface temperature anomalies into the surface during mixing events can cause positive (negative) SST anomalies (see e.g. Schneider and Miller, 2001; Zhang and Wu, 2010). Several avenues for further observational and modelling work that could be used to better understand links between SST variability around southern New Zealand and ocean adjustment to wind forcing are discussed in Sections 6.9 and 7.2.

6.6 Results Part 2: Trends in SST at the S-STF

To date, the only analysis of temperature variability across the S-STF around New Zealand that is of comparable length to that presented in this study is from a shorter, 21 year (1985-2004) analysis of the thermal properties of the Southland Front by Hopkins et al. (2010). The study by Hopkins et al. (2010) noted that there were "*only very weak linear trends*" in the SST and SST gradient of the Southland Front between 1985-2004. However, Hopkins et al. (2010) did not quantify the magnitude, nor the statistical significance, of these trends. The present study addresses this shortcoming, by performing a detailed analysis of multi-decadal changes in SST across the S-STF around southern New Zealand since the early 1980s. Least-squares linear regression was used to estimate multi-decadal trends in the frontal time series within the 1982-2011 time period (Fig. 6.15), with the statistical significance assessed using Student's t test (see Section 6.3.4).

Over the 1982-2011 period, the temperature differential across the S-STF around southern New Zealand has undergone a significant strengthening, with a mean trend of 0.12 ± 0.06°C per decade ($p < 0.05$) (Fig. 6.15e). The magnitude of this trend is considerable: averaged over the study region around southern New Zealand (Fig. 6.1) the S-STF temperature differential has an annual-mean (1982-2011) of 1.6°C (Fig. 6.2). Over the past three decades, the S-STF temperature differential has increased by approximately 0.36°C (Fig. 6.15e-f), equivalent to a strengthening of 22%.

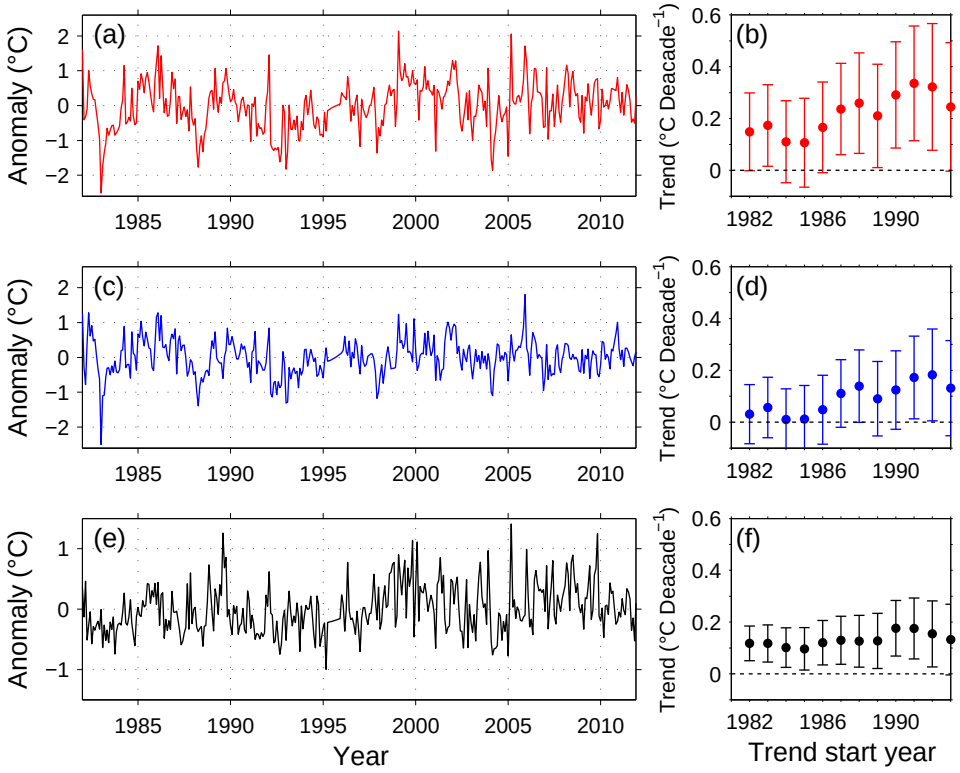

Figure 6.15: Monthly-resolution frontal time series for the S-STF around southern New Zealand. Shown are the time series of anomalies of (a) subtropical SSTs (c) Subantarctic SSTs and (e) the temperature differential across the S-STF. Values in each frontal time series are anomalies relative to the long-term monthly means of each time series computed over 1982-2011. Also shown are estimates of multi-decadal linear trends in (b) subtropical SST anomalies, (d) Subantarctic SST anomalies and (f) the temperature differential across the S-STF. Linear trends are computed from the monthly-resolution frontal time series over periods of between 19 and 30 years ending in 2011 (circles), with 95% confidence intervals determined from a t-test (Section 6.3.4) (solid lines).

An examination of changes in SST on the subtropical and Subantarctic side of the S-STF (Fig. 6.15a-d) reveal that the strengthening of the S-STF temperature differential reflects an increase in subtropical SSTs, north of the S-STF. These data show that subtropical SSTs have warmed with a mean trend of 0.15±0.15°C per decade over the 1982-2011 period (Fig. 6.15a-b). In contrast, there has been a much weaker warming in Subantarctic SSTs to the south of the S-STF (0.03±0.09°C) over the same period (Fig. 6.15c-d).

There appears to be some low-frequency (i.e. interannual to decadal scale) variability in the frontal time series in Figure 6.15. This suggests that the magnitude and significance of trends in the frontal time series in the past few decades may be sensitive to the time period over which the trends are calculated. To assess the sensitivity of the SST trends across the S-STF to different trend start dates, linear trends were calculated from the frontal time series for periods beginning in the years 1982 through 1992 and ending in 2011 (Fig. 6.15b, d, f).

Evidence of a strengthening of the temperature differential across the S-STF is seen across all of the sensitivity tests, with significant positive trends of between 0.10°C to 0.18°C per decade (Fig. 6.15f). A significant warming trend is seen in subtropical SSTs in the majority of the sensitivity tests, with the exception of trend periods starting in 1984 and 1985 (Fig. 6.15b), when subtropical SST anomalies reached a five-year maximum (Fig. 6.15a). Multi-decadal trends in the Subantarctic SSTs are not statistically significant prior to 1987, but do show a general warming trend for periods starting between 1987 to 1992 (Fig. 6.15d). The strongest multi-decadal trends in the frontal time series are found for trends computed over a 21 year period from 1991 to 2011. Linear trends computed over this period indicate significant warming trends in both subtropical and Subantarctic SST anomalies, equivalent to 0.34±0.16°C per decade and 0.17±0.12°C per decade, respectively (Fig. 6.15b,d). As a consequence of subtropical SSTs warming at a faster rate than Subantarctic SST anomalies, the temperature differential across the S-STF around southern New Zealand also intensified over the 1991 to 2011 period at a rate of 0.18±0.09°C per decade (Fig. 6.15f).

6.7 Discussions of SST trends

6.7.1 Comparison with other studies

Examining the 30 year (1982-2011) frontal time series revealed that subtropical SSTs have warmed at a faster rate between 1982 and 2011 (0.15±0.15°C per decade, Fig. 6.15b) than Subantarctic SSTs (0.03±0.09°C per decade, Fig. 6.15d). In turn, the temperature differential across the S-STF south of New Zealand has strengthened over this period by approximately 22% (0.12 ± 0.06°C per decade, Fig. 6.15f). It should be noted that whilst subtropical SSTs show a warming tendency between 1982 and 2011, the uncertainty on the linear trend is as large as the trend itself. As a result, the subtropical warming trend between 1982 and 2011 is not statistically significant compared to no warming at the 95% confidence level (Fig. 6.15b). Statistical significance aside, a similar pattern of stronger warming on the subtropical side of the S-STF around southern New Zealand, compared to the Subantarctic side (i.e. over the Campbell Plateau) is seen in analyses of centennial-scale (1900-2008) temperature trends in SST and surface air temperature products (Wu et al., 2012). This suggests that the multi-

decadal strengthening of the temperature differential across the S-STF, which is reported here, might be part of a much longer-term trend around southern New Zealand.

Another important finding of this study is that there are stronger, and statistically significant, positive trends in subtropical SSTs (0.17±0.12°C per decade) and the temperature differential across the S-STF (0.34±0.16°C per decade) over a more recent 21 year period (1991-2011) (Fig. 6.15b,d,f). These findings are consistent with a recent study of SST trends across the confluence region of the subtropical and Subantarctic boundary currents east of New Zealand (Fernandez et al., 2014). Fernandez et al. (2014) reported a strengthening of the temperature differential between STW and SAW east of New Zealand between the mid-1980s and 2010, similar to that noted here around southern New Zealand. They further noted that much of this multi-decadal trend seemed to come from a more rapid increase in the temperature differential between these water masses between the 1990s and present. During this period, there is evidence that a significant warming of the wider South Pacific gyre took place, with Sutton et al. (2005) and Roemmich et al. (2007) indicating warming down to 800 m in the eastern Tasman Sea (of 1.2°C (0.5°C) at surface (800 m depth), between 1996-2001 - inclusive) and by more than 0.4°C over a broad region of the South Pacific Ocean (1990-1999) (see Fig. 10 in Roemmich et al., 2007). Results from Roemmich et al. (2007) also indicate that warming of SSTs during this period (1990-1999) was higher around southern of New Zealand (0.8°C), on the subtropical side of the S-STF, than over the Subantarctic waters that cover the Campbell Plateau (<0.2°C). The results of these previous studies are intriguing because combined with the analysis of linear trends in this study (Fig. 6.15), they suggest that there has been not only a marked warming of subtropical waters in the New Zealand region during the period between the 1990s and 2010s, but also as a large-scale strengthening of the temperature differential across the S-STF in the South Pacific.

A question raised by the results of this study is what caused the periods of warming of subtropical waters (i.e. 1982 to 2011 and the 1990s to 2011) around southern New Zealand and in turn, the strengthening of the temperature differential across the S-STF? For brevity, the longer-term period of subtropical warming between 1982 and 2011 (Fig. 6.15a-b) is focused on here.

6.7.2 Wind-driven trends?

In light of the findings of this study that SST variability across the S-STF around southern New Zealand is significantly correlated with variability in the local wind stress, local wind stress curl and the basin-wide South Pacific wind stress curl (Sections 6.4-6.5), a potential driver of these trends to consider is changes in surface winds over the South Pacific. The potential role of wind field changes is assessed qualitatively by examining the magnitude

and statistical significance of linear trends in wind stress and wind stress curl over the South Pacific during the 1982 to 2011 time period and comparing these to trends in the frontal time series (Section 6.6). Linear trends were calculated from the three wind time series for eleven multi-decadal periods beginning in years between 1982 through 1992 and ending in 2011, which are shown in Figure 6.16.

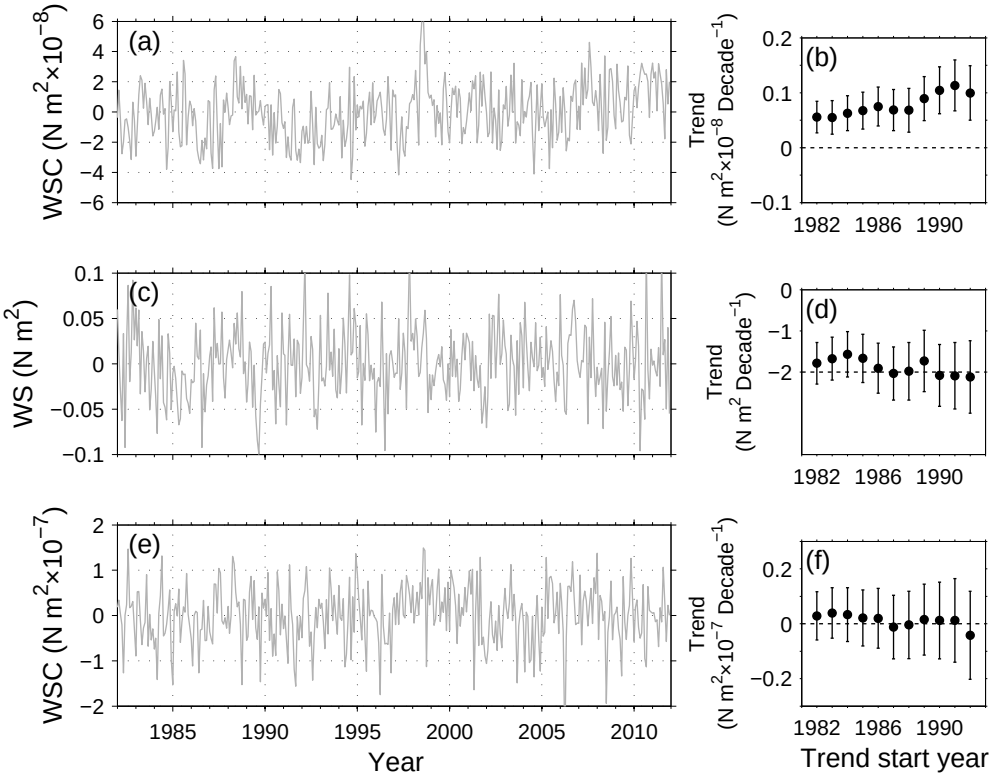

Figure 6.16: Monthly-resolution time series of South Pacific wind variables. Shown are the time series of anomalies of (a) the basin-wide South Pacific wind stress curl, (c) the local-scale New Zealand zonal wind stress and (e) the local-scale New Zealand wind stress curl. Values in each wind time series are anomalies relative to the long-term monthly means of each time series computed over 1982-2011. Monthly anomalies are shown by grey lines. Also shown are estimates of multi-decadal linear trends in (b) the basin-wide South Pacific wind stress curl, (d) the local-scale New Zealand zonal wind stress and (f) the local-scale New Zealand wind stress curl. Linear trends are computed from the monthly-resolution wind time series over periods of between 19 and 30 years ending in 2011 (circles), with 95% confidence intervals determined from a t-test (Section 6.3.4) (solid lines).

Over the period 1982 to 2011, anomalies of the basin-wide wind stress curl for the South Pacific exhibit an upward trend of 0.56±0.29 10^{-8} N m^{-2} decade^{-1} (significant at the 95% confidence level) (Fig. 6.16a-b). This trend runs parallel to the longer-term (1948-2007) intensification of wind stress curl over the South Pacific identified previously by Hill et al. (2008). Focusing on the most recent few decades, statistically significant positive trends in basin-average South Pacific wind stress curl are observed for trends starting in years between 1982 and 1992 and ending in 2011. The magnitudes of the trend are sensitive to the start

date and are seen to be strongest for the period 1991-2011 (1.13±0.46 10^{-8} N m^{-2} $decade^{-1}$) (Fig 6.16a-b). This increase in the basin-wide wind stress curl is concurrent with the observed periods of warming in subtropical waters around southern New Zealand and subsequent strengthening of the temperature difference across the S-STF (Section 6.6). However, with the data in hand, it is not possible to make any firm statement regarding causality.

In contrast to basin-average wind stress curl, there are no statistically significant linear trend in zonal wind stress nor wind stress curl around southern New Zealand over these periods. While there is a tendency towards stronger westerlies (2.2±0.5 10^{-3} N m^{-2} $decade^{-1}$) between 1982 to 2011, the linear trend is not statistically significant compared to a trend of zero at the 95% confidence level (Fig. 6.16d). Similarly, whilst there is a positive trend in wind stress curl around southern New Zealand over the 1982 to 2011 time period, this is not statistically significant at the 95% confidence level (Fig. 6.16f). Linear trends of wind stress and wind stress curl computed for periods beginning in the years 1982 to 1992 and ending in 2011 also show an increase, but none of these are statistically significant at the 95% confidence level (Fig. 6.16d,f). This suggests that the warming observed around southern New Zealand is unlikely to have been caused by any changes in the wind field that are local to southern New Zealand.

6.7.3 Potential links to warming ongoing in the Tasman Sea

Beside changes in the South Pacific wind field, a 'leaking' of anomalously warm waters from the Tasman Sea around southern New Zealand might also play a role in the warming tendency seen in STW between 1982 and 2011. A previous study by Hopkins et al. (2010) noted a marked increase in the thermal gradient of the Southland Front during the 1997-1998 El Niño. They hypothesised the increased gradient might be caused by an advection of warm temperature anomalies observed in the eastern Tasman Sea during the late 1990s (Sutton and Roemmich, 2001) around southern New Zealand, but were unable to examine with their data the temperature anomalies in the surface waters bordering the front. The results in this Chapter confirm that the period between 1997 and 1998 was associated with anomalously warm SSTs around southern New Zealand (see e.g. Fig. 6.16a).

There is evidence for a persistent physical connectivity between the eastern Tasman Sea and waters around southern New Zealand. As described **in Chapter 2**, there is a weak (3-4 cm s^{-1}), eastward surface intensified trans-Tasman flow at 40-41°S, which primarily arises from separations of the EAC extension (Ridgway and Dunn, 2003). A component of this eastward flow is forced southward along the southern flank of the Challenger Plateau and feeds into a southward advection of 1-2 Sv of STW along the west coast of the South Island, New Zealand and around the southwest corner of the South Island, New Zealand (Morris

et al., 2001; Ridgway and Dunn, 2003; Sutton, 2003; Chiswell et al., 2015). This poleward flow of waters from the Tasman Sea is also evident from the southward dip of isotherms and isohalines against the west coast of New Zealand (Uddstrom and Oien, 1999; Hamilton, 2006). Intriguingly, the warming tendency observed in subtropical SSTs around southern New Zealand between 1982 and 2011 runs parallel to a Tasman-wide warming of SSTs observed over a similar period between 1982 and 2007 (Matear et al., 2013). A leaking of this warm water from the Tasman Sea, following a pathway similar to that suggested above, could plausibly lead to a warming of subtropical waters around southern New Zealand.

With the data in hand, it is only possible to speculate on the possible causes of the warming tendency observed in subtropical SSTs around southern New Zealand between 1982 and 2011. A different approach, going beyond the analyses of time series conducted here, will be required to discriminate the causes of this warming, and its possible links to trends in wind stress curl and warming taking place in the Tasman Sea. One possible approach to elucidate the causes of this warming would be to examine ocean state estimates. These products provide observationally constrained estimates of the oceans full depth T and S fields (see e.g. Reanalyses.org), and have already been used successfully in the New Zealand region to investigate the nature and mechanisms of decadal variability in the EAC extension and the Tasman Front (Hill et al., 2011). One would first need to examine whether there are ocean state estimates that reproduce the warming observed in this study around southern New Zealand and, if so, one might be able to analyse the data in the framework of a mixed layer heat budget (see e.g. Rintoul and England, 2002; Deser et al., 2010) and examine the contribution of possible mechanisms (i.e. changes in air-sea flux, Ekman pumping, geostrophic advection) to the observed warming. Such an investigation is beyond the time frame of this thesis.

6.8 Sensitivity to methodology

Before concluding, some remarks are necessary on an issue that was identified in the course of this analysis regarding how the frontal time series were compiled and interpreted (Section 6.2). Scenarios could occur if data from front segments that are not associated with the S-STF were inadvertently incorporated into the frontal time series, or, if the S-STF occurs a mutlifrontal structure (i.e. as two or more fronts). In such circumstances, spurious variability could be introduced into the frontal time series, making them less representative of the 'true' variability of subtropical and Subantarctic SSTs and the temperature differential across the S-STF that are of interest here. Thus, it is possible that the 'warm' ('cold') side of some front segments within the study region might actually sample (1) on the Subantarctic (subtropical)

side of the S-STF, or (2) within the frontal zone itself (i.e. within a mixture of STW and SAW).

6.8.1 Alternative frontal time series

To assess the sensitivity of the results to the methodology used to compile the frontal time series, the cross-correlation analyses (Section 6.4) and trend analyses (Section 6.7) were repeated using frontal time series calculated from the PFV5.2 SST data set (**Chapter 4**) in an alternative manner. The alternative frontal time series were derived from area-averaging PFV5.2 monthly composite SST images within two geographic regions, one inshore of the S-STF (i.e. on the subtropical side) and one offshore of the S-STF (i.e. on the Subantarctic side) (Fig. 6.17). This consisted of four processing steps:

1. Two geographic regions were defined, positioned approximately 50 km inshore and offshore of the climatological mean position of the S-STF (Fig. 6.17). These are defined as the 'STW box' and 'SAW box' respectively. Each contained ~2000 satellite pixels.

2. The monthly area-average of SST was calculated within the STW box and SAW box, for each month within the 30 year data set. The monthly difference between area-averaged in the STW box and SAW box was then calculated. This yielded three 'alternative' frontal-time-series.

3. The frontal time series were converted into anomaly time series by subtracting the 30 year monthly means.

4. Three months of missing data present in each frontal time series during 1995 were filled using linear-interpolation.

Repeating the cross-correlation analyses (Section 6.4) and trend analyses (Section 6.6) using the alternative frontal time series, which are derived from areas clearly located over the STW and SAW sides of the S-STF (Fig. 6.17), enables the representivity of the original frontal time series to be assessed.

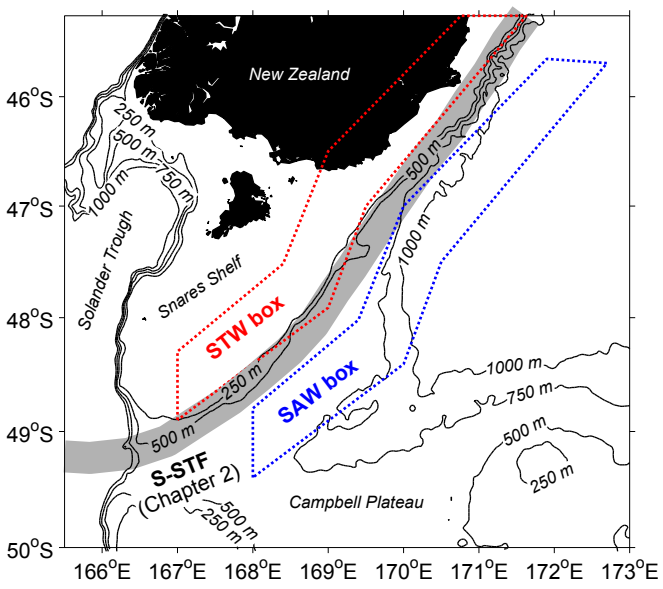

Figure 6.17: Locations of the geographic regions around southern New Zealand used to derive the alternative frontal time series (coloured dashed lines). Also shown is a schematic of the S-STF pathway (grey shading) from Figure 3.11.

6.8.2 Comparison of results

The main results from the cross-correlation analysis – in terms of the time-lag of peak cross-correlations and their statistically significance – are consistent between the 'original' and 'alternative' time series (Fig. 6.18-6.20). Using either the 'original' or 'alternative' time series, subtropical and Subantarctic SST anomalies are most strongly - and statistically significantly - negatively correlated with zonal wind stress around southern New Zealand at a time lag of one season (Fig. 6.18a-b). The 'alternative' time series results in a peak cross-correlation between the temperature differential across the S-STF and the zonal winds stress at a lag of one season, which is smaller by approximately 0.1 in the 'alternative' time series, but remains statistically significant (Fig. 6.18c).

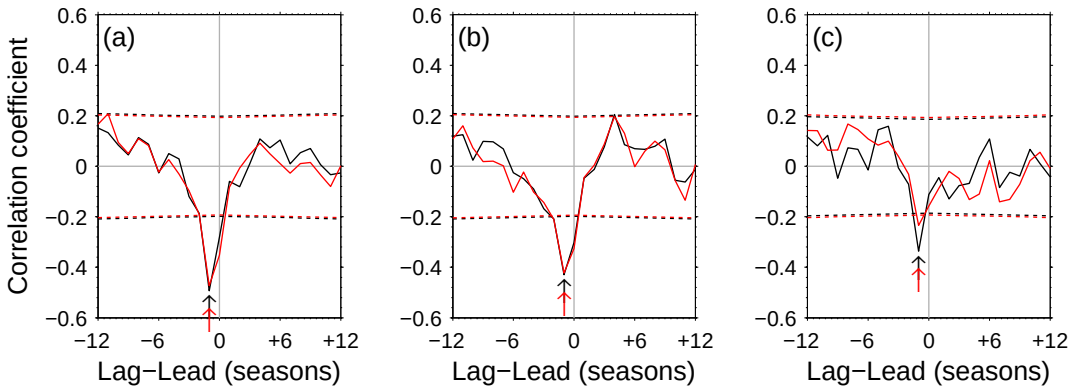

Figure 6.18: As Fig. 6.11, but cross-correlation calculated separately using the original (black) and the alternative (red) frontal time series.

In terms of cross-correlations with the basin-average wind stress curl (Fig. 6.19), for the 'original' and the 'alternative' time series, subtropical and Subantarctic SST anomalies are most strongly - and statistically significantly - positively correlated with the basin-average wind stress curl over the South Pacific at time lags of between two and three seasons (Fig. 6.19a-b). The 'alternative' time series results in a maximum lag cross-correlation with the temperature differential across the S-STF at a time lag of three seasons rather than four seasons in the 'original' time series (Fig. 6.19c) and is smaller by 0.07, but otherwise remains statistically significant. One curiosity is that the sensitivity testing shows the temperature differential across the S-STF, in the 'alternative' time series, is statistically significantly lag-correlated with the local winds stress curl at a time-lag of one season ($r = 0.38$, $p < 0.05$) (Fig. 6.20c). This is a curious result because there are no significant correlations observed in the bordering water masses, and is a result that needs further work to understand.

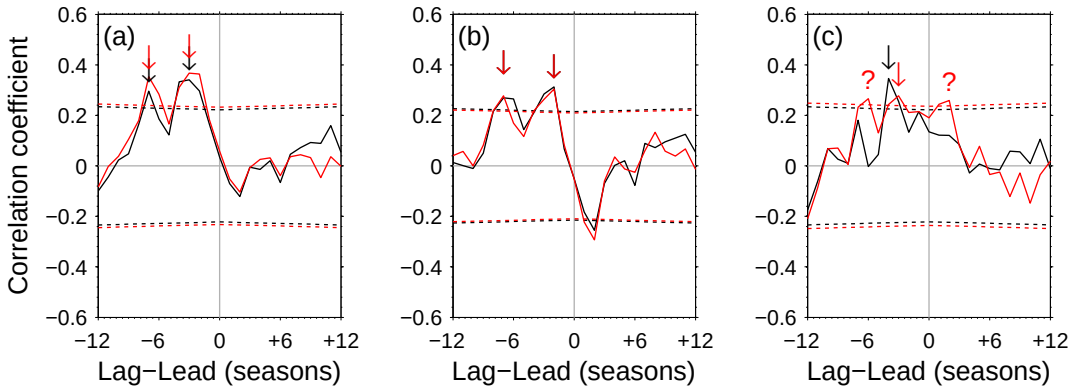

Figure 6.19: As Fig. 6.9, but cross-correlation calculated separately using the original (black) and the alternative (red) frontal time series.

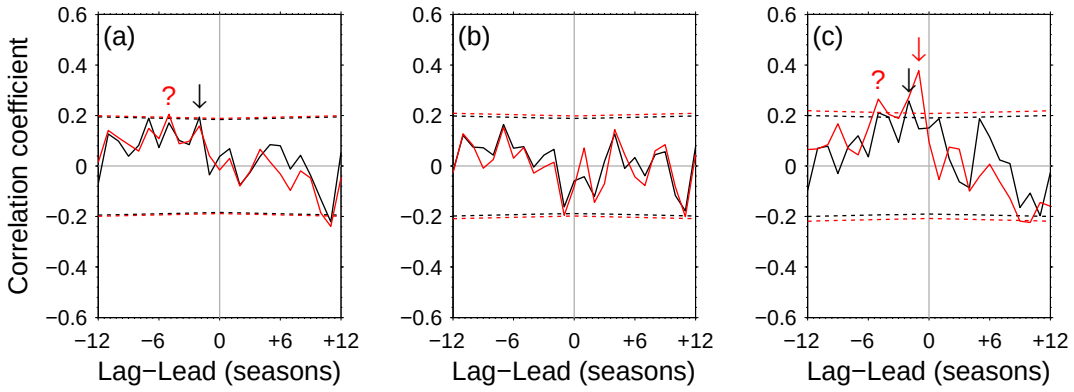

Figure 6.20: As Fig. 6.13, but cross-correlation calculated separately using the original (black) and the alternative (red) frontal time series.

The main results of the trend analysis – that the temperature differential across the S-STF has strengthened between 1982-2011, and more strongly between 1991-2011, in response to

stronger warming of subtropical compared to Subantarctic SSTs - still stands for the alternative time series (Fig. 6.21). For the long-term trend in the S-STF temperature differential, a statistically significant strengthening is seen in the 'original' and 'alternative' frontal time series over all time-spans (Fig. 6.21a).

For the long-term trends of subtropical and Subantarctic SSTs, warming rates (or lack thereof) on the subtropical side exceeds that in Subantarctic waters, and their statistical significance shows a similar pattern (Fig. 6.21b-c). Interestingly, the 'alternative' time series displays a strengthening trend that is on average 60 % larger than in the 'original' time series (Fig. 6.21a). This reflects the fact that the warming rate of Subantarctic SSTs is on average 60% lower in the 'alternative' time series than in the 'original' frontal time series. Results from Matear et al. (2013) show a long-term warming trend in SSTs around southern New Zealand between the early 1980s and late 2000s, which decreases sharply and then turns negative moving offshore from the S-STF (see e.g. Fig. 6 in Matear et al. (2013)). It therefore seems possible that the smaller warming rate in the 'alternative' SAW time series, compared to the original SAW time series, is be due to the geographic region being used to compile the alternative SAW time series being positioned further offshore from the S-STF.

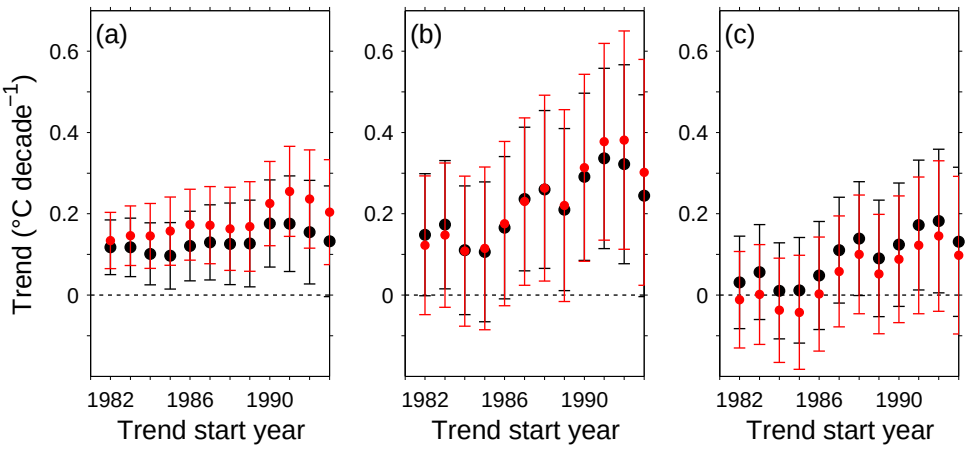

Figure 6.21: As Fig. 6.15b-d-f, but linear trends calculated separately using the original (black) and the alternative (red) frontal time series.

6.8.3 Outcome of the sensitivity tests

While there are some subtle differences in absolute strength of cross-correlations and trends, the fact that the major patterns and statistical significance of cross-correlations and trends are insensitive to the use of the 'original' or 'alternative' frontal time series suggests that (1) the front-averaging method used to produce the original frontal time series does not introduce spurious variability, and (2) that the original interpretation of the frontal time series as being

representative of SSTs over the near frontal STW and SAW, and in turn the temperature differential across the S-STF, is reasonable.

6.9 Future work

A couple of points are noted regarding potential weaknesses of the present study. The first is that the use of the PFV5.2 SST images might be considered both a strength and a potential weakness of the present study. The PFV5.2 data set has sufficient duration (30 years), temporal resolution (monthly or finer) and spatial coverage to enable us to investigate SST variability over an extensive region of the upper continental slope around southern New Zealand, and its links to changes in winds over the South Pacific, for a recent 30 year (1982-2011) period. However, like many oceanographic studies that take advantage of long-term climate record offered by remotely sensed SST images, it is only possible in this work to examine the surface expression of the S-STF – and its bordering water masses - and then only their thermal properties. Therefore, it is necessary to acknowledge that the long-term trends and correlation signals revealed in this study reflect surface thermal realizations; these do not necessarily extend below the oceanic mixed layer, nor might they necessarily reflect changes in the density structure, and hence geostrophic transport, associated with this section of the S-STF.

Ideally, these types of questions would be examined further by analysing direct in-situ T-S and/or mooring data. However, as highlighted in **Chapter 2**, the historical hydrography across the S-STF in the South Pacific is sporadically sampled in time and space, with the existing repeat hydrography (i.e. along the Macquarie Ridge-Solander Trough) of too shorter duration for investigating the types of questions about variability of the S-STF examined in this Chapter. During future studies of the S-STF in the South Pacific based on remotely sensed SST data, the integration of data from satellite altimetry might assist in examining variability in transport associated with the S-STF, although there are also issues around using such data given both the absence of historical hydrography (for providing accurate estimates of the mean dynamic topography) and the complex and shallow topography around southern New Zealand.

There is room for further progress in determining the role of "local" winds in forcing the observed SST variability. This work finds that interannual variations of SST in the frontal region south of New Zealand are significantly correlated with zonal wind stress averaged over waters to the west and east of the South Island, New Zealand (i.e. blue region in Fig. 6.5). In contrast, they are only weakly correlated with wind stress curl averaged over this same region. However, if the region over which the "local" winds are calculated was reduced, to match more closely with the size of the frontal zone, it is possible that strength of these

correlations may change, modifying some of the conclusions drawn here. That said, the area of strongest correlations between subtropical and subantarctic SST anomalies and zonal wind stress already lie outside (or extend outside) the frontal region (Fig. 6.12). This suggests that wind stress forcing from outside the frontal region is likely to be more important for interannual SST anomalies than forcing from within it. However, a similar analysis of spatial correlations was not conducted between SST anomalies and wind stress curl, due to the relatively weak correlations observed between interannual SST variations and local wind stress curl (Fig. 6.13). Further study, examining wind forcing inside and outside the frontal region separately, will need to be undertaken in order to fully resolve the role of "local" winds in driving interannual variations in SST around southern New Zealand.

This study (Section 6.4) finds significant correlations between SST variability across the S-STF around southern New Zealand and both local-scale and basin-wide winds over the South Pacific. Whilst not-conclusive evidence, these correlations suggest that wind-driven mechanisms play a role in the observed interannual variations of SST south of New Zealand. Further studies are needed to tease apart the physical mechanisms that are involved. An improved understanding of the impact that ocean adjustment to wind forcing has on SSTs around southern New Zealand region could come from an observational and modelling study similar to that of Zhang and Wu (2010) for the North Atlantic. Zhang and Wu (2010) examined the predictability of SST variations over the North Atlantic Ocean using a baroclinic Rossby wave model. They reveal significant correlations between interannual variability of North Atlantic SST and SSH, and show subsequently that SST variability can be skillfully predicted in several regions of the North Atlantic based on SSH anomalies predicted by a baroclinic Rossby wave model.

For the area south of New Zealand, a similar investigation could be carried out by forcing an ocean general circulation model with reanalysis wind stress and then correlating the modeled variations of SSH around southern New Zealand with the observed SST variability in this region (as in Zhang and Wu, 2010). The results would provide a basis with which to assess the contribution that ocean adjustment to wind forcing, via barotropic and baroclinic Rossby waves, makes to SST variability around southern New Zealand, as is speculated on in this study. They would also enable an investigation of the extent to which interannual SST variations off southeast New Zealand might be predictable several seasons ahead based on wind forcing over the South Pacific, as is suggested by the results of the present study. Given the considerable influence of SSTs around New Zealand on terrestrial air-temperatures and rainfall (e.g. Sutton et al., 2005), the results of such study would likely have implications for seasonal forecasting.

A final open question is whether wind-driven mechanisms are the main processes causing changes in SST around southern New Zealand, or whether other mechanisms and drivers,

such as air-sea heat fluxes, are more important? Recent work by Bowen et al. (2017) suggests horizontal heat advection, heat flux between the atmosphere and the ocean, as well as convergence of ocean heat transport caused by wind-driven barotropic Rossby waves, all play significant roles in the interannual variability of sea surface temperature in the southwest Pacific. A deeper understanding of the underlying dynamical processes that cause interannual variations in SST in the waters southeast of New Zealand, and their relative importance, could come from an examination of the heat budget in the mixed layer. The mixed layer heat budget represents a balance between several terms (i.e. air-sea heat fluxes, horizontal heat advection, vertical entrainment and eddy processes) that influence the temperature of the oceans mixed layer (see e.g. Dong et al., 2007). An idea of the lowest-order heat balance expected in this region could be obtained by estimating the magnitude of each of the terms in the heat budget at the interannual time scale using information from the published literature (see e.g. Rintoul and England, 2002). Alternatively, analyses of both observations and/or a numerical model could be used to estimate each of the terms in the heat budget as a function of time (see e.g. Chen et al., 2015; Bowen et al., 2017); however, such a detailed investigation of the mixed layer heat balance is unfortunately outside the scope of this thesis.

6.10 Summary and conclusions

An analysis of 30 years (1982-2011) of remotely sensed SST data and atmospheric reanalysis data has enabled this Chapter to examine SST variability across the S-STF around southern New Zealand, and the role that changes in wind stress curl and wind stress over the South Pacific play in this variability.

The results show that around southern New Zealand, (a) subtropical and Subantarctic SST anomalies and (b) the temperature differential across the S-STF are significantly lag-correlated with variations in surface winds over the South Pacific. The strongest lag-correlations are found with variability in zonal wind stress around southern New Zealand, at a lag of one season; periods of anomalously strong (weak) westerly winds are associated with anomalous cooling (warming) of subtropical and Subantarctic SSTs and a weakening (strengthening) of the S-STF temperature differential. The second strongest lag-correlations are found with variability in the basin-wide South Pacific wind stress curl, at time-lags of between two and four seasons; periods of anomalous strong (weak) basin-averaged wind stress curl are associated with anomalous warming (cooling) of subtropical and Subantarctic SSTs and a strengthening (weakening) of the S-STF temperature differential.

Changes in the basin-wide South Pacific wind stress curl have previously been implicated in driving interannual and longer time-scale changes in ocean temperature and circulation in the Tasman Sea and the wider South Pacific gyre (Roemmich et al., 2007; Hill et al., 2008,

2011; Holbrook et al., 2011; Oliver and Holbrook, 2014). Given the limitations inherent in any correlative study, the results presented here need to be treated with a degree of caution, and further work is required to be more definitive about the issue of causality and the underlying physical processes. Nonetheless, the evidence from the cross-correlations strongly suggest that changes in winds over the South Pacific – in terms of both the basin-wide South Pacific wind stress curl and the wind stress around southern New Zealand – also play a significant role in driving SST variability across the S-STF around southern New Zealand.

The results also show that the temperature differential across the S-STF around southern New Zealand has increased (a) over the 1982-2011 period and (b) more strongly over a recent 21 year period between 1991-2011. The data suggests that this strengthening is primarily associated with a surface warming in subtropical north of the S-STF over these periods. An objective for future effort is to elucidate the underlying processes responsible for the multi-decadal periods of surface warming in subtropical waters, and their possible connectivity with previously identified periods of warming within the Tasman Sea (see e.g. Sutton et al., 2005; Roemmich et al., 2007; Matear et al., 2013).

Regardless of its causes, the strengthening of S-STF temperature differential might have implications for the induced baroclinic transport associated with the STF - through increasing the density gradient across the front. There is recent evidence of an increase in the thermal gradient across the confluence region separating the S-STF and SAF east of New Zealand (Fernandez et al., 2014). This signal is concurrent with the strengthening of the temperature difference across the S-STF around southern New Zealand described here, raising the possibility of a large scale strengthening of the transport associated with the S-STF in the New Zealand region between 1982-2011.

This study has presented evidence that the thermal strength of the S-STF on the Campbell Plateau and SSTs in the near-frontal water masses are related to changes in both the zonal wind stress around southern New Zealand and the basin-wide South Pacific wind stress curl. The research points towards the variability in the thermal properties of the S-STF around southern New Zealand as being influenced not only by the fronts interaction with the steeply shelving bathymetry of the upper continental slope (**Chapter 3, 5**), but also by changes in winds over the South Pacific (this Chapter).

Chapter 7

General conclusions

The main focus of this work has been to examine the nature of temporal variability of the STF in the Tasman Sea, using a combination of repeat hydrographic sections and remotely sensed SST and SSS data. This work set out to analyse how the physical state of the STF in this area - such as its position, intensity and SSTs in its bordering water masses - vary in time. This work also sought to discover what role topography and surface winds play in the frontal variability. This final Chapter summarises the main findings and contributions of **Chapters 3**, **5** and **6** (Section 7.1) and then discusses a number of possible directions for further research (Section 7.2).

7.1 Main findings

Chapter 3 contributes to an improved understanding of the position and nature of a section of the STF that passes around southern New Zealand, by combining information from hydrographic sections and remotely sensed SST images collected during the austral autumns of 2007, 2008 and 2011. From this study, the following points are highlighted:

- The latitudinal position of the S-STF as it crosses the Macquarie Ridge (~164°E) was found to be remarkably consistent during the austral autumns of 2007, 2008 and 2011, where it crosses the ridge in water depths of 100 - 700 m, north of a seamount at 49.6°S. East of 165°E, the S-STF turns equatorward to closely follow the 400 - 600 m isobaths along the upper continental slope that borders the Snares shelf.

- The poleward limit of the S-STF around southern New Zealand is 100-200 km further south than the frontal pathway across the Snares shelf suggested in some earlier studies (i.e. Chiswell, 1996; Belkin and Cornillon, 2003; Belkin et al., 2009) and the S-STF crossing of Butler et al. (1992). The position of the S-STF is remarkably similar to the STF pathway around the Snares shelf inferred by Heath (1985) and the southern

extent of the STFZ given by Carter et al. (1998), which each draw on data collected at different times of the year to this study. It is concluded from this that the around-shelf pathway is the most likely position of the S-STF, rather than just a seasonal deflection during austral autumn.

- The position and variability of the S-STF is explained in terms of the front following a preferred pathway around bathymetry in order to conserve potential vorticity, with the front being topographically steered by bathymetry of approximately 500 m depth as it passes around southern New Zealand.

- The S-STF is well-defined in its passage across the Macquarie Ridge and along the upper continental slope. In contrast, within the Solander Trough the front is more diffuse and forms a distinct meander. This behaviour is linked to topographic intensification of the S-STF across the Macquarie Ridge, giving rise to flow disruption and increased mesoscale variability downstream of the ridge. The S-STF then re-intensifies as it is topographically steered along the upper continental slope.

- The presence of mesoscale eddies, a meandering S-STF and a series of shallow fronts that lie north of the S-STF may explain the range of reported positions of the STF around southern New Zealand.

- A 50-100 m deep mixed layer composed of modified SAW that becomes increasing salty is observed extending north of the S-STF, suggesting the N-STF lies north of the study region.

Chapter 5 provided new insights into the surface expressions of the STF and how they vary in position over seasonal and longer-time scales, and across a larger region of the Tasman Sea. This was achieved by synthesising information from a long-term data set of remotely sensed SST images and a novel, recently available data set of remotely sensed SSS images. A long-term (1982-2011), statistical view of the position of S-STF at the borders of the Tasman Sea was developed, by examining the distribution of hundreds of thermal fronts that are identified as being surface expressions of the S-STF. The following main points are highlighted:

- It is apparent that on monthly time scales, the S-STF has strong ($\nabla SST \geq 2.5$°C 100 km^{-1}) surface thermal expressions near the land boundaries of Australia and New Zealand, contrary to a previous suggestion that in the Tasman Sea the S-STF lacks a surface thermal signature (Uddstrom and Oien, 1999). This is supported by strong correspondence found between the spatial patterns of occurrence of (1) thermal fronts detected in monthly-composite satellite SST images and (2) the S-STF defined by surface isohalines using satellite SSS images, at both the western (153°E) and eastern

(165°E) borders of the Tasman Sea, as well as south of New Zealand (167°E). In contrast with the S-STF, surface temperature expressions of the N-STF in the Tasman Sea could not be readily identified.

- In the western Tasman Sea (153°E), it is apparent from thermal front observations that surface expressions of the S-STF occur most frequently between 45.0-45.5°S, corroborating previous estimates of the climatological position of the STF (Deacon, 1982; Heath, 1985) and S-STF (Hamilton, 2006), derived from temporally limited hydrographic survey data.

- In the eastern Tasman Sea (165°E), the results from thermal fronts suggest that surface expressions of the S-STF have at least one modal position located between 48.5-49.0°S. Here, there is also an intriguing bimodal distribution in the pattern of occurrence of thermal fronts, as well as in the 34.7 surface isohaline (S-STF). This bimodality contains the tentative suggestion that the S-STF might be bimodal along the Macquarie Ridge, with a mode near 48.5-49.0°S and second near 47°S, close to the poleward positions of the S-STF reported in this area by Hamilton (2006), Heath (1981; 1985) and in **Chapter 3**. The bimodality in thermal fronts also exists seasonally, raising the further possibility of a transition between these two modes on a sub-seasonal timescale.

- South of New Zealand, surface expressions of the S-STF appear to occur most frequently in the Snares Depression between 48.5-49.0°S, in waters depths of between 200 and 600 m. This agrees with the typical positions of the STF inferred by Heath (1981; 1985) and that of the S-STF inferred in **Chapter 3**.

- In the western Tasman Sea (153°E) and south of New Zealand (167°E), the analysis of thermal fronts suggests that if the S-STF does migrate seasonally, then it is to within the 0.5° latitude resolution of the analysis of thermal fronts and is thus not resolved. In the eastern Tasman Sea (165°E), there is some evidence of an approximately 1.0° poleward migration of the S-STF between the austral summer and winter. The new constrains that can be placed on the likely seasonal migration of the S-STF in the Tasman Sea do not support the notion that the STFZ undergoes a seasonal migration of 5-7° latitude in each basin (Graham and de Boer, 2013). Any seasonal migration of the S-STF in the Tasman Sea would appear to be have a similar range to that found by previous studies (~1° degree latitude) in the eastern South Atlantic (Burls and Reason, 2006; Billany et al., 2010) and southeast Indian Ocean (James et al., 2002).

Finally, **Chapter 6** contributes toward an improved understanding of factors that control SST variability across the S-STF around southern New Zealand, by examining 30 year time

series (1982-2011) of subtropical and Subantarctic SSTs, and their links to changes in surface winds over the South Pacific. The following key outcomes from this study are highlighted:

- The SSTs of subtropical and Subantarctic waters south of New Zealand are found to be lag-correlated by one season (3 months) to variations in surface westerly winds. Periods of anomalously strong (weak) westerly winds around southern New Zealand are found to be associated with anomalous cooling (warming) of subtropical and Subantarctic SSTs south of New Zealand and a weakening (strengthening) of the temperature differential across the S-STF is also found to weaken (strengthen). It is postulated that zonal wind stress anomalies over the southern Tasman Sea generate SST anomalies in this area via anomalous northward Ekman transport that, in turn, are advected eastward by the prevailing surface flow to the S-STF around southern New Zealand.

- Subtropical and Subantarctic SST variations south of New Zealand are also found to be lag-correlated to variability in basin-wide wind stress curl. The strongest correlations occur when changes in wind stress curl lead subtropical and Subantarctic SST anomalies by three seasons (9 months) and two seasons (6 months), respectively. Periods of anomalously strong (weak) basin-averaged wind stress curl are associated with anomalous warming (cooling) of subtropical and Subantarctic SSTs and a strengthening (weakening) of the temperature differential across the S-STF. Although the mechanism by which variations in basin-wide wind stress curl influence SSTs south of New Zealand is not yet clear, the observed time-lags suggest that oceanic Rossby waves may be involved.

- During the period studied (1982-2011), the temperature difference between the cross-frontal water masses has also increased by ~22% (0.12 ± 0.06°C per decade). This trend is associated primarily with a warming trend observed in STW over the study period (0.15±0.15°C per decade). The cause of this warming has not yet been determined, but it is concurrent with an increase in SSTs over the wider Tasman Sea (Matear et al., 2013), as well as a strengthening of local-scale and basin-wide South Pacific wind stress curl.

7.2 Directions for further research

The findings of **Chapters 3**, **5** and **6** have some broader implications and raise the following questions and suggested improvements that could be explored by further research.

The hydrographic and satellite-based observations presented in **Chapter 3** provide new insights into the pathway of the S-STF and its interaction with the marked topography of southern New Zealand. Follow-up experiments with an ocean model could help to better

understand the role that topographic steering plays in the observed behaviour – for instance, in determining the latitude(s) at which the S-STF can cross the Macquarie Ridge, or in locally intensifying and destabilising flow at the Macquarie Ridge leading to the formation of mesoscale eddies that pass across the Solander Trough. One possibility would be to use the Regional Ocean Modeling System (Shchepetkin and McWilliams, 2005) for a domain that includes southern New Zealand and to then conduct sensitivity experiments to examine how the position and intensity of the S-STF varies with idealized regional bathymetry – such as modifying the position and/or configuration of seamounts along the Macquarie Ridge or the position and depth of the Snares Depression.

Data from experiments in which an ocean model is forced by realistic boundary conditions might be used to examine the physical mechanisms in the eastern Tasman Sea (i.e. ocean circulation and winds) responsible for the poleward deflection of the S-STF around southern New Zealand, which at present remain unclear (**Chapter 3**). Numerical modelling and additional hydrographic observations collected over the continental shelf south of New Zealand could also help explain the composition and dynamics of an unusually persistent thermal front zone that has previously been observed extending across the Snares Shelf (Belkin and Cornillon, 2003).

The topographic interactions between the S-STF and sharply defined bathymetry around southern New Zealand described in **Chapter 3** appear to have biological implications. A comparison of the schematic of the S-STF pathway around southern New Zealand (Fig. 3.11) with a density distribution of satellite-tracked Southern Royal Albatross tracks over the Campbell Plateau (see Fig. 1 in Waugh et al., 2002) reveals bird activity is concentrated in a zone along the topographically steered section of the S-STF within the Snares Depression. Globally, frontal zones that are predictable in space and time (such as in areas where a front is associated with a bathymetric feature) have been found to form pelagic foraging hotspots for seabirds and marine mammals (see e.g. Bost et al., 2009; Scales et al., 2014). From the crude comparisons conducted here, it seems plausible that front-topography interactions around southern New Zealand may be responsible for making the S-STF in this area an important foraging habitat for pelagic seabirds.

This research also presents detailed observations of the position and structure of the S-STF in the vicinity of a seamount that rises to within 60 m of the surface along the Macquarie Ridge (**Chapter 3**). Seamounts have been described as areas in the world's oceans with enhanced productivity, biomass and biodiversity (see e.g. Kvile et al., 2014). The oceanographic and geophysical attributes of seamounts vary widely however and not all seamounts show these effects (Kvile et al., 2014). A recent study by Morato et al. (2016) suggests that oceanic fronts may act as a driver of seamount productivity if they frequently occur at an individual seamount. In **Chapter 3**, the consistency of the position of the S-STF in the vicinity

of a seamount near 49.6°S along the Macquarie Ridge over three surveys (2007, 2008 and 2011) was noted. Results in **Chapter 5** also suggest that the S-STF frequently crosses the Macquarie Ridge close to the latitude of this seamount. Related work by Sokolov and Rintoul (2007) suggests that the interaction of Southern Ocean fronts with topography can enhance upwelling of limiting nutrients to the upper ocean and as a result enhance primary productivity. A preliminary analyses of the annual-mean field of a 4 km daily SST climatology derived from PFV4 data set (1982-2008) (Casey et al., 2010) has revealed a 'pool' of cooler surface waters located directly above the seamount identified along the Macquarie Ridge near 49.6°S (not shown), suggestive of persistent upwelling at this seamount. The questions that these observations raise regarding whether this seamount is a hotspot for productivity and what role front-topography interactions might play in the seamount productivity await further observations and research.

Strong changes taking place off eastern Australia, where the poleward extension of the EAC has strengthened and shifted southward by ~350 km post-1940 under increased wind stress curl and a spin up of the South Pacific subtropical gyre (e.g. Cai, 2006; Hill et al., 2008; Wu et al., 2012), are likely to have implications for the STF in the Tasman Sea. Not only does the EAC extension transport STW into the STF in the western Tasman Sea (e.g. Hamilton, 2006), but its eastward separations also form a zonal flow between Tasmania and New Zealand of ~3 Sv of STW that is located just north of the STF (Stramma et al., 1995; Ridgway and Dunn, 2003) and feeds into poleward flow of STW directed towards the STF around southern New Zealand (Stanton, 1976; Ridgway and Dunn, 2003). Between the 1990s and 2060s, the poleward flow of the EAC extension is projected to further increase by ~40% with a Tasman Sea-wide warming (Matear et al., 2013; Oliver and Holbrook, 2014). This begs the questions of how changes in the EAC extension might be directly affecting the STF in the western Tasman Sea and will (or has already) the trans-Tasman export of STW toward New Zealand increase to affect the STF in the central and eastern Tasman Sea? The results in **Chapters 3**, **5** and **6** provide a baseline set of observations of the STF concurrent with strong changes ongoing in the Tasman Sea that may provide the basis for future investigations of these questions.

Strong thermal fronts detected using 30 years (1982-2011) of PFV5.2 SST images were integrated with 27 months (2013-2015) of Aquarius satellite SSS measurements to investigate the surface temperature expressions of the N-STF and S-STF in the Tasman Sea (**Chapter 5**). Evidence was found that the S-STF has a strong ($\nabla SST \geq 2.5$°C 100 km^{-1}) surface thermal expressions near the land boundaries of Australia and New Zealand, but this study was limited to examining long-term (30 year) annual-mean and seasonal-mean distributions of thermal front occurrence. This study could be extended considerably by investigating surface expressions of the N-STF and S-STF in the Tasman Sea using a combination of thermal

front distributions and satellite SSS measurements complied over a shorter time scale (i.e. over a single month). For example, thermal fronts in the Tasman Sea could be detected using cloud-free daily merged microwave and infrared SST images (similar to the study of Miller et al. (2013) for the North Atlantic). The next step of this analysis would be to compare the distributions of thermal fronts detected over the course of a month with the positions of the N-STF and S-STF estimated using proxy criteria (Hamilton, 2006) applied to satellite SSS measurements from the SMOS (Font et al., 2004) or Aquarius sensors (Lagerloef et al., 2008). The comparison of the thermal front distributions and ancillary information from satellite SSS measurements may allow the positions of surface thermal expressions of the N-STF and S-STF to be inferred on a synoptic time-scale and could therefore enable meridional shifts in their positions in the open-ocean to be tracked over time.

An additional source of data that has not been examined in this thesis are CTD profiles from Argo profiling floats. These have been repeatedly deployed into the Southern Ocean since the late 1990s (Riser et al., 2016), and now offer an extensive source of observational data for remotely studying oceanographic processes on timescales from days to a decade. Argo floats gather temperature and salinity data from the upper 2000 m at an ~10 day sampling period, whilst their displacements between profiles can provide estimates of ocean circulation at the surface and depths of around 1000 m (Ollitrault and Rannou, 2012; Rosell-Fieschi et al., 2013). Data collected by Argo floats complements that collected by other ocean observing systems (Riser et al., 2016), for example, these data can help to place ocean remote sensing data into a vertical and 3D context (see e.g. Buckingham et al., 2014; Chow et al., 2017). Argo can also provide repeat observations of physical, biological and chemical properties in otherwise remote locations, such as the Southern Ocean.

Data collected by Argo floats since the late 1990s have produced relatively uniform, repeat sampling of the Southern Ocean at 1° lat-lon resolution (see e.g. Fig. 2 in Riser et al., 2016). This has already proven valuable in examining the physical oceanography of the Southern Ocean fronts. For example, data collected by Argo floats have been used to describe the recent positions of the ACC fronts (e.g. Boehme et al., 2008; Giglio and Johnson, 2016), the physical characteristics of the STF water mass boundary (Graham and de Boer, 2013), temporal variations in heat and freshwater content in the water masses bordering the ACC fronts (Giglio and Johnson, 2016) and to assess temporal variability in the zonal velocity of the ACC (Kosempa and Chambers, 2014). In the region of interest in this thesis, Argo float data has also enabled substantial knowledge to be resolved on the circulation of surface and intermediate waters in the waters off Australia and New Zealand (Rosell-Fieschi et al., 2013; Chiswell et al., 2015). Several questions that arise from this thesis that Argo float data could help address are discussed below.

This study provides some initial constraints on the likely upper bounds on seasonal migration of the S-STF at the borders of the Tasman Sea (**Chapter 5**). However, as yet there are no constraints on the seasonal migration of the S-STF in the central Tasman Sea, nor for the N-STF in the Tasman Sea. A limitation of this research is that surface expressions of the N-STF in the Tasman Sea and the S-STF in the central Tasman Sea could not be identified based on the 30 year annual-mean distributions of thermal fronts. One alternative approach for evaluating seasonal migration of the N-STF and S-STF would entail evaluating the seasonal extent of the STF zone in the Tasman Sea by applying a water mass classification scheme to data collected by Argo floats. For instance, Hamilton (2006) developed a classification scheme for describing the vertical layering of STW and SAW in T-S profiles collected in the Tasman Sea. Applied to a geographic set of T-S profile, this enables one to estimate the extent of the STF zone in the Tasman Sea; the N-STF being defined by the equatorward limit of surface SAW in the water column and the S-STF by the poleward limit of subsurface STW. Here, the application of Hamilton's (2006) classification scheme to seasonal composites of Argo CTD profiles collected within the Tasman Sea since the 2000s may help improve the determination of the seasonal migration of the N-STF and the S-STF within the Tasman Sea.

A bimodal distribution of thermal fronts is apparent along the Macquarie Ridge (**Chapter 5**). Analyses conducted here suggest that the bimodal distribution of thermal fronts may indicate bimodality in the latitude at which the S-STF typically crosses the Macquarie Ridge, with a northern mode in which the S-STF crosses the ridge at ~47°S and a southern mode in which the S-STF crosses the ridge at ~49°S. This interpretation remains speculative because of a positive bias in the Aquarius SSS images around southern New Zealand (Section 5.5.3), which hinders interpretation of the likely origin of thermal fronts in the northern mode. Aside from conducting further repeat hydrographic surveys, the existence of bimodality in the position of the S-STF along the Macquarie Ridge might be further investigated by examining the position of the S-STF in this region inferred using satellite SSS measurements from the Soil Moisture and Ocean Salinity sensor (Font et al., 2004), or by examining variability in the locations of water types (STW and SAW) by applying Hamilton's (2006) classification scheme to the growing number of Argo float CTD profiles collected in the eastern Tasman Sea post-2000.

The possibility that the position of the S-STF along the Macquarie Ridge has a bimodal character also raises several further questions - such as, does the position of the S-STF switch between the two modes or can the S-STF exist simultaneously in both positions - i.e. meander between them? how fast is the transition between these states? once in a particular state, how long does it remain? and how far to the east and west of the Macquarie Ridge does the bimodality extend?

A priority for further research related to **Chapter 6** is to examine whether the significant lag-correlations observed between basin-wide South Pacific wind stress curl and SST anomalies around southern New Zealand are also demonstrable between basin-wide wind stress curl and both SSH anomalies and thermocline depth anomalies around southern New Zealand. This would help to better understand the potential role of oceanic adjustment via propagating barotropic and/or baroclinic waves in linking SST anomalies around southern New Zealand with variations in South Pacific wind stress curl. This could be achieved by using remotely sensed and/or tide gauge SSH data for New Zealand (see e.g. Sasaki et al. (2008)) in conjunction with subsurface temperatures from an ocean state estimate - such as the Simple Ocean Data Assimilation (Carton and Giese, 2008).

Given the important role known to be played by first-mode baroclinic Rossby waves in explaining interannual to decadal SSH variability in the South Pacific (e.g. Qiu and Chen, 2006) and the Tasman Sea (e.g. Sasaki et al., 2008), it would be very interesting to investigate the SST variability in this region on the basis of the first-mode baroclinic Rossby wave model – like in the studies of Schneider and Miller (2001) in the North Pacific and Zhang and Wu (2010) in the North Atlantic. This would help understand further the possible role of ocean adjustment to remote wind forcing in modulating SSTs around southern New Zealand, as well as the extent to which SST variations in this area may be predictable based on wind forcing over the South Pacific.

Estimates of multi-decadal trends in SST were also made across the S-STF around southern New Zealand (**Chapter 6**). An examination of decadal variability in the heat budget of the upper-ocean mixed layer around southern New Zealand between the 1980s and 2010s using horizontal and vertical temperature and velocity data from an ocean reanalysis product (e.g. Carton and Giese, 2008) could be subject to further investigation. This might provide further information about the relative contribution of air-sea fluxes, horizontal heat advection and vertical heat advection in explaining the multi-decadal warming trend observed in STW and their links with changes taking place in the EAC extension (Hill et al., 2008).

References

Barale, V., Gower, J., and Alberotanza, L. 2010. *Oceanography from Space. Revisited. Springer, Dordrecht, Netherlands*. Springer, Dordrecht, Netherlands, 374 pp.

Bard, E. and Rickaby, R. E. M. 2009. Migration of the subtropical front as a modulator of glacial climate. *Nature*, **460** (7253), 380–383.

Bartlett, M. S. 1935. Some Aspects of the Time-Correlation Problem in Regard to Tests of Significance. *J. R. Stat. Soc.*, **98** (3), 536–543.

Beal, L. M., De Ruijter, W. P. M., Biastoch, A., and Zahn, R. 2011. On the role of the Agulhas system in ocean circulation and climate. *Nature*, **472** (7344), 429–436.

Beaugrand, G. and Reid, P. C. 2003. Long-term changes in phytoplankton, zooplankton and salmon related to climate. *Glob. Change Biol.*, **9** (6), 801–817.

Belkin, I. M. 1988. Main hydrological features of the central south Pacific (in Russian). In M. E. Vinogradov and M. V. Flint (Eds.), *Ecosystems of the Subantarctic Zone of the Pacific Ocean*, 12–17. Nauka, Moscow. English Translation, Pacific Subantarctic Ecosystems, 12-17, N. Z. Translation Centre, Wellington, 1997. Available from: http://www.library.niwa.co.nz/.

Belkin, I. M. 2002. Front. In J. W. Nybakken, W. W. Broenkow, and T. L. Vallier (Eds.), *Interdisciplinary Encyclopedia of Marine Sciences*, 433–436. Grolier, Danbury.

Belkin, I. M. and Cornillon, P. 2005. Bering Sea thermal fronts from Pathfinder data: Seasonal and interannual variability. *Pac. Oceanogr.*, **3** (1), 6–20.

Belkin, I. M. and Cornillon, P. C. 2003. SST Fronts of the Pacific Coastal and Marginal Seas. *Pac. Oceanogr.*, **1** (2), 90–113.

Belkin, I. M., Cornillon, P. C., and Sherman, K. 2009. Fronts in Large Marine Ecosystems. *Prog. Oceanogr.*, **81** (1-4), 223–236.

Belkin, I. M. and Gordon, A. L. 1996. Southern Ocean fronts from the Greenwich meridian to Tasmania. *J. Geophys. Res. Oceans*, **101** (C2), 3675–3696.

Belkin, I. M. and O'Reilly, J. E. 2009. An algorithm for oceanic front detection in chlorophyll and SST satellite imagery. *J. Mar. Syst.*, **78** (3), 319–326. Special Issue on Observational Studies of Oceanic Fronts.

Billany, W., Swart, S., Hermes, J., and Reason, C. 2010. Variability of the Southern Ocean fronts at the Greenwich Meridian. *J. Mar. Syst.*, **82** (4), 304–310.

Boehme, L., M, L., and Todd, C. 2014. Comparison of gridded sea surface temperature datasets for marine ecosystem studies. *Mar. Ecol. Prog. Ser.*, **516**, 7–22.

Boehme, L., Meredith, M. P., Thorpe, S. E., Biuw, M., and Fedak, M. 2008. Antarctic Circumpolar Current frontal system in the South Atlantic: Monitoring using merged Argo and animal-borne sensor data. *J. Geophys. Res. Oceans*, **113**, 2156–2202. C09012.

Boland, F. and Church, J. 1981. The East Australian Current 1978. *Deep Sea Res.*, **28**, 937–957.

Bost, C., Cotté, C., Bailleul, F., Cherel, Y., Charrassin, J., Guinet, C., Ainley, D., and Weimerskirch, H. 2009. The importance of oceanographic fronts to marine birds and mammals of the southern oceans. *J. Mar. Syst.*, **78** (3), 363–376.

Bostock, H. C., Hayward, B. W., Neil, H. L., Sabaa, A. T., and Scott, G. H. 2015. Changes in the position of the Subtropical Front south of New Zealand since the last glacial period. *Paleoceanography*, **30** (7), 824–844.

Bowen, M., Markham, J., Sutton, P., Zhang, X., Wu, Q., Shears, N. T., and Fernandez, D. 2017. Interannual Variability of Sea Surface Temperature in the Southwest Pacific and the Role of Ocean Dynamics. *J. Clim.*, **30** (18), 7481–7492.

Box, G. E. P. and Jenkins, G. M. 1976. *Time Series Analysis: Forecasting and Control, Revised Edition.* San Francisco: Holden Day, 575 pp.

Boyd, P., LaRoche, J., Gall, M., Frew, R., and McKay, R. M. L. 1999. Role of iron, light, and silicate in controlling algal biomass in subantarctic waters SE of New Zealand. *J. Geophys. Res. Oceans*, **104** (C6), 13395–13408.

Bradford, J. M., Cranfield, H. J., and Michael, K. P. 1991. Phytoplankton biomass in relation to the surface hydrography of southern New Zealand and possible effects on the food chain. *N. Z. J. Mar. Freshwater Res.*, **25** (2), 133–144.

Bradford-Grieve, J. M., Chang, F. H., Gall, M., Pickmere, S., and Richards, F. 1997. Size-fractionated phytoplankton standing stocks and primary production during austral winter and spring 1993 in the Subtropical Convergence region near New Zealand. *N. Z. J. Mar. Freshwater Res.*, **31** (2), 201–224.

Bretherton, C. S., Widmann, M., Dymnikov, V. P., Wallace, J. M., and Bladé, I. 1999. The Effective Number of Spatial Degrees of Freedom of a Time-Varying Field. *J. Clim.*, **12** (7), 1990–2009.

Brown, E., Colling, A., Park, D., Phillips, J., Rothery, D., and Wright, J. 2001. *Ocean Circulation, 2nd Edition*. Oxford: Open University, 286 pp.

Buckingham, C. E., Cornillon, P. C., Schloesser, F., and Obenour, K. M. 2014. Global observations of quasi-zonal bands in microwave sea surface temperature. *J. Geophys. Res. Oceans*, **119** (8), 4840–4866.

Burls, N. J. and Reason, C. J. C. 2006. Sea surface temperature fronts in the midlatitude South Atlantic revealed by using microwave satellite data. *J. Geophys. Res. Oceans*, **111** (C8), C08001.

Butler, E. C. V., Butt, J. A., Lindstrom, E., Teldesley, P., Pickmere, S., and Vincent, W. 1992. Oceanography of the Subtropical Convergence Zone around southern New Zealand. *N. Z. J. Mar. Freshwater Res.*, **26** (2), 131–154.

Cai, W. 2006. Antarctic ozone depletion causes an intensification of the Southern Ocean super-gyre circulation. *Geophys. Res. Lett.*, **33** (3), L03712.

Campanelli, A., Massolo, S., Grilli, F., Marini, M., Paschini, E., Rivaro, P., Artegiani, A., and Jacobs, S. 2011. Variability of nutrient and thermal structure in surface waters between New Zealand and Antarctica, October 2004-January 2005. *Polar Res.*, **30**, 7064.

Canny, J. 1986. A Computational Approach To Edge Detection. *IEEE Trans. Pattern Anal.*, **8** (6), 679698.

Carranza, M. M., Gille, S. T., Piola, A. R., Charo, M., and Romero, S. I. 2017. Wind modulation of upwelling at the shelf-break front off Patagonia: Observational evidence. *Journal of Geophysical Research: Oceans*, **122** (3), 2401–2421.

Carter, L., Garlick, R., Sutton, P., Chiswell, S., Oien, N., and Stanton, B. 1998. Ocean Circulation New Zealand. NIWA Chart Miscellaneous Series No.76.

Carter, L., McCave, I., and Williams, M. J. 2008. Circulation and Water Masses of the Southern Ocean: A Review. In F. Florindo and M. Siegert (Eds.), *Developments in Earth and Environmental Sciences*, Volume 8, 85–114. Elsevier.

Carton, J. A. and Giese, B. S. 2008. A Reanalysis of Ocean Climate Using Simple Ocean Data Assimilation (SODA). *Mon. Wea. Rev.*, **136** (8), 2999–3017.

Casey, K. S., Brandon, T. B., Cornillon, P., and Evans, R. 2010. The Past, Present, and Future of the AVHRR Pathfinder SST Program. In V. Barale, J. F. R. Gower, and L. Alberotanza (Eds.), *Oceanography from space: revisited.*, 273–287. Dordrecht, Heidelberg, London, New York: Springer.

Castelao, R. M., Mavor, T. P., Barth, J. A., and Breaker, L. C. 2006. Sea surface temperature fronts in the California Current System from geostationary satellite observations. *J. Geophys. Res. Oceans*, **111** (C9), C09026.

Cayula, J.-F. 1988. Edge detection for SST images. Master's thesis, Department of Electrical Engineering, University of Rhode Island, 91 pp.

Cayula, J.-F. and Cornillon, P. 1992. Edge Detection Algorithm for SST Images. *J. Atmos. Oceanic Technol.*, **9** (1), 67–80.

Cayula, J.-F. and Cornillon, P. 1995. Multi-Image Edge Detection for SST Images. *J. Atmos. Oceanic Technol.*, **12** (4), 821–829.

Chang, Y. and Cornillon, P. 2015. A comparison of satellite-derived sea surface temperature fronts using two edge detection algorithms. *Deep Sea Res. Part II*, **119**, 40–47.

Chang, Y., Shimada, T., Lee, M.-A., Lu, H.-J., Sakaida, F., and Kawamura, H. 2006. Wintertime sea surface temperature fronts in the Taiwan Strait. *Geophys. Res. Lett.*, **33** (23), L23603.

Chelton, D. B., deSzoeke, R. A., Schlax, M. G., El Naggar, K., and Siwertz, N. 1998. Geographical Variability of the First Baroclinic Rossby Radius of Deformation. *J. Phys. Oceanogr.*, **28** (3), 433–460.

Chelton, D. B. and Schlax, M. G. 1996. Global observations of oceanic Rossby waves. *Science*, **272**, 234–238.

Chelton, D. B., Schlax, M. G., Freilich, M. H., and Milliff, R. F. 2004. Satellite Measurements Reveal Persistent Small-Scale Features in Ocean Winds. *Science*, **303** (5660), 978–983.

Chelton, D. B. and Wentz, F. J. 2005. Global Microwave Satellite Observations of Sea Surface Temperature for Numerical Weather Prediction and Climate Research. *Bull. Amer. Meteor. Soc.*, **86** (8), 1097–1115.

Chen, K., Gawarkiewicz, G., Kwon, Y.-O., and Zhang, W. G. 2015. The role of atmospheric forcing versus ocean advection during the extreme warming of the Northeast U.S. continental shelf in 2012. *J. Geophys. Res. Oceans*, **120**, 4324–4339.

Chiswell, S. M. 1994. Variability in sea surface temperature around New Zealand from AVHRR images. *N. Z. J. Mar. Freshwater Res.*, **28** (2), 179–192.

Chiswell, S. M. 1996. Variability in the Southland Current, New Zealand. *N. Z. J. Mar. Freshwater Res.*, **30** (1), 1–17.

Chiswell, S. M., Bostock, H. C., Sutton, P. J., and Williams, M. J. 2015. Physical oceanography of the deep seas around New Zealand: a review. *N. Z. J. Mar. Freshwater Res.*, **49** (2), 286–317.

Chow, C. H., Cheah, W., and Tai, J.-H. 2017. A rare and extensive summer bloom enhanced by ocean eddies in the oligotrophic western North Pacific Subtropical Gyre. *Scientific Reports*, **7** (1), A6199.

Ciasto, L. M. and England, M. H. 2011. Observed ENSO teleconnections to Southern Ocean SST anomalies diagnosed from a surface mixed layer heat budget. *Geophys. Res. Lett.*, **38** (9), L09701. L09701.

Comiso, J. C., McClain, C. R., Sullivan, C. W., Ryan, J. P., and Leonard, C. L. 1993. Coastal zone color scanner pigment concentrations in the Southern Ocean and relationships to geophysical surface features. *J. Geophys. Res. Oceans*, **98** (C2), 2419–2451.

Conway, C. E., Bostock, H. C., Baker, J. A., Wysoczanski, R. J., and Verdier, A.-L. 2012. Evolution of Macquarie Ridge Complex seamounts: Implications for volcanic and tectonic processes at the Australia-Pacific plate boundary south of New Zealand. *Mar. Geol.*, **295-298** (0), 34 – 50.

Currie, K., Reid, M., and Hunter, K. 2011. Interannual variability of carbon dioxide drawdown by subantarctic surface water near New Zealand. *Biogeochemistry*, **104** (1), 23–34.

Currie, K. I. and Hunter, K. A. 1998. Surface water carbon dioxide in the waters associated with the subtropical convergence, east of New Zealand. *Deep Sea Res. Part I*, **45** (10), 1765–1777.

Davis, R. 1998. Preliminary results from directly measuring middepth circulation in the tropical and South Pacific. *J. Geophys. Res. Oceans*, **103** (C11), 24619–24639.

De Boer, A. M., Graham, R. M., Thomas, M. D., and Kohfeld, K. E. 2013. The control of the Southern Hemisphere Westerlies on the position of the Subtropical Front. *J. Geophys. Res. Oceans*, **118** (10), 5669–5675.

Deacon, G. 1933. A general account of the hydrology of South Atlantic Ocean. *Discovery Reports*, **7**, 171–238.

Deacon, G. 1937. The hydrology of the Southern Ocean. *Discovery Reports*, **15**, 1–124.

Deacon, G. 1982. Physical and biological zonation in the Southern Ocean. *Deep Sea Res. Part A*, **29** (1), 1–15.

Deacon, G. E. R. 1945. Water circulation and surface boundaries in the oceans. *Q. J. Roy. Meteor. Soc.*, **71**, 11–25.

Dee, D., Fasullo, J., Shea, D., Walsh, J., and Staff., N. 2016. The Climate Data Guide: Atmospheric Reanalysis: Overview and Comparison Tables. Available from: https://www.climatedataguide.ucar.edu/climate-data/atmospheric-reanalysis-overview-comparison-tables. [Online; accessed July-2013].

Deser, C., Alexander, M. A., Xie, S.-P., and Phillips, A. S. 2010. Sea Surface Temperature Variability: Patterns and Mechanisms. *Annual Review of Marine Science*, **2**, 115–143.

Dong, S., Gille, S. T., and Sprintall, J. 2007. An Assessment of the Southern Ocean Mixed Layer Heat Budget. *J. Clim.*, **20** (17), 4425–4442.

Dong, S., Sprintall, J., and Gille, S. T. 2006. Location of the Antarctic Polar Front from AMSR-E Satellite Sea Surface Temperature Measurements. *J. Phys. Oceanogr.*, **36** (11), 2075–2089.

Dufour, C. O., Griffies, S. M., de Souza, G. F., Frenger, I., Morrison, A. K., Palter, J. B., Sarmiento, J. L., Galbraith, E. D., Dunne, J. P., Anderson, W. G., and Slater, R. D. 2015. Role of Mesoscale Eddies in Cross-Frontal Transport of Heat and Biogeochemical Tracers in the Southern Ocean. *Journal of Physical Oceanography*, **45** (12), 3057–3081.

Dunn, M. R., Hurst, R., J., R., Francis, R. I. C. C., Devine, J., and McKenzie, A. 2009. *Fish abundance and climate trends in New Zealand*. New Zealand Aquatic Environment and Biodiversity Report No. 31, 75 pp.

Edwards, R. and Emery, W. 1982. Australasian Southern Ocean Frontal Structure during Summer 1976-77. *Aust. J. Mar. Freshwater Res.*, **33**, 3–22.

Emery, W. J. and Thomson, R. E. 2001. *Data Analysis Methods in Physical Oceanography*. Elsevier Science, 638 pp.

Evans, R., Vasquez, J., and Casey, K. S. 2009. 4 km Pathfinder Version 5 User Guide. Available from: https://www.nodc.noaa.gov/sog/pathfinder4km/userguide.html. [Online; accessed May-2011].

Fedorov, A. V. and Brown, J. N. 2009. Equatorial Waves. In J. H. Steele (Ed.), *Encyclopedia of Ocean Sciences*, 3679–3695. Academic.

Fedorov, K. 1986. *The Physical Nature and Structure of Oceanic Fronts*. Springer-Verlag, New York, 333 pp.

Fernandez, D., Bowen, M., and Carter, L. 2014. Intensification and variability of the confluence of subtropical and subantarctic boundary currents east of New Zealand. *J. Geophys. Res. Oceans*, **119** (2), 1146–1160.

Fletcher, M. S. E., Gruber, N., Jacobson, A. R., Doney, S. C., Dutkiewicz, S., Gerber, M., Follows, M., Joos, F., Lindsay, K., Menemenlis, D., Mouchet, A., Müller, S. A., and Sarmiento, J. L. 2006. Inverse estimates of anthropogenic CO2 uptake, transport, and storage by the ocean. *Glob. Biogeochem. Cycles*, **20** (2), GB2002.

Font, J., Lagerloef, G. S. E., LeVine, D. M., Camps, A., and Zanife, O. Z. 2004. The determination of surface salinity with the European SMOS space mission. *IEEE Trans. Geosci. Remote Sens.*, **42**, 2196–2204.

Frankignoul, C. and Hasselmann, K. 1977. Stochastic climate models, Part II. *Tellus*, **29**, 289–305.

Freeman, N. M. and Lovenduski, N. S. 2016. Mapping the Antarctic Polar Front: weekly realizations from 2002 to 2014. *Earth Syst. Sci. Data*, **8** (1), 191–198.

Fuller, W. A. 1995. *Introduction to Statistical Time Series*. Wiley-Interscience, 728 pp.

Garner, D. M. 1959. The sub-tropical convergence in New Zealand surface waters. *N.Z. J. Geol. Geophys.*, **2** (2), 315–337.

Garner, D. M. 1969. The geopotential topography of the Ocean surface around New Zealand. *N. Z. J. Mar. Freshwater Res.*, **3** (2), 209–219.

Ghil, M., Allen, M. R., Dettinger, M. D., Ide, K., Kondrashov, D., Mann, M. E., Robertson, A. W., Saunders, A., Tian, Y., Varadi, F., and Yiou, P. 2002. Advanced spectral methods for climatic time series. *Rev. Geophys.*, **40** (1), 1–41.

Giglio, D. and Johnson, G. C. 2016. Subantarctic and Polar Fronts of the Antarctic Circumpolar Current and Southern Ocean Heat and Freshwater Content Variability: A View from Argo. *J. Phys. Oceanogr.*, **46**, 749–768.

Gille, S. T. 1994. Mean sea surface height of the Antarctic Circumpolar Current from Geosat data: Method and application. *J. Geophys. Res. Oceans*, **99** (C9), 18255–18273.

Gille, S. T. 2008. Decadal-Scale Temperature Trends in the Southern Hemisphere Ocean. *J. Clim.*, **21** (18), 4749–4765.

Gillett, N. P. and Thompson, D. W. J. 2003. Simulation of Recent Southern Hemisphere Climate Change. *Science*, **302** (5643), 273–275.

Graham, R. M. and de Boer, A. M. 2013. The Dynamical Subtropical Front. *J. Geophys. Res. Oceans*, **118**, 5676–5685.

Graham, R. M., de Boer, A. M., Heywood, K. J., Chapman, M. R., and Stevens, D. P. 2012. Southern Ocean fronts: Controlled by wind or topography? *J. Geophys. Res. Oceans*, **117** (C8), C08018.

Hall, A. and Visbeck, M. 2002. Synchronous Variability in the Southern Hemisphere Atmosphere, Sea Ice, and Ocean Resulting from the Annular Mode. *J. Clim.*, **15** (21), 3043–3057.

Hamilton, L. 2006. Structure of the Subtropical Front in the Tasman Sea. *Deep Sea Res. Part I*, **53** (12), 1989–2009.

Heath, R. 1980. Eastwards oceanic flow past northern New Zealand. *N. Z. J. Mar. Freshwater Res.*, **14** (2), 169–182.

Heath, R. 1981. Oceanic fronts around southern New Zealand. *Deep Sea Res. Part A*, **28** (6), 547–560.

Heath, R. A. 1975. *Oceanic circulation and hydrology off the southern half of South Island, New Zealand*. New Zealand Oceanographic Institute, Wellington, 36 pp.

Heath, R. A. 1976. Models of the diffusive-advective balance at the subtropical convergence. *Deep Sea Res. Oceanogr. Abstr.*, **23** (12), 1153 – 1164.

Heath, R. A. 1982. What drives the mean circulation on the New Zealand west coast continental shelf? *N. Z. J. Mar. Freshwater Res.*, **16** (2), 215–226.

Heath, R. A. 1985. A review of the physical oceanography of the seas around New Zealand - 1982. *N. Z. J. Mar. Freshwater Res.*, **19** (1), 79–124.

Hickox, R., Belkin, I., Cornillon, P., and Shan, Z. 2000. Climatology and seasonal variability of ocean fronts in the East China, Yellow and Bohai seas from satellite SST data. *Geophys. Res. Lett.*, **27** (18), 2945–2948.

Hill, K. L., Rintoul, S. R., Coleman, R., and Ridgway, K. R. 2008. Wind forced low frequency variability of the East Australia Current. *Geophys. Res. Lett.*, **35** (8), L08602.

Hill, K. L., Rintoul, S. R., Oke, P. R., and Ridgway, K. 2010. Rapid response of the East Australian Current to remote wind forcing: The role of barotropic-baroclinic interactions. *J. Mar. Res.*, **68** (3-4), 413–431.

Hill, K. L., Rintoul, S. R., Ridgway, K. R., and Oke, P. R. 2011. Decadal changes in the South Pacific western boundary current system revealed in observations and ocean state estimates. *J. Geophys. Res. Oceans*, **116** (C1), C01009.

Hines, K. M., Bromwich, D. H., and Marshall, G. J. 2000. Artificial Surface Pressure Trends in the NCEP/NCAR Reanalysis over the Southern Ocean and Antarctica. *J. Clim.*, **13** (22), 3940–3952.

Holbrook, N. J., Goodwin, I. D., McGregor, S., Molina, E., and Power, S. B. 2011. ENSO to multi-decadal time scale changes in East Australian Current transports and Fort Denison sea level: Oceanic Rossby waves as the connecting mechanism. *Deep Sea Res. Part II*, **58** (5), 547–558.

Hopkins, J., Challenor, P., and Shaw, A. G. P. 2011. A New Statistical Modeling Approach to Ocean Front Detection from SST Satellite Images. *J. Atmos. Oceanic Technol.*, **27** (1), 173–191.

Hopkins, J., Shaw, A. G. P., and Challenor, P. 2010. The Southland Front, New Zealand: Variability and ENSO correlations. *Cont. Shelf Res.*, **30** (14), 1535–1548.

Hopkins, J. E. 2008. *Statistical Modelling and Variability of the Subtropical Front, New Zealand*. Ph. D. thesis, University of Southampton, 195 pp.

Huppert, H. E. and Bryan, K. 1976. Topographically generated eddies. *Deep Sea Res. Oceanogr. Abstr.*, **23** (8), 655–679.

Hurlburt, H. E., Metzger, E. J., Hogan, P. J., Tilburg, C. E., and Shriver, J. F. 2008. Steering of upper ocean currents and fronts by the topographically constrained abyssal circulation. *Dyn. Atmos. Oceans*, **45** (3-4), 102–134.

ISCCP 2009. International Satellite Cloud Climatology Project. Available from: https://isccp.giss.nasa.gov. [Online; accessed Aug-2017].

Jain, R., Kasturi, R., and Schunck, B. G. 1995. *Machine Vision*. McGraw-Hill, 549 pp.

James, C., Tomczak, M., Helmond, I., and Pender, L. 2002. Summer and winter surveys of the Subtropical Front of the southeastern Indian Ocean 1997-1998. *J. Mar. Syst.*, **37** (1-3), 129–149.

Jayne, S. R. and Marotzke, J. 2002. The Oceanic Eddy Heat Transport. *J. Phys. Oceanogr.*, **32** (12), 3328–3345.

Jeffrey, M. Z. 1986. *Climatological features of the subtropical convergence in Australian and New Zealand waters*. Sydney, N.S.W.: Ocean Sciences Institute Report No. 17. University of Sydney, 95 pp.

Jillett, J. B. 1969. Seasonal hydrology of waters off the Otago peninsula, South-Eastern New Zealand. *N. Z. J. Mar. Freshwater Res.*, **3** (3), 349–375.

Kahru, M., Di Lorenzo, E., Manzano-Sarabia, M., and Mitchell, B. G. 2012. Spatial and temporal statistics of sea surface temperature and chlorophyll fronts in the California Current. *J. Plankton Res.*, **34** (9), 749–760.

Kalnay, E., Kanamitsu, M., Kistler, R., Collins, W., Deaven, D., Gandin, L., Iredell, M., Saha, S., White, G., Woollen, J., Zhu, Y., Leetmaa, A., Reynolds, R., Chelliah, M., Ebisuzaki, W., Higgins, W., Janowiak, J., Mo, K. C., Ropelewski, C., Wang, J., Jenne, R., and Joseph, D. 1996. The NCEP/NCAR 40-Year Reanalysis Project. *Bull. Amer. Meteor. Soc.*, **77** (3), 437–471.

Karstensen, J. and Quadfasel, D. 2002. Water subducted into the Indian Ocean subtropical gyre. *Deep Sea Res. Part II*, **49**, 1441–1457.

Kearns, E. J., Hanafin, J. A., Evans, R. H., Minnett, P. J., and Brown, O. B. 2000. An Independent Assessment of Pathfinder AVHRR Sea Surface Temperature Accuracy Using the Marine Atmosphere Emitted Radiance Interferometer (MAERI). *Bull. Amer. Meteor. Soc.*, **81** (7), 1525–1536.

Khatiwala, S., Primeau, F., and Hall, T. 2009. Reconstruction of the history of anthropogenic CO2 concentrations in the ocean. *Nature*, **462** (7271), 346–349.

Kida, S., Mitsudera, H., Aoki, S., Guo, X., Ito, S.-i., Kobashi, F., Komori, N., Kubokawa, A., Miyama, T., Morie, R., Nakamura, H., Nakamura, T., Nakano, H., Nishigaki, H., Nonaka, M., Sasaki, H., Sasaki, Y. N., Suga, T., Sugimoto, S., Taguchi, B., Takaya, K., Tozuka, T., Tsujino, H., and Usui, N. 2015. Oceanic fronts and jets around Japan: a review. *Journal of Oceanography*, **71** (5), 469–497.

Killworth, P. D., Chelton, D. B., and DeSzoeke, R. 1997. The speed of observed and theroretical long extra-tropical planetary waves. *J. Phys. Oceanogr.*, **27**, 1946–1966.

Kilpatrick, K. A., Podestá, G. P., and Evans, R. 2001. Overview of the NOAA/NASA advanced very high resolution radiometer Pathfinder algorithm for sea surface temperature and associated matchup database. *J. Geophys. Res. Oceans*, **106** (C5), 9179–9197.

Kistler, R., Collins, W., Saha, S., White, G., Woollen, J., Kalnay, E., Chelliah, M., Ebisuzaki, W., Kanamitsu, M., Kousky, V., van den Dool, H., Jenne, R., and Fiorino, M. 2001. The NCEP/NCAR 50-Year Reanalysis: Monthly Means CD-ROM and Documentation. *Bull. Amer. Meteor. Soc.*, **82** (2), 247–267.

Kohfeld, K., Graham, R., de Boer, A., Sime, L., Wolff, E., Le Quéré, C., and Bopp, L. 2013. Southern Hemisphere westerly wind changes during the Last Glacial Maximum: paleo-data synthesis. *Quat. Sci. Rev.*, **68**, 76–95.

Kondrashov, D., Feliks, Y., and Ghil, M. 2005. Oscillatory modes of extended Nile River records (A.D. 622-1922). *Geophys. Res. Lett.*, **32** (10), L10702.

Kondrashov, D. and Ghil, M. 2006. Spatio-temporal filling of missing points in geophysical data sets. *Nonlinear Proc. Geophys.*, **13** (2), 151–159.

Kosempa, M. and Chambers, D. P. 2014. Southern Ocean velocity and geostrophic transport fields estimated by combining Jason altimetry and Argo data. *J. Geophys. Res. Oceans*, **119**, 4761–4776.

Kostianoy, A. G., Ginzburg, A. I., Frankignoulle, M., and Delille, B. 2004. Fronts in the Southern Indian Ocean as inferred from satellite sea surface temperature data. *J. Mar. Syst.*, **45** (1-2), 55–73.

Kvile, K. O., Taranto, G., Pitcher, T. J., and Morato, T. 2014. A global assessment of seamount ecosystems knowledge using an ecosystem evaluation framework. *Biol. Conserv.*, **173**, 108–120.

Lagerloef, G., Colomb, R., Le Vine, D., Wentz, F., Yueh, S., Ruf, C., Lilly, J., Gunn, J., Chao, Y., Decharon, A., Feldman, G., and Swift, C. 2008. The Aquarius/SAC-D mission: special issue on salinity. *Oceanography*, **21** (1), 69–81.

Lagerloef, G., Kao, H.-Y., Meissner, T., and Vazquez, J. 2015. Aquarius salinity validation analysis data version 4.0. Available from: http://www.podaac.jpl.nasa.gov/SeaSurfaceSalinity/Aquarius. [Online; accessed October-2015].

Lan, K.-W., Kawamura, H., Lee, M.-A., Chang, Y., Chan, J.-W., and Liao, C.-H. 2009. Summertime sea surface temperature fronts associated with upwelling around the Taiwan Bank. *Continental Shelf Research*, **29** (7), 903–910.

Lenton, A., Tilbrook, B., Law, R. M., Bakker, D., Doney, S. C., Gruber, N., Ishii, M., Hoppema, M., Lovenduski, N. S., Matear, R. J., McNeil, B. I., Metzl, N., Mikaloff Fletcher, S. E., Monteiro, P. M. S., Rödenbeck, C., Sweeney, C., and Takahashi, T. 2013. Sea-Air CO2 fluxes in the Southern Ocean for the period 1990-2009. *Biogeosciences*, **10** (6), 4037–4054.

L'Heureux, M. L. and Thompson, D. W. J. 2006. Observed Relationships between the El Niño-Southern Oscillation and the Extratropical Zonal-Mean Circulation. *J. Clim.*, **19** (2), 276–287.

Li, J., Sun, C., and Jin, F.-F. 2013. NAO implicated as a predictor of Northern Hemisphere mean temperature multidecadal variability. *Geophys. Res. Lett.*, **40** (20), 5497–5502.

Li, X.-F., Li, J., and Li, Y. 2015. Recent Winter Precipitation Increase in the Middle-Lower Yangtze River Valley since the Late 1970s: A Response to Warming in the Tropical Indian Ocean. *J. Clim.*, **28** (9), 3857–3879.

Li, Y., Li, J., and Feng, J. 2012. A Teleconnection between the Reduction of Rainfall in Southwest Western Australia and North China. *J. Clim.*, **25** (24), 8444–8461.

Lilly, J. and Lagerloef, G. 2008. Aquarius Level 3 Processing Algorithm Theoretical Basis Document. Available from: http://oceancolor.gsfc.nasa.gov/AQUARIUS/DOCS/Aquarius-gridding-implementation.feb2009.pdf. [Online; accessed April-2015].

Lin, J. 1991. Divergence measures based on the Shannon Entropy. *IEEE Trans. Inf. Theory*, **37** (1), 145–150.

Lovenduski, N. S. and Gruber, N. 2005. Impact of the Southern Annular Mode on Southern Ocean circulation and biology. *Geophys. Res. Lett.*, **32** (11), L11603.

Luis, A. J. and Pednekar, S. 2010. Hydrodynamics between Africa and Antarctica during Austral Summer 2008. *J. Mar. Syst.*, **83**, 45 – 57.

Lumpkin, R. and Pazos, M. 2007. Measuring surface currents with Surface Velocity Program drifters: the instrument, its data, and some recent results. In A. Griffa, A. D. J. Kirwan, A. J. Mariano, T. Özgökmen, and H. T. Rossby (Eds.), *Lagrangian Analysis and Prediction of Coastal and Ocean Dynamics*, Chapter 2. Cambridge University Press.

Lutjeharms, J., Valentine, H., and van Ballegooyen, R. 1993. On the subtropical convergence in the south Atlantic Ocean. *S. Afr. J. Sci.*, **89**, 552–559.

Manucharyan, G. E. and Timmermans, M.-L. 2013. Generation and Separation of Mesoscale Eddies from Surface Ocean Fronts. *Journal of Physical Oceanography*, **43** (12), 2545–2562.

Marshall, D. 1995. Topographic Steering of the Antarctic Circumpolar Current. *J. Phys. Oceanogr.*, **25** (7), 1636–1650.

Marshall, G. J. 2003. Trends in the Southern Annular Mode from Observations and Reanalyses. *J. Clim.*, **16** (24), 4134–4143.

Marshall, G. J. and Harangozo, S. A. 2000. An appraisal of NCEP/NCAR reanalysis MSLP data viability for climate studies in the South Pacific. *Geophys. Res. Lett.*, **27** (19), 3057–3060.

Marullo, S., Buongiorno Nardelli, B., Guarracino, M., and Santoleri, R. 2007. Observing the Mediterranean Sea from space: 21 years of Pathfinder-AVHRR sea surface temperatures (1985 to 2005): re-analysis and validation. *Ocean Sci.*, **3** (2), 299–310.

Mata, M. M., Tomczak, M., Wijffels, S., and Church, J. A. 2000. East Australian Current volume transports at 30°S: Estimates from the World Ocean Circulation Experiment hydrographic sections PR11/P6 and the PCM3 current meter array. *J. Geophys. Res. Oceans*, **105** (C12), 28509–28526.

Matano, R. P. and Palma, E. D. 2008. On the Upwelling of Downwelling Currents. *Journal of Physical Oceanography*, **38** (11), 2482–2500.

Matear, R. J., Chamberlain, M. A., Sun, C., and Feng, M. 2013. Climate change projection of the Tasman Sea from an Eddy-resolving Ocean Model. *J. Geophys. Res. Oceans*, **118** (6), 2961–2976.

McCartney, M. 1977. Subantarctic mode water. A voyage of discovery. *Deep Sea Res.*, **24**, 103–119.

Miller, P. 2009. Composite front maps for improved visibility of dynamic sea-surface features on cloudy SeaWiFS and AVHRR data. *J. Mar. Syst.*, **78** (3), 327 – 336. Special Issue on Observational Studies of Oceanic Fronts.

Miller, P. I., Read, J. F., and Dale, A. C. 2013. Thermal front variability along the North Atlantic Current observed using microwave and infrared satellite data. *Deep Sea Res. Part II*, **98**, 244–256.

Ministry of Fisheries, W. 2008. The State of our Fisheries 2008. Available from: http://www.fish.govt.nz/NR/rdonlyres/87304079-4450-4025-9B08-37E036C56768/0/thestateofourfisheries2008.pdf. [Online; accessed September-2014].

Minnett, P. 2009. Satellite remote sensing of sea surface temperatures. In J. H. Steele, K. K. Turekian, and S. A. Thorpe (Eds.), *Encyclopedia of Ocean Sciences (Second Edition)*, 91–102. Elsevier.

Minnett, P., Evans, R., Kearns, E., and Brown, O. 2002. Sea-surface temperature measured by the Moderate Resolution Imaging Spectroradiometer (MODIS). In *Geoscience and Remote Sensing Symposium, 2002. IGARSS '02. 2002 IEEE International*, Volume 2, 1177–1179.

Minobe, S., Kuwano-Yoshida, A., Komori, N., Xie, S.-P., and Small, R. J. 2008. Influence of the Gulf Stream on the troposphere. *Nature*, **452** (7184), 206–209.

Mitchell, J. M., Dzerdzeevskii, B., Flohn, H., Hofmeyr, W. L., Lamb, H. H., Rao, K. N., and C., W. C. 1966. *Climatic Change Technical Note 79*. World Meteorological Organization, Geneva, 79 pp.

Moore, J. K. and Abbott, M. R. 2000. Phytoplankton chlorophyll distributions and primary production in the Southern Ocean. *J. Geophys. Res. Oceans*, **105** (C12), 28709–28722.

Moore, J. K. and Abbott, M. R. 2002. Surface chlorophyll concentrations in relation to the Antarctic Polar Front: seasonal and spatial patterns from satellite observations. *J. Mar. Syst.*, **37** (1-3), 69–86.

Moore, J. K., Abbott, M. R., and Richman, J. G. 1997. Variability in the location of the Antarctic Polar Front (90-20°W) from satellite sea surface temperature data. *J. Geophys. Res. Oceans*, **102** (C13), 27825–27833.

Moore, J. K., Abbott, M. R., and Richman, J. G. 1999. Location and dynamics of the Antarctic Polar Front from satellite sea surface temperature data. *J. Geophys. Res. Oceans*, **104** (C2), 3059–3073.

Moore, J. K., Abbott, M. R., Richman, J. G., Smith, W. O., Cowles, T. J., Coale, K. H., Gardner, W. D., and Barber, R. T. 1999. SeaWiFS satellite ocean color data from the Southern Ocean. *Geophys. Res. Lett.*, **26** (10), 1465–1468.

Morato, T., Miller, P. I., Dunn, D. C., Nicol, S. J., Bowcott, J., and Halpin, P. N. 2016. A perspective on the importance of oceanic fronts in promoting aggregation of visitors to seamounts. *Fish Fish*, **17** (4), 1227–1233.

Morris, M., Stanton, B., and Neil, H. 2001. Subantarctic oceanography around New Zealand: Preliminary results from an ongoing survey. *N. Z. J. Mar. Freshwater Res.*, **35** (3), 499–519.

Mudelsee, M. 2010. *Climate Time Series Analysis: Classical Statistical and Bootstrap Methods. First edition.* Springer, Dordrecht Heidelberg London New York, 454 pp.

Mullan, A. B. 1998. Southern hemisphere sea-surface temperatures and their contemporary and lag association with New Zealand temperature and precipitation. *Int. J. Climatol.*, **18** (8), 817–840.

Murphy, R. J., Pinkerton, M. H., Richardson, K. M., Bradford-Grieve, J. M., and Boyd, P. W. 2001. Phytoplankton distributions around New Zealand derived from SeaWiFS remotely-sensed ocean colour data. *N. Z. J. Mar. Freshwater Res.*, **35** (2), 343–362.

Nagata, Y., Michida, Y., and Umimura, Y. 1988. Variations of positions and structures of the ocean fronts in the Indian Ocean sector of the Southern Ocean in the period from 1965 to 1987. In D. Sahrhage (Ed.), *Antarctic Ocean and Resources Variability*, 92–98. Springer-Verlag, New York.

Nakamura, H., Sampe, T., Goto, A., Ohfuchi, W., and Xie, S.-P. 2008. On the importance of midlatitude oceanic frontal zones for the mean state and dominant variability in the tropospheric circulation. *Geophys. Res. Lett.*, **35** (15), L15709.

Neil, H. L., Carter, L., and Morris, M. Y. 2004. Thermal isolation of Campbell Plateau, New Zealand, by the Antarctic Circumpolar Current over the past 130 kyr. *Paleoceanography*, **19** (4), PA4408.

Nieto, K., Demarcq, H., and McClatchie, S. 2012. Mesoscale frontal structures in the Canary Upwelling System: New front and filament detection algorithms applied to spatial and temporal patterns. *Remote Sens. Environ.*, **123**, 339–346.

Nikolaidis, N. and Pitas, I. 1998. Nonlinear processing and analysis of angular signals. *IEEE T. Signal Proces.*, **46** (12), 3181–3194.

Nilsson, C. and Cresswell, G. 1980. The formation and evolution of East Australian current warm-core eddies. *Prog. Oceanogr.*, **9** (3), 133–183.

Nodder, S. D., Pilditch, C. A., Probert, P., and Hall, J. A. 2003. Variability in benthic biomass and activity beneath the Subtropical Front, Chatham Rise, SW Pacific Ocean. *Deep Sea Res. Part I*, **50** (8), 959–985.

NSIDC 2008. Instrument Description: Spaceborne Scatterometers. Available from: http://www.goo.gl/7csuTg. [Online; accessed March-2015].

Oliver, E. C. J. and Holbrook, N. J. 2014. Extending our understanding of South Pacific gyre "spin-up": Modeling the East Australian Current in a future climate. *J. Geophys. Res. Oceans*, **119** (5), 2788–2805.

Ollitrault, M. and Rannou, J.-P. 2012. ANDRO: An Argo-Based Deep Displacement Dataset. *J. Atmos. Oceanic Technol.*, **30** (4), 759–788.

Oram, J. J., McWilliams, J. C., and Stolzenbach, K. D. 2008. Gradient-based edge detection and feature classification of sea-surface images of the Southern California Bight. *Remote Sens. Environ.*, **112** (5), 2397–2415.

Orsi, A. H., Whitworth III, T., and Nowlin Jr., W. D. 1995. On the meridional extent and fronts of the Antarctic Circumpolar Current. *Deep Sea Res. Part I*, **42** (5), 641–673.

Pedlosky 1996. *Ocean Circulation Theory*. Springer, NY, 435 pp.

Pond, S. and Pickard, G. L. 1983. *Introductory Dynamical Oceanography*. 2d ed. Pergamon 329 pp.

Przeslawski, R., Williams, A., Nichol, S. L., Hughes, M. G., Anderson, T. J., and Althaus, F. 2011. Biogeography of the Lord Howe Rise region, Tasman Sea. *Deep Sea Res. Part II*, **58** (7-8), 959–969.

Pyper, B. J. and Peterman, R. M. 1998. Comparison of methods to account for autocorrelation in correlation analyses of fish data. *Can. J. Fish. Aquat. Sci.*, **55** (9), 2127–2140.

Qiu, B. and Chen, S. 2006. Decadal Variability in the Large-Scale Sea Surface Height Field of the South Pacific Ocean: Observations and Causes. *J. Phys. Oceanogr.*, **36** (9), 1751–1762.

Rahmstorf, S. 1992. Modelling ocean temperatures and mixed-layer depths in the Tasman sea off the South Island, New Zealand. *N. Z. J. Mar. Freshwater Res.*, **26** (1), 37–51.

Reason, C. J. C. and Jagadheesha, D. 2005. Relationships between South Atlantic SST Variability and Atmospheric Circulation over the South African Region during Austral Winter. *J. Clim.*, **18** (16), 3339–3355.

Richardson, A. J. and Schoeman, D. S. 2004. Climate Impact on Plankton Ecosystems in the Northeast Atlantic. *Science*, **305** (5690), 1609–1612.

Ridgway, K. and Dunn, J. 2003. Mesoscale structure of the mean East Australian Current System and its relationship with topography. *Prog. Oceanogr.*, **56** (2), 189–222.

Ridgway, K. R. 2007. Long-term trend and decadal variability of the southward penetration of the East Australian Current. *Geophys. Res. Lett.*, **34** (13), L13613.

Ridgway, K. R., Coleman, R. C., Bailey, R. J., and Sutton, P. 2008. Decadal variability of East Australian Current transport inferred from repeated high-density XBT transects, a CTD survey and satellite altimetry. *J. Geophys. Res. Oceans*, **113** (C8), C08039.

Rintoul, S., Donguy, J., and Roemmich, D. 1997. Seasonal evolution of upper ocean thermal structure between Tasmania and Antarctica. *Deep Sea Res. Part I*, **44** (7), 1185–1202.

Rintoul, S. R. 2007. Antarctic Circumpolar Current. In B. Riffenburgh (Ed.), *Encyclopedia of the Antarctic*, 234–239. Routledge.

Rintoul, S. R. and Bullister, J. L. 1999. A late winter hydrographic section from Tasmania to Antarctica. *Deep Sea Res. Part I*, **46** (8), 1417 – 1454.

Rintoul, S. R. and England, M. H. 2002. Ekman Transport Dominates Local Air-Sea Fluxes in Driving Variability of Subantarctic Mode Water. *J. Phys. Oceanogr.*, **32** (5), 1308–1321.

Riser, S. C., Freeland, H. J., Roemmich, D., Wijffels, S., Troisi, A., Belbeoch, M., Gilbert, D., Xu, J., Pouliquen, S., Thresher, A., Le Traon, P.-Y., Maze, G., Klein, B., Ravichandran, M., Grant, F., Poulain, P.-M., Suga, T., Lim, B., Sterl, A., Sutton, P., Mork, K.-A., Velez-Belchi, P. J., Ansorge, I., King, B., Turton, J., Baringer, M., and Jayne, S. R. 2016. Fifteen years of ocean observations with the global Argo array. *Nature Clim. Chang.*, **6** (2), 145–153.

Rivas, A. L. and Pisoni, J. P. 2010. Identification, characteristics and seasonal evolution of surface thermal fronts in the Argentinean Continental Shelf. *J. Mar. Syst.*, **79** (1-2), 134 – 143.

Robertson, D., Roberts, P., and Wilson, J. 1978. Mesopelagic faunal transition across the Subtropical Convergence east of New Zealand. *N. Z. J. Mar. Freshwater Res.*, **12**, 295–312.

Robinson, I. 2004. *Measuring the Oceans from Space*. Springer-Praxis Publishers Ltd, Chichester, UK, 670 pp.

Robinson, I. S. 2010. *Discovering the Ocean from Space*. Springer Berlin Heidelberg, 638 pp.

Roden, G. I. 1975. On North Pacific Temperature, Salinity, Sound Velocity and Density Frontsand their Relation to the Wind and Energy Flux Fields. *J. Phys. Oceanogr.*, **5** (4), 557–571.

Roemmich, D., Gilson, J., Davis, R., Sutton, P., Wijffels, S., and Riser, S. 2007. Decadal Spinup of the South Pacific Subtropical Gyre. *J. Phys. Oceanogr.*, **37** (2), 162–173.

Roemmich, D. and Sutton, P. 1998. The mean and variability of ocean circulation past northern New Zealand: Determining the representativeness of hydrographic climatologies. *J. Geophys. Res. Oceans*, **103** (C6), 13041–13054.

Rosell-Fieschi, M., Rintoul, S. R., Gourrion, J., and Pelegrí, J. L. 2013. Tasman Leakage of intermediate waters as inferred from Argo floats. *Geophys. Res. Lett.*, **40** (20), 5456–5460. 2013GL057797.

Sallée, J. B., Speer, K., and Morrow, R. 2008. Response of the Antarctic Circumpolar Current to Atmospheric Variability. *J. Clim.*, **21** (12), 3020–3039.

Santer, B. D., Wigley, T. M. L., Boyle, J. S., Gaffen, D. J., Hnilo, J. J., Nychka, D., Parker, D. E., and Taylor, K. E. 2000. Statistical significance of trends and trend differences in layer-average atmospheric temperature time series. *J. Geophys. Res. Atmos.*, **105** (D6), 7337–7356.

Saraceno, M., Provost, C., Piola, A. R., Bava, J., and Gagliardini, A. 2004. Brazil Malvinas Frontal System as seen from 9 years of advanced very high resolution radiometer data. *J. Geophys. Res. Oceans*, **109** (C5), C05027.

Sasaki, Y. N., Minobe, S., Schneider, N., Kagimoto, T., Nonaka, M., and Sasaki, H. 2008. Decadal Sea Level Variability in the South Pacific in a Global Eddy-Resolving Ocean Model Hindcast. *J. Phys. Oceanogr.*, **38** (8), 1731–1747.

Scales, K. L., Miller, P. I., Embling, C. B., Ingram, S. N., Pirotta, E., and Votier, S. C. 2014. Mesoscale fronts as foraging habitats: composite front mapping reveals oceanographic drivers of habitat use for a pelagic seabird. *J. R. Soc. Interface*, **11** (100), 20140679.

Schlax, M. G. and Chelton, D. B. 2008. The influence of mesoscale eddies on the detection of quasi-zonal jets in the ocean. *Geophys. Res. Lett.*, **35** (24), L24602.

Schneider, N. and Miller, A. J. 2001. Predicting Western North Pacific Ocean Climate. *J. Clim.*, **14** (20), 3997–4002.

Schneider, N., Miller, A. J., and Pierce, D. W. 2002. Anatomy of North Pacific Decadal Variability. *J. Clim.*, **15** (6), 586–605.

Schodlok, M. P., Tomczak, M., and White, N. 1997. Deep sections through the South Australian Basin and across the Australian-Antarctic Discordance. *Geophys. Res. Lett.*, **24** (22), 2785–2788.

Sen Gupta, A. and England, M. H. 2006. Coupled Ocean-Atmosphere-Ice Response to Variations in the Southern Annular Mode. *J. Clim.*, **19** (18), 4457–4486.

Serra, J. 1982. *Image Analysis and Mathematical Morphology*. Academic Press, New York, 610 pp. ISBN 0-12-637240-3.

Shaw, A. 1998. *Variability of the Southland Front*. Ph. D. thesis, University of Otago, 248 pp.

Shaw, A. and Vennell, R. 2000. A Front-Following Algorithm for AVHRR SST Imagery. *Remote Sens. Environ.*, **72** (3), 317 – 327.

Shaw, A. and Vennell, R. 2001. Measurements of an Oceanic Front Using a Front-Following Algorithm for AVHRR SST Imagery. *Remote Sens. Environ.*, **75** (1), 47–62.

Shaw, A. G. P., Kavalieris, L., and Vennell, R. 1999. Seasonal and Inter-Annual Variability of SST off the East Coast of the South Island, New Zealand. *Geocarto International*, **14** (3), 29–34.

Shchepetkin, A. F. and McWilliams, J. C. 2005. The regional oceanic modeling system (ROMS): a split-explicit, free-surface, topography-following-coordinate oceanic model. *Ocean Modelling*, **9** (4), 347–404.

Shimada, T., Sakaida, F., Kawamura, H., and Okumura, T. 2005. Application of an edge detection method to satellite images for distinguishing sea surface temperature fronts near the Japanese coast. *Remote Sens. Environ.*, **98** (1), 21 – 34.

Simpson, J. 1990. On the accurate detection and enhancement of oceanic features observed in satellite data. *Remote Sens. Environ.*, **33** (1), 17 – 33.

Small, R., deSzoeke, S., Xie, S., O'Neill, L., Seo, H., Song, Q., Cornillon, P., Spall, M., and Minobe, S. 2008. Air-sea interaction over ocean fronts and eddies. *Dyn. Atmos. Oceans*, **45** (3-4), 274–319.

Small, R. J., Tomas, R. A., and Bryan, F. O. 2014. Storm track response to ocean fronts in a global high-resolution climate model. *Climate Dynamics*, **43** (3), 805–828.

Smith, R. O., Vennell, R., Bostock, H. C., and Williams, M. J. 2013. Interaction of the subtropical front with topography around southern New Zealand. *Deep Sea Res. Part I*, **76**, 13–26.

Smythe-Wright, D., Chapman, P., Rae, C., Shannon, L., and Boswell, S. 1998. Characteristics of the South Atlantic subtropical frontal zone between 15°W and 5°E. *Deep Sea Res. Part I*, **45** (1), 167–192.

Sokolov, S. and Rintoul, S. R. 2002. Structure of Southern Ocean fronts at 140°E. *J. Mar. Syst.*, **37** (1-3), 151–184.

Sokolov, S. and Rintoul, S. R. 2007a. Multiple Jets of the Antarctic Circumpolar Current South of Australia. *J. Phys. Oceanogr.*, **37** (5), 1394–1412.

Sokolov, S. and Rintoul, S. R. 2007b. On the relationship between fronts of the Antarctic Circumpolar Current and surface chlorophyll concentrations in the Southern Ocean. *J. Geophys. Res. Oceans*, **112** (C7), C07030.

Sokolov, S. and Rintoul, S. R. 2009a. Circumpolar structure and distribution of the Antarctic Circumpolar Current fronts: 1. Mean circumpolar paths. *J. Geophys. Res. Oceans*, **114** (C11), C11018.

Sokolov, S. and Rintoul, S. R. 2009b. Circumpolar structure and distribution of the Antarctic Circumpolar Current fronts: 2. Variability and relationship to sea surface height. *J. Geophys. Res. Oceans*, **114** (C11), C11019.

Soloviev, A., Lukas, R., and Matsuura, H. 2002. Sharp frontal interfaces in the near-surface layer of the tropical ocean. *J. Mar. Syst.*, **37**, 47–68.

Spall, M. A. 1995. Frontogenesis, subduction, and cross-front exchange at upper ocean fronts. *Journal of Geophysical Research: Oceans*, **100** (C2), 2543–2557.

Stammer, D. 1998. On Eddy Characteristics, Eddy Transports, and Mean Flow Properties. *J. Phys. Oceanogr.*, **28** (4), 727–739.

Standard, J. 1961. Submarine geology of the Tasman Sea. *Geol. Soc. Am. Bull.*, **72** (12), 1777–1788.

Stanton, B. 1976. Circulation and hydrology off the west coast of the South Island, New Zealand. *N. Z. J. Mar. Freshwater Res.*, **10** (3), 445–467.

Stanton, B. and Moore, M. 1992. Hydrographic observations during the Tasman Boundary Experiment off the west coast of South Island, New Zealand. *N. Z. J. Mar. Freshwater Res.*, **26** (3-4), 339–358.

Stanton, B. and Ridgway, N. M. 1988. An oceanographic survey of the subtropical convergence zone in the Tasman Sea. *N. Z. J. Mar. Freshwater Res.*, **22** (4), 583–593.

Stanton, B. R. 1981. An oceanographic survey of the Tasman Front. *N. Z. J. Mar. Freshwater Res.*, **15** (3), 289–297.

Stanton, B. R., Sutton, P. J. H., and Chiswell, S. M. 1997. The East Auckland Current, 1994-95. *N. Z. J. Mar. Freshwater Res.*, **31** (4), 537–549.

Steele, J. H., Thorpe, S. A., and Turekian, K. K. 2009. *Elements of Physical Oceanography: A derivative of the Encyclopedia of Ocean Sciences*. Academic Press, 647 pp.

Stewart, R. H. 2008. *Introduction to physical oceanography*. Texas A & M University, 313 pp.

Stramma, L. 1992. The South Indian Ocean Current. *J. Phys. Oceanogr.*, **22** (4), 421–430.

Stramma, L. and Peterson, R. G. 1990. The South Atlantic Current. *J. Phys. Oceanogr.*, **20** (6), 846–859.

Stramma, L., Peterson, R. G., and Tomczak, M. 1995. The South Pacific Current. *J. Phys. Oceanogr.*, **25** (1), 77–91.

Streten, N. A. 1980. Some Synoptic Indices of the Southern Hemisphere Mean Sea Level Circulation 1972-77. *Mon. Wea. Rev.*, **108** (1), 18–36.

Stukel, M. R., Aluwihare, L. I., Barbeau, K. A., Chekalyuk, A. M., Goericke, R., Miller, A. J., Ohman, M. D., Ruacho, A., Song, H., Stephens, B. M., and Landry, M. R. 2017. Mesoscale ocean fronts enhance carbon export due to gravitational sinking and subduction. *Proceedings of the National Academy of Sciences*, **114** (6), 1252–1257.

Sutton, P. 2001. Detailed structure of the Subtropical Front over Chatham Rise, east of New Zealand. *J. Geophys. Res. Oceans*, **106** (C12), 31045–31056.

Sutton, P. J., Bowen, M., and Roemmich, D. 2005. Decadal temperature changes in the Tasman Sea. *N. Z. J. Mar. Freshwater Res.*, **39** (6), 1321–1329.

Sutton, P. J. H. 2003. The Southland Current: A subantarctic current. *N. Z. J. Mar. Freshwater Res.*, **37** (3), 645–652.

Sutton, P. J. H. and Bowen, M. 2014. Flows in the Tasman Front south of Norfolk Island. *J. Geophys. Res. Oceans*, **119** (5), 3041–3053.

Sutton, P. J. H. and Roemmich, D. 2001. Ocean temperature climate off North-East New Zealand. *N. Z. J. Mar. Freshwater Res.*, **35** (3), 553–565.

Swart, N. C. and Fyfe, J. C. 2012. Observed and simulated changes in the Southern Hemisphere surface westerly wind-stress. *Geophys. Res. Lett.*, **39** (16), L16711.

Szymanska, K. and Tomczak, M. 1994. Subduction of central water near the subtropical front in the southern Tasman Sea. *Deep Sea Res. Part I*, **41** (9), 1373–1386.

Talley, L. D., Pickard, G. L., Emery, W. J., and Swift, J. H. 2011. *Descriptive Physical Oceanography: An Introduction (Sixth Edition)*. Boston: Academic Press, 555 pp.

Tate, P. M. 1988. Monthly mean surface thermal structure in the Tasman Sea from satellite imagery, 1979-84. *Aust. J. Mar. Freshwater Res.*, **39** (5), 579–588.

Tate, P. M. and Gay, S. L. 1986. Satellite oceanography of the southern Tasman Sea. Ocean Sciences Institute Report No. 16. University of Sydney, 10 pp.

Tate, P. M., Jones, I. S., and Hamon, B. 1989. Time and space scales of surface temperatures in the Tasman Sea, from satellite data. *Deep Sea Res. Part A*, **36** (3), 419–430.

Thompson, D. W. J. and Solomon, S. 2002. Interpretation of Recent Southern Hemisphere Climate Change. *Science*, **296** (5569), 895–899.

Tilburg, C. E., Hurlburt, H. E., O'Brien, J. J., and Shriver, J. F. 2002. Remote Topographic Forcing of a Baroclinic Western Boundary Current: An Explanation for the Southland Current and the Pathway of the Subtropical Front East of New Zealand. *J. Phys. Oceanogr.*, **32** (11), 3216–3232.

Tippins, D. and Tomczak, M. 2003. Meridional Turner angles and density compensation in the upper ocean. *Ocean Dyn.*, **53** (4), 332–342.

Tomczak, M. and Godfrey, J. 2003. *Regional Oceanography: an Introduction (Second Edition)*. Daya Publishing House, Delhi, 390 pp.

Tomczak, M., Pender, L., and Liefrink, S. 2004. Variability of the Subtropical Front in the Indian Ocean south of Australia. *Ocean Dyn.*, **54** (5), 506–519.

Uddstrom, M. J. and Oien, N. A. 1999. On the use of high-resolution satellite data to describe the spatial and temporal variability of sea surface temperatures in the New Zealand region. *J. Geophys. Res. Oceans*, **104** (C9), 20729–20751.

Uenzelmann-Neben, G., Grobys, J., Gohl, K., and Barker, D. 2009. Neogene sediment structures in Bounty Trough, eastern New Zealand: Influence of magmatic and oceanic current activity. *Geol. Soc. Am. Bull.*, **121** (1-2), 134–149.

Ullman, D. S. and Cornillon, P. C. 1999. Satellite-derived sea surface temperature fronts on the continental shelf off the northeast U.S. coast. *J. Geophys. Res. Oceans*, **104**, 23459–23478.

Ullman, D. S. and Cornillon, P. C. 2000. Evaluation of Front Detection Methods for Satellite-Derived SST Data Using In Situ Observations. *J. Atmos. Oceanic Technol.*, **17** (12), 1667–1675.

Ullman, D. S. and Cornillon, P. C. 2001. Continental shelf surface thermal fronts in winter off the northeast US coast. *Cont. Shelf Res.*, **21** (11-12), 1139–1156.

Ullman, D. S., Cornillon, P. C., and Shan, Z. 2007. On the characteristics of subtropical fronts in the North Atlantic. *J. Geophys. Res. Oceans*, **112** (C1), C01010.

Ummenhofer, C. C., Sen Gupta, A., and England, M. H. 2009. Causes of Late Twentieth-Century Trends in New Zealand Precipitation. *J. Clim.*, **22** (1), 3–19.

Wall, C. C., Muller-Karger, F. E., Roffer, M. A., Hu, C., Yao, W., and Luther, M. E. 2008. Satellite remote sensing of surface oceanic fronts in coastal waters off west-central Florida. *Remote Sens. Environ.*, **112** (6), 2963 – 2976.

Warmus, K. 1989. *Subtropical convergence. R.V. Franklin Cruise FR11/88-data report. Ocean Sciences Institute Technical Report No. 20*. University Of Sydney, 36 pp.

Waugh, S., Troup, C., Filippi, D., and Weimerskirch, H. 2002. Foraging Zones of Southern Royal Albatrosses. *The Condor*, **104** (3), 662–667.

Williams, A., Althaus, F., Clark, M., and Gowlett-Holmes, K. 2011. Composition and distribution of deep-sea benthic invertebrate megafauna on the Lord Howe Rise and Norfolk Ridge, southwest Pacific Ocean. *Deep Sea Res. Part II*, **58** (7-8), 948–958.

Woodson, C. B. and Litvin, S. Y. 2015. Ocean fronts drive marine fishery production and biogeochemical cycling. *Proc. Natl. Acad. Sci. U.S.A.*, **112** (6), 1710–1715.

Wu, L., Cai, W., Zhang, L., Nakamura, H., Timmermann, A., Joyce, T., McPhaden, M. J., Alexander, M., Qiu, B., Visbeck, M., Chang, P., and Giese, B. 2012. Enhanced warming over the global subtropical western boundary currents. *Nature Clim. Chang.*, **2** (3), 161–166.

Wyrtki, K. 1962. The subsurface water masses in the Western South Pacific Ocean. *Aust. J. Mar. Freshwater Res.*, **13**, 18–47.

Zar, J. 1998. *Biostatistical Analysis, 4th Edition*. Prentice Hall, 929 pp.

Zhang, H. and Wu, L. 2010. Predicting North Atlantic sea surface temperature variability on the basis of the first-mode baroclinic Rossby wave model. *J. Geophys. Res. Oceans*, **115** (C9), C09030.

Appendix A

Geostrophic velocities calculated from cruise TAN0704, TAN0803 and TAN1106

Absolute geostrophic velocities were calculated for the hydrographic sections analysed in **Chapter 3**. The velocities are calculated following the dynamic method (Pond and Pickard, 1983) and using the sea floor as a level of no motion, as assumed by earlier studies in this region (Morris et al., 2001; Sutton, 2003).

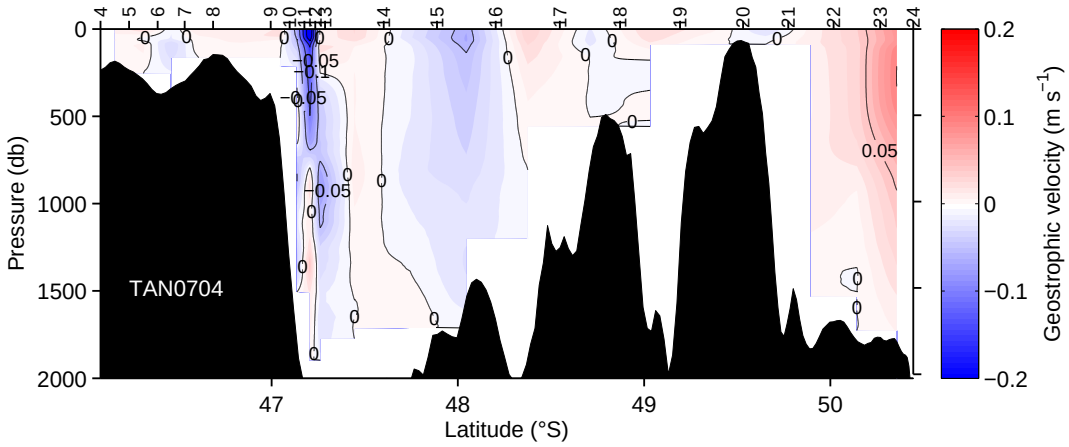

Figure A.1: Geostrophic velocity through the upper 2000 m along the Macquarie Ridge during cruise TAN0704. Contour intervals are 0.05 ms^{-1}. Station numbers are indicated on the top axis. Positive values are to the east. The level of no motion is set at the sea floor.

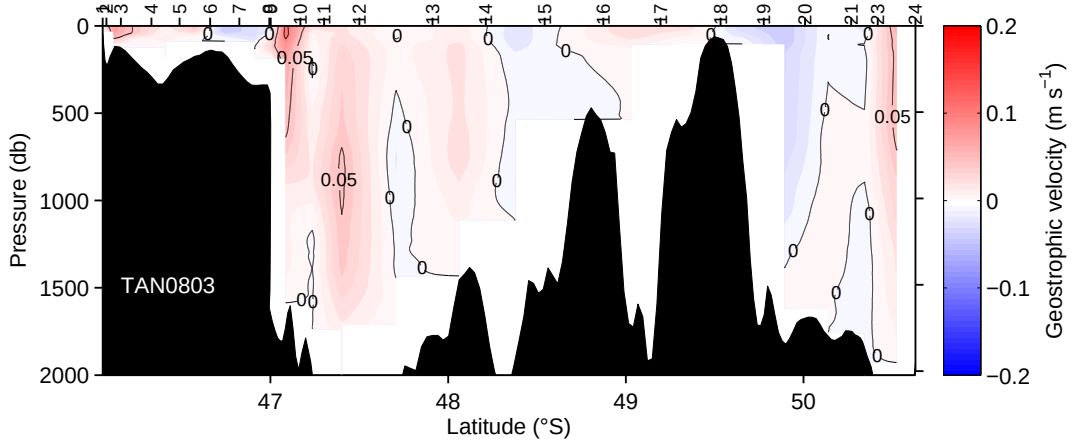

Figure A.2: Geostrophic velocity through the upper 2000 m along the Macquarie Ridge during cruise TAN0803. Contour intervals are 0.05 ms^{-1}. Station numbers are indicated on the top axis. Positive values are to the east. The level of no motion is set at the sea floor.

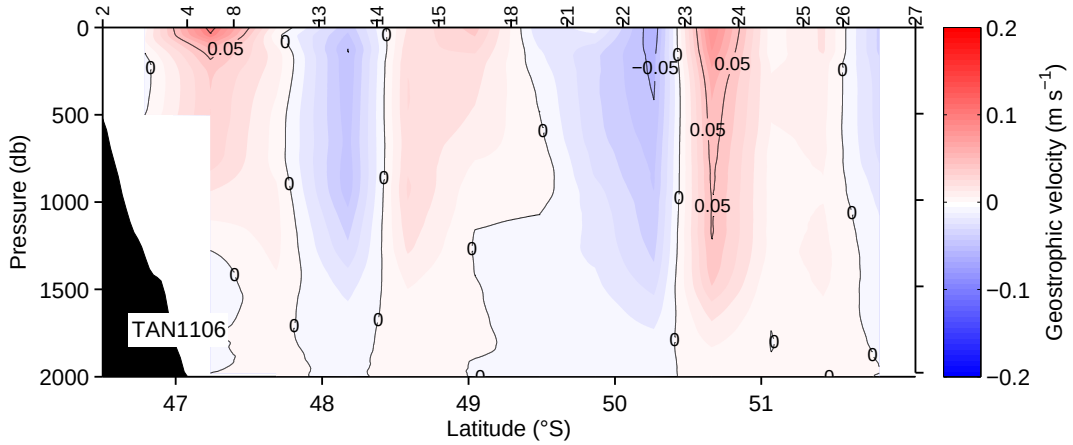

Figure A.3: Geostrophic velocity through the upper 2000 m of the Solander Trough during cruise TAN1106. Contour intervals are 0.05 ms^{-1}. Station numbers are indicated on the top axis. Positive values are to the east. The level of no motion is set at the sea floor.

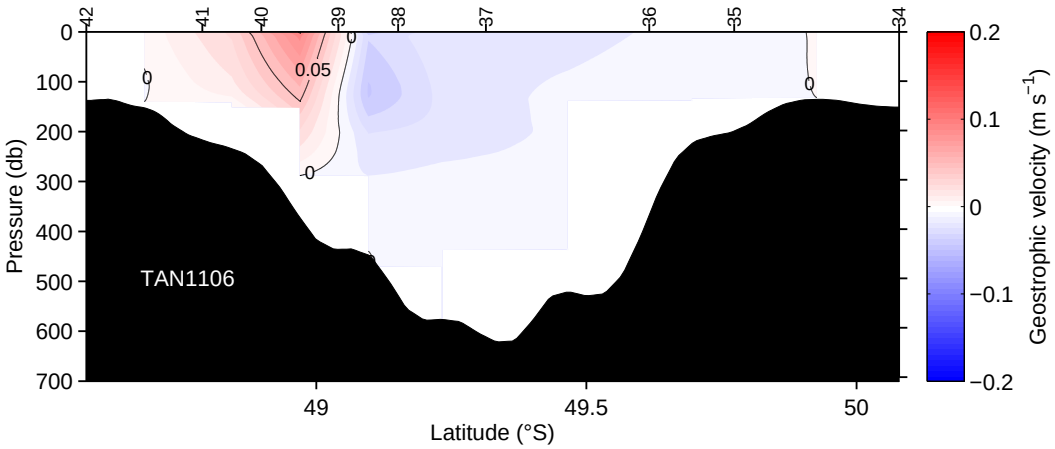

Figure A.4: Geostrophic velocity through the upper 700 m of the Snares Depression during cruise TAN1106. Contour intervals are 0.05 ms^{-1}. Station numbers are indicated on the top axis. Positive values are to the east. The level of no motion is set at the sea floor.

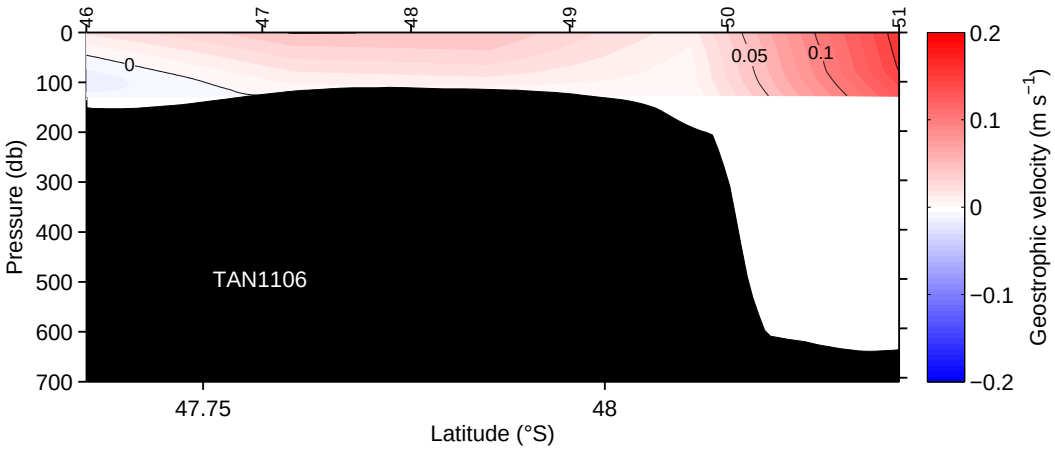

Figure A.5: Geostrophic velocity through the upper 700 m of the shelf break of the Snares Shelf and upper continental slope during cruise TAN1106. Contour intervals are 0.05 ms^{-1}. Station numbers are indicated on the top axis. Positive values are to the north. The level of no motion is set at the sea floor.

Appendix B

Mathematical Morphology

Mathematical Morphology is a concept based on set theory that provides tools to modify the shape of sets of pixels in a binary image, composed of zeroes (0s) and ones (1s) (Serra, 1982). An example of a binary image is shown in A.1. Morphology operations transform a binary image, *B*, into an output image, *B*', with the same dimensions as the input image using set operations. Applying a local morphology operation the output value at a specific coordinate within *B*' is dependent on the input values from *B* in the neighbourhood of that coordinate. The neighbourhood is defined by a structuring element, *S*, which consists of a small binary matrix, much smaller than the input image, composed of a pattern of 0s and 1s that define the neighbourhood about a central pixel defined here as the origin.

The morphological operation utilised in the front analysis algorithm (**Chapter 3**) is a dilation operation; dilation operations causes sets of pixels to grow in size. The amount of growing is set by the neighbourhood structure defined in the structuring element. Following Serra (1982), operations on an image refer here to operations on the set of all locations in a binary image that are set to 1s (i.e. pixels), rather than the image as a whole. Below, the principles of dilation operation are briefly outlined. Full mathematical backgrounds to image morphology techniques are given in Serra (1982).

Suppose that a binary image, *B*, contains an object *A*, composed of the set of pixels $A = B_1(i,j), B_2(i,j), \ldots, B_n(i,j)$, where the subscripts (i,j) define co-ordinates of the pixels within *B*. Let us define a structuring element, *S*, that consists of a matrix defining an arbitrary local neighbourhood structure. If *S* is placed in the binary image *B* with its origin at (i,j), we denote it by $S(i,j)$. The dilation ($\oplus$) of *B* by *S*, is the union ($\cup$) of copies of *S* centered and placed at every pixel location in *B* where $B(i,j) \in A$, where $\in$ is the symbol for an element of:

$$B' = B \oplus S = \bigcup_{(i,j) \in A} S(i,j). \tag{B.1}$$

Thus, the dilation operation loops over the pixels of B where $B(i, j) \in A$ and places a copy of S, in the output image B'. Figure B.1 illustrates the dilation of an object A, consisting of a set of 3 pixels marked by 1s in the binary input image B, with a structuring element, S, designed to dilate the frontal segment northward by 1 pixel. Also shown is the resulting output image, B' containing the dilation of object A. In Section 4.8 the dilation operation is used as a computationally efficient procedure to rearrange a set of pixel masks, used to sample the surface hydrographic conditions surrounding a thermal front.

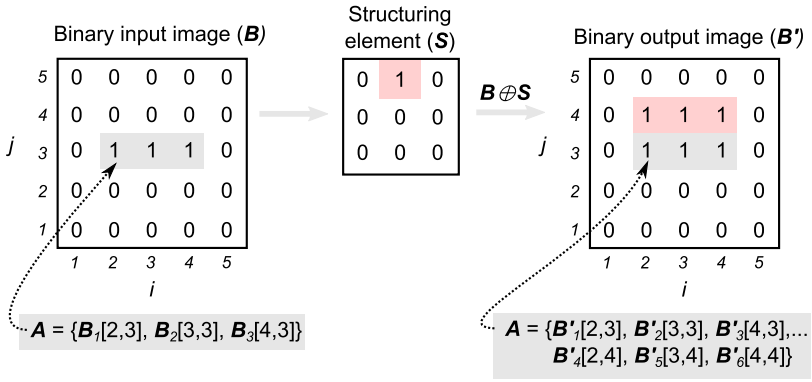

Figure B.1: Example of the mathematical morphology operation of dilation on a binary input image (left) using the structuring element S (centre). The location of pixels in the binary input image are highlighted by grey shading. Pixel values in the output image (right) that have been modified by the dilation operation are highlighted by pink shading.

Appendix C

Hypothesis testing of thermal front histograms

In **Chapter 4**, the statistical significance of front frequency (at the 0.05 level) within each of the four regions was assessed by comparing the number of front segments found within each bin, within a given region, to the number that would be expected to be found in that bin if front segments were distributed randomly throughout the region, in proportion to the number of months a bin was clearly viewed, as a homogenous Poisson process with a mean frequency of occurrence and variance $\sigma^2 = \lambda$,

$$\lambda = \frac{\sum nf}{\sum O}, \tag{C.1}$$

where nf is the total number of front segments observed within a region, summed over all bins and over 30 years, and O is the total number of months that all bins were clearly viewed, summed over 30 years. The Poisson distribution was used to estimate upper and lower critical values for the number of thermal fronts that might be expected to occur in each bin, if fronts were distributed randomly in this way. Bins with a front-count that falls between these critical levels indicates the number of fronts detected in a bin is statistically indistinguishable from a random distribution of the same number of fronts throughout the bins, whereas, bins with a front count outside these critical levels indicate that the number of fronts detected in a bin is statistical significant ($p < 0.05$) compared to the number of fronts that would be expected had the front been randomly distributed (Ullman and Cornillon, 1999).

To illustrate this hypothesis testing, consider, for example, the bin centered at 48.75°S in Region 3 (Fig. C.1). The bin was observed to contain 47 thermal fronts (Fig. C.1a) out of 120 clearly viewed months (Fig. C.1b), for the period 1982-2011, translating to an annual average front frequency of 0.39 (Fig. C.1c). The annual average front frequency for this

region is $\lambda = 0.22$. Using the Poisson distribution, one estimates upper and lower critical values for the number of strong fronts we expect to observe in the bin, given 120 clearly viewed months, as falling between 35 and 14 fronts. Converting these critical values into a front frequency by dividing by 120 (number of observable months), we obtain a critical front frequencies of 0.12 (0.05) and 0.29 (0.95). The observed front frequency (0.39) is outside these critical values, implying that the observed front frequency is statistically significant ($p < 0.05$) compared to the front frequency that would be expected had the fronts been randomly distributed throughout the region (Fig. C.1c).

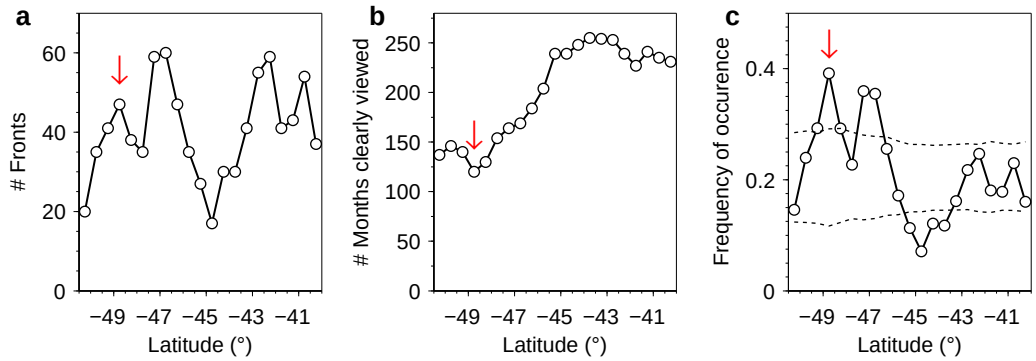

Figure C.1: Example of the hypothesis testing of the frequency of occurrence of thermal fronts detected in Region 3 (Fig. 4.2) of the period 1982-2011 and described in the text. (a) Front count histogram. (b) Clear count histogram. (c) Frequency of occurrence of thermal fronts histogram.

Appendix D

Sensitivity of front frequency to the definition of a strong thermal front

An experiment was performed to test the sensitivity of the patterns of annual-mean (1982-2011) thermal front occurrence (Fig. 5.7-5.10) with respect to the definition of a strong, thermal front.

Five subsets of thermal fronts were extracted from the data set of thermal fronts detected in 30 years (1982-2011) the PFV5.2 monthly composite SST images (**Chapter 4**). A minimum threshold on the mean SST gradient magnitude at a thermal front was chosen and used to extract each subset. Five thresholds were chosen, set at between 2°C 100 $km^{-1}$and 6°C 100 km^{-1} in 1°C increments. In relative terms, these thresholds are between approximately two and seven times the 0.8°C 100 km^{-1}annual-mean ambient meridional SST gradient magnitude in the Tasman Sea (Uddstrom and Oien, 1999). The statistical analysis of thermal front occurrence (Section 5.4.1) was then repeated in turn for Regions 1-4 using each of these data subsets (Fig. D.1).

Generally speaking, the distributions of the frequency of occurrence of strong, thermal fronts are insensitive to the criteria chosen to define a strong thermal front. Bands of higher front frequency identified in the distributions of thermal fronts that have a gradient stronger than 2.5°C 100 km^{-1} (Fig. 5.7-5.10) are also evident when using a stricter criteria on what is considered a strong thermal front (Fig. D.1). For example, in the western Tasman Sea (Region 1) there are two identifiable peaks in the distribution of thermal fronts that have an SST gradient magnitude > 2.5°C 100 km^{-1}, located near 42°S and 45°S, respectively (Fig. 5.7b). These identifiable peaks are also evident in the distribution of thermal fronts along this transect that have a minimum SST gradient magnitude of between 2°C 100 $km^{-1}$and 4°C 100 km^{-1}, though these peaks become less distinguishable at gradient magnitudes of above 4°C 100 km^{-1}(Fig. D.1a).

Generally the same can be said for the distributions of thermal fronts in the central Tasman Sea (Region 2, Fig. D.1b), eastern Tasman Sea (Region 3, Fig. D.1c) and south of New Zealand (Region 4, Fig. D.1d), although small (<1° latitude) differences in the location of identifiable peaks in the thermal front distributions are evident in the central Tasman Sea (Fig. D.1b). This suggests that the bands of elevated occurrence of thermal fronts identified in this study are unlikely to be artifact due to the choice of criteria used to define a strong, thermal front, but are fairly robust features.

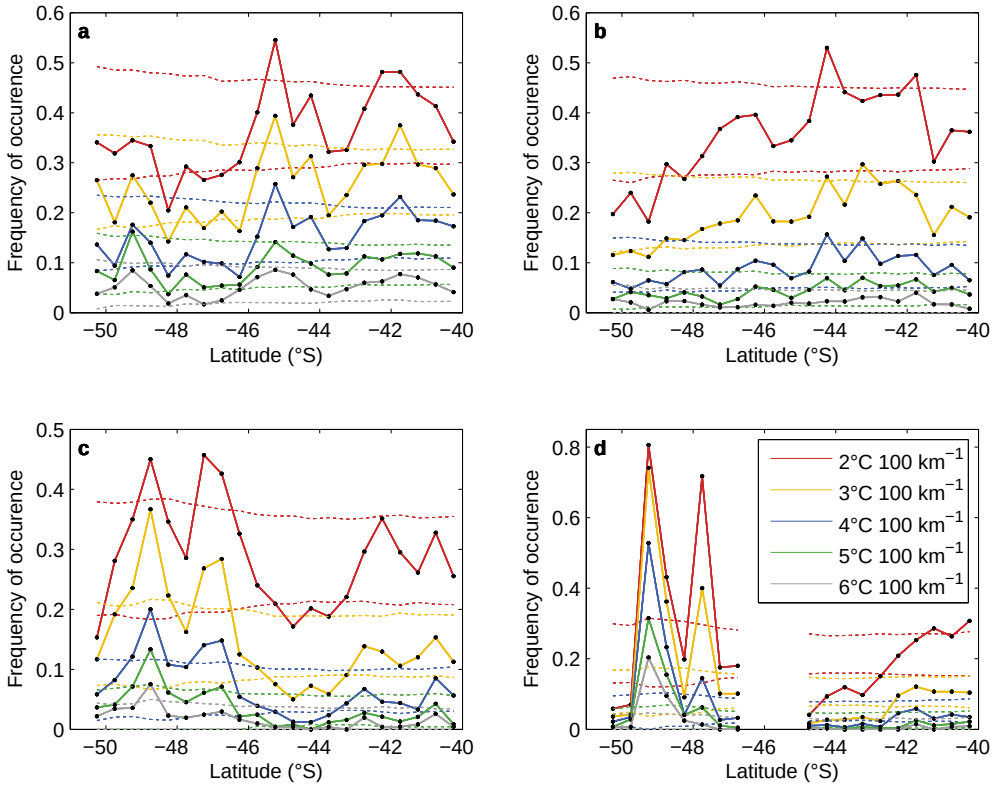

Figure D.1: Histograms of the annual-mean (1982-2011) frequency of occurrence of strong thermal fronts across (a) Region 1 (western Tasman Sea), (b) Region 2 (central Tasman Sea), (c) Region 3 (eastern Tasman Sea) and (d) Region 4 (southern New Zealand) for a range of different thresholds on the definition of a 'strong' thermal front (colours). The dashed lines represent the critical values, outside which the number of fronts found within a bin is significantly significant (at the 0.05 level) compared to that which would be expected if the fronts were distributed randomly throughout the bins, in proportion to the number of months each bin was clearly viewed (see Appendix C).

Appendix E

Gap filling of the S-STF time series

In this study, a set of short data gaps in the three frontal time series (Section 6.2.2, Fig. E.1) are filled using the Singular Spectrum Analysis (SSA) gap-filling method (Kondrashov and Ghil, 2006). Emery and Thomson (2001) discuss several basic mathematical techniques available to fill short gaps in geophysical data series, the most basic being linear interpolation and reconstruction of missing data using cubic splines. The motivation for using the newer SSA-based technique (Kondrashov and Ghil, 2006) is that it is designed specifically for geophysical time series; it uses robust, oscillatory modes identified within an incomplete time series to fill gaps, and in doing so preserves low-frequency signals and discards variance associated with noise. The quality of the filled-in data is optimized by a series of cross-validation experiments, which also allow the quality of the filled-in data to be assessed. The method has also been used to fill short gaps in geophysical time series similar to those faced with in the present study (see e.g. Kondrashov et al., 2005; Kondrashov and Ghil, 2006). A short description of the SSA gap-filling method and its implementation in this study is given below; further details are given in Kondrashov and Ghil (2006) .

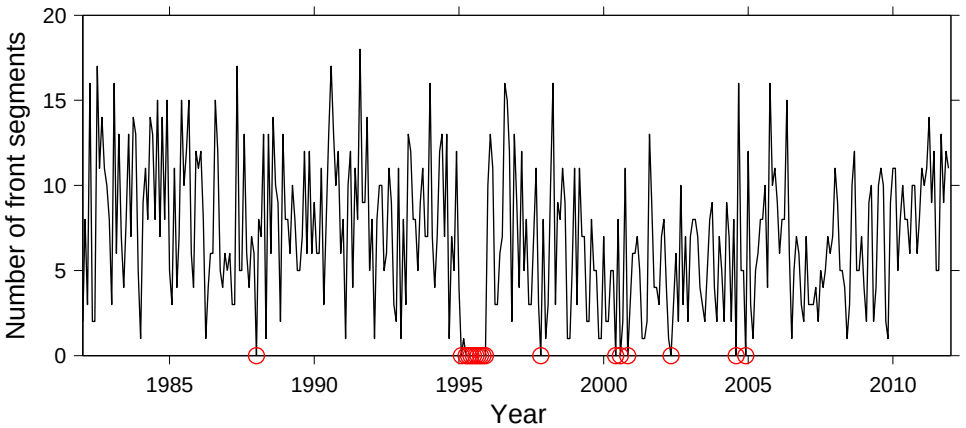

Figure E.1: The number of front segments that contribute in a weighted fashion to the frontal time series. Months where no front segments were detected within the S-STF region (Fig. 6.1) are highlighted with red circles.

The SSA gap-filling method involves generating a reconstruction of an original, gap-filled time series based on an optimum combination of oscillatory components, or modes, embedded in that time series. Data from this reconstruction are then used to fill gaps in the original time series. A SSA-based algorithm (Kondrashov and Ghil, 2006) is used to compute the oscillatory modes embedded in a time series, and combine these to produce a reconstructed time series. An overview of the principles of SSA, which is beyond the scope of this thesis, are covered in Ghil et al. (2002). The SSA gap-filling method uses a set of 30 cross-validation (CV) experiments to optimize the window width (M) and the number of leading oscillatory modes (K) used by the SSA algorithm to produce the actual reconstructed time series; here M determines the longest period of an oscillatory component that can be captured by the SSA-algorithm. In each CV experiment, a fixed fraction of the original time series data is selected at random, then flagged as CV points and set to missing. Reconstructions of these 'synthetic' time series are then produced over a range of plausible values for M and K. The optimal combination of parameters (M* and K*) for producing the final reconstruction are determined by the global minimum root-mean-square (RMS) error - between the original time series and reconstructed time series at CV points - averaged over all CV experiments as a function of M and K. The final reconstruction is obtained by applying the SSA-based algorithm to the original time series, using the optimal parameters obtained from the cross-validation experiments (M* and K*).

In this study, the SSA-gap filling procedure (Kondrashov and Ghil, 2006) was applied to the frontal time series (Section 6.2.2), to form temporally complete 30 year (1982-2011) records. The optimum SSA parameters (M and K) for filling gaps in each frontal time series were found by carrying out three sets of 30 cross-validation experiments, with one set of experiments for each of the three frontal time series. In each CV experiment, 5% of the available data was removed from the time series in a manner consistent with the structure of the actual data gaps (Fig. E.1), consisting of one continuous 12 month gap and six individual months selected at random. This means the total amount of missing data in each CV experiment is approximately twice that in the original time series, consisting of two 12-month gaps and 14 individual months. In the cross-validation experiments, the ranges of M and K searched were M = 40 to 140 (months) at intervals of 10 and K = 1 to 40 at intervals of 1. These ranges of M were chosen to ensure that low-frequency ENSO-related variability (36-60 months), together with any lower frequency variability that might be present in the time series, could be captured by the SSA-algorithm. The SSA-based algorithm, as implemented in the SSA-MTM Toolkit (http://www.atmos.ucla.edu/tcd/ssa) was used to perform the time series reconstructions.

Figure E.2 shows the results of the 30 cross-validation experiments for each of the S-STF time series. Cross-validation results for the subtropical SST time series (Fig. E.2a) suggests

that the optimum SSA parameters for gap-filling are M* = 50 (i.e. 50 months) and K* = 3 (i.e. three oscillatory modes); these parameters minimise the global RMS error between reconstructions and cross-validation points averaged over the 30 CV experiments.

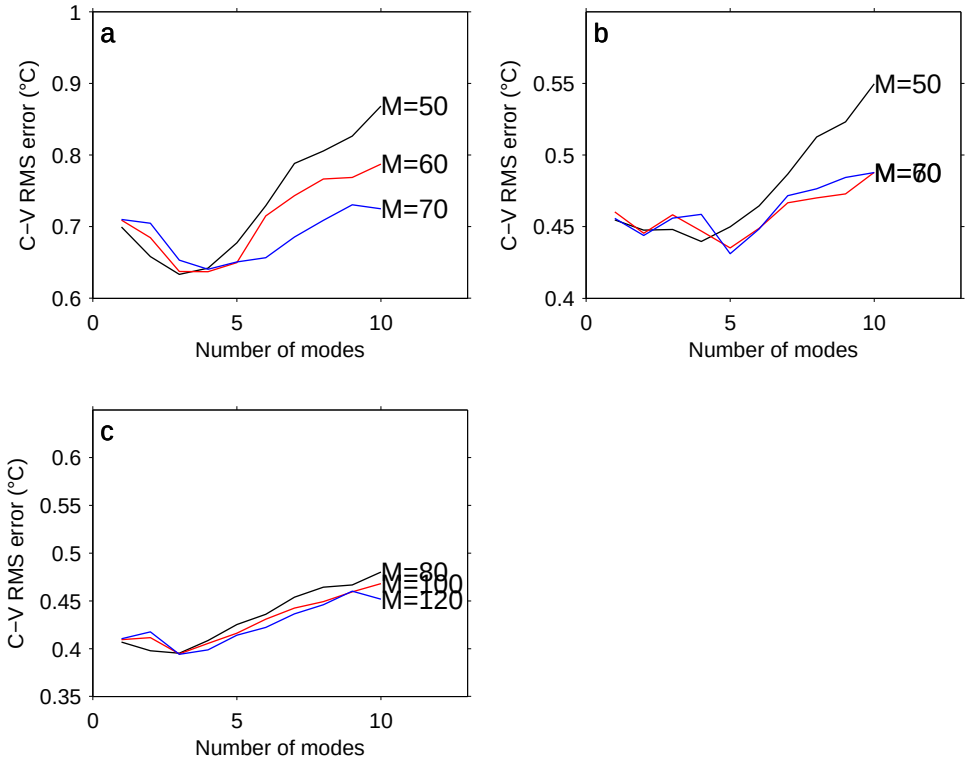

Figure E.2: Results of cross-validation experiments for the SSA-gap filling procedure for (a) the subtropical SST, (b) Subantarctic SST and (c) S-STF temperature differential time series. Experiments with both larger and smaller window sizes (M) than those shown above, and with a larger numbers of oscillatory modes (K), resulted in lager RMS errors and thus poorer quality reconstructions.

The CV experiments for the Subantarctic SST time series (Fig. E.2b) suggest optimum SSA parameters for gap-filling are M*=70 and K* = 5. The CV experiments for the S-STF temperature differential time series (Fig. E2.c) show optimum SSA-parameters for gap filling are a longer window size of 120 months (M = 120) and three leading oscillatory modes (K=3). To assess the quality of the gap-filled data, we compared the average RMS error of the gap-filled data (i.e. the values shown in Fig. E.2 at the optimum SSA-parameters described above) with the standard deviation of the remotely sensed SST data that went in to calculating the monthly-mean values in each time series, averaged across each of the respective time series. The RMS error on the gap-filled data, using the optimum SSA-parameters described above, are 0.64°C, 0.44°C and 0.40°C for the subtropical, Subantarctic and temperature differential time series, respectively (Fig. E.2). The standard deviation of the of the remotely sensed SST data that went in to calculating the monthly-mean values in each time series,

averaged across each of the respective time series, are approximately 0.48°C, 0.37°C and 0.40°C, respectively. The fact that RMS errors on the gap-filled data are of the same order of magnitude, and indeed relatively close, to the spread in the actual data provides confidence that the gap-filled data are reasonable. SSA-gap filling was therefore performed on each of the three S-STF time series, using the optimum SSA-parameters described in the text above.